COMPUTER MODELING AND ANALYSES OF MULTISECTION DISTRIBUTED FEEDBACK LASERS

by

So-Kuen C. Liew

June, 1995

A Dissertation

Submitted in partial fulfillment of the requirements

for the degree of

Doctor of Philosophy

in

Department of Electronic Engineering

The Chinese University of Hong Kong

TA
1700
.L44
1995
ult

ABSTRACT

The past three decades have witnessed the rapid advancement of the semiconductor laser technology. It has evolved from a laboratory novelty to an off-the-shelf component on one hand, and a sophisticated device in highly specialized applications on the other. Spurred on by the demand of single-wavelength transmitters with narrow linewidth for applications in optical transmission and monolithic optoelectronic integrated systems, the *distributed feedback* (DFB) laser has emerged as the laser of choice. As the technology advances, the design of DFB lasers has become more and more sophisticated and complex. It is imperative to have a computer model to help in the design process. This thesis is an endeavor in this subject matter. It is also a step toward a *Computer-Aided-Design* (CAD) tool for future optoelectronic-integrated-circuit similar to the CAD tool that is used today for silicon circuits. This report is organized into two parts. The first part describes and explains a general nonlinear numerical model developed in this work. To demonstrate the applicability of the model, the second part presents the analyses of two novel DFB laser designs.

For the calculation of the static laser properties at above-threshold conditions, a modeling approach called the power matrix method is chosen. This method is based on the commonly used transfer-matrix approach and the coupled-wave theory. It also takes into account nonlinear effects such as spontaneous emission, gain saturation, and carrier-induced index change. This work generalizes this approach for DFB lasers with up to three sections. The description of the grating is also extended to second-order gratings, gain-grating with induced index-grating, and absorptive-grating with loss saturation. Other modifications are aimed at improving the accuracy of the calculation. They include an expansion of the method to enable a fully multimode calculation, and the direct and more accurate computation of the spectral lineshape, output power and photon density.

The above-threshold model is first applied to a novel three-section second-order distributed-feedback-distributed-Bragg-reflector (DFBDBR) laser. This marks the first above-threshold analysis of this laser. The laser has a center pumped section that is terminated by two unpumped grating sections. The calculated results are consistent with earlier experimental observation that the laser operates with a peaked nearfield intensity distribution along the laser cavity. The analysis also reveals some new results which lead to better understanding of the mode-selection mechanism. The critical design parameters are identified. Their values for optimized performance are obtained which indicate good tolerance. The DFBDBR laser is also found to have reduced longitudinal spatial hole burning and a smaller effective linewidth enhancement factor compared with those of a uniformly pumped single-section second-order DFB laser. These improvements can be explained in large part by the concept of effective reflectivity bandwidth.

Next, the complex-coupled DFB (CCDFB) lasers with index- and loss-coupled gratings are analyzed at above-threshold conditions. Since the common concern is the extra loss introduced by the absorptive grating, the analysis focuses on the threshold current and front-facet power slope efficiency. As expected, the extra loss can be reduced to an acceptable level by using a small grating duty cycle. Furthermore, the use of asymmetric facet coating can boost the output power from the front facet at small coupling coefficients. Hence, low-threshold and high-efficiency CCDFB lasers with absorptive gratings are possible. However, these improvements are also accompanied by the degradation of the single-mode property of the loss-coupled DFB laser. Since the degradation can be inferred from the theoretical single-mode yield, a yield analysis of the purely loss-coupled DFB laser is carried out. The results suggest that small reduction in yield can be achieved by choosing appropriate coupling coefficients. Thus, the use of asymmetric facet coating is a viable method in improving the performance of loss-coupled DFB lasers.

ACKNOWLEDGMENTS

I would like to express my deepest gratitude to my beloved husband, Dr. Soung-Chang Liew. Without his never-ceasing encouragement and support, throughout the good and the bad times, this work could not have been possible. I would also like to dedicate this work to my two sons, Vincent Hau-Yian and Austin Jun-Yian for making my life much more colorful and vibrant, although exhausting at times.

My special thanks to Dr. Kam Tai Chan, my thesis supervisor, for his kind support and guidance and Prof. Omar Wing for generous financial support.

I would also like to express my appreciation to my colleagues at the David Sarnoff Research Center for making my stay there feel like a 'home' away from home. Special thanks to Dr. Nils W. Carlson (now at the Lawrence Livermore National Laboratory, California, U. S. A.), whose insights and valuable discussions have always been a source of inspirations to me. I am also indebted to Dr. Robert Amantea for guidance and suggestions at the beginning of this project, Dr. Joseph H. Abeles and Prof. Gary A. Evans (now at Southern Methodist University, Texas, U. S. A.) for stimulating and helpful discussions.

Warmest thanks to Dr. Robert H. Rediker (Massachusetts Institute of Technology, Massachusetts, U. S. A.) for introducing me to the exciting world of semiconductor lasers.

Finally, no words can express my gratitude to my parents for making the sacrifices that they have made to provide me with the timely opportunities to achieve all that I have achieved.

TABLE OF CONTENTS

COMPUTER MODELING AND ANALYSES OF MULTISECTION DISTRIBUTED FEEDBACK LASERS

1 INTRODUCTION

This chapter presents the background information on the *distributed feedback* (DFB) lasers and discusses the motivations for the development of a nonlinear multisection DFB model (*Section 1.1*). This is followed by an overview of the major achievements of this work, which include the development of a precise theoretical model (*Section 1.2*) and the analyses of two novel DFB devices (*Section 1.3*). Finally, *Section 1.4* outlines the overall organization of this thesis.

1.1 Distributed Feedback Lasers

The past three decades have witnessed the rapid advancement of the semiconductor laser technology. It has evolved from a laboratory novelty to an off-the-shelf component in popular commercial products (e. g. the compact disc player) on one hand, and a sophisticated device in highly specialized applications on the other. Today, the emission wavelengths of diode lasers cover the optical spectrum from the blue (ZnSe compounds) to the infrared (lead-salt compound). In the last two decades or so, spurred on by the demand of single-wavelength transmitters with narrow

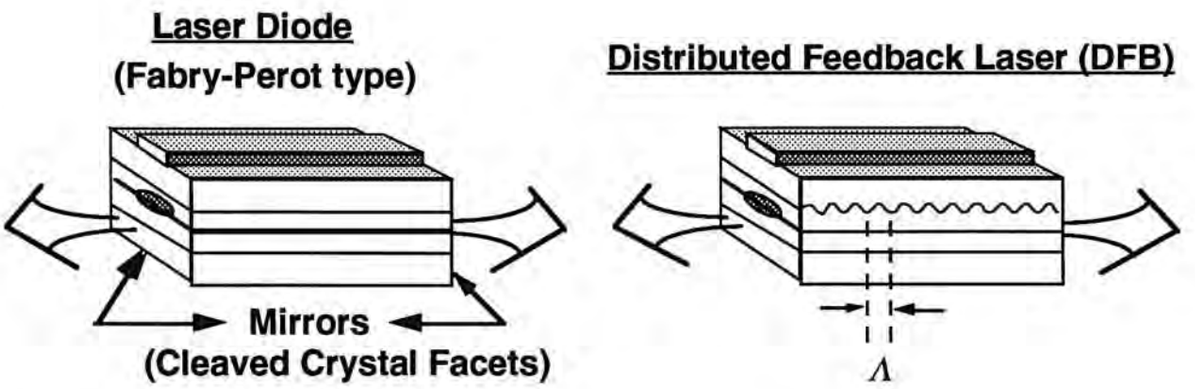

Fig. 1.1 *Gratings are used in lieu of facet mirrors for optical feedback in a DFB laser. Λ denotes the period of the grating.*

linewidth for applications in optical transmission and monolithic optoelectronic integrated systems, one particular class of semiconductor lasers has emerged as the laser of choice. It is called the *distributed feedback* laser.

The DFB laser outperforms the conventional *Fabry Perot* (FP) laser (Fig. 1.1) in many ways. In the FP laser, the optical feedback that is essential for lasing action is provided by the cleaved crystal facets that act as mirrors. Because there is little discrimination among the laser modes, the side-mode-suppression ratio (SMSR) is only about 10 dB to 13 dB. SMSR is the ratio between the peak power of the lasing mode and that of its most dominant side-mode. The laser typically operates with 3 or 4 laser lines. The temperature dependence of the wavelength is quite large, $\frac{d\lambda}{dT}$~5.0 to 10.0 Å/°C. As a result, the operation is not very stable.

The DFB laser, on the other hand, relies on the monolithic Bragg diffractive gratings for optical feedback. The grating is defined on an epitaxial layer and is embedded within the laser structure as shown in Fig. 1.1. The resulting periodic change in refractive index along the laser cavity gives rise to frequency-selective reflectivity. The grating period is given by $\Lambda = \frac{m\lambda_B}{2n}$, where m, an integer, is the

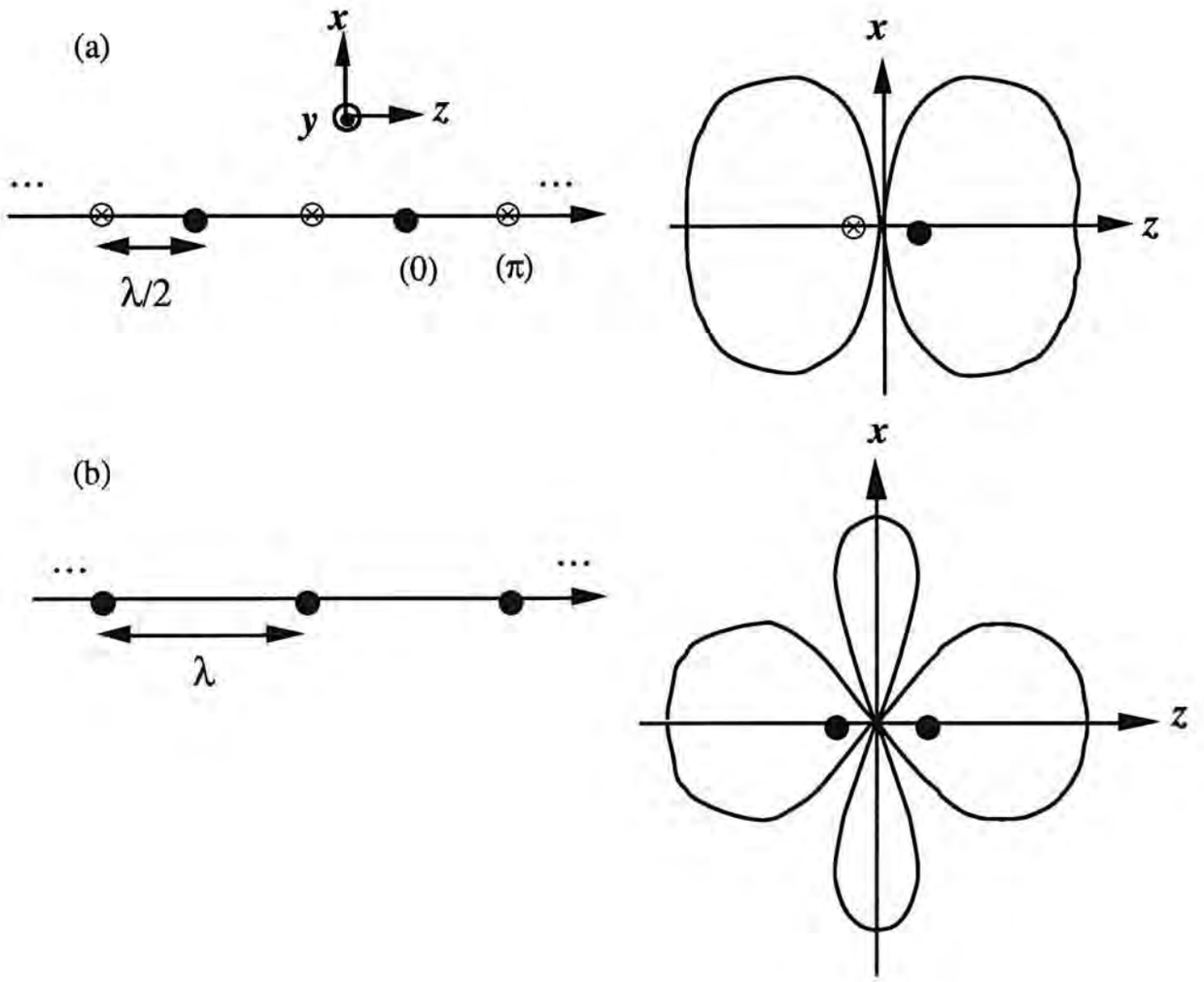

Fig. 1.2 *Grating as an array of dipole elements: (a) First-order grating: radiation pattern of one pair of adjacent dipoles indicates destructive interference in x-direction (perpendicular to junction plane); (b) Second-order grating: constructive interference in x-direction.*

diffraction order; λ_B is the free-space Bragg wavelength, and n is the effective index of refraction. For first-order gratings, m =1 and for second-order grating, m =2. Physically, the grating teeth are one half-wavelength apart for first order and one full wavelength apart for second order. The second-order gratings are easier to fabricate because of the larger spacing. However, the average maximum reflectivity per unit length is half that of a first-order grating with the same refractive-index step. There is another important difference. As illustrated in Fig. 1.2, each grating tooth may be

regarded as a dipole-element that re-radiates the light. If the teeth are one half-wavelength apart, then there is a π-phase shift between adjacent dipole-elements. As a result, constructive interference of the radiation is only in the horizontal direction (along laser cavity or z). In contrast, constructive interference for teeth at one-wavelength spacing also occurs in the direction perpendicular to the junction plane (transverse direction or x). Consequently, the second-order grating radiates at right angles as well as reflecting along its length [Carr93]. Unlike those of the FP lasers, the different lasing modes of the DFB lasers have rather different threshold gain (gain that is required to reach lasing threshold), g_{th}, due to the spectral filtering effects of the grating. In particular, the modes nearest to the Bragg frequency have the lowest g_{th} or loss. As a result, the operation is very often single-moded. The SMSR is typically 20 dB to 30 dB. The spectral linewidth is also narrow. Since λ is determined by the grating, the temperature (T) dependence of the lasing wavelength (λ) is a function of the change of n with respect to T. The value is typically ~0.5 to 1.0 Å/°C. It means that the operation is stable and not easily affected by changes in the ambient temperature.

To summarize, compare with FB laser, DFB laser has the advantages of exact wavelength specification, stable single-mode operation with high SMSR, and narrow spectral linewidth. In addition, its planar design offers greater flexibility and ease in the monolithic integration with other optoelectronic components such as amplifiers and modulators. Other merits include properties that are shared by other semiconductor lasers: compactness, high efficiency, the capability of being directly modulated at gigabits-per-second rates, and long operation lifetime. All these contribute to the popularity of the DFB lasers. The wavelengths for optical-communication applications are typically chosen to be at 1.3 μm and 1.55 μm to take advantage of the zero dispersion and minimum loss of the optical fiber at these wavelengths. In addition, wavelength at 1.55 μm meets the eye-safety requirement in free-space-

transmission applications such as free-space optical communication and range finding. In this work, 1.55 μm is assumed in all the analyses.

Despite these attractive properties, there are several long-standing problems with the DFB lasers. They are especially pertinent to applications in which the laser must meet very stringent requirements on the spectral properties and output power. These applications include coherent-optical-transmission systems [Koch90], monolithic master-oscillator-power-amplifier (MOPA) and other optoelectronic-integrated-circuits (OEIC).

One major shortcoming is the inherent mode degeneracy of the lasing modes associated with the conventional index-coupled DFB laser with first-order grating and zero facet reflectivity. This often means uncertainty in the lasing wavelength and instability. Another is the sensitivity to external optical feedback (such as backscattering from distant optical elements which is very difficult to eliminate in practice) [Stre75a], [Tkac86], [Hash92]. One example is the monolithic MOPA in which the master-oscillator (often a DFB or DBR laser) is monolithically integrated with a ridge-guided or fanned-out waveguided power-amplifier [Carl92] [Park93]. It is of crucial importance that residual reflection from the amplifier output facet does not cause self-oscillation of the power-amplifier, or the destabilization of the single-frequency oscillator. A more subtle problem has to do with the stability of the single wavelength and the spatial mode at high drive current or under adverse conditions. All these effects are related to the spectral purity and may be quantified by the SMSR. In general, lasers with SMSR of over 30 dB can meet the requirements of optical communication applications. However, this value is very often difficult to sustain at high drive current. The reason is the increased significance of nonlinear effects such as gain saturation and longitudinal spatial hole burning (LSHB). These effects are widely known to lead to nonlinear power-current behavior and abrupt changes of the

lasing wavelength. They often manifest as mode-hops, jitters, undesirable beam steering and multiple lasing wavelengths.

Efforts to improve the SMSR include: asymmetric coating of the end-facets; incorporation of one or more phase-shifters [Haus76], [Agra88a], [Kino90], [Kita93], modulated stripe width [Naka88], and modulated corrugation-pitch [Okai91]; and more recently, the use of chirped gratings [Mort90b], [Hill93], [Hill94b] and gain/loss-coupled gratings [Luo91], [Borc94]. All these schemes have their own merits along with their flaws. To date, research is an on-going process in the study of some of these approaches and in the pursuit of better and more practicable solutions.

1.2 Computer Model

As the design of DFB lasers becomes more and more sophisticated and complex, the need for a computer model is imperative. A general model is an indispensable and valuable tool that will aid in the study and design of novel DFB lasers. Moreover, such a model can be developed into a unified model that considers a network of active and passive optoelectronic devices [Lowe90], [Aman90], [Aman94]. It means having a computer-aided-design (CAD) tool for future OEIC's much like the way CAD is being used nowadays in the design of silicon integrated circuits.

The motivation in the use of numerical methods arises from the complexity of the problem itself, which is mainly caused by the nonlinear interaction between photons and carriers as well as their influence on the refractive index. The analysis is especially difficult when the device structure under investigation is very complicated. Examples include multisection devices, DFB with gain- and index-coupled gratings, or nonuniform device parameters along the laser cavity. There is as yet no closed-form solution available, particularly for operation at above-threshold conditions.

Besides, a computer model offers greater flexibility in the study of different DFB designs. An accurate computer model shortens development time and lowers costs by cutting down on the required number of trial cycles.

There are currently a number of theoretical DFB models that have been developed. The approaches taken are somewhat different. They include early linear transfer-matrix models [Maki88b] [Whit89], CLADISS [Vank90], transmission-line laser model [Lowe90], power-matrix method [Zhan92], time-domain method [Zhan94], and simplified two-stage method [Kino94].

The power-matrix method is chosen in this thesis for the calculation of the static laser properties at above-threshold conditions. This method is based on the commonly used transfer-matrix approach and the coupled-wave theory. It is nonlinear and self-consistent. It takes into account nonlinear effects such as spontaneous emission, gain saturation, and carrier-induced index change. This work generalizes this approach for the analysis of DFB lasers with up to three sections. The description of the grating is also extended to a larger variety of gratings. It encompasses first- and second-order gratings (and therefore calculation of surface emission), gain-grating with induced index-grating, and absorptive-grating with loss saturation at high photon densities. Other modifications are aimed at improving the accuracy of the calculation. The first one is an expansion of the method to enable a fully multimode calculation. The second one is the direct and more accurate computation of the spectral lineshape, output power and photon density.

The model is one-dimensional in space. A three-dimensional DFB laser has to be converted to one-dimensional by methods such as the effective-index method. The maximum number of sections along the longitudinal direction is chosen to be three, although the approach is applicable to an arbitrary number of sections. Each section is further divided into a cascade of equal-length segments. Within each segment, the material and grating parameters, and drive current are assumed to be constant.

Therefore, the linear coupled-wave theory may be applied to relate the forward- and reverse-traveling waves. Nonetheless, the parameters are allowed to vary from segment to segment to take account of longitudinal variations. Thus, the LSHB effect is automatically considered. The spontaneous-emission noise is assumed to originate between segments. It is the driving force of the system and is a function of the carrier density.

The resulting coupled-wave equations are difficult to solve because of the random phases of the spontaneous fields. First, the field equations are expressed in a matrix format and the transfer matrix approach is taken. Second, a technique is therefore introduced to convert the field equations to power equations for the calculation of power and photon density. Finally, iterations are performed to obtain a self-consistent solution above threshold. Results that can be computed with this model include the single-mode yield, the steady-state power-current curve, the lasing spectrum and the longitudinal distribution of carrier density, photon density and near-field intensity.

The validity of the model is confirmed by comparing the calculated results with experimental data as well as those by other independently developed models in the literature. For example, it yields the same results as those reported in [Zhan92]. It also explains experimental data of a three-section DFB device (see below and *Chapter 3*) and gives physical insights into its mode-selection mechanism. Further validation is obtained through a comparison with the theoretical yield data obtained by the CLADISS method [Davi91b].

1.3 Analyses

To demonstrate the applicability of the model, the analyses of two novel DFB laser designs are presented. The first device is a three-section *distributed-feedback*

distributed-Bragg-reflector (DFBDBR) laser and the second is a *complex-coupled DFB* (CCDFB) laser with index- and loss-coupling.

The DFBDBR laser with a continuous second-order grating is analyzed for below- and above-threshold behaviors. The name arises from the fact that it incorporates important features from both the DFB and the *distributed Bragg reflector* (DBR) lasers. This device is studied because experimental results have shown stable single-mode operation with narrow linewidth and very low threshold current. It has also been successful in forming grating-surface-emitting coherent arrays and as a single-frequency master-oscillator in a monolithic MOPA. The applications include free-space optical communications such as satellite-to-satellite communication in which a light source is required with the following desirable properties: high power, narrow linewidth, light weight and good beam quality with low far-field divergence so that bulky optics is not needed.

The laser has a pumped center-section that is terminated by two unpumped grating-sections. This work marks the first above-threshold analysis on this laser. It provides new results and better understanding of the workings of this device. The calculated results are consistent with earlier experimental observation that the laser operates with a peaked nearfield-intensity distribution along the laser cavity. The values of the grating parameters and the active-section-to-total-cavity-length ratio associated with this mode of operation are obtained. They indicate good tolerance in these critical design parameters. The dependence on the section lengths can be explained by the reflectivity bandwidths of the DFB and the DBR components. The DFBDBR laser is also found to have reduced LSHB and a smaller effective linewidth enhancement factor compared with those of a uniformly pumped single-section second-order DFB laser. These improvements are caused by the coupling of the pumped section to an extended passive resonator. The introduction of asymmetric passive grating sections in the DFBDBR laser results in poorer SMSR.

Besides the DFBDBR laser, the CCDFB laser with three sets of end-facets is analyzed at above-threshold conditions. The built-in grating is assumed to provide loss-coupling and index-coupling only, and no gain-coupling. The analysis focuses on the threshold current and front-facet power slope efficiency under the influence of facet coatings at two grating duty cycles. It has been suggested that antireflection coating on one facet and high-reflection coating on the other (AR-HR) can enhance the output power from the low-reflectivity facet (or front facet) [Naka92]. In contrast, the improvement on the front-facet power efficiency is not possible on conventional index-coupled DFB without significant degradation in SMSR. In this work, however, it is discovered that significant improvement is mainly limited to CCDFB lasers with small coupling coefficients.

For this type of CCDFB lasers, the common concern is the extra loss introduced by the absorptive grating and therefore the increase in threshold current. This work confirms an earlier suggestion that the extra loss can be reduced to an acceptable level by using a small grating duty cycle. For CCDFB with both perfectly antireflection-coated (AR-AR) facets, the threshold current only experiences a slight to moderate increase (grating duty cycle=0.15). A comparison of the contour plots of the threshold current indicate that the grating duty cycle has a strong influence on the threshold current at large grating coupling coefficients. In addition, when the end-facets are AR-HR, the threshold current is reduced substantially. Hence, low threshold and high efficiency CCDFB lasers with absorptive gratings are possible with the careful choice of the grating duty cycle and the use of AR-HR coatings together with appropriate coupling coefficient.

Although the application of AR-HR coatings improves the threshold current and efficiency, it also degrades the single-mode property of the loss-coupled DFB laser. Since the degradation can be inferred from the expected single-mode yield, a yield analysis of the purely loss-coupled DFB (LCDFB) laser is carried out. The calculation

assumes three criteria: the product of the threshold gain margin and cavity length must be greater than or equal to 0.3; the normalized variance of photon density distribution must be less than or equal to 0.1; and the threshold current must be less than 35 mA. The last two requirements are not normally imposed in the calculation of the theoretical yield. However, this work shows that their importance should not be ignored because of the significant yield reduction that may result. For example, the yield of the LCDFB with AR-HR coatings exhibits an interesting double-peaked profile as a function of the coupling coefficient when the threshold current criterion is imposed. These yield results suggest that the use of AR-HR coatings does not cause severe degradation in the single-mode property provided that the coupling coefficient is appropriately chosen.

1.4 Organization of Thesis

This thesis is divided into two major parts. The first is on the development and implementation of the computer model. The second is on the device analyses.

Chapter 1 provides the background information on DFB lasers, and an overview of the thesis..

Chapter 2 contains all aspects of computer modeling. They include a comparison of the available DFB laser models (*Section 2.1*), common assumptions and approximations (*Section 2.2*), and relevant fundamental theories (*Section 2.3*). In addition, detailed discussions on the above-threshold model can be found in *Section 2.4*. The topics include an in-depth description of the model, computer implementation techniques, and challenges encountered along with their solutions. This chapter concludes with a discussion on the validation of the model, a summary and a list of possible topics for future research in the area of theoretical modeling (*Section 2.5*).

The device analyses using the model are presented in *Chapter 3* and *Chapter 4*. *Chapter 3* gives the linear and above-threshold analyses of the three-section DFBDBR laser. The linear analysis in *Section 3.2* reveals that the carrier-induced index change in the pumped section is the mechanism responsible for the peaked-nearfield operation. The above-threshold analysis in *Section 3.3* further supports and expands this explanation and also suggests the advantages of reduced linewidth enhancement factor and reduced LSHB. A summary of major results is given in *Section 3.4*.

Chapter 4 presents the calculated results for another type of DFB lasers: DFB lasers with absorptive gratings. *Section 4.1* is an introduction on the CCDFB lasers. *Section 4.2* describes a procedure for the incorporation of the aborptive grating in the laser structure. In *Section 4.3*, the complex-coupled DFB laser with two grating duty cycles and three combinations of facet reflectivities are analyzed at above-threshold conditions. In *Section 4.4*, the linear yield results of the purely LCDFB laser and the index-coupled QWDFB laser are compared. *Section 4.5* is the conclusion for this chapter.

A recapitulation of the results and a conclusion, along with a list of topics for future studies are included in *Chapter 5*.

This chapter is then followed by a list of *References*, then the *Appendices* and the *Index*. There are seven appendices. *Appendix A* is the detailed derivations of the noise power, the trace of the field vector and the gain-coupling coefficient. *Appendix B* gives brief descriptions of all the subroutines in the computer program. *Appendices C, D, E,* and *F* are respectively the lists of figures, tables, acronyms, and symbols. *Appendix G* is a list of publications by the author.

2 COMPUTER MODEL

Numerical simulations are indispensable for the researchers working on the leading edge of the DFB laser technology. Sophisticated devices are often not analyzable in closed form. The difficulty has to do with the nonlinear interaction between photons and carriers as well as their influence on the refractive index. In addition, unlike the conventional Fabry-Perot laser, the laser parameters such as the carrier and photon densities can be highly inhomogeneous along the cavity. This positional dependence makes the search of an analytical solution to the wave equations almost impossible. Nonlinear effects such as gain saturation at large photon density further exacerbate the already complex problem. There is as yet no closed-form solution available. In addition, the complexity is compounded when a complicated device structure is under investigation. Examples include multisection devices, DFB laser with gain and index-coupled gratings, and devices with nonuniform parameters along the laser cavity. Consequently, researchers generally resort to numerical methods for the optimization of the device design, the analysis of device performance and the calculation of the expected yield. In addition, a computer model offers great flexibility in the study of different DFB designs. Of course, there are other obvious advantages such as shorter development time and lower costs by cutting down on the number of trial cycles.

The remainder of this chapter is organized as follows. *Section 2.1* compares various DFB models as reported in the literature. *Section 2.2* discusses the assumptions and approximations that are often encountered including those that have been adopted in this work. *Section 2.3* reviews the fundamental theories including

the coupled-wave equations and the transfer matrix approach. Then, a detailed description of the nonlinear model and its computer implementation are presented in *Section 2.4*. Finally, this chapter concludes with a discussion on the validation of the model (*Section 2.5.1*), a summary (*Section 2.5.2*), and a list of suggested future work in the area of theoretical modeling (*Section 2.5.3*).

2.1 Comparison of Theoretical Models

There are a number of theoretical DFB models that have been developed [Bjor87], [Agra88b], [Maki88b], [Whit89], [Vank90], [Lowe90], [Hans92], [Zhan92]. All of them are one-dimensional in space with the position variable along the laser cavity; a three-dimensional laser structure may be analyzed by first reducing the problem to one-dimensional one with the effective-index method. They all employed the segmentation technique that splits the laser cavity into equal-length segments. This method solves the positional dependence problem and offers flexibility in the study of complicated DFB designs.

These models are different in other ways. The earlier models are linear models [Maki88b], [Whit89], and are only valid for the analysis of DFB lasers below or near threshold. The usage is therefore rather limited. At above-threshold conditions, nonlinear effects can not be ignored and self-consistent solutions must be obtained. The models by Lowery [Lowe90], Hansmann [Hans92], [Hans94] and Zhang *et. al.* [Zhan92] are all nonlinear models that are suitable for above-threshold analyses. While Lowery employs the transmission-line laser model, others use the transfer-matrix approach [Maki88b], [Hans92], [Zhan92] and the coupled-wave theory [Whit89], [Zhan92]. In the transmission-line model, the gain, reflection, *etc.* are represented by their equivalence in electrical circuit like conductance and impedance. This representation has the potential advantage in the development of a future unified OEIC CAD tool. However, the coupled-wave theory describes the physical phenomenon in a more straightforward manner. It relates the forward- and the reverse-propagating waves. Hansmann expressed the wave interaction at each dielectric discontinuity (reflection and transmission at each grating tooth) with a transfer matrix. Zhang, *et. al.* and Whiteaway [Whit89] assumed a grating coupling coefficient (reflection per unit length) and based their transfer matrix on the coupled-

wave equations. The Hansmann model is therefore more appropriate for the study of strongly-coupled DFB lasers which are not well-approximated by the coupled-wave theory.

Perhaps, the most notable difference between Zhang's model (Power Matrix Method, PMM) and the others is that it is a deterministic model in mixed frequency and time domain rather than a stochastic time-domain model [Lowe92], [Tsan94a]. It provides average response and eliminates the inherent uncertainty in the phase of the spontaneous emission (more details in *Section 2.3*). This deterministic approach is especially well-suited for the static analysis. One example is the lasing spectrum (optical intensity versus wavelength) that can be computed directly in the frequency domain. Thus, the signal obtained is very smooth and noise-free. For stochastic models, to take into account the random phase of spontaneous emission, the same simulation has to be repeated for a number of times until the continuous wave (cw) condition is reached. The optical spectrum is then obtained by averaging and Fourier transform of the multiple results. The outcome is usually plagued by noise and jitters (because of the limited number of iterations and the finite window size used in the transform). Comparatively, the PMM eliminates a number of computational steps. The time-domain models, on the other hand, are more suitable for dynamic analysis because the response is calculated directly in time domain. Despite all the dissimilarities and unique advantages, the results obtained by these models show good agreement in static, small and large signal regimes. Therefore, the choice of theoretical model depends heavily on the characteristics to be analyzed and the application.

In this thesis, the main focus is on the static behaviors of the DFB lasers. In particular, the major concerns are the power-current curve, optical spectrum and the longitudinal distributions of effective index, carriers and photons. Hence, the PMM is chosen as the basis for the nonlinear model that was developed.

2.2 Assumptions and Approximations

The DFB laser is a very complicated device. There are many effects and processes that take place simultaneously. Some of them are important and have to be considered for the model to be useful while others may be ignored with negligible loss of accuracy. There is generally a tradeoff between accuracy and computational effort that precludes us from considering all the phenomena. The following examines some of these effects, including those that are adopted in the model.

2.2.1 Longitudinal Spatial Hole Burning

One of the nonlinear effects that is considered in our model is the *longitudinal spatial hole burning* (LSHB) effect. The effect has been identified as an important nonlinear effect in DFB lasers [Soda87], [Rabi89], [Whit89], [Kuo90], [Kete91], [Phil92]. The associated instability increases in a nonlinear manner above threshold and is particularly severe in devices with built-in phase-shifters. It is caused by the interaction of the axially varying optical intensity with the injected carriers. The resulting inhomogeneous carrier density distribution then gives rise to a nonuniform active layer refractive index through carrier-induced index change. This index change in effect creates a spatially-varying grating pitch, which alters the longitudinal intensity distribution of the modes. This mechanism influences all aspects of the device performance and results in soft threshold, nonlinear power-current characteristic, blue shifted static tuning and a less than flat FM response [Vank89]. In particular, mode hops, instability and multiple lasing modes can occur at low or moderate power with strong LSHB. The study of this nonlinear effect usually necessitates the division of the longitudinal laser cavity into subsections (even in simplified model [Kino94]). The LSHB effect is so important that there is continual research efforts in designing

lasers that are less affected by it (by having more uniform photon density distribution) [Agra88a], [Mort90b], [Davi91b], [Sudo93].

2.2.2 Spontaneous Emission

It is routine in most linear models and in some nonlinear models (e.g. [Hans92]) to ignore the spontaneous emission. The main difficulty is in the treatment of the random phase (the lack of coherence) of the spontaneous radiation. For above-threshold models that do not consider spontaneous emission, a clear distinction has to be made between subthreshold and above-threshold operations because spontaneous emission dominates in the subthreshold regime. Different strategies are then applied to the two regimes. A direct consequence is a disjointed transition at threshold which manifests as an abrupt change in the power-current curve. Another shortcoming is the inherent inaccuracy. Since spontaneous emission dominates below threshold, the counter-propagating traveling waves have no mutual coherence. It is not rigorously correct to ignore this and to assume the frequency-dependent coherent coupling by the grating is operable below threshold.

Our model is a unified model that takes into consideration the incoherent nature of the spontaneous emission, and no distinction is needed between subthreshold and above-threshold operation. The advantage is apparent in the smooth transition at threshold in the power-current characteristics (for example, see Fig. 3.10b). In the model, the spontaneous emission spectrum is assumed to be flat with respect to the optical frequency over the bandwidth of the spontaneous emission spectrum, Δf_{sp}. The spontaneous emission is treated as the driving current in PMM. It directly affects the numerical value of the output power. Nevertheless, the approximation is a good one given the fact that the bandwidth of Bragg gratings is about 5 nm and Δf_{sp} is larger by about one order of magnitude. More details can be found in *Section 2.3*.

2.2.3 Nonlinear Gain Saturation

Another nonlinear effect that has been included in our model is *gain saturation* [Yama78b], [Agra87], [Butl89], [Agra90], [Goma90], [Pan92]. At large photon densities, the gain is reduced in a nonlinear fashion that is characterized by a phenomenological *gain suppression factor* , ε. The nonlinear field gain is often expressed as

$$g = \frac{\Gamma a\,(N-N_t)}{2(1+\varepsilon\psi)}\,, \qquad (2.2.2\text{-}1)$$

where Γ is the confinement factor, a is the differential gain [Moze85], N is the carrier density, N_t is the carrier density at transparency, and ψ is the photon density. The nonlinear gain factor is usually calculated by the density matrix formalism. Its typical values are on the order of 10^{-17} to 10^{-16} cm^3 [Uomi91]. Since ε is only weakly dependent on the lasing wavelength[1], it is assumed to be constant in our model for simplicity.

The exact causes of this nonlinear gain are still under debate. For example, the spectral hole burning [Agra87], [Uomi91], intraband carrier relaxation [Agra90] are some of the proposed mechanisms. Spectral hole burning refers to the slight suppression in gain around the spectral region of the lasing wavelength due to the finite intraband relaxation time of carriers[2]. However, [Goma90] concluded that the dynamic carrier heating effects produced by stimulated emission and free-carrier absorption, and cooling by relaxation processes are responsible. One other suggestion is that the presence of standing waves in the laser cavity contribute significantly to ε [Pan92]. Yet, another report linked the effective gain compression to the laser structure in addition to nonlinear material gain [Duan92].

---

1 For example, ε is increased by 1.0×10^{-17} cm^3 over ~200 nm [Uomi91].

2 At the lasing wavelength, intense stimulated emission depletes carriers in the wavelength neighborhood faster than the rate at which carriers can fill in the hole.

Gain saturation, like the spatial hole burning effect, affects many laser characteristics. When the laser operates at a wavelength detuned from the gain peak, it is accompanied by a change in the modal refractive index. The coupling between gain and index nonlinearities limits the modulation bandwidth, and influences the spectral linewidth adversely in the form of a linewidth floor at high output power. In addition, the coupling causes linewidth rebroadening when the laser operates on the longer wavelength side of the gain peak because of the increase in the effective linewidth enhancement factor. In DFB lasers, it can also restrict the range of single-longitudinal mode operation when the Bragg wavelength is detuned from the gain peak by a large margin [Agra87].

2.2.4 Carrier-Induced Index Change

The last nonlinear effect to be considered in our model is the carrier-induced index change [Dutt84], [West86]. The index change includes an anomalous dispersion component [Osin87] and a free carrier component that is due to the plasma effect in the conduction band [Mura93]. The former is a result of the bandgap change due to injected carriers.[1] Under normal operating conditions, the variations in the charge density is relatively small, and the corresponding changes in the refractive index and gain can be assumed to be linear. The effective index change can then be approximated by,

$$\Delta n = -\frac{\alpha_H \lambda_o}{4\pi} a\Gamma (N-N_t) \quad , \tag{2.2.3-1}$$

where Δn is the change in the effective index, α_H is the linewidth enhancement factor [Henr82] and λ_o is lasing wavelength in free space. For faster computation, the change in the effective index of the laser is inferred from the change in the refractive

1 The index change arises from the asymmetry of the gain curve that produces a dispersion curve for the refractive index with the zero at a frequency higher than that of the gain peak. Since the gain varies with the carrier density, the refractive index will also depend on the carrier density.

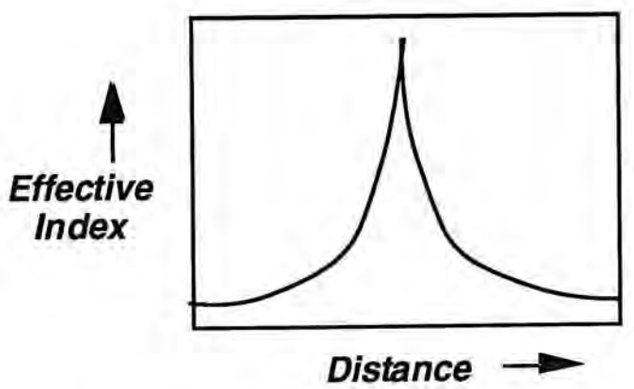

Fig. 2.1 The effective index distribution of a quarterwave phase-shifted DFB.

index of the active region by the use of the multiplicative factor Γ. The free carrier component of the index change is proportional to the square of the lasing wavelength; thus, it may be important for long-wavelength lasers. Because the functional dependence can be very complicated, it is not treated in our model. In fact, none of the numerical DFB models in the literature considers this phenomenon for the sake of simplicity.

The major effect of an index change on a DFB laser is a wavelength or frequency chirp. The frequency chirp, $\Delta\omega$, can be expressed as

$$\Delta\omega = -\frac{2\pi v_g \Delta n}{\lambda_o}, \qquad (2.2.3\text{-}2)$$

where v_g is the group velocity. It comes about because the index change is associated with the change in the mean carrier-density as perceived by the lasing mode. A good illustration of the process is the quarterwave phase-shifted DFB with a κL product (grating-coupling-coefficient-cavity-length product) greater than ~1.2 [Whit92] because of strong LSHB. As the output power increases, the carrier density in the neighborhood of the phase-shifter (located in the center of the cavity) falls sharply; in contrast, the carrier density at the cavity ends rises. As a result, the refractive index in

the center is much larger than that at the ends (see Fig. 2.1). The Bragg reflection near the ends therefore detunes to shorter wavelengths relative to the center section. In other words, the Bragg reflection at the lasing wavelength decreases, and the mode intensity at the facets and the resulting loss increase. The unit round-trip gain condition necessitates an increase in the mean carrier density (gain), and consequently the emission wavelength shortens.

2.2.5 Single-mode Operation Assumption

Many earlier DFB models made the assumption of single-mode operation to simplify the problem. In our model, we make no such assumption and a full multimode rate equation is implemented. This is of major importance in the design of DFB lasers when we do not always have *a priori* information of the lasing spectrum. The benefits are better accuracy in power and efficiency calculations, a simple and direct computation on the SMSR and spectral linewidth, and better understanding of the device operation through the calculated spectra.

2.2.6 Others

Other assumptions are needed in order to make the modeling task more manageable.

The carrier diffusion in the longitudinal direction is ignored although the effect could be considered by adding an extra term in the carrier rate equation ('$D\nabla^2 N$' where D is the diffusion coefficient). The main effect of diffusion is to wash out the spatial holes burnt by the standing waves formed by the counter-propagating waves in the forward and reverse directions since their spacing $\frac{m\lambda_B}{2n}$ is much smaller than the diffusion length (~ 2 to 3 μm). Therefore, to a good degree of accuracy, the carrier

diffusion may be ignored. Again, since this is a one-dimensional model, the lateral carrier diffusion is not taken into account.[1]

For simplicity, the current-induced temperature increase on the effective index is not considered. Most theoretical models in the literature do not take into account this effect with the exception of [Hans92]. The effect can be described as follows. With the increase in local carrier density, the temperature increases. The effective index of refraction is then enhanced. As a result, in the presence of a Bragg grating, the Bragg wavelength is effectively shifted to longer wavelength. This implies that for devices with uniform carrier density distribution (i.e. no LSHB), the temperature effect only shifts the entire laser spectrum but not the relations among the lasing modes. However, for lasers with inhomogeneous carrier-density profile (e.g. with strong LSHB), the laser behaviors will be influenced in a more complicated manner. In particular, it actually has a smoothing effect that reduces the nonuniformity of the effective-index distribution. Localized temperature effect can be included by [Hans92],

$$\frac{\partial n}{\partial I} = \frac{1}{2n} \frac{\mathrm{d}n^2}{\mathrm{d}T} \frac{\mathrm{d}T}{\mathrm{d}I}, \qquad (2.2.6\text{-}1)$$

where $\frac{\mathrm{d}T}{\mathrm{d}I}$ is the temperature change with current $\frac{\mathrm{d}n^2}{\mathrm{d}T}$ is the material coefficient. For device analysis, the values of these parameters are often estimated. It means that the accuracy of the results is dubious. Because of the uncertainty, the temperature effect is not considered.

Finally, saturable absorption is not taken into account except in the lossy grating (see *Section 4.2.2*). It describes the decrease in loss at high photon density. In DFB laser with absorptive grating, this is reflected as a reduction in the loss-coupling coefficient. It can also be included in the general laser cavity by introducing a nonlinear absorption compression factor similar to the expression for gain saturation

---

1 For example, see [Yu94] for an analysis that includes the lateral carrier diffusion.

(see Eq. (2.2.2-1)). In real devices with saturable absorbers, self-pulsation as well as bistable operation can occur. However, a study of self-pulsation requires a more general dynamic model.

To summarize, the above-threshold DFB model developed in this work is based on the PMM. It considers nonlinear effects such as LSHB, spontaneous emission, gain saturation and carrier-induced index change. It is a fully multimode model and makes no assumption of single-mode operation. It does, however, make approximation on the spontaneous emission spectrum profile and ignores the carrier diffusion and temperature dependence. The decision on what to include and what to ignore is centered around the goal of a useful model with sufficient accuracy that is not burdened by unreasonable computational effort.

2.3 Theories and Approaches

2.3.1 Coupled Wave Theory

Since our modeling relies heavily on the coupled wave theory, a review is given here. The emphasis is placed on relevant topics such as general expression of the complex grating coupling coefficient, second-order DFB, nearfield distribution of various lasing modes and mode discrimination.

Description

The theoretical analysis of the first-order DFB was first performed by Kogelnik and Shank [Koge72] and at a later time by others [Stre77], [Yama78a]. This analysis is linear and is therefore only valid near threshold. The grating is treated as a dielectric or gain perturbation along z, the propagation direction.

As shown in Fig. 2.2, the DFB can be visualized as a series of planes separated by $\frac{\lambda}{2}$, where feedback and transmission take place. Since the laser is a self-oscillator, no external optical injection is present. The optical power starts from zero at the facets and increases as it traverses through the gain medium. At each plane, energy is exchanged; part of the energy is coupled with the counter-propagating wave through reflection and the remaining portion is transmitted. Mathematically, for the first-order DFB, the field may be decomposed into a forward- and a reverse-propagating waves, with complex amplitudes, $F(z)$ and $R(z)$, respectively. For example, $F(z)$ starts at 0 at $z = -\frac{L}{2}$ (L is the cavity length), and grows as z increases. A fraction of $F(z)$ is coupled with $R(z)$ continuously in z and flattens somewhat as $z \rightarrow \frac{L}{2}$ at the output end. The same is true for $R(z)$. The assumptions include:

1. uniform waveguide, grating, and injected current in z;

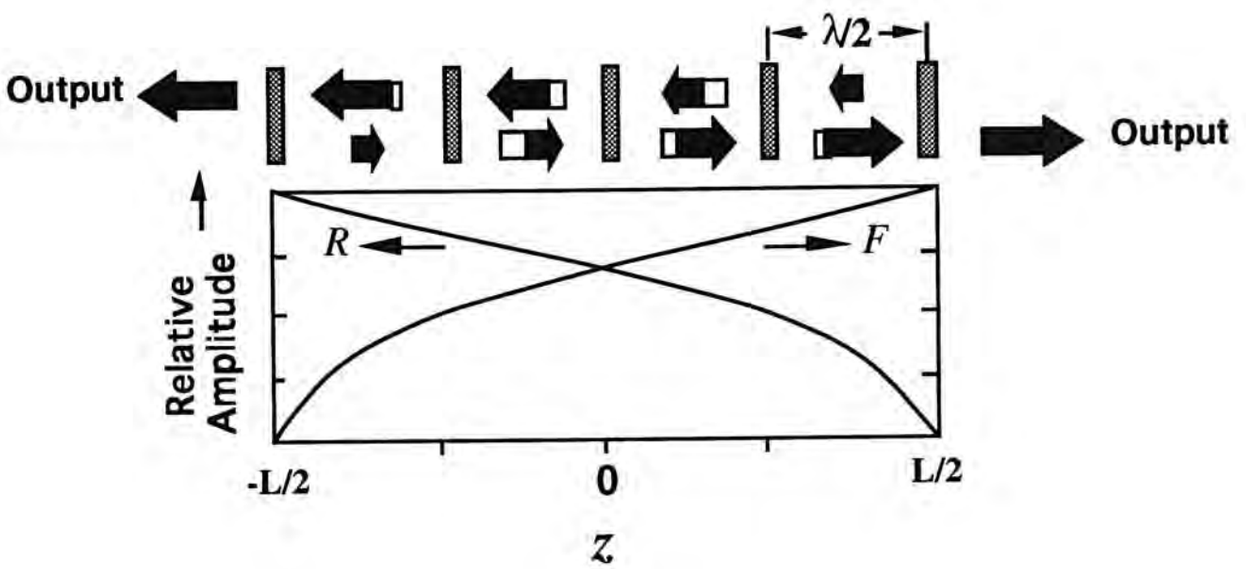

Fig. 2.2 A schematic drawing of the forward- and reverse-propagating fields (F and R) along the laser cavity of length L.

2. slowly varying amplitudes (i.e. $\frac{\partial^2 F}{\partial z^2}$ and $\frac{\partial^2 R}{\partial z^2}$ are neglected); and,

3. all diffraction orders are negligible except for the two phase-matched orders near Bragg frequency.

Another approach for the analysis is called the Floquet-Bloch theorem [Dabb72], [Hadj90]. The grating is represented by a periodic modulation on permittivity (refractive index). It uses a Fourier expansion of the field in terms of Floquet-Bloch modes (waves with an infinite number of "partial waves" (space harmonics) with amplitudes which are inherently adjusted as to satisfy the grating boundary conditions). Partial waves with matching phase experience energy exchange, or coupling. In DFB lasers, coupling takes place in forward and backward wave harmonics. This theorem is similar to the one that is applied to the analysis of crystals. As pointed out by Yariv and Gover [Yari75], the coupled-mode and the truncated form of the Floquet-Bloch expansion are indeed equivalent. However, the

coupled-mode formalism offers better insights into the physical processes and yields simpler analytical results.

For TE-polarization, the electric field $E(x,z)$ of the fundamental mode propagating in a waveguide with periodic corrugations is given by

$$E(x,z) = \left(F(z)\ exp\ (i\beta_B z) + R(z)\ exp\ (-i\beta_B z) \right) E_0(x) \qquad (2.3.1\text{-}1)$$

where x is in the transverse direction, and $E_0(x)$ describes the transverse field profile which depends on the waveguide geometry. Based on the coupled wave equations Koge72], [Kapo82], F and R are related by:

$$\frac{dF}{dz} = AF + BR \quad , \text{and}$$

$$\frac{dR}{dz} = -AR - CF \quad , \qquad (2.3.1\text{-}2)$$

where for second-order gratings, $A = i\Delta\beta + (g - \alpha/2) - \xi$, $B = i\,(\kappa_{fr} + i\xi)$ and $C = i\,(\kappa_{rf} + i\xi)$. The deviation from Bragg condition is given by $\Delta\beta = \beta - \beta_B$, where the Bragg wavenumber is $\beta_B = m\pi/\Lambda$. The propagation constant in the absence of the grating is $\beta = \frac{2\pi n}{\lambda_0}$. Parameter α is the power loss coefficient which includes the material loss and scattering losses. Parameters κ_{fr} and κ_{rf} are respectively the complex-coupling coefficients that couple the forward into the reverse wave and vice versa. They are written as [Davi91b]:

$$\kappa_{fr} = \kappa_n(N) + i\,(\kappa_g(N) - \kappa_l)\,e^{i\theta}, \text{ and}$$

$$\kappa_{rf} = \kappa_n(N) + i\,(\kappa_g(N) - \kappa_l)\,e^{-i\theta}. \qquad (2.3.1\text{-}3)$$

Parameter κ_n is the index grating coupling coefficient which includes the contribution from the induced index grating by the gain grating (see *Appendix A.3*). It is therefore a function of N. It is real and can be positive or negative depending on the detail of the grating. Parameter κ_g is the gain grating coupling coefficient which is also a function of N. Parameter κ_l is the loss coupling coefficient for the loss (or

absorptive) grating which is independent of N. Both are taken to be real and positive without loss of generality. Parameter θ is the phase angle between the index and the gain/loss gratings. Parameter ξ is the radiation coefficient that describes the surface emission perpendicular to the junction plane in the presence of second-order grating [Stre76a], [Stre76c]. That means, for first-order grating, $\xi=0$. Second-order gratings are used extensively in grating-surface-emitting lasers [Evan93] for the coherent surface radiation and longitudinal coupling among laser elements. It is also utilized in near infrared devices ($\leq$ 1.0 μm) for its larger grating period (compared with first-order gratings).

Assume that $F(z) = a\,e^{\gamma z} + b\,e^{-\gamma z}$ and $R(z) = c\,e^{\gamma z} + d\,e^{-\gamma z}$. Coefficients a, b, c, d and γ are to be determined. Substitution of $F(z)$ and $R(z)$ into Eq. (2.3.1-1) yields solutions that can be rewritten in matrix format:

$$\begin{bmatrix} F(z) \\ R(z) \end{bmatrix} = \mathbf{T} \begin{bmatrix} F(z-l) \\ R(z-l) \end{bmatrix}. \tag{2.3.1-4}$$

T is the transfer matrix given by:

$$\mathbf{T} = \begin{pmatrix} \cosh(\gamma l) + \frac{A}{\gamma}\sinh(\gamma l) & \frac{B}{\gamma}\sinh(\gamma l) \\ -\frac{C}{\gamma}\sinh(\gamma l) & \cosh(\gamma l) - \frac{A}{\gamma}\sinh(\gamma l) \end{pmatrix}, \tag{2.3.1-4}$$

with the complex propagation constant, $\gamma = \sqrt{A^2 - BC}$ and l being the segment length. That is, if F and R are known at $(z-l)$, $F(z)$ and $R(z)$ can be calculated. By applying the boundary conditions (meaning facet reflectivities), exact solutions can be obtained. Note that if θ is zero or π (this is automatically satisfied if the index and gain/loss-coupling are caused by the same grating), $B = C$ (i. e. $\kappa_{fr} = \kappa_{rf}$). The solution then reduces to the familiar form as in [Koge72]. (More on gain/loss-coupled DFB lasers in *Chapter 4*.)

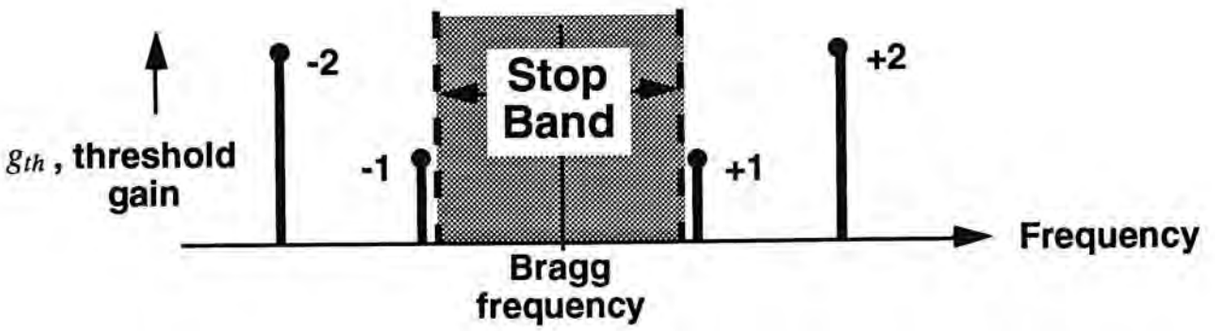

Fig. 2.3 *Schematic drawing of the stop band in optical frequency domain.*

Stop-Band

For purely index-coupled DFB lasers (i. e. $B = C$), a direct consequence of the complex propagation constant, $\gamma = \sqrt{A^2 - B^2}$, is the *stop-band*, where no propagation can occur when $B^2 - A^2 < 0$. On the other hand, purely gain-coupled DFB (GCDFB) or loss-coupled DFB (LCDFB) lasers have no stop-band. The lowest-loss mode (i. e. the lasing mode) is located at the Bragg wavelength.

For first order index-coupled DFB with zero facet reflectivities (optical feedback is provided entirely by the gratings), mode degeneracy exists. Both modes (labeled '+1' and '-1' in Fig. 2.3) nearest the stop-band have the same lowest threshold gain, g_{th}. The degeneracy leads to uncertainty in the lasing mode, strong mode competition and often multimoded operation, and is therefore undesirable in practice.

The associated nearfield patterns of the '+1' and '-1' modes are shown in Fig. 2.4. Typically, Mode '-1' exhibits a minimum in the middle of the laser cavity because of destructive interference resulted from a π phase-shift between $F(z)$ and $R(z)$. In contrast, Mode '+1' possesses a maximum in the cavity center because $F(z)$ and $R(z)$ are in phase and therefore constructively interfere.

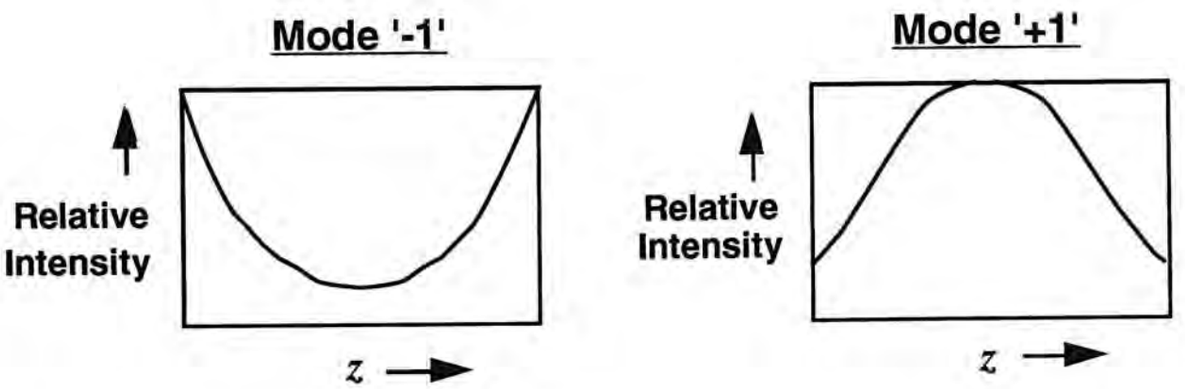

Fig. 2.4 The optical intensity distributions of Mode '-1' and Mode '+1' of the first-order index-coupled DFB with zero facet reflectivities.

Second-Order DFB Laser

For second-order index-coupled DFB lasers, however, g_{th} is lowest for Mode '-1'. There is an extra loss associated with the surface radiation that is coupled out of the laser cavity along the entire length of the laser. Its magnitude is proportional to the internal optical intensity. Since the nearfield pattern of Mode '-1' consists of a minimum in the center of the laser cavity, the radiation loss is therefore smaller compared with that of Mode '+1', in which the nearfield intensity is peaked in the center. The minimized loss is the reason why Mode '-1' is the lowest-loss mode. In practice, for surface emitting output, this mode is not desirable because it gives rise to a double-lobed far field pattern. For instance, it makes coupling into a fiber very difficult. Mode '+1' is preferred because it yields a single-lobed far field.

DFB Designs To Improve SMSR

There are many schemes aimed at the removal of the mode degeneracy. One way is to incorporate a design feature to ensure the absence of inherent mode degeneracy. Another approach is to introduce asymmetry into the laser structure such

that g_{th} are different for different modes, especially those located on opposite sides of the stop-band.

In the first category is the DFB laser with gain/loss-coupled grating (nonzero κ_g or κ_l). That is, κ_{fr} and κ_{rf} (κ, in short) are purely or partially imaginary. Another is the DFB laser with zero facet reflectivity and an odd multiples of quarterwave phase-shifter in the center of the laser cavity. Both structures produce a lowest-loss mode exactly at the Bragg frequency. The LCDFB is constructed with the grating formed on a lossy epitaxial layer, whereas the GCDFB has its grating fabricated directly on or very close to the active region. With the advancement in device fabrication, there is a resurgence of interest in the gain/loss-coupled DFB laser in recent years. Recent research [Luo91], [Li93c], [Borc94], [Tsan94b], [Lowe94] has demonstrated important advantages of the GCDFB and LCDFB over the index-coupled DFB.

Among the devices mentioned above, the quarterwave phase-shifted DFB has been extensively studied. Although it removes the degeneracy, it is very susceptible to LSHB because of its highly nonuniform photon density distribution. Figure 2.5 is the intensity distribution of a DFB with a quarterwave phase-shifter in the middle of the laser. The photons tend to accumulate at the phase-shifter in an exponential fashion. This pile-up leads to the highly localized depletion of carriers. The laser becomes unstable with mode hops and is incapable of sustaining single-mode operation. Moreover, the single-mode yield is usually poorer than that of the index-coupled DFB (even with mode degeneracy) due to the presence of residual facet reflectivities.

In the second category, the most commonly encountered structure is the conventional index-coupled DFB with asymmetric facet reflectivities [Hen85]. Others include index-coupled DFB with modulated stripe width [Naka88], modulated corrugation-pitch [Okai91]; and more recently, chirped gratings [Mort90b], [Hill94b]. These schemes all serve to break the symmetry to result in a unique lowest-loss mode.

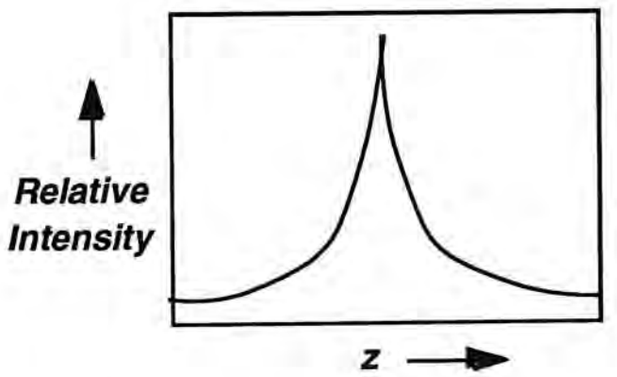

Fig. 2.5 Optical intensity of the quarterwave phase-shifted DFB along the laser cavity.

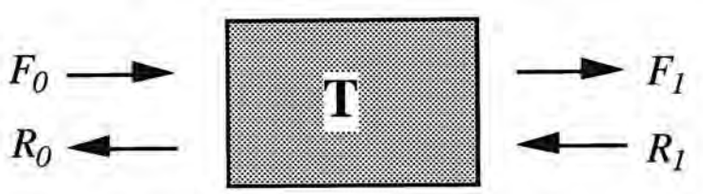

*Fig. 2.6 Transfer matrix, **T**, relates the outputs F_1, R_1 to the inputs F_0 and R_0.*

2.3.2 Transfer Matrix Approach

The transfer matrix formalism may be considered as a modified form of the scattering matrix approach [Haus84]. The action of a partially transmitting mirror (or a slab of optical medium) is described in terms of a linear set of relationships between the two incident, and two transmitted/reflected wave amplitudes. This relationship is illustrated in Fig. 2.6. The forward- (reverse-) propagating fields are represented by F_0 and F_1, (R_0 and R_1). The index '0' denotes input and '1' the output. Their relationship can be written in matrix form as $\overrightarrow{\mathbf{V}_1} = \mathbf{T}\,\overrightarrow{\mathbf{V}_0}$, with $\overrightarrow{\mathbf{V}_m} = \begin{bmatrix} F_m \\ R_m \end{bmatrix}$, where m is an integer. A general transfer matrix is given by

$$\mathbf{T} = \begin{bmatrix} t_{11} & t_{12} \\ t_{21} & t_{22} \end{bmatrix}. \qquad (2.3.2\text{-}1)$$

However, only three out of the four complex coefficients are independent because of the reciprocity principle for an isotropic medium. As a result, Det(**T**)=1. Symmetry in a device further imposes a restriction on the off-diagonal terms, i. e. $t_{21} = - t_{12}$, which gives only two independent coefficients. A comparison with Eq. (2.3.1-4) reveals that the general transfer matrix in our model is only symmetrical if $B=C$; that is, when $\theta = 0$ or π (this is automatically satisfied if the index- and gain/loss-coupling are caused by the same grating). Finally, the matrix does not possess the time-reversal or power conservation properties because the medium is not lossless.

This review discusses the important coupled-wave theory and the transfer matrix approach as applied in our model and also provides background information on second-order index-coupled DFB, GCDFB and LCDFB.

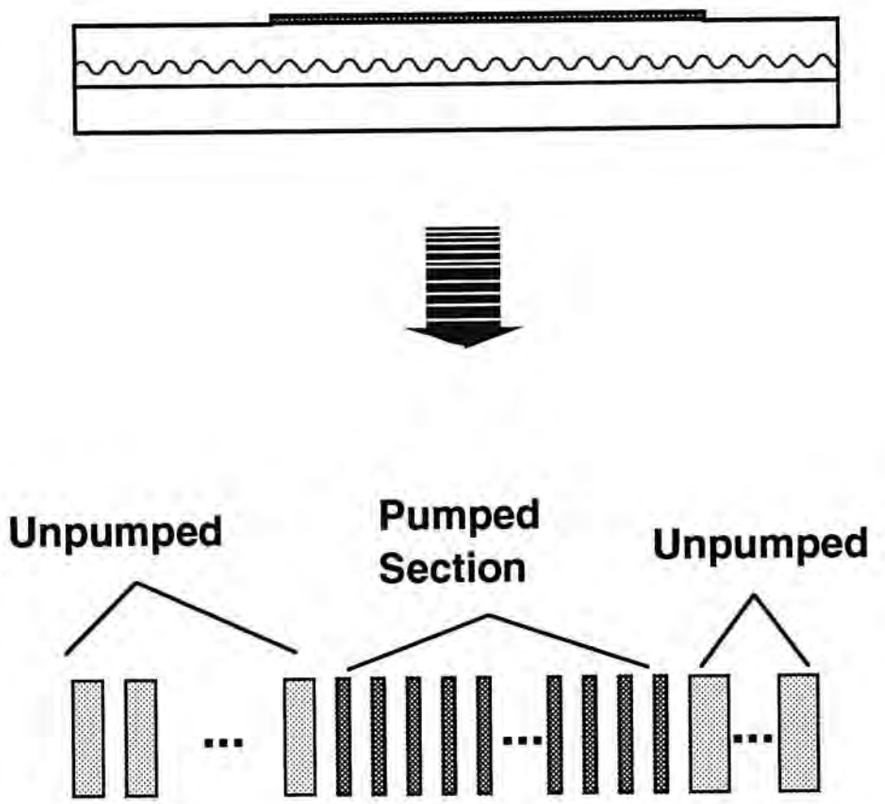

Fig. 2.7 Each section of a three-section DFBDBR laser (one center pumped section and two unpumped end-sections) is segmented into a number of equal-length segments. The length chosen for each section may be different.

2.4 Above-Threshold Model

2.4.1 Introduction

This section details the above-threshold model developed in this work. The principles of the model is applicable to complex multisection DFB devices although in this work, it is specifically tailored for a three-section DFBDBR laser (*Chapter 3*) and the complex-coupled DFB (CCDFB) (*Chapter 4*). Thus, only the center section of a three-section device is assumed to be injected with drive current. The sections at the ends are presumed passive. The conventional single-section DFB laser is therefore a special case of this structure.

As mentioned earlier, the nonlinear multisection model is based on the transfer matrix method (*Section 2.3.1*) and coupled-wave theory (*Section 2.3.2*). The model is a mixed frequency-time domain model (PMM) based on [Zhan92]. This deterministic model is especially appropriate for static analyses (*Section 2.1.1*). The model incorporates nonlinear effects such as spontaneous emission (*Section 2.2.2*), LSHB (*Section 2.2.1*), gain saturation (*Section 2.2.3*) and carrier-induced index change (*Section 2.2.4*). The model is one-dimensional in space. A three-dimensional device, however, can be reduced to a one-dimensional problem by the effective-index method. The laser can have up to three sections along the longitudinal direction, although in theory the formalism can handle an arbitrary number of sections. Each section is further divided into a cascade of equal-length segments. An example of this procedure performed on a three-section DFBDBR laser is depicted in Fig. 2.7. Note that the segment length chosen for each section need not be the same. Within each segment, drive current and the parameters related to material and grating are assumed to be constant. Therefore, the linear coupled wave theory is applicable. Nevertheless, the parameters are allowed to vary from segment to segment to take account of the longitudinal variations. Thus, the LSHB effect is automatically taken care of. The spontaneous emission noise is assumed to originate between segments. It is the driving force of the system and is a function of the carrier density. The resulting coupled wave equations are difficult to solve because of the random phases of the spontaneous fields. Therefore, the field equations are converted to power equations in a matrix format and the transfer matrix approach is taken. Iterations are also needed in order to obtain a self-consistent solution. Results that can be computed with this model include the single-mode yield, the steady-state power-current curve, the lasing spectrum and the longitudinal distributions of effective index, carrier, photon densities and nearfield intensity.

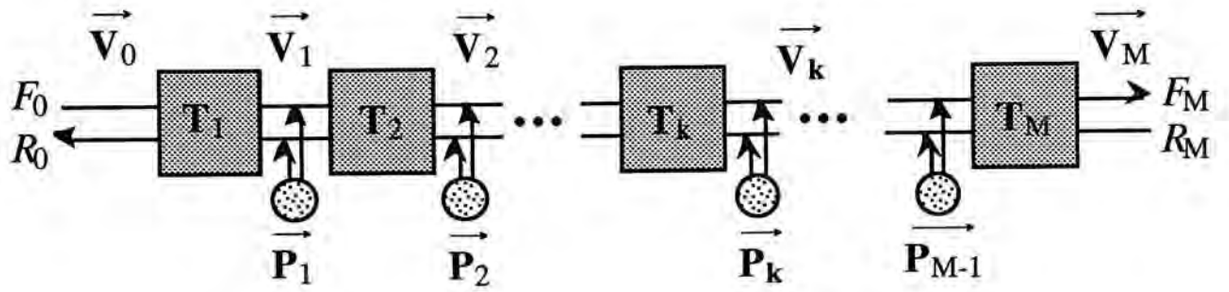

Fig. 2.8 Schematics of the transfer matrix approach with the noise vector, $\vec{\mathbf{P}}_k$, introduced between adjacent segments with indices, k and k+1.

2.4.2 Formalism

As illustrated in Fig. 2.8, the spontaneous emission is introduced between adjacent segments and is modeled by the spontaneous driving currents for the forward and reverse waves (i_F and i_R, respectively). The time-independent coupled wave equations can be written as

$$\frac{dF}{dz} = AF + BR + i_F \text{ , and}$$

$$\frac{dR}{dz} = -AR - CF + i_R \text{ .} \qquad (2.4.2\text{-}1)$$

The definitions of the coefficients are the same as those introduced in *Section 2.3.1* and they are listed in the *Appendix C.4*. But they are replicated here for convenience: $A = i\Delta\beta + (g - \alpha/2) - \xi$, $B = i(\kappa_{fr} + i\xi)$ and $C = i(\kappa_{rf} + i\xi)$. Except z, all the variables and coefficients must be labeled for each segment. Consequently, the traveling wave field vector for the k-th segment is written as $\vec{\mathbf{V}}_k = \begin{bmatrix} F_k \\ R_k \end{bmatrix}$, and the noise vector between the k-th and $(k+1)$-th segments is represented by $\vec{\mathbf{P}}_k = \begin{bmatrix} i_{Fk} \\ i_{Rk} \end{bmatrix}$. With these definitions, the field vectors in adjacent segments are related by a transfer matrix, $\mathbf{T}_k$, as follows:

$$\vec{\mathbf{V}}_k = \mathbf{T}_k \vec{\mathbf{V}}_{k-1} + \vec{\mathbf{P}}_k, \qquad (2.4.2\text{-}2)$$

where the transfer matrix is given by

$$\mathbf{T}_k = \begin{pmatrix} \cosh(\gamma l) + \frac{A}{\gamma}\sinh(\gamma l) & \frac{B}{\gamma}\sinh(\gamma l) \\ -\frac{C}{\gamma}\sinh(\gamma l) & \cosh(\gamma l) - \frac{A}{\gamma}\sinh(\gamma l) \end{pmatrix}, \tag{2.4.2-3}$$

in which l is the length of the k-th segment and the associated complex propagation constant is given by $\gamma = \sqrt{A^2 - BC}$.

In this way, the coupled wave equations can be solved. The derivation is as follows [Zhan92]:

$$\vec{\mathbf{V}}_1 = \mathbf{T}_1 \vec{\mathbf{V}}_0 + \vec{\mathbf{P}}_1$$

$$\vec{\mathbf{V}}_2 = \mathbf{T}_2 \vec{\mathbf{V}}_1 + \vec{\mathbf{P}}_2 = \mathbf{T}_2\mathbf{T}_1 \vec{\mathbf{V}}_0 + \mathbf{T}_2\vec{\mathbf{P}}_1 + \vec{\mathbf{P}}_2$$

$$\vdots$$

$$\vec{\mathbf{V}}_m = \mathbf{T}_m \vec{\mathbf{V}}_{m-1} + \vec{\mathbf{P}}_m = \prod_{k=1}^{m} \mathbf{T}_k \vec{\mathbf{V}}_0 + \sum_{k=1}^{m} \prod_{j=k+1}^{m} \mathbf{T}_j \vec{\mathbf{P}}_k$$

$$\vdots$$

$$\vec{\mathbf{V}}_M = \mathbf{T}_M \vec{\mathbf{V}}_{M-1} = \sum_{m=1}^{M-1} \mathbf{S}^{(m+1)} \vec{\mathbf{P}}_m + \mathbf{S}^{(1)} \vec{\mathbf{V}}_0 \tag{2.4.2-4}$$

where $\mathbf{S}^{(m)} = \prod_{k=m}^{M} \mathbf{T}_k$. $\prod_k$ denotes matrix multiplication over index k, and M is the total number of segments. Therefore, if $\vec{\mathbf{V}}_0$ (or $\vec{\mathbf{V}}_M$), is known, the field vectors in between can be obtained easily. Applying the boundary conditions at the ends of the device (facet reflectivity), we note that $F_0 = r_1 R_0$ and $R_M = r_2 F_M$ where r_1 and r_2 are the reflection coefficients of the left and right facets. Hence,

$$\vec{\mathbf{V}}_0 = \begin{bmatrix} r_1 R_0 \\ R_0 \end{bmatrix}, \text{ and } \vec{\mathbf{V}}_M = \begin{bmatrix} F_M \\ r_2 F_M \end{bmatrix}. \tag{2.4.2-5}$$

By direct substitution, we obtain

$$\vec{\mathbf{V}}_M - \mathbf{S}^{(1)}\vec{\mathbf{V}}_0 = \begin{bmatrix} 1 & -r_1 s_{11} - s_{12} \\ r_2 & -r_1 s_{21} - s_{22} \end{bmatrix} \begin{bmatrix} F_M \\ R_0 \end{bmatrix} = \mathbf{K} \begin{bmatrix} F_M \\ R_0 \end{bmatrix} \tag{2.4.2-6}$$

where s_{11}, s_{12}, s_{21} and s_{22} are elements of matrix $\mathbf{S}^{(1)}$. Further manipulation yields

$$\begin{bmatrix} F_M \\ R_0 \end{bmatrix} = \mathbf{K}^{-1} \sum_{k=1}^{M-1} \mathbf{S}^{(k+1)} \vec{\mathbf{P}}_k. \tag{2.4.2-7}$$

With Eq. (2.4.2-5), $\vec{\mathbf{V}}_0$ (or $\vec{\mathbf{V}}_M$) can be deduced by multiplying both sides of Eq. (2.4.2-7) by a singular matrix $\mathbf{D}_l$ (or $\mathbf{D}_r$). They are given by

$$\mathbf{D}_l = \begin{bmatrix} 0 & r_1 \\ 0 & 1 \end{bmatrix} \text{ and } \mathbf{D}_r = \begin{bmatrix} 1 & 0 \\ r_2 & 0 \end{bmatrix}. \tag{2.4.2-8}$$

As a result, we obtain

$$\vec{\mathbf{V}}_0 = \mathbf{D}_l \mathbf{K}^{-1} \sum_{k=1}^{M-1} \mathbf{S}^{(k+1)} \vec{\mathbf{P}}_k \text{ and}$$

$$\vec{\mathbf{V}}_M = \mathbf{D}_r \mathbf{K}^{-1} \sum_{k=1}^{M-1} \mathbf{S}^{(k+1)} \vec{\mathbf{P}}_k. \tag{2.4.2-9}$$

Clearly, $\vec{\mathbf{V}}_M$ can also be deduced from Eq. (2.4.2-4) once $\vec{\mathbf{V}}_0$ is known.

At this point, the only obstacle to a full description of the device operation is the unknown noise vector, $\vec{\mathbf{P}}$. Since this vector represents the spontaneous emission, the exact phase is undetermined (being equally likely over 2π radians). Nevertheless, its magnitude can be computed as a function of the carrier density. It is given by $i_F^* i_F = i_R^* i_R = \zeta_1 l\, \omega N^2$ where ζ_1 is a coefficient based on the device structure and the material parameters, and '$*$' denotes complex conjugate. More details can be found in *Appendix A.1*. Next, the field equations are converted to power equations so as to eliminate the ambiguities of the random phase associated with the spontaneous emission. Finally, the equations can be solved and useful physical quantities can be obtained.

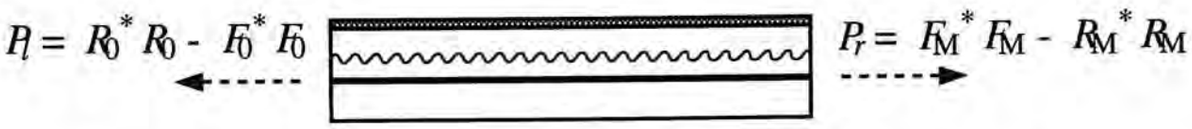

Fig. 2.9 *Output power from the left and right end-facets of a DFB laser.*

The following is the derivations leading to the facet and surface emission power, optical spectrum, and along the longitudinal direction, the photon density and nearfield distributions.

Facet Output Power and Optical Spectrum

As shown in Fig. 2.9, the power leaving the left side of the device is

$$P_l = R_0^* R_0 - F_0^* F_0. \tag{2.4.2-10}$$

The product of $\overrightarrow{\mathbf{V}_0}$ and its adjoint (that is, complex-conjugate transpose, denoted by '†') is given by

$$\overrightarrow{\mathbf{V}_0}^{\dagger}\overrightarrow{\mathbf{V}_0} = \begin{bmatrix} r_1^* R_0^* & R_0^* \end{bmatrix} \begin{bmatrix} r_1 R_0 \\ R_0 \end{bmatrix} = \left(1 + r_1^* r_1\right) R_0^* R_0 . \tag{2.4.2-11}$$

Therefore,

$$P_l = \frac{1 - r_1^* r_1}{1 + r_1^* r_1} \overrightarrow{\mathbf{V}_0}^{\dagger}\overrightarrow{\mathbf{V}_0} \quad , \tag{2.4.2-12a}$$

and similarly, the power leaving the right side of the device is

$$P_r = \frac{1 - r_2^* r_2}{1 + r_2^* r_2} \overrightarrow{\mathbf{V}_M}^{\dagger}\overrightarrow{\mathbf{V}_M}. \tag{2.4.2-12b}$$

The detailed derivation of the product of the field vector and its adjoint for each segment can be found in *Appendix A.2* It makes use of the incoherent nature of the spontaneous emission with the following properties:

$$|i_{Fk}| = |i_{Rk}| ;$$

$$i_{Fm}^{*} i_{Fn} = |i_{Fm}|^2 \delta_{mn} = \varphi_m \delta_{mn} ;$$

$$i_{Rm}^{*} i_{Rn} = |i_{Rm}|^2 \delta_{mn} = \varphi_m \delta_{mn};$$

$$i_{Fm}^{*} i_{Rn} = 0 ;$$

$$i_{Rm}^{*} i_{Fn} = 0 . \qquad (2.4.2\text{-}13)$$

where $\varphi_k = |i_{Fk}|^2 = |i_{Rk}|^2$. The results are:

$$\overrightarrow{\mathbf{V}_k}^{\dagger} \overrightarrow{\mathbf{V}_k} = \sum_{j=1}^{M-1} \mathrm{tr}\left(\left(\mathbf{Y}_j^{(k)} \right)^{\dagger} \left(\mathbf{Y}_j^{(k)} \right) \right) \varphi_j , \qquad (2.4.2\text{-}14)$$

where '$\mathrm{tr}\left(\mathbf{Y}^{\dagger}\mathbf{Y}\right)$' is the trace of $\mathbf{Y}^{\dagger}\mathbf{Y}$, which is the sum of the magnitude-square of each of the elements of $\mathbf{Y}$, and $\mathbf{Y}_j^{(k)}$ is defined as

$$\mathbf{Y}_j^{(k)} = \left(\prod_{i=1}^{k} \mathbf{T}_i \right) \mathbf{X}_{1j} + \mathbf{I}\delta_{kj} \qquad (2.4.2\text{-}15)$$

with

$$\mathbf{X}_{1k} = \mathbf{D}_1 \mathbf{K}^{-1} \mathbf{S}^{(k+1)} \text{ and } \mathbf{X}_{rk} = \mathbf{D}_r \mathbf{K}^{-1} \mathbf{S}^{(k+1)}. \qquad (2.4.2\text{-}16)$$

$\mathbf{I}$ is the identity matrix; $\mathbf{I} = \begin{bmatrix} 1 & 0 \\ 0 & 1 \end{bmatrix}$.

Equation (2.4.2-14) is a very important result. All subsequent calculations of the output power, photon density and optical intensity (nearfield) distributions are based on it. Note that no phase information of the spontaneous emission is needed in the expression.

The departure from [Zhan92] is as follows: the unit of φ_j and subsequently the product of $\overrightarrow{\mathbf{V}_k}$ and its adjoint is power per unit optical frequency. By restating Eqs. (2.4.2-12a) and (2.4.2-12b) with the new result, the facet output power at angular frequency, ω, becomes:

$$P_l(\omega) = \frac{1 - r_1^* r_1}{1 + r_1^* r_1} \sum_{j=1}^{M-1} \mathrm{tr}\left(\mathbf{Y}_j^{(0)\dagger} \mathbf{Y}_j^{(0)}\right) \varphi_j ,$$

and

$$P_r(\omega) = \frac{1 - r_2^* r_2}{1 + r_2^* r_2} \sum_{j=1}^{M-1} \mathrm{tr}\left(\mathbf{Y}_j^{(M)\dagger} \mathbf{Y}_j^{(M)}\right) \varphi_j . \qquad (2.4.2\text{-}17)$$

The optical spectrum is taken to be the sum of these output power versus frequency. The total output power from each end can be computed by an integration of $P_l(\omega)$ or $P_r(\omega)$ over the optical frequency.

Photon Density Distribution

Photon density, which is assumed to be constant within a segment, is proportional to the average power in the segment. The power at each end of a segment is given by the product of the field vector and its adjoint. Therefore, the average power within the k-th segment can be approximated by the average of the power at both sides of the segment as follows:

$$P_k(\omega) = \frac{1}{2}\left(\overrightarrow{\mathbf{V}_{k-1}}^{\dagger} \overrightarrow{\mathbf{V}_{k-1}} + \overrightarrow{\mathbf{V}_k}^{\dagger} \overrightarrow{\mathbf{V}_k}\right) . \qquad (2.4.2\text{-}18)$$

The photon density at ω in the k-th segment is then given by

$$\psi_k(\omega) = \frac{1}{h\, v_g A_0}\left(\frac{P_k(\omega)}{\omega}\right), \qquad (2.4.2\text{-}19)$$

where A_0 is the optical intensity cross-sectional area. (The area is approximated by $A_0 = w_{\|} \times w_{\perp}$, the product of the waveguide width ($w_{\|}$) and the FWHM of the transverse optical intensity in the waveguide ($w_{\perp}$). We have set $w_{\|} = w$ for

simplicity.) The total photon density in the segment can then be calculated by integrating $\psi_k(\omega)$ over ω.

Variance of Photon Density Distribution

The normalized variance of the photon density distribution (*photon variance*, in short) is a measure of the fluctuation of the photon density (ψ) from its mean value ($\overline{\psi}$) along z. It is therefore a good indicator for LSHB of a laser. The photon variance is defined as [Whit92]:

$$\sigma_\psi = \frac{1}{L_m} \int_{\substack{Pumped \\ Section}} \frac{(\psi - \overline{\psi})^2}{\overline{\psi}^2} dz \qquad (2.4.2\text{-}20)$$

where L_m is the length of the pumped section. The photon density is proportional to the sum of the magnitude-squares of the two counter-propagating waves: $\psi \propto |F|^2 + |R|^2$. A smaller variance implies a flatter distribution along the laser cavity and less LSHB. For example, $\sigma_\psi = 0$ represents a uniform distribution. It is also well-known that quarterwave phase-shifted DFB has a relatively flat distribution ($\sigma_\psi = 0.01$) at $\kappa L_{tot} = 1.25$ [Whit89]. A laser with $\sigma_\psi \geq 0.3$ may be regarded as having strong LSHB.

Nearfield Distribution

The nearfield intensity of the k-th segment is proportional to $|F_k + R_k|^2$. It can be obtained by defining a new singular matrix **G** such that [Yu93]

$$\mathbf{G} = \begin{bmatrix} 1 & 1 \\ 0 & 0 \end{bmatrix}, \qquad (2.4.2\text{-}21)$$

and a new nearfield vector

$$\overrightarrow{\mathbf{U}_k} = \mathbf{G}\overrightarrow{\mathbf{V}_k} = \begin{bmatrix} F_k + R_k \\ 0 \end{bmatrix}. \qquad (2.4.2\text{-}22)$$

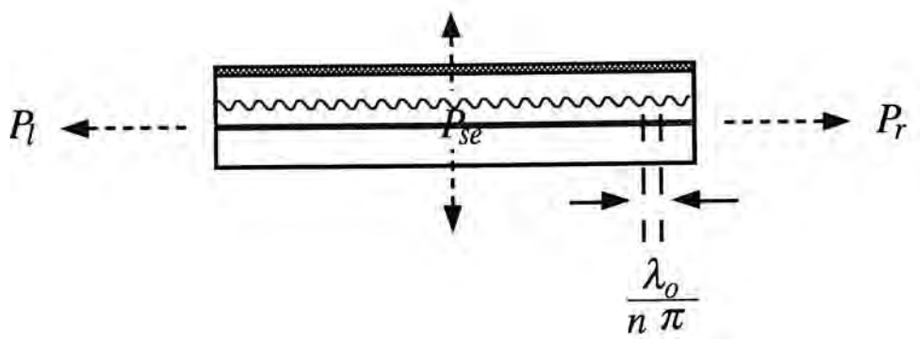

Fig. 2.10 *Schematic drawing of the surface emitting power (P_{se}), left-facet output power (P_l) and right-facet output power (P_r) of a second-order DFB laser.*

The nearfield intensity is then proportional to the trace of $\overrightarrow{\mathbf{U}_k}^{\dagger}\overrightarrow{\mathbf{U}_k}$. The derivation of the product of the nearfield vector and its adjoint is exactly the same as that for the field vector (see *Appendix A.2*). This quantity is again dependent on ω.

Surface Emission Power via Second-Order Grating

For a DFB with second-order gratings, there is an additional radiation power emitting from the surface of the device. This power calculation has not been performed by Zhang, *et. al.*. It is studied here because the ratio of surface-emitting power to edge-emitting power is of interest. The surface emitting power can be deduced from the nearfield intensity distribution and is dependent on the radiation coefficient ξ. In general, the surface emitting power is given by [Glin87]:

$$P_{se} = 2\,\xi \int_{z_1}^{z_2} |F+R|^2 dz\,. \tag{2.4.2-23}$$

Under the transfer matrix approach, it is represented by

$$P_{se}(\omega) = 2 \sum_{k=1}^{M} l_k \xi_k \overrightarrow{\mathbf{U}_k}^{\dagger}\overrightarrow{\mathbf{U}_k}\,. \tag{2.4.2-24}$$

Again, the total power is obtained by an integration over ω.

Note that this method does not take into account the total internal reflections at the superstrate or substrate. It only represents the amount of generated power that is emitted in the direction perpendicular to the junction plane. For symmetric grating profiles, the power of the surface emission through both the up and down directions are equal, whereas asymmetric and blazed gratings can direct more or all of the light preferentially in one direction [Stre76b], [Tami77], [Mats92].

Power-Current Characteristics

The power-current characteristics are computed by repeating the power calculations at a number of input drive currents. Since the calculation at higher current is based on the results obtained at lower current, it has to proceed sequentially, typically starting at the transparency current. As mentioned earlier, no distinction has to be made between below- and above-threshold operations and the same algorithm applies.

The carrier density is calculated from the input current by solving the rate equation with $\frac{dN}{dt} = 0$ for static analysis. The rate equation of the carrier density (e. g. [Agra93]) is given by

$$\frac{dN}{dt} = \frac{J}{ed} - \frac{N}{\tau} - B_N N^2 - C_N N^3 - \frac{a\,(N-N_t)}{(1+\varepsilon\psi)} v_g\,\psi \qquad (2.4.2\text{-}25)$$

where J is the injected current density, e is the electron charge, τ is the carrier lifetime, B_N is the bimolecular recombination coefficient, and C_N is the Auger recombination coefficient. This third-order polynomial equation is solved by standard method.

Initially, the carrier density is assumed to be uniformly distributed among all the pumped segments and $\psi = 0$ for all segments. Then the noise powers and the gain coefficients are computed with Eq. (2.2.2-1) and Eq. (A.1-1), respectively. They are then followed by the calculation of the transfer matrices and subsequently, the output powers at ω at the left and right facets by Eq. (2.4.2-17) and the surface emission in

the case of second-order DFB by Eq. (2.4.2-24). The photon density in each segment can also be obtained by means of Eq. (2.4.2-19). These steps are repeated for each ω value. The final results are then summed over a desired frequency window which should be large enough to contain the major lasing modes.

After each completion of calculation over frequency, the solution is checked for self-consistency. The photon density distribution is used as the criterion. If the solution converges, the carrier density and the effective index distributions are computed. The index is obtained by Eq. (2.2.3-1) and is used as the criterion for a second test on self-consistency. Note that the effective index is only altered after a solution is located which has already met the first convergence requirement. This is to avoid a strong shifting of the mode frequency which it clearly would if the refractive index profile was changed. If the solution meets the convergence and other requirements, it is saved. The calculation then proceeds at the next current level until the final current is reached or no solution can be found. The result is a power-current curve that begins at transparency.

Optical spectrum

The optical spectrum is taken as the total facet output power versus optical frequency. Its computation has been briefly described in the previous section. Basically, the total output power from the ends are calculated over an optical frequency (or wavelength) window at regular intervals. Since the spectral linewidth is often 2 to 3 orders of magnitude smaller than the mode separation, the choice of the frequency stepsize that is good for the linewidth calculation is almost always at odd with the desire to consider more than one lasing mode. This problem is solved by applying a *zoom-in* method (see also *Section 2.4.3*). First, a frequency stepsize, not necessarily small, is selected. Then the locations of the peaks (lasing modes) in the resulting spectrum are recorded. A smaller frequency stepsize is then used in the neighborhood

of each peak and power is only computed in those regions leaving the gaps between the modes unchanged. This process is repeated until the FWHM (spectral linewidths) of the lasing modes converge. Finally, the optical spectrum, along with the linewidths and the SMSR are obtained directly with no additional approximation.

Here again is another important departure from Zhang's approach. Instead of making an assumption about the lineshape of the lasing modes (e.g. Lorentzian function) for faster power computation, the power distribution in frequency is directly calculated. This method requires no single-mode assumption and the spectral linewidth is obtained automatically. It also gives better accuracy. It may seem to be more computational intensive but is really not so. The convergence on the linewidth takes place quite quickly. It also desensitizes the choice of the initial frequency stepsize and allows a more accurate output power calculation.

Note that during the course of developing this model, it was discovered that the true lineshape obtained by direct computation could be asymmetrical and could differ quite significantly from the Lorentzian lineshape. The deviation is especially apparent under subthreshold operation and in the case when the lasing mode is close to the edges of the stop-band. The latter case has been observed experimentally. According to [Mart94], the spectral lineshape is quite asymmetrical for a number of second-order DFB lasers. More details on the theoretical lineshape analysis can be found in Chapter 2 of [Zory93]. For operation at much higher current with respect to the threshold current, the lineshape is well approximated by the Lorentzian function with negligible loss in accuracy.

Subthreshold Analysis

Subthreshold analysis[1] can also be performed based on the same DFB model with the exception that iterations are omitted and carrier-induced index change and zoom-in are ignored. This means the optical spectrum as a function of g_{th} is calculated assuming that none of the modes have reached threshold. As a result, g_{th} for each mode is obtained. The lowest-loss mode is the one with the smallest g_{th}. The difference in g_{th} (Δg_{th}) between the two lowest-loss modes is often used as an indicator of the quality of single-mode behavior. Better mode discrimination can be inferred from a larger Δg_{th}.

Linear Yield Analysis

Theoretical yield of a laser design is an extension of the subthreshold analysis. The yield is the percentage of useful devices (those that meet a set of requirements) that may be expected from a large sample of fabricated devices. For DFB lasers, the uncertainty arises from the fact that the grating phase at the cleaved facet is random and uncontrollable. This phase angle can have a positive or negative effect on the laser performance and its sensitivity varies with different laser designs. The yield is therefore a good indicator of the robustness of the design and its manufacturability. In this work (*Section 4.4*), the phase angle is assumed to be completely random and its value is uniformly distributed between zero and 2π. The random phases of the facet reflectivities are simulated with 20×20 combinations (20 increments from 0 to 2π radians for each facet). For each phase combination, the Δg_{th} of the two lowest-loss modes is obtained. The σ_ψ and I_{th} for the lowest-loss mode are also saved. These three values are then tested to see if they pass the criteria

---

1 Strictly speaking, the analysis is linear (no iteration) but not subthreshold since we are seeking to simulate the above-threshold behavior. However, the term 'subthreshold' is widely used and accepted in the literature.

for positive yield. This test is repeated until all phases combinations are exhausted. The percentage of passes is then the expected yield of the laser design.

2.4.3 Computer Implementation

As mentioned before, the approach and methodology are general in nature and are applicable to DFB with an arbitrary number of sections. However, on balancing the scope and functionalities of the model with the limited time and resources, the computer implementation focuses on the three-section DFB-type devices only. The computer program is written in FORTRAN 77 on a Macintosh Quadra 950 with a clock rate of 33 MHz. The same program has subsequently been exported to a DEC Alpha workstation with a faster clock rate of 100 MHz.

The remainder of this section details the computer implementation of the above-threshold multisection model. It first gives an outline of the computer program in the form of a flowchart. Next, the subroutines are described with the help of calling sequences. Finally, the discussion on the numerical performance concludes this section.

Flowchart

The flowchart of the computer program is shown in Fig. 2.11. The steps are (step numbers correspond to those in the figure):

1. Enter the device, material and grating parameters for initialization.
2. Specify the final injection current and the current distribution along z (pumped section versus unpumped section).
3. Choose subthreshold or above-threshold analysis.

4. For subthreshold analysis, compute the threshold gain versus frequency or the yield by iterations over the phase angle of the facet reflectivity. The yield that meets the requirements imposed by the desired Δg_{th}, LSHB, or the threshold current can then be calculated.

5. For above-threshold analysis, start calculation at current just above transparency assuming zero trial photon density and uniform distribution of carrier density over the pumped section.

6. Update the effective index profile.

7. Compute the carrier density and then the gain distribution based on the trial photon density distribution and the input drive current.

8. For each frequency step within a user-set frequency range, compute the transfer matrices, then the output power from the facets and the photon density distribution as functions of optical frequency detuning from the Bragg condition. When completed, sum all powers and photon densities for convergence test and output purposes.

9. Search for the peaks in the spectrum and use zoom-in technique for better accuracy.

10. Check if the average photon density along the laser cavity converges. If convergence fails, repeat steps *7* to *9* with an updated trial photon density. This modification in the trial photon density is determined by the *Secant Method* [John82] for faster convergence. Go to next step if photon density converges.

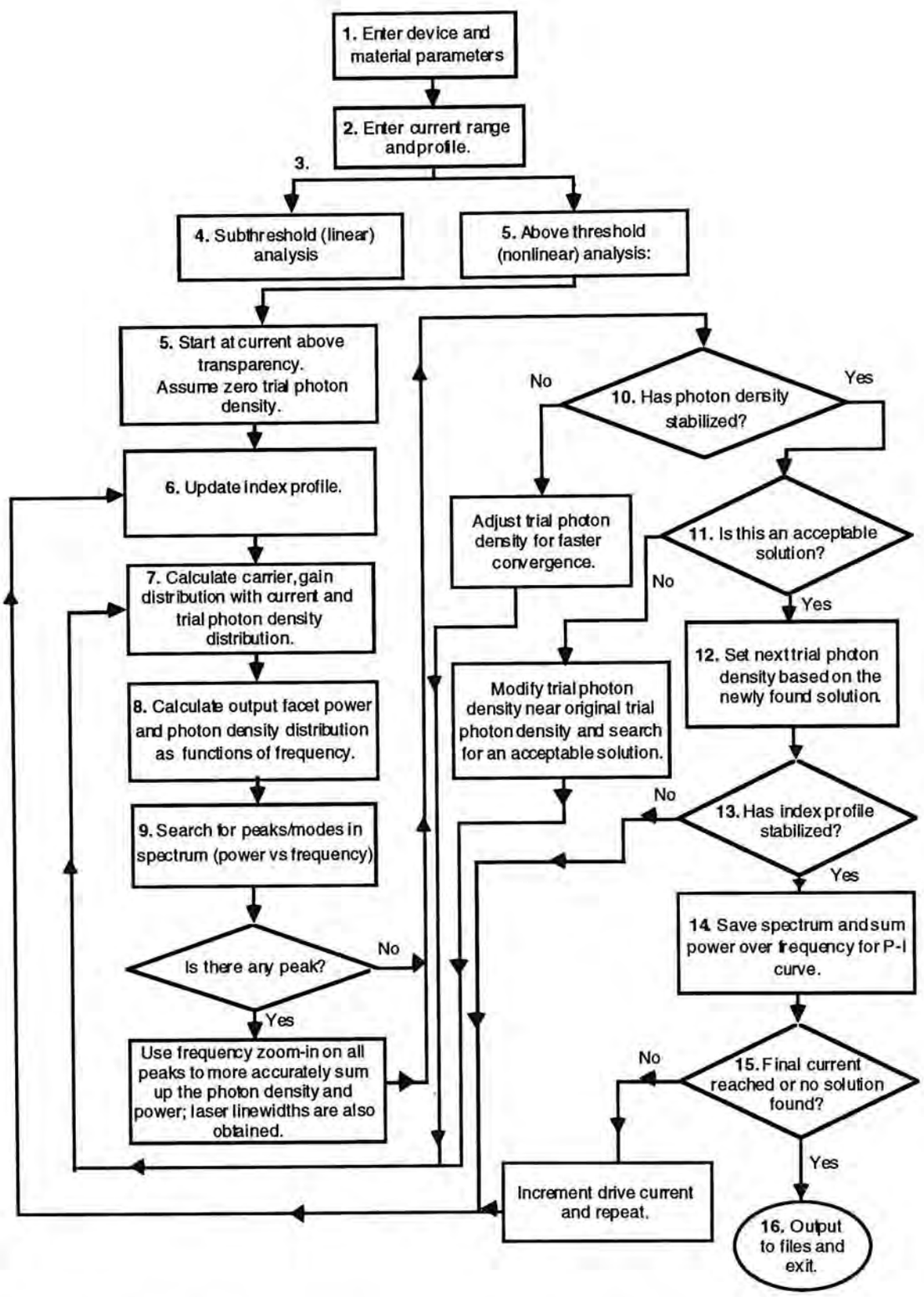

Fig. 2.11 *Flow chart of the computer model: the numbers correspond to the step numbers in the text.*

11. Check if this newly found solution is acceptable. The reason for this step is that an unphysical or erroneous numerical solution may result because the starting point (the assumed photon density) is too far away from the solution. This sometimes manifests as a huge sudden drop in output power. If the solution is not acceptable, modify the assumed photon density and repeat steps *7* to *11*. Or, if a preset maximum number of iterations is reached and the *adaptive stepsize* option is selected (*next section*), reduce the current stepsize and repeat steps *7* to *11*. Otherwise, go to next step.

12. If the solution is acceptable, alter the effective index profile based on the converged photon density and its associated carrier distributions.

13. Check if the effective index converges. If not, repeat steps *6* to *12*. Again the method employed for faster convergence is the Secant method.

14. If the effective index stabilizes, assume that the self-consistent solution is found. The desired outputs are saved.

15. Iterate steps *6* to *14* for the next drive current until the final current is reached or an acceptable solution can not be found. The trial effective index and photon density distributions for the next current step are based on the newly obtained results. If the *adaptive stepsize* option is selected, modify the current stepsize according to the output power. If the power rises too rapidly, discard the results and repeat steps *6* to *14* with a smaller current stepsize.

16. Output results to files; these include the optical spectrum, carrier, nearfield and photon distributions, the power-current characteristic as well as the mean value of the effective index, SMSR, linewidth, lasing frequency, photon density distribution variance, and the effective grating coupling coefficients.

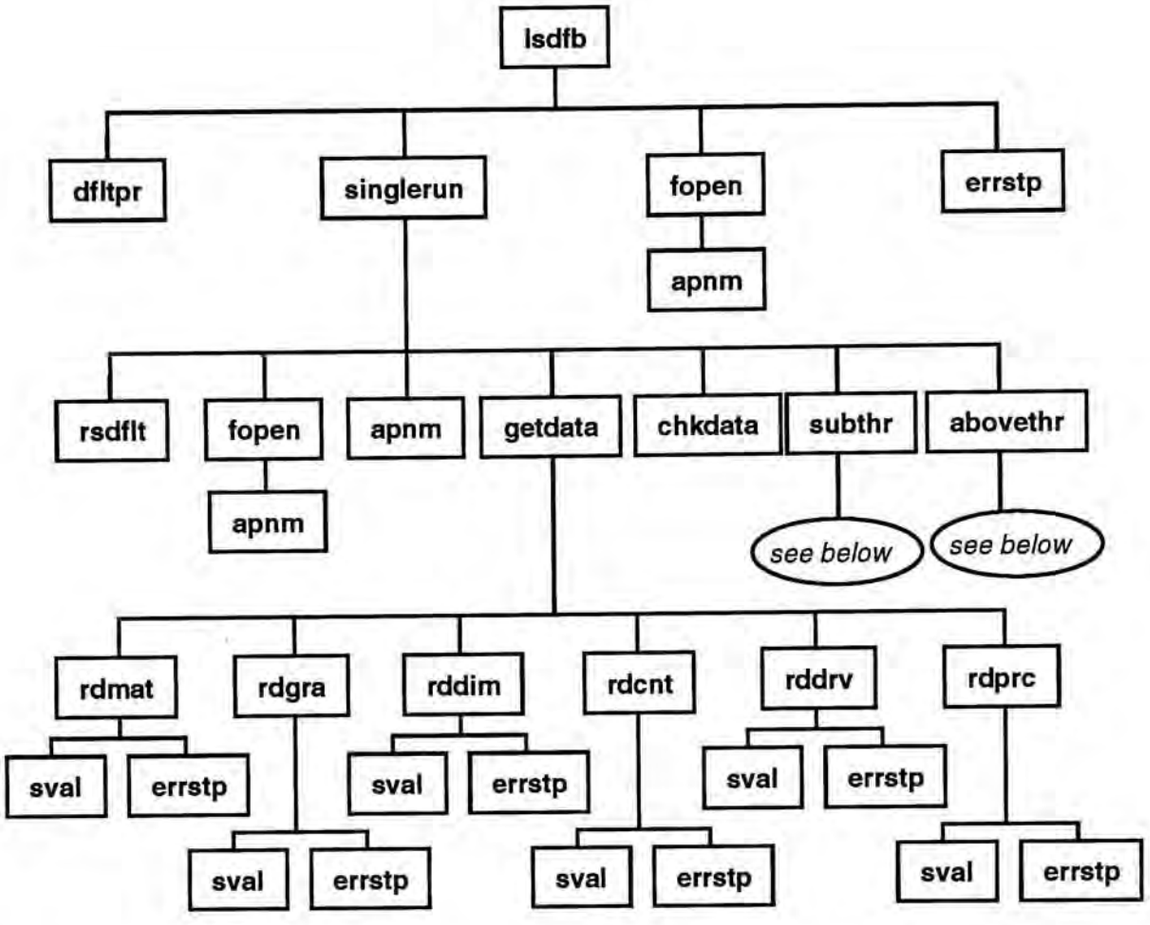

Fig. 2.12a *Calling sequence of the main program, 'lsdfb'. Each block contains the name of a subroutine or function.*

If the user-set maximum number of iterations is reached at the three check points (steps *10*, *11* and *13*), the execution of the program is transferred to step *16* and is then terminated.

Subroutines

The computer program is implemented in modular form which makes it easier to modify and expand in the future. For instance, the calculation of the gain coefficient is in a separate subroutine. If a more accurate model (e.g. [Ma95]) is desired, only this subroutine has to be altered. Similarly, the increase in the number of sections can be

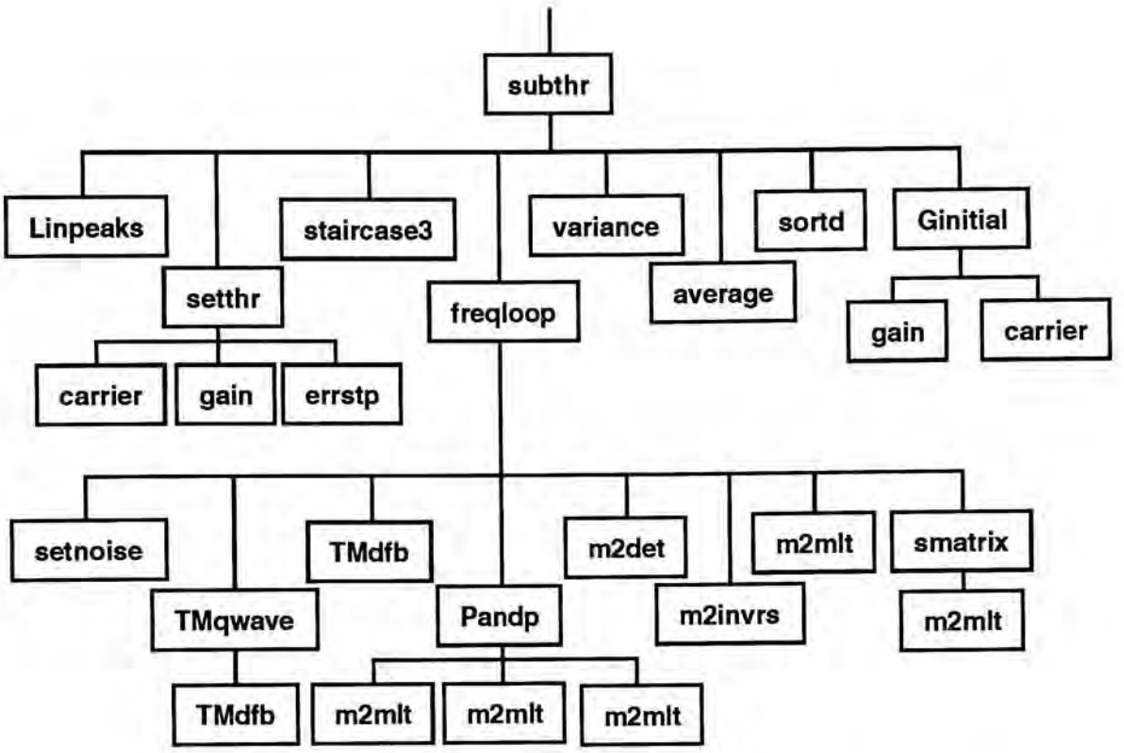

Fig. 2.12b *Calling sequence of the subroutine 'subthr'.*

accommodated without rewriting the entire program. All the subroutines are grouped by functionality and their listings are stored in four files. The listings can be found in *Appendix B*. The first is file 'drive.f' which contains all the input reading procedures that basically transforms an ASCII input file into machine recognizable numerical and logical data. The 'core.f' contains subroutines that perform all the major calculations and convergence tests. The 'initial.f' sets and resets parameters for each iteration. The 'misc.f' contains miscellaneous subroutines that do simple calculations such as matrix multiplication, gain coefficient, carrier density, and so on.

The calling sequence of each subroutine is listed in Fig. 2.12a through Fig. 2.12d. The roles of the subroutines are described in *Appendix B*. Some of the major ones are discussed as follows.

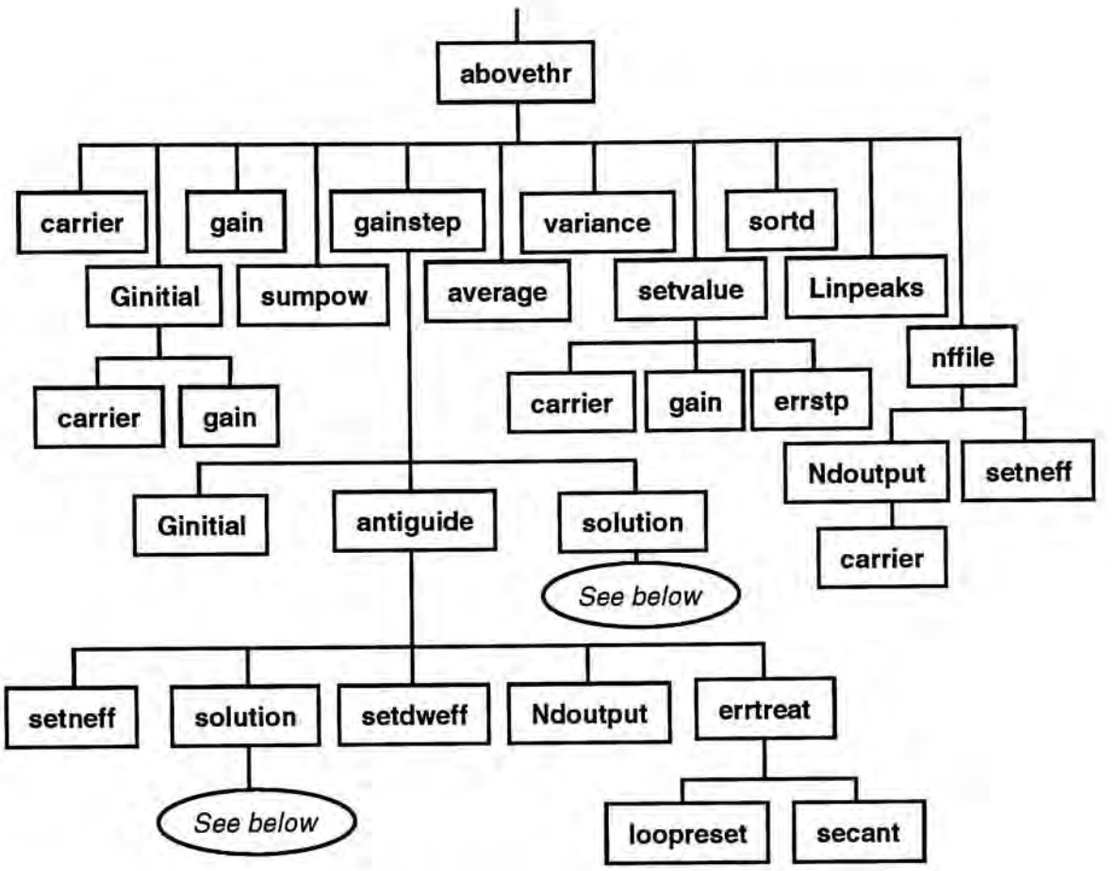

Fig. 2.12c *Calling sequence of the subroutine 'abovethr'.*

Subroutine 'subthr'

Subroutine 'subthr' calculates the subthreshold spectrum as a function of threshold gain, the single-mode yield and Δg_{th} between the two lowest-loss modes. This process is based on the same nonlinear model with the exception that no iteration is performed.

Subroutine 'abovethr'

This subroutine performs the above-threshold analysis of a DFB laser as described earlier. The user can choose to use constant current stepsize or adaptive current stepsize. In general, the computation is faster with constant stepsize but the

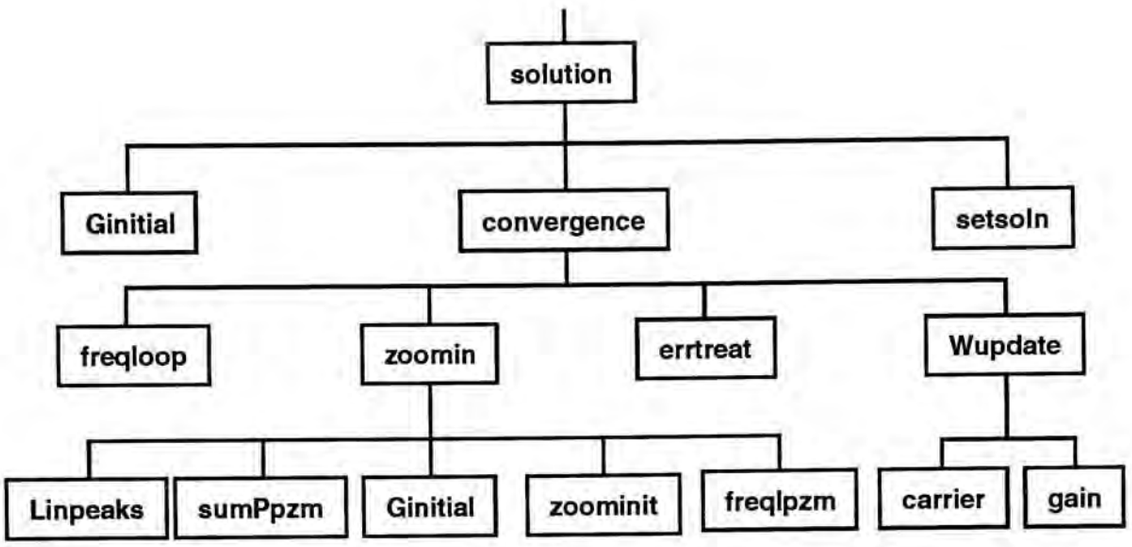

Fig. 2.12d *Calling sequence of the subroutine 'solution'. Note that both 'freqlpzm' and 'freqloop' call the same sets of subroutines as shown in Fig. 2.12b.*

accuracy may suffer depending on the value selected. At the transition region near the threshold, the power may rise very rapidly. Hence, smaller stepsize is usually needed. The adaptive stepsize option is particularly useful when the threshold of the laser is unknown.

Subroutine 'antiguide'

Subroutine 'antiguide' ensures that the effective index distribution in the final solution has converged. It modifies the effective index caused by the presence of carriers ('*setneff*') and calculates the shift in frequency ('*setdweff*'). The alteration is only performed after the solution has passed other convergence tests. The trial solution is estimated by the secant method.

Subroutine 'solution'

This subroutine compares the solutions in the present current level to the one in the previous current loop. If the current solution does not meet certain criteria, it is

discarded. The search of a physically meaningful solution is attempted again either with a smaller current stepsize or with modified trial solutions which hopefully are placed within close proximity to the real solution. If an acceptable solution is found, the current stepsize may be increased for faster computation. The input at the next current step is adjusted according to the current stepsize.

Subroutine 'convergence'

This subroutine performs a search for a converged solution. It computes the power and photon density over a broad frequency range (*'freqloop'*), performs a frequency expansion to improve accuracy (*'zoomin'*), reconstructs the optical spectrum with the results, and checks for self-consistency. Finally, this process is repeated until a converged solution is found or until the number of iterations becomes too large (*'errtreat'*).

Subroutine 'secant'

Subroutine 'secant' [John82] derives the trial solution for the next iteration from the results obtained in the previous and the current convergence loops. It enables faster convergence and is part of an error-treatment procedure. The method is very similar to the *Newton-Raphson method* [Math87] and it usually arrives at a solution in less than 4 tries.

More descriptions on other subroutines can be found in *Appendix B*.

Runtime, Numerical Stability

This computer model has reasonable execution time. With the laser cavity divided into 20 segments, 100 current loops and 100 frequency points, the runtime is about 30 minutes on a Macintosh Quadra 950 when the final current level is reached without premature termination of the program. If the search of an acceptable solution fails at any of the three convergence check points, the runtime is generally increased

by a factor of two to four. It all depends on the maximum number of attempts at the solution search and the maximum number of iterations that the user sets. The calculation errors also depend on the number of segments, iteration steps, and convergence criteria. When the analysis is performed on the DEC Alphastation, the runtime is typically reduced by a factor of 3 because of the faster clock rate.

The possible reasons for the failure in finding a solution are (1) the lasing longitudinal mode no longer exists continuously; and (2) the numerical method or algorithm becomes unstable. The typical scenario is as follows. Initially, the solution can be found very easily (rarely requires any additional attempts), starting from the transparency current to the threshold. Beyond threshold, as the drive current increases, the number of attempts required to reach a converged solution increases. Approaching the breakpoint at which no solution is feasible, the current stepsize has to be shrunk in order to locate a valid solution. The situation usually deteriorates after that and the stepsize has to go through a number of reductions. Finally, the program quits because the stepsize is unreasonably small or the maximum number of attempts has been reached.

There is no easy way in each and every case to identify which of the two events is responsible by simply investigating the outcome. In order to reduce the likelihood of the second possibility, a number of strategies have been built into the program. They include, as mentioned earlier, the adaptive current stepsize, the secant method in both the '*convergence*' and the '*antiguide*' subroutines, and the different trial solutions in subroutine '*solution*'. All these strategies are attempts to bring the trial solution closer to the true solution and to reduce the accumulated error. This endeavor is fairly exhaustive. That means, if a solution indeed exists continuously, it is highly unlikely that it is missed.

In conclusion, if we fail to obtain a converged solution, the most probable reason is that the stable mode no longer exists continuously. In other words, the

mode becomes unstable if the calculation tends to diverge. A mode-hop to other stable mode is presumed to happen. The occurrence is usually preceded with a rapid rise in the number of iterations. It is also more severe when the antiguiding factor is large. In addition, as briefly discussed in [Kino94], the instability is likely to occur before Δg_{th} reaches zero (that is, the next mode has the same gain as the lasing mode). This is also confirmed by our observations. The trend of numerically slow convergence just before the mode-hop might be related to the mode-hopping noise in DFB lasers.

It should be noted that a change in the relative intensities of the lasing modes (a shift to another dominant mode or multimoded operation) does not necessarily incur numerical instabilities as described in the last paragraph. In the case when Δg_{th} reaches zero, the transition from one dominant mode to another is usually smooth and there is no difficulty in obtaining a self-consistent solution. Even in cases when the transition is abrupt, a solution could be located. Finally, it is worthwhile to point out that the mode-instability problem in theoretical modeling is rarely discussed in the literature. It is not getting much attention although the problem is real and often encountered [Soda87].

2.5 Discussion, Summary and Future Work

2.5.1 Validation of the DFB Model

For the validation of the DFB model, calculated results are compared with those by other models. In addition, comparisons are made with experimental data whenever possible. Overall, they are in good agreement especially when the same parameter values are used and direct comparison can be carried out. The lasers selected for validation purposes are QWDFB, DFBDBR and LCDFB. The QWDFB laser is more frequently examined because it is often selected as a case in point by other researchers.

A direct comparison is made with the analysis on a QWDFB laser as reported in [Zhan92]. For validation, the same parameter values are chosen and they are listed in Table 2.1. The calculated power-current curve is shown in Fig. 2.13. The insets are the spectral lineshapes at 40 mA, 45 mA and 50 mA. The power is the sum of the output power from both facets. The threshold current is about 33 mA. As shown in Fig. 2.14, the laser linewidth agrees well with the inverse power dependence and is about 52 MHz at 50 mA. The linewidth also appears to hit the linewidth floor at 52 MHz beyond 47 mA. These results are almost identical to those in [Zhan92], which in turn agree well with those in [Whit89]. They therefore validates the DFB model as well as its computer implementation.

To further validate our model, the simulated spectral linewidth is compared to a widely used analytical expression as follows. The spectral linewidth ($\Delta\nu$) for a Fabry-Perot laser is given by the modified Schawlow-Townes formula [Henr82]:

$$\Delta\nu = \frac{v_g^2 \, h\nu \, G_{th} \, n_{sp} \, \alpha_m}{8 \, \pi \, P_r} (1 + \alpha_H) \qquad (2.5.1\text{-}1)$$

Parameters	*Values*
Linear carrier lifetime (τ)	∞
Bimolecular carrier recombination coefficient (B_N)	1.0×10^{-10} cm^3s^{-1}
Auger carrier recombination coefficient (C_N)	3.0×10^{-29} cm^6s^{-1}
Differential gain (a)	3.0×10^{-16} cm^2
Nonlinear gain compression factor (ε)	3.0×10^{-17} cm^3
Transparency carrier density (N_t)	1.5×10^{18} cm^{-3}
Linewidth enhancement factor (α_H)	4.86
Absorption and scattering loss (α)	40.0 cm^{-1}
Grating coupling coefficient (κ)	50.0 cm^{-1}
Effective phase refractive index (n)	3.28
Effective group refractive index (n_g)	3.7
Length of the laser cavity (L)	400.0 μm
Active layer thickness (d)	0.18 μm
Effective width parallel to junction ($w_{\|\|}$)	3.5 μm
Effective width perpendicular to junction ($w_\perp$)	0.47 μm
Far-field angular divergence parallel to junction ($\theta_{\|\|}$)	20.0°
Far-field divergence perpendicular to junction ($\theta_\perp$)	50.0°
Active layer confinement factor (Γ)	0.35
Bandwidth of spontaneous emission spectrum (Δf_{sp})	80.0 nm
Approximate emission wavelength (λ_o)	1.55 μm
Number of divided segments including the phase shifter	13

Table 2.1 *Parameters used in quarterwave phase-shifted DFB simulation*

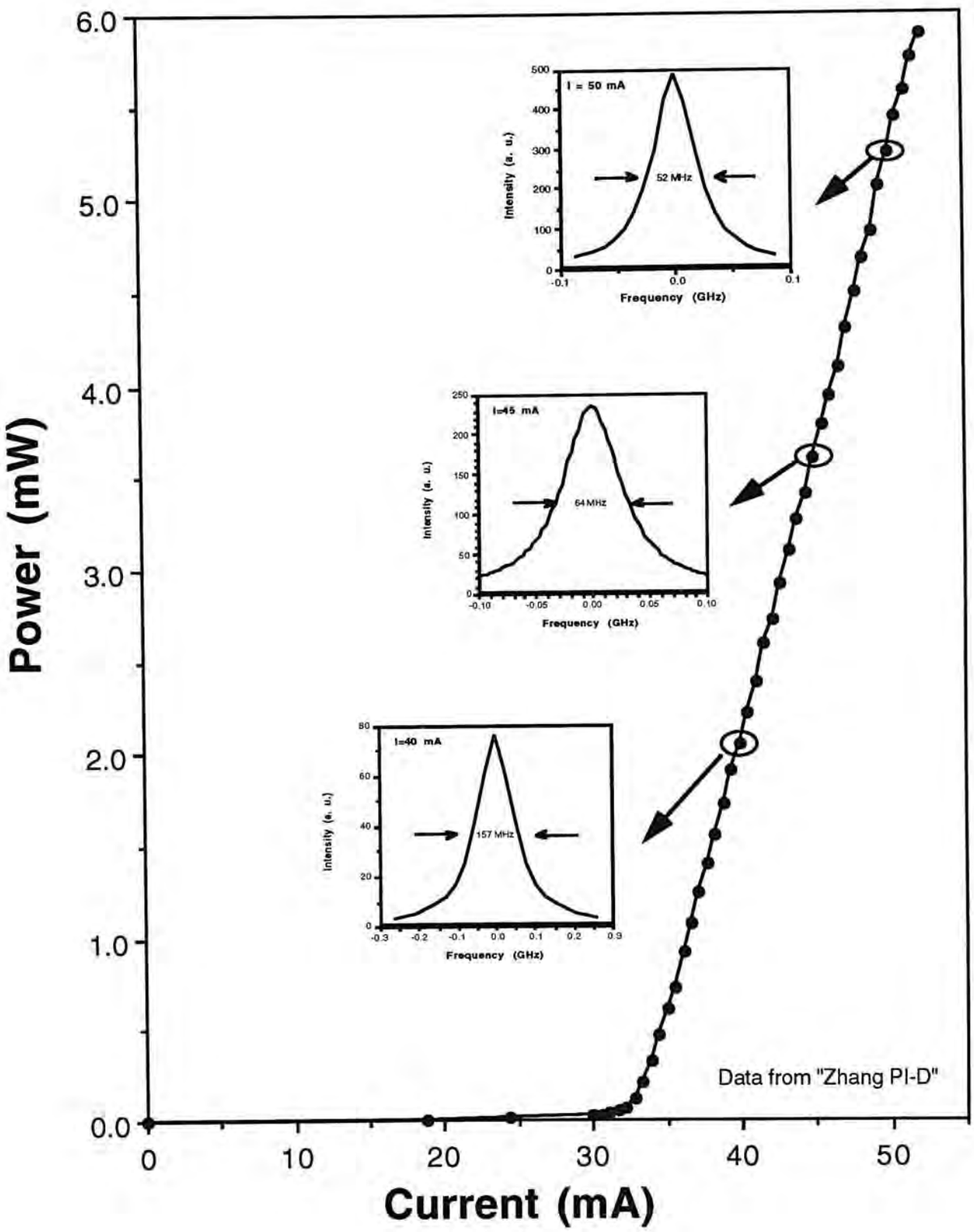

Fig. 2.13 Calculated power-current curve of quarterwave phase-shifted DFB laser with parameters listed in Table 2.1.

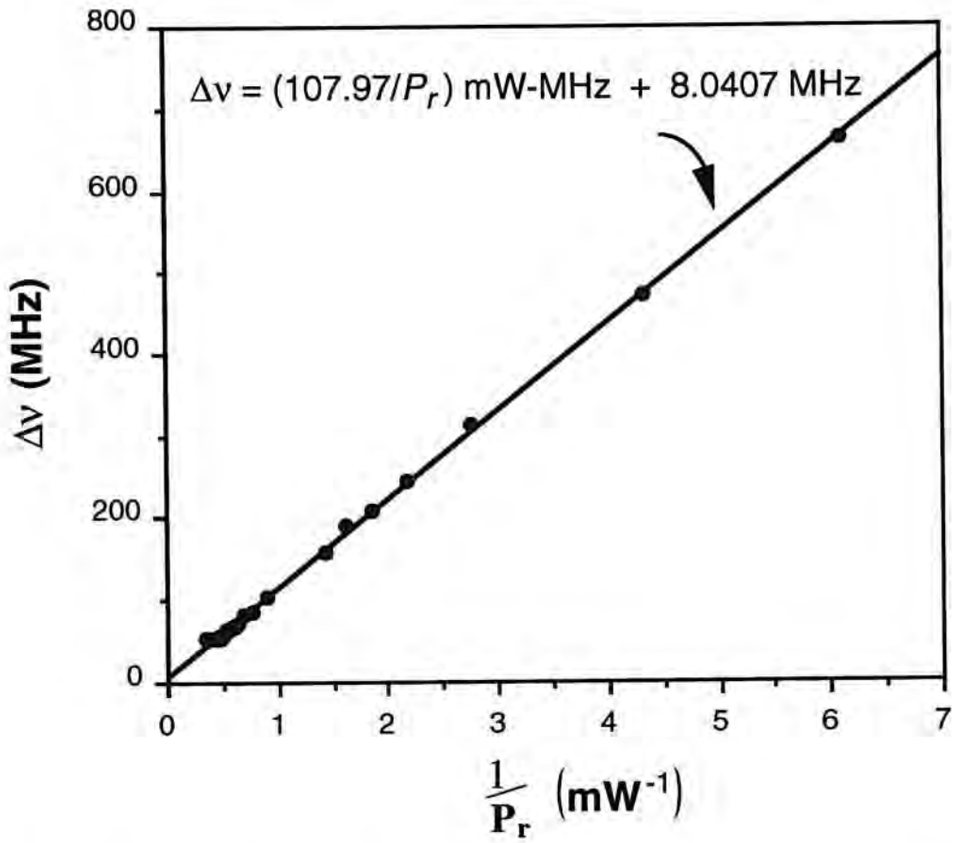

Fig. 2.14 *Calculated spectral linewidth as a function of inverse power from one facet for the QWDFB with parameter values listed in Table 2.1. The straight line is the best linear fit of the data.*

where h is the Planck's constant,ν is the lasing frequency, G_{th} is the threshold power gain, n_{sp} is the spontaneous emission factor, α_m is the mirror power loss and P_r is the output power from one facet. The threshold gain and mirror loss are related by $G_{th} = \alpha_m + \alpha_o$, where α_o is the material loss. n_{sp} is a statistical factor that accounts for incomplete population inversion. For semiconductor laser, $n_{sp} \cong 2.5 \rightarrow 3.0$ [Osin87].

Equation (2.5.1-1) is also applicable to DFB lasers by replacing α_m with the effective output power loss ($\overline{\alpha}$). In this case, $G_{th} \cong 74$ cm^{-1} is obtained. This gives $\overline{\alpha} = 34$ cm^{-1} with $\alpha_o = 40$ cm^{-1}. Substituting these and other values from Table 2.1 into Eq. (2.5.1-1), we obtained

$$\Delta\nu = \frac{n_{sp}}{P_r}(20.78 \text{ mW-MHz}) \qquad (2.5.1\text{-}2)$$

Since our description of spontaneous emission does not make use of n_{sp}, it is left in the expression.

Before comparing this result with the simulated linewidth, it should be noted that, for DFB laser with small facet reflectivity, $\Delta\nu$ is enhanced by an extra multiplicative factor. This correction factor (F) has been calculated using the Green's function method [Koji88]. For this example with $\kappa L = 2.0$ and zero facet reflectivity, $F \cong 1.2$ and we obtained,

$$\Delta\nu = \frac{F\, n_{sp}}{P_r}(20.78 \text{ mW-MHz}) = \frac{n_{sp}}{P_r}(24.94 \text{ mW-MHz}). \qquad (2.5.1\text{-}3)$$

Assume that $n_{sp} = 3.0$ for semiconductor laser. The expected linewidth is therefore: $\Delta\nu \cong \frac{74.82}{P_r}$(mW-MHz). As shown in Fig. 2.14, the simulated linewidth is, $\Delta\nu_{sim} \approx \frac{1}{P_r}(107.97 \text{ mW-MHz})$. This result is about 44% higher than the expected value. The discrepancy can be attributed in large part to the larger effective linewidth enhancement factor (as opposed to the material α_H) caused by spatial hole burning. The increase in α_H is on the order of 20% [Olof92]. Substituting the higher α_H value yields $\Delta\nu \cong \frac{106.37}{P_r}$(mW-MHz), which is in good agreement with the simulated result. It gives strong support for the validity of the model.

In addition, this comparison also serves to illustrate the fact that the simulated linewidth calculation already includes the effects of the nonuniform distributions of the carrier density and refractive index as well as gain saturation. As a result, the effective linewidth enhancement factor can be deduced. This procedure is performed in *Section 3.3.5* for the three-section DFBDBR laser.

Another example is the analysis of the three-section second-order DFBDBR laser (*Section 3.2*). The subthreshold findings are very similar to those reported in [Carl91]. As the reported results were obtained with a principally different network

model [Aman90], the similarity points to further validation of the model. As to the above-threshold analysis of this laser, since it is performed in this thesis for the first time, no theoretical comparison is possible. Nevertheless, the experimental data on this device [Liew91] supports the calculated results. In particular, devices with about 18 combinations of active and passive section lengths were examined experimentally. With the exception of only two combinations, the mode of operation agrees with our findings (see *Section 3.3.3*). It therefore gives an important experimental confirmation of the model. Furthermore, the model is able to explain the experimentally observed peaked nearfield pattern over a large range of parameter values. It also provides insights into the workings of this laser and suggests values of the design parameters for optimized performance.

The last supporting example for the validity of the model is based on two subthreshold yield analyses. The method of calculation is given in *Section 4.4*. The lasers involved are the as-cleaved purely LCDFB laser and the QWDFB laser with 1%-reflectivity facet coatings. These devices are chosen because relevant information is available for comparison. In particular, a comparison is made with [Davi91b] because this model has been validated by theoretical and experimental data.

The calculated yield data of the as-cleaved LCDFB laser (also shown in Fig. 4.24) are compared. Two curves are graphed in Fig. 2.15. The broken curve is taken directly from Fig. 14 of [Davi91b]. The solid curve is obtained by our model. The same threshold gain margin (≥ 0.3) is required and no other criterion is imposed. Although the device parameters are somewhat different, the numerical values agree quite well. In addition, the discrepancy is partly attributed to the fact that absorptive grating is assumed in our calculation and gain-grating is used in the referenced report. The results from both models indicate high single-mode yield when the product of the coupling coefficient (κ) and the cavity length (L) is greater than ~1.5.

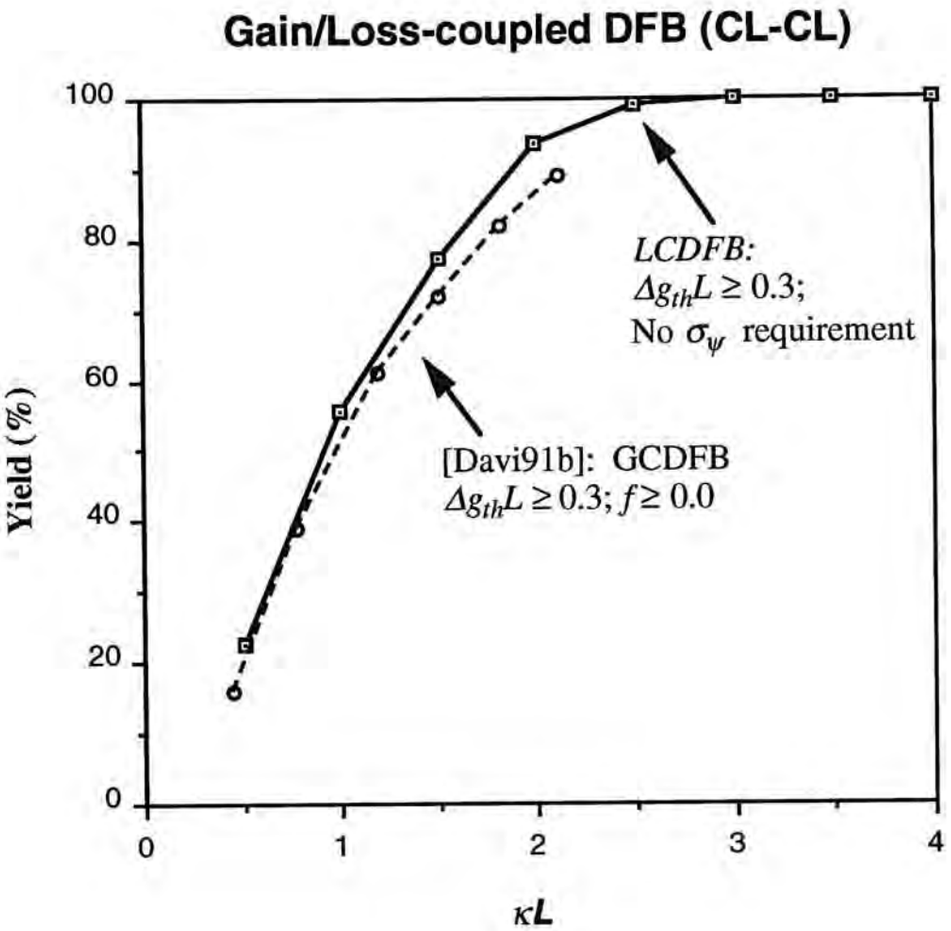

Fig. 2.15 *Comparison of calculated yield for purely gain/loss-coupled DFB laser with as-cleaved facets; only the threshold gain margin requirement is imposed.*

Finally, the calculated yield data for the QWDFB laser with 1%-reflectivity facet coatings are compared. Again, in this case, the same threshold gain margin criterion is applied. In addition, a requirement on the photon density uniformity is imposed. Since the parameters defined in the two models are different, direct comparison is difficult. In our case, the uniformity is described by the photon variance. In [Davi91b], a factor, f = (minimum intensity ÷ maximum intensity), is applied instead. In Fig. 2.16, the yield with $f \geq 0.4$ (replicated here from Fig. 5d of [Davi91b]) is plotted along with the yield with $\sigma_\psi \leq 0.1$ (also shown in Fig. 4.20) and $\sigma_\psi \leq 0.05$

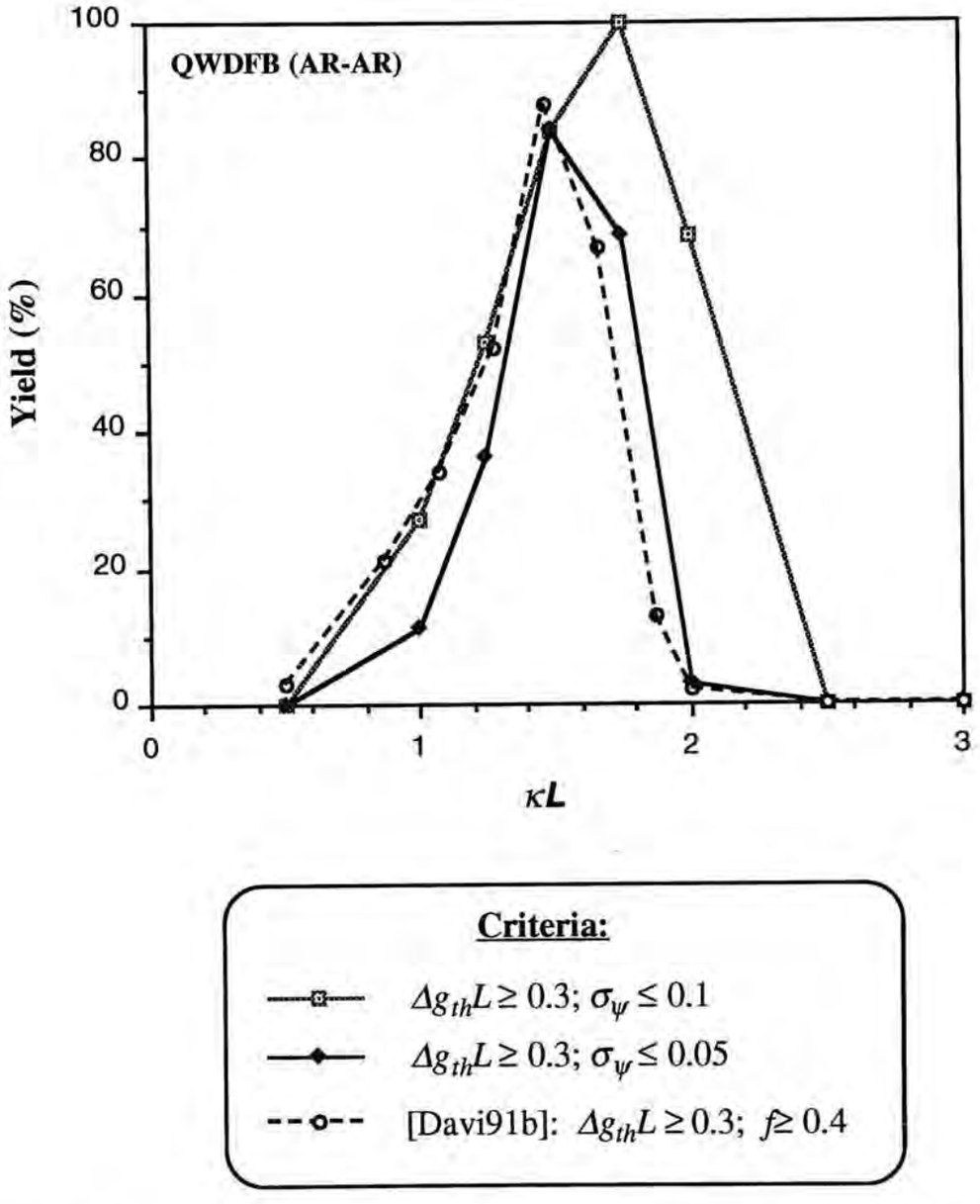

Fig. 2.16 *Comparison of calculated yield for quarterwave phase-shifted DFB laser with 1% reflectivity.*

obtained with our model. The data obtained with the more stringent requirement ($\sigma_\psi \leq 0.05$) bear closer resemblance to the reported result. The agreement is better for $\kappa L > 1.0$. Besides the dissimilar criterion, the device parameters are also causes for the discrepancies. Despite the differences, the two yield distributions reveal similar dependence on the coupling coefficient. The maximum yield is near $\kappa L \approx 1.5$ and the minimum yield (0%) is at $\kappa L < 0.5$ and $\kappa L \geq 2.5$.

As discussed above, results from the subthreshold, above-threshold and yield analyses are in good agreement with those found in published reports. Therefore, they give strong confirmation of the validity of the DFB model.

2.5.2 Summary

In this chapter, we have discussed in detail the nonlinear three-section DFB model that has been developed. It has been compared with other models in the literature. The assumption and approximations are described in *Section 2.2* which include the nonlinear effects such as LSHB, spontaneous emission, nonlinear gain saturation and carrier-induced index change. The formalism of this model is applicable to arbitrarily complex DFB lasers with multisection. The theories and approaches, namely, the coupled wave theory and the transfer matrix method, are presented in *Section 2.3*. In this section, the concepts and theories on second-order DFB and complex-coupled DFB lasers are introduced. These are then followed by *Section 2.4* in which detailed derivations of the necessary formulas and discussions on computer algorithm, subroutines and numerical stability are presented. The computer implementation performed in this work is tailored to a three-section DFBDBR laser with second-order grating. It is later modified to include gain and loss gratings. A number of examples are presented for the validation of the model. They include an above-threshold analysis of a QWDFB laser including a comparison of the spectral linewidth, a subthreshold analysis of the DFBDBR laser along with comparison with experimental data, and finally the yield analyses of QWDFB and LCDFB lasers.

Overall, we have achieved our goal in developing a general purpose above-threshold model. Although the fundamental principles are based on [Zhan92], the implementation and some of the approaches and techniques are unique as discussed in *Section 2.3* and *2.4*. These deviations enable the implementation of a fully

multimoded model and the analysis of a three-section device. They allow a direct and more accurate computation of the spectral linewidths, output power and photon density. In addition, devices with more sophisticated gratings can now be studied. The various gratings include first- and second-order gratings, gain-grating with induced index grating, and absorptive-grating with loss saturation at high photon densities.

As discussed in the preceding section, mode instability can be a problem that should be explored in depth even though it has not prevented us from gaining useful information of devices under study. However, the user should keep in mind of the potential difficulties by carefully setting the convergence criteria and other control parameters.

2.5.3 Topics for Future Work in Theoretical Modeling

Although the model that we have set out to develop is completed, there are areas for further improvements. These and other suggested topics are left for future endeavors. Some of these have been found to be worthwhile for further exploration based on the experience of developing the model. Others are ideas from the literature. They are as follows.

- *Mode Instability*

  As discussed in the preceding section, this phenomenon needs more serious investigation.

- *Small and Large Signal Dynamic Analysis*

  A small signal dynamic analysis can be implemented in a fairly straightforward manner by solving the carrier rate equation. An extension to a large-signal model is more difficult because our model is deterministic in a mixed time/frequency domain (*Section 2.1*). A purely time-domain model is a better approach for dynamic analysis [Lowe92], [Tsan94a].

- *All Active Sections*

  A generalization to all active sections will enable the calculations of tunable DFB lasers [Cold87], which are important in WDM (wavelength division multiplexing) applications [Pan94].

- *More Than Three Sections*

  Another generalization to a larger number of sections will enable the calculations of DFB laser arrays and other complicated devices. The implementation is straightforward although it will certainly increase the computational complexity. Furthermore, it may not be a more viable approach when compared with other models such as a two-dimensional network model [Aman90].

- *Grating Coupling Coefficients*

  In our model, the grating coupling coefficients are entered by the user. A more accurate approach is to calculate the values by considering the grating profile and the laser structure. One way is to multiply a large number of 2×2 transfer matrices, each represents a portion of the grating tooth [Maki91], [Hans92]. Others include the computation of the standard overlap integral [Stre75b], and a simplified method based on the ray optics approach [Luo94].

- *Gain Coefficient*

  The inclusion of a separate calculation of the differential gain, a, and therefore the gain coefficient, g, is now underway. This takes into account the laser structure (including strained quantum wells), the dependence on the lasing wavelength and the smoothing effect of the intraband scattering of the carriers [Zory93]. An alternative simplified

approach may also be pursued to reduce computational complexity [Ma95].

- *Spontaneous Emission Spectrum*

  Similar to the gain coefficient calculation, the spontaneous emission spectrum can also be computed for the laser structure of interest. This addition eliminates the need to estimate the spontaneous emission bandwidth and has direct consequences to the noise power calculation. In a different approach, the noise power can also be calculated relating the spontaneous emission factor [Henr86].

- *Temperature Dependence*

  Temperature dependence may be included by following a similar treatment by Hansmann [Hans92]. The calculated results can then be compared directly with experimental data.

- *Two- and Three-Dimensional DFB Model*

  Right now, a three-dimensional problem has to be converted to one-dimension by effective index method. The spatial mode is assumed to be the fundamental mode in both the lateral and the transverse directions. For a more comprehensive user interface, the effective index method can first be incorporated into the DFB model. This can be followed by considering the lateral modes [Yu94]. Finally, it can be further developed into a unified model that considers the lateral and transverse structural variations, a network of active and passive optoelectronic devices and so on [Lowe90], [Aman90], [Aman94]. In general, one can integrated available computer software while developing other necessary modules. This is a long-term project and is the most difficult one on the list. Nonetheless, it is a worthwhile project because the potential reward is far-reaching. It

means having a CAD tool to design future OEIC's much like the way CAD is being used nowadays in the design of silicon integrated circuits.

3 ANALYSIS OF DFBDBR LASER

This chapter marks the beginning of the second part of this thesis: device analysis. It details an analysis of the first of two DFB-type lasers under investigation. The device is the DFBDBR laser; so named because it incorporates important features from both the DFB and DBR lasers. An introduction (*Section 3.1*) is given below, followed by a subthreshold analysis (*Section 3.2*), an above-threshold analysis (*Section 3.3*) and a conclusion (*Section 3.4*).

3.1 Introduction

Three-section second-order index-coupled DFBDBR lasers is studied here because of its good performance and its potentials in free-space-optical-communication applications such as satellite-to-satellite communications and lidars for environmental measurements and distance ranging. This laser has been successful in forming grating-surface-emitting coherent arrays and as a single-frequency master-oscillator in a monolithic MOPA. These are especially suitable for satellite-to-satellite communication applications because these systems require high power, narrow linewidth, light weight and good beam quality with low far-field divergence so that bulky optics is not needed. The last requirement is met since the surface radiation from the grating-surface-emitters is emitted over a large area. The result is an output beam with very narrow far-field divergence.

Experimentally, the DFBDBR lasers with a pumped DFB center section and two unpumped Bragg reflector end-sections have demonstrated stable single longitudinal mode operation at six times threshold [Liew90], [Liew91]. Thresholds as low as 9

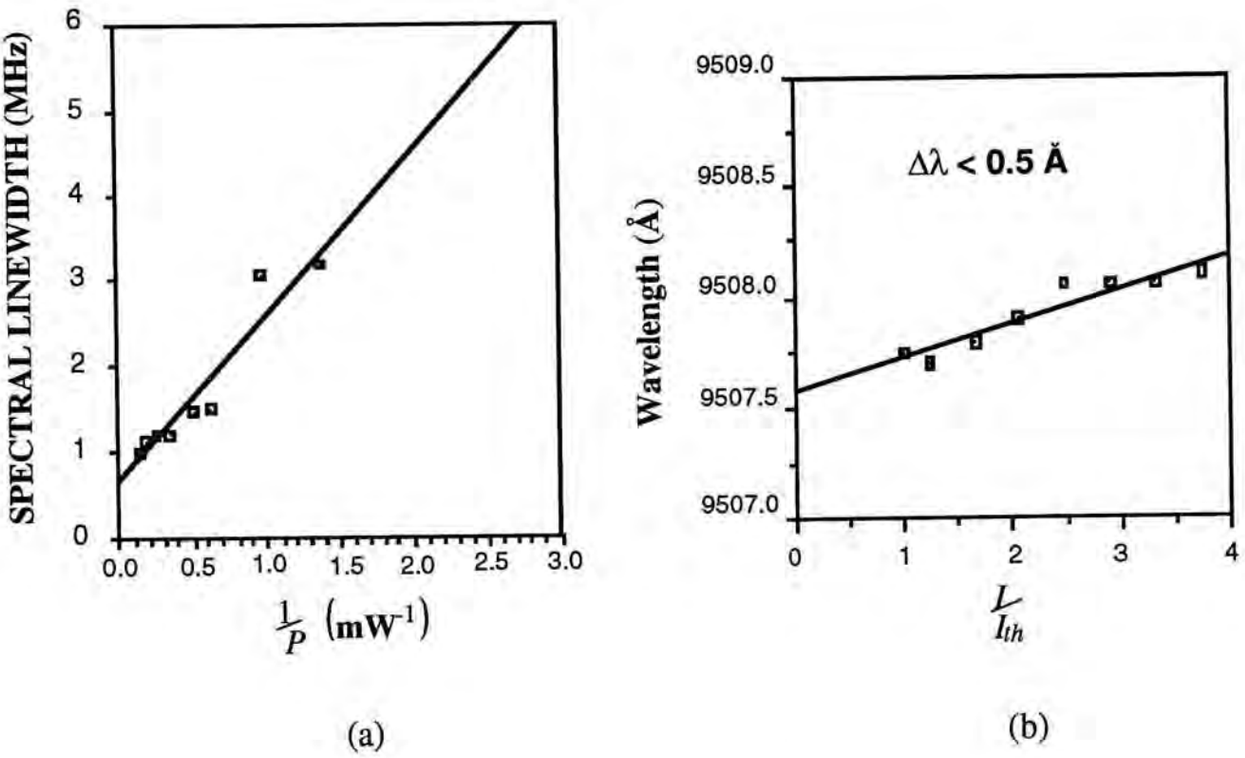

Fig. 3.1 *Experimental data [Liew91] of a DFBDBR laser with 500 μm long gain section and 200 μm long unpumped grating sections. (a) Spectral linewidth as a function of inverse surface-emitting power. (b) Lasing wavelength as a function of normalized current with respect to the threshold current. The straight lines represent the linear fit of the data points.*

mA from a 5 μm wide single-element ridge-guided device was demonstrated and more recently 4 mA was achieved [Liew93]. Narrow linewidth and small wavelength shift were obtained over a large range of drive conditions. For instance, the laser operated in a stable single longitudinal mode with SMSR of 30 dB and linewidth of around 1 MHz [Liew91] (see Fig. 3.1a). The lasing wavelength as a function of current revealed no mode hop and the difference in wavelength is less than 0.5 Å over the range of four times the threshold current (see Fig. 3.1b). The wavelength as a function of temperature yields a slope of 0.7 Å/°C, a characteristic of DFB lasers that the optical feedback is provided by the gratings and not the facets.

The fabrication of this laser is briefly described as follows [Liew91], [Bour91]. The wafers were grown by a two-step organometallic chemical vapor deposition process. In the first growth step, an *n*-GaAs buffer layer, $Al_{0.5}Ga_{0.5}As$ *n*-clad, undoped $Al_{0.1}Ga_{0.9}As$ separate confinement heterostructure and strained InGaAs quantum well, 2000 Å $Al_{0.5}Ga_{0.5}As$ barrier layer, and 800 Å *p*-GaAs grating layer were deposited. The wafer was removed from the reactor for grating fabrication. The grating (with a 2779 Å period) was defined by holographic photolithography and replicated down to the barrier layer by ion beam etching. This grating fabrication technique provides good controllability of the grating height and reduces photoresist thickness nonuniformity because of planar surface fabrication. After a brief wet chemical etch, the wafer was returned to the reactor for the growth of the remaining (1.2 μm *p*-$Al_{0.5}Ga_{0.5}As$) *p*-clad and (2000 Å p^+ -GaAs) *p*-cap layers. Finally, part of the *n*-metallization was removed to create a 50-μm-wide window running along the propagation direction. In this way, surface radiation could be coupled out of the transparent substrate when the device was mounted *p*-side down.

The nonlinear model is developed with this laser in mind. The number of sections is therefore limited to 3 to accommodate the center pumped section and the two unpumped end-sections.

In the absence of unpumped end-sections, a second-order DFB with zero facet reflectivity is known to lase with a split nearfield distribution (null in the center of the laser cavity) because of minimized radiation loss [Kaza85], [Maki88a] (*Section 2.3.1*). In contrast, as pointed out by an earlier linear analysis [Carl91], the dominant lasing mode for the DFBDBR laser is associated with a nearfield intensity distribution that peaked at the center of the laser cavity because of carrier-induced index depression in the gain section. The apparent contradiction can also be explained by the increase of effective reflectivity and from the perspectives of grating reflectivity bandwidths. The theoretical finding is confirmed by the experimental observation of the nearfield

patterns at threshold, twice threshold and 5 times threshold, that were obtained by measuring the surface emission [Liew90]. The measurements revealed no 'depression' in the middle of the laser cavity. The far field associated with the surface emission is predominantly single-lobed and diffraction-limited, indicating the absence of a π phase-shift between the counter-propagating fields. As a result, it can be shaped with simple optics into an output beam with a unity aspect ratio [Liew92]. This circular output beam is more desirable from a practical point of view. In fact, many lasers of this type, with various gain section lengths and unpumped grating section lengths have been studied, and all of them exhibited similar nearfield and farfield patterns. The relatively flat intensity distribution also makes spatial hole burning less of a problem in DFBDBR than in, for example, QWDFB lasers [Kita93].

There are a number of approaches devised to reduce the longitudinal spatial hole burning effects. (A detailed discussion of LSHB can be found in *Section 2.2.1*) They all aim at creating a uniform photon density distribution without compromising on the single-moded quality of the laser. These methods include the incorporation of multiple phase-shifters [Agra88a], the use of modulated stripe width [Naka88], modulated corrugation-pitch [Okai91], chirped grating [Mort90b], [Hill94b], [Salz94] and gain/loss-coupled grating [Mort90a], [Luo91], [Li93a], [Borc93], [Lowe94]. The fabrication of these DFB lasers are often complicated and difficult. Recently, the fabrication of chirped grating is simplified by the use of bent waveguide on homogeneous grating [Hill94b], [Salz94] although the bending loss may pose a limitation on its usefulness. The DFBDBR laser is comparatively easy to make, and combined with low threshold and stable single mode operation, is an attractive light source for integrated optical devices such as the monolithic master-oscillator-power-amplifier [Carl93], [Obri94] and monolithic grating-surface-emitting diode laser arrays [Evan93], [Carl94].

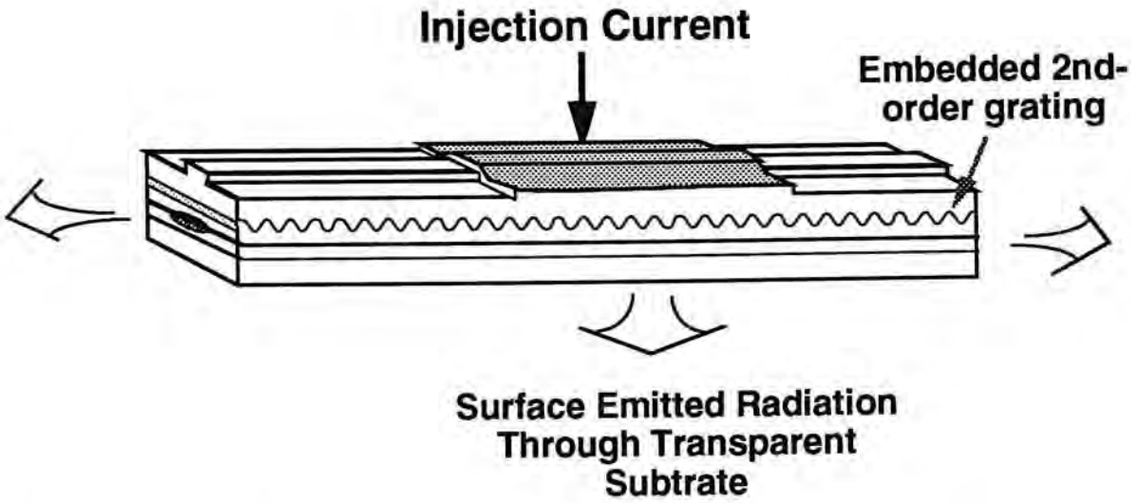

Fig. 3.2 *Schematic drawing of a DFBDBR semiconductor laser showing the center pumped section, the continuous buried second-order grating and the light emission through the end-facets and the transparent substrate.*

A schematic drawing of the DFBDBR laser is shown in Fig. 3.2. The three sections were fabricated on a common continuous ridge waveguide and they shared a buried second-order grating with the same periodicity and tooth-height. Since the grating is embedded in the p-clad layer, there is no fabricated dielectric discontinuity or phase-shifters at the interfaces between the gain and the passive sections. While coupling loss is an important issue in DBR lasers, the use of buried grating in the DFBDBR lasers virtually eliminates the coupling loss between the sections. It is because the effective indices of the waveguide mode in the pumped and unpumped sections are essentially the same with a difference of less than 1.0×10^{-6}. The facets are uncleaved and far from the edges of the laser bar to ensure zero facet reflectivities. The light output was obtained through surface emission while radiation along the waveguide served to power or couple additional integrated devices. Surface emission requires that all epilayers of the structure in the beam path be transparent to the lasing wavelength of the quantum well active layer [Bour91]. Alternatively, the laser may be

a separate entity with its facets cleaved and then antireflection-coated, in which case, edge-emitting output is then possible.

Compared with distributed-reflector (DR) type lasers [Komo89], [Arim90a], [Shim91], a closely related device, the DFBDBR laser is considerably easier to fabricate. The DR-type laser consists of one active and one passive first-order Bragg reflectors with the same grating period but different tooth-heights. Stable single-mode operation relies on the unequal grating coupling coefficients in the two sections and the phase-shifter between them. These parameters have to be precisely controlled in order to achieve high performance. On the other hand, the DFBDBR laser employs a continuous second-order grating with no phase-shifter, making it more tolerant of fabrication variations. High performance is obtained through the choice of section lengths, coupling coefficient and radiation coefficient. Our simulation results indicate that these parameters have good tolerance and do not have to be finely controlled.

3.2 Subthreshold Analysis

3.2.1 Introduction

As a demonstration of the DFB model, a subthreshold analysis is included here. The procedure and the results are similar to those reported in [Carl91]. However, the method of calculation is different. The model employed by Carlson *et. al.* is based on a linear network approach [Aman90] and the carrier-induced index change is simulated by a predetermined shift in Bragg wavelength in the pumped section. In our case, the linear model simulates the same effect by a fixed index change. Since the two models are independently developed and principally different, the similar results further confirms the validity of our model.

For the subthreshold analysis, the DFBDBR laser is chosen to operate at around 1.55 μm. The parameters are given in Fig. 3.3 and in Table 3.1. The facet reflectivity is zero. As a preliminary study, the lengths of the two unpumped grating sections are assumed to be equal. They are changed at a later time in the study of the effects of asymmetry. The smaller effective index in the pumped section is assumed to be constant with drive current. As detailed in *Section 2.4.3*, no iteration is performed. The optical spectrum is calculated at each gain step as if no lasing took place. The purpose is to study the threshold gain difference of the potential lasing modes. Consequently, the solutions are valid only at below or near threshold conditions.

The subthreshold analysis (similar to that reported in [Liew93]) focuses on the effects on g_{th} as the unpumped grating sections are added to a pumped second-order DFB laser. Three cases are considered:

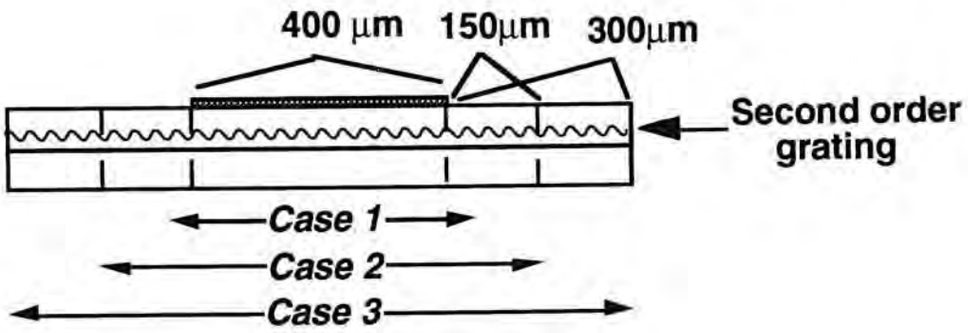

Parameteres:

$r_1 = r_2 = 0$

$\alpha = 5\ \text{cm}^{-1}$

$\kappa = 20\ \text{cm}^{-1}$

$\xi = 2\ \text{cm}^{-1}$

$\Delta n = -0.002$

$I = 11.0 \rightarrow 60.0\ \text{mA}$

$g_{th} = 1.4 \rightarrow 86.0\ \text{cm}^{-1}$

$\Delta\omega = -700 \rightarrow 1800\ 2\pi\text{GHz}$

Fig. 3.3 *The three cases that are analyzed with the linear model.*

Case 1. the classic single-section DFB laser with second order grating and zero facet reflectivities;

Case 2. a DFBDBR laser with 150 μm unpumped grating section on each end of the pumped section; and

Case 3. similar to *Case 2*, except that the unpumped sections are 300 μm long.

The pumped section is 400 μm long, the same for all three cases. The coupling coefficient is 20.0 cm^{-1} and the radiation coefficient is 2.0 cm^{-1}. The input gain coefficient varies from 1.4 cm^{-1} to 86.0 cm^{-1} and the angular frequency detuning from Bragg condition spans from -700 to 1800 2πGHz. Both the gain and frequency are divided into 100 calculation points. The resulting spectrum does not center at zero detuning because of the smaller effective index in the gain section.

Parameters	*Values*
Linear carrier lifetime (τ)	1.0 ns
Bimolecular carrier recombination coefficient (B_N)	1.0×10^{-10} cm^3s^{-1}
Auger carrier recombination coefficient (C_N)	3.0×10^{-29} cm^6s^{-1}
Differential gain (a)	6.0×10^{-16} cm^2
Nonlinear gain compression factor (ε)	3.0×10^{-17} cm^3
Transparency carrier density (N_t)	1.5×10^{18} cm^{-3}
Linewidth enhancement factor (α_H)	2.0
Absorption and scattering loss (α)	5.0 cm^{-1}
Grating coupling coefficient (κ)	20.0 cm^{-1}
Grating radiation coefficient (ξ)	2.0 cm^{-1}
Effective phase refractive index (n)	3.289
Effective group refractive index (n_g)	3.75
Length of pumped middle section (L_m)	400.0 μm
Index change in the pumped section (Δn)	-0.002
Active layer thickness (d)	0.045 μm
Effective width parallel to junction ($w_{\|\|}$)	2.0 μm
Effective width perpendicular to junction ($w_\perp$)	0.44 μm
Far-field angular divergence parallel to junction ($\theta_{\|\|}$)	30.0°
Far-field divergence perpendicular to junction ($\theta_\perp$)	55.8°
Active layer confinement factor (Γ)	0.087
Approximate emission wavelength (λ_o)	1.55 μm
Number of divided segments in middle section	21

Table 3.1 *The parameters values used in the linear analysis of the DFBDBR lasers.*

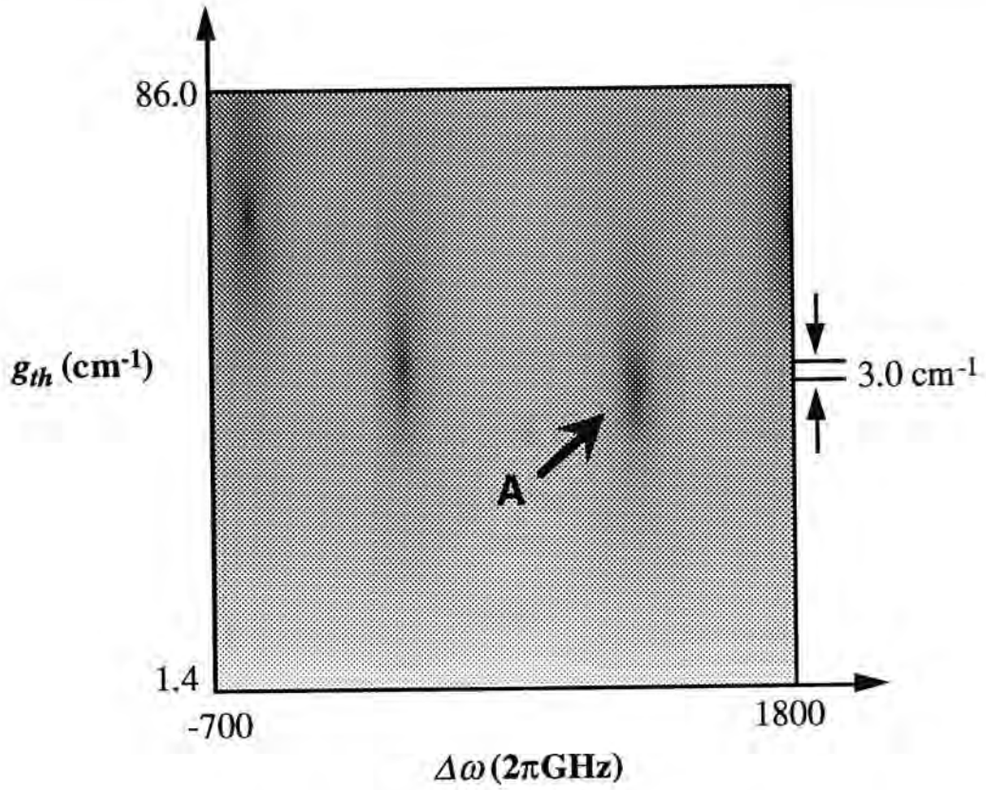

Fig. 3.4 The contour plot of the subthreshold output power as a function of Bragg detuning and threshold gain for Case1.

3.2.2 Results

Symmetric End-Sections

The contour plot of the logarithmic output power for the single-section second-order DFB laser (*Case 1*) as a function of the frequency detuning (horizontal axis) and the threshold gain (vertical axis) are shown in Fig. 3.4. The darker shading corresponds to higher output power. Black indicates that a mode has reached threshold. The optical spectrum at a given g_{th} is then represented by the shading along the horizontal direction. In Fig. 3.4, the mode labeled 'A' is the lowest-loss mode (lowest on the vertical axis) with g_{th}=53.54 cm^{-1} and I_{th}=35.51 mA. It is located on the shorter wavelength side (higher frequency) of the stop-band because κ is assumed to be positive. The Δg_{th} between mode 'A' and the next lowest-loss mode is only 3 cm^{-1}.

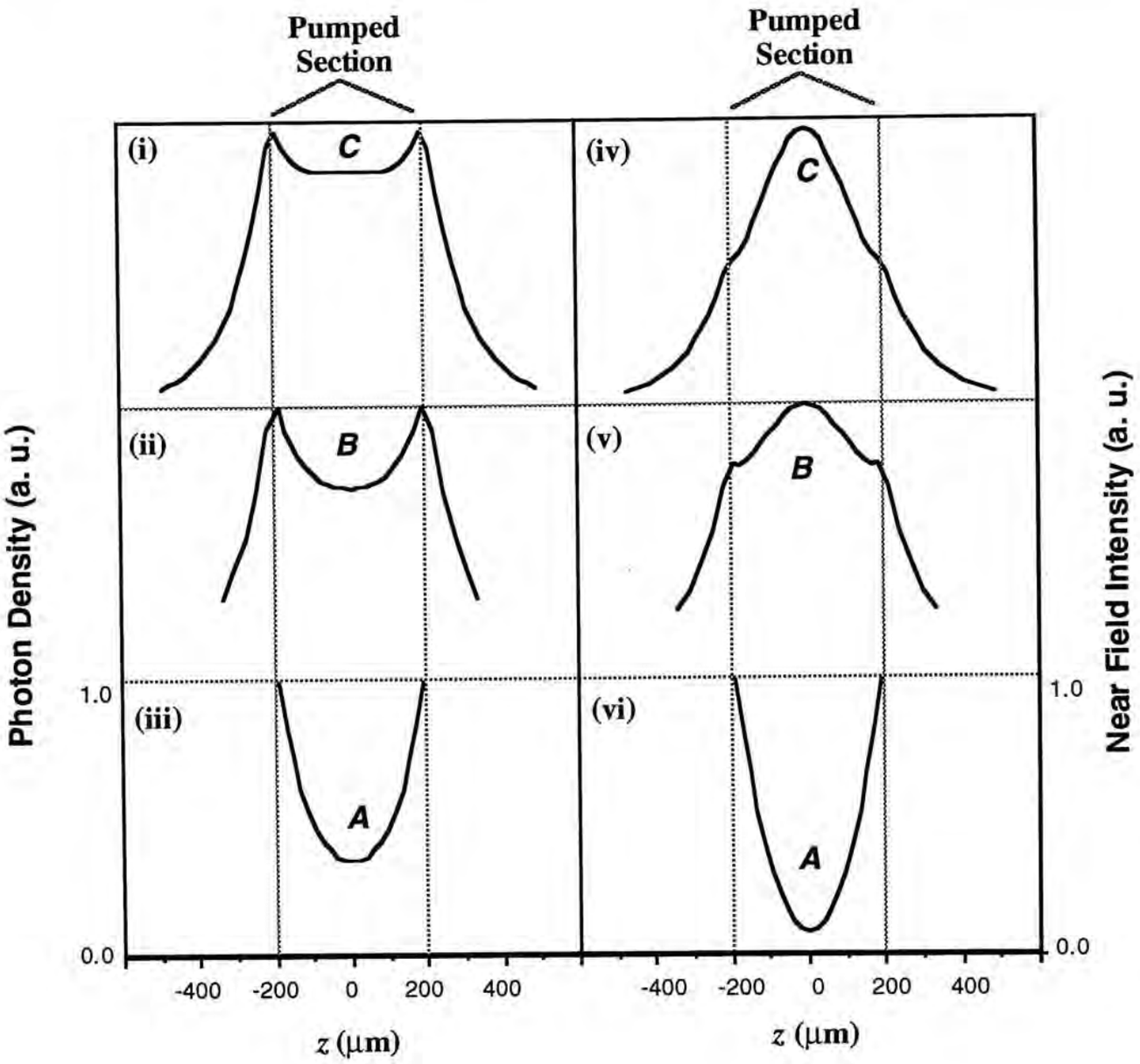

Fig. 3.5 *The photon density distributions and the nearfield distributions of the lasing modes 'A', 'B' and 'C' for the three cases under investigation. Curves (iii) and (vi) are obtained with no unpumped sections. Curves (ii) and (v) are obtained with 150 μm-long unpumped sections and curves (i) and (iv) are for 300 μm-long unpumped grating sections. The light vertical lines mark the boundaries between the pumped and unpumped sections.*

The nearfield pattern at g_{th} =53.54 cm^{-1} is plotted at the bottom in Fig. 3.5 (plot *vi*). The distribution represents a summation over frequencies. It shows a minimum in the middle of the gain section in agreement with [Kaza85]. The profile is a consequence of the destructive interference between the forward- and the reverse-

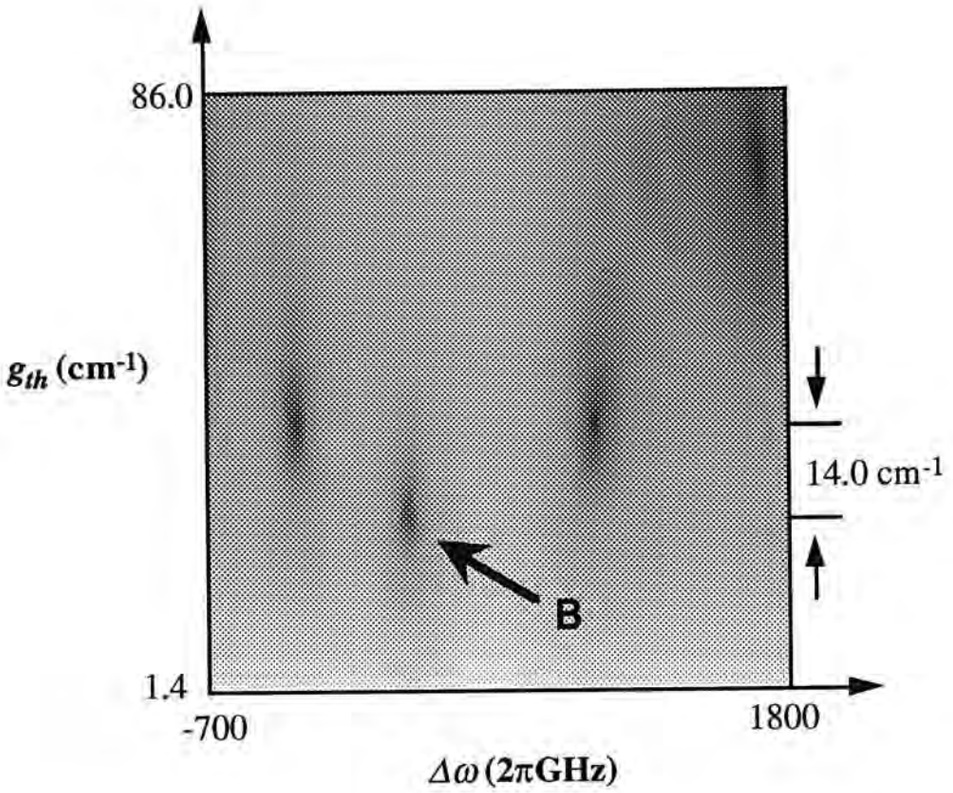

Fig. 3.6 *The contour plot of the subthreshold output power as a function of Bragg detuning and threshold gain for Case2.*

traveling waves which are anti-phased [Henr85]. The minimum does not reach zero because of the finite segment length and the residual power in the side modes. The photon density distribution (Fig. 3.5 (*iii*)) also reveals a similar profile.

For *Case 2*, with the addition of the 150 μm-long unpumped grating sections, the laser behaves very differently. Fig. 3.6 is a contour plot of the power spectrum. It should be noted that the mode separation is smaller than that in *Case 1* because of the longer laser cavity. The lowest-loss mode is labeled 'B' at g_{th}=34.87 cm^{-1} and I_{th}=24.94 mA. This represents a large reduction in g_{th} as compared to the *Case 1* scenario. The indicator of mode discrimination, Δg_{th}, is equal to 14.0 cm^{-1}, another significant improvement. Interestingly, the lasing mode is now on the longer wavelength side of the stop-band. The corresponding nearfield intensity distribution

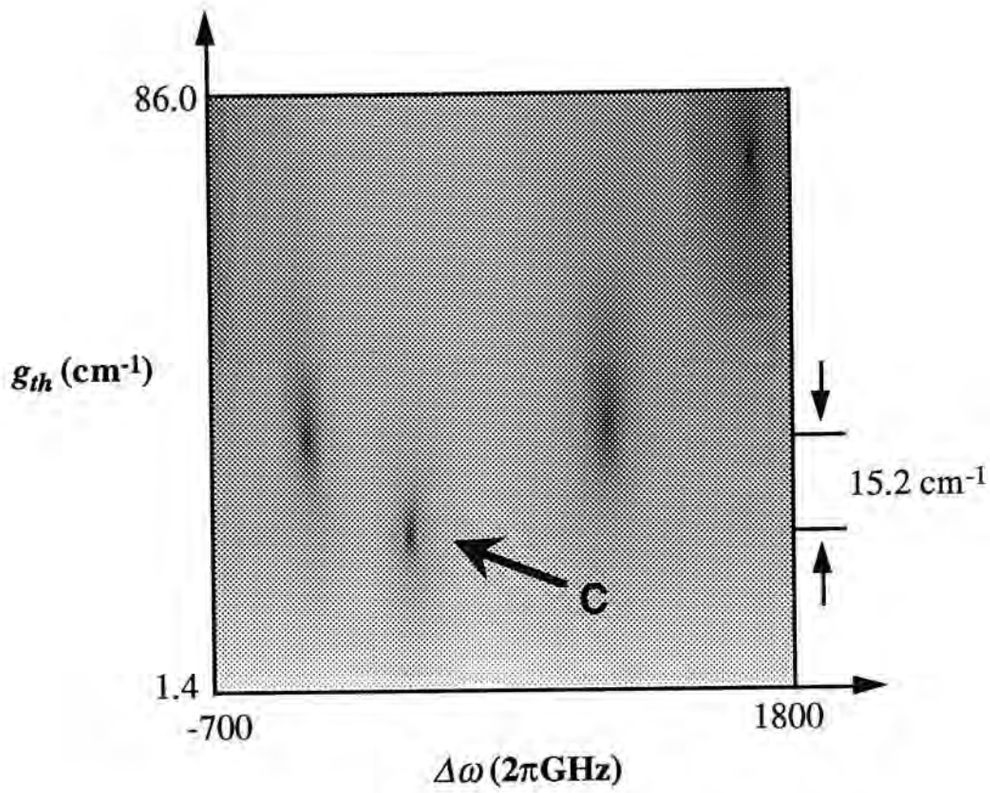

Fig. 3.7 *The contour plot of the subthreshold output power as a function of Bragg detuning and threshold gain for Case 3.*

(Fig. 3.5 plot (v)) is peaked in the middle of the pumped section in sharp contrast with *Case 1*. This is because the counter-propagating fields associated with mode 'B' are in-phase with each other and therefore interfere constructively. Note also that the intensities in the unpumped lossy end-sections decay exponentially towards the edges as expected. It is obvious that the extra grating sections increase the wavelength-selective reflectivities and thus give rise to lower threshold and enhanced mode discrimination.

For *Case 3*, with 300 μm-long unpumped grating sections, there is further improvement in Δg_{th}. The power spectrum is shown in Fig. 3.7. The lowest-loss mode is marked by 'C' at g_{th}=31.97 cm^{-1} and I_{th}=23.5 mA. The threshold is slightly lower than that in *Case 2*. The threshold gain difference, Δg_{th}=15.2 cm^{-1}, is higher

as well. Mode 'C' is again on the longer wavelength side of the stop band (same as mode 'B') and corresponds to a 'peaked' nearfield pattern. The nearfield distribution at g_{th} =31.97 cm^{-1} is shown in Fig. 3.5 plot (*iv*) in which the maximum is in the middle of the gain section. Remarkably, the photon density profile is relatively flat, and this points to a potential advantage in terms of low LSHB (see *Section 3.3.4*).

The nearfield profiles in *Case 2* and *Case 3* compare well with reported experimental data despite the differences in lasing wavelength, section lengths, drive conditions, and other parameters. The absence of any intensity minimum is found to be generally true experimentally for devices with a variety of section lengths and other parameters.

At this point, one can conclude that the introduction of unpumped grating sections increases the effective end-reflectivity which in turns brings more optical power back into the laser cavity. Subsequently, the intensity in the middle of the gain section is raised and Δg_{th} is enhanced. The lasing mode is located on the opposite side of the stop-band and is associated with the peaked nearfield. Yet, the mode selection mechanism and the dependence on critical parameters are not very clear. More insights into the workings of this laser is given in the above-threshold analysis (*Section 3.3*) when the reflectivity bandwidths of the DFB and DBR sections are discussed.

Asymmetric End-Sections

A study of the effects of asymmetric unpumped section lengths is carried out as follows. For the next two calculations (*Case 4* and *Case 5*), the length of the gain section remains at 400 μm and the lengths of the unpumped grating sections are (100 μm, 500 μm) in *Case 4* , and (0 μm, 600 μm) in *Case 5*. The total cavity length is 1000 μm for these two cases and the symmetric DFBDBR in *Case 4*. Other parameters remain unchanged.

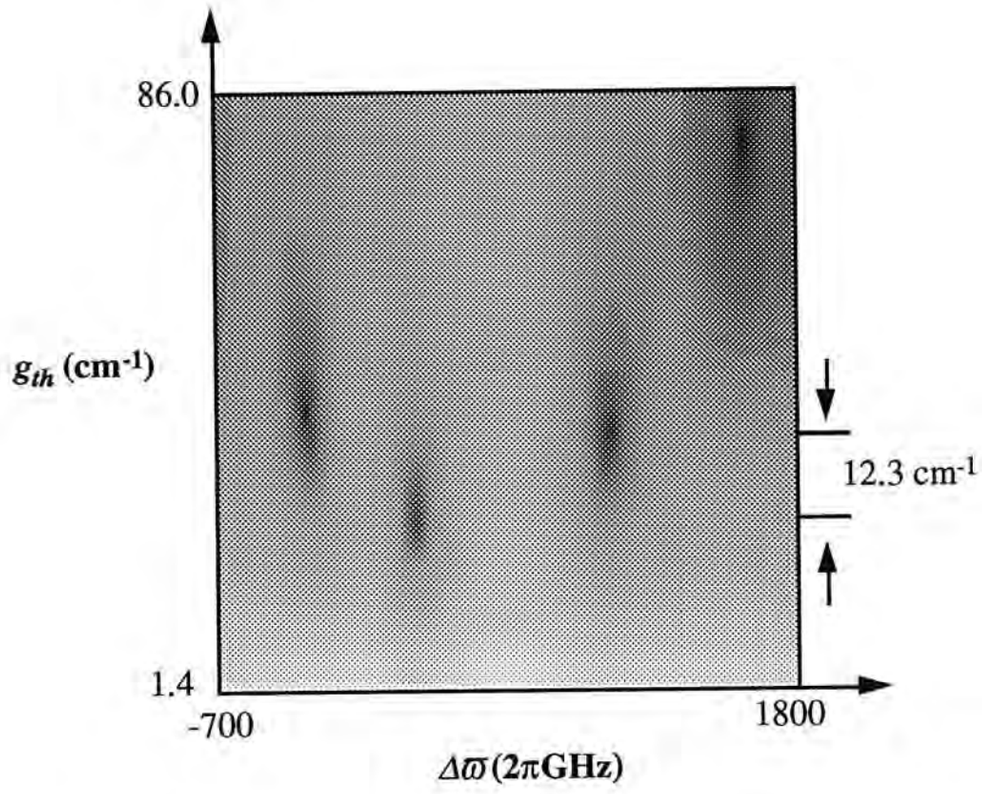

Fig. 3.8 *The contour plot of the subthreshold output power as a function of Bragg detuning and threshold gain for Case 4.*

The resulting optical spectra are plotted in Fig. 3.8 and Fig. 3.9. For *Case 4*, the resulting spectrum can be seen in Fig. 3.8. The value of Δg_{th} is reduced to 12.3 cm^{-1} from 15.2 cm^{-1} in the symmetric case. For *Case 5*, the extreme asymmetric case, Δg_{th} =9.8 cm^{-1}. It is apparent that Δg_{th} deteriorates with the increase in asymmetry. The reasons for this are discussed in *Section 3.3* from the perspectives of reflectivity bandwidths.

In conclusion, the apparent paradox with the second-order DFB and the DFBDBR lasers is resolved. One has a null in the middle of the nearfield pattern while the other consists of a maximum. The difference is explained by the presence of unpumped grating sections that changes the lasing conditions. As a result, the lasing mode on the opposite side of the stop-band has the lowest loss and the

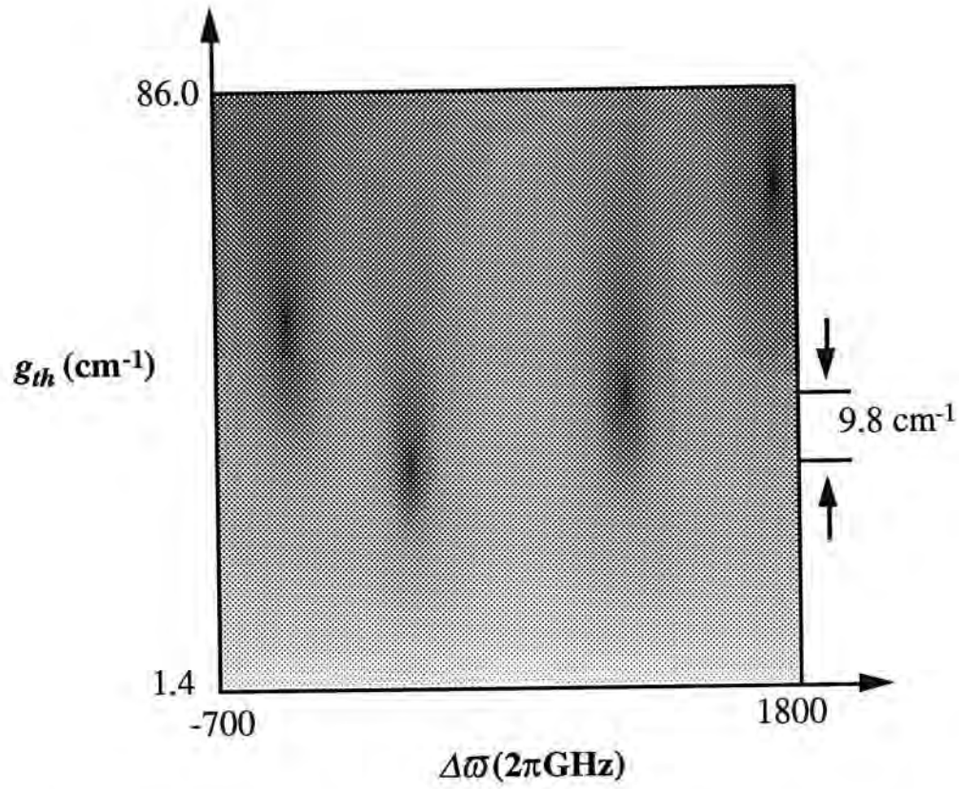

Fig. 3.9 *The contour plot of the subthreshold output power as a function of Bragg detuning and threshold gain for Case 5.*

associated nearfield profile is modified. It is also accompanied by a reduction of threshold current and a drastic increase in the threshold gain margin. The results from the subthreshold analysis agree well with the reported experimental data. In addition, the introduction of asymmetric unpumped section lengths reduces Δg_{th} and hence the mode discrimination. More in-depth understanding of the workings of the DFBDBR laser requires the above-threshold model which can more accurately simulate the important nonlinear effects.

3.3 Above-threshold Analysis

This work is an extension of the linear analysis on the DFBDBR laser as presented in *Section 3.2*. The linear DFB model, like many others, assumes that the effects of the frequency dependent coherent loss of the grating output coupling is operable below threshold, which is not rigorously correct. This is because the spontaneous emission, which is incoherent, dominates below threshold and the counter-propagating waves have no mutual coherence. The effect of the carrier-induced index change, an important mode selection mechanism in the DFBDBR laser, is simulated by lowering the effective index of the active DFB section. The index is assumed to be constant with gain which is again not correct. Nevertheless, the model provides physical insights into the mode selection mechanism. The index change, a function of the carrier density, only comes into effect when the laser is pumped. Therefore, this and other nonlinear effects can only be correctly taken into account in a nonlinear model.

In this work [Liew94], [Liew95a], the DFBDBR laser has been analyzed at below and above threshold conditions using the nonlinear multisection DFB model. Our simulation results give the design rules in terms of the specification on the coupling coefficient, radiation coefficient and active-section-length-to-total-cavity-length ratio (length ratio, in short). The criteria for high performance will also be discussed. Typical values to consider in the design of the DFBDBR lasers are κL_{tot} =1.5 to 2.5, ξ/κ=0.1 to 0.3 and L_m/L_{tot} =0.5 to 0.7 where L_m is the length of the pumped section and L_{tot} is the total cavity length. In addition, the DFBDBR laser is found to have reduced LSHB and a smaller effective linewidth enhancement factor when compared with the uniformly pumped second-order DFB laser. The introduction of asymmetry in the DFBDBR laser results in poorer side-mode suppression compared with the symmetric DFBDBR laser.

3.3.1 Analysis

The analysis first focuses on the symmetric DFBDBR laser with both passive sections of equal length. For the laser structure, we have selected a separate-confinement heterostructure with four quantum-wells. The schematic drawing of the laser structure is shown in Fig. 3.10. The effective index is calculated to be 3.26. The active layer and the grating layer confinement factors are 0.032 and 0.047, respectively. The FWHM of the transverse optical intensity distribution is 0.4 μm and the corresponding far field angular divergence is 51.2°. For the analysis, the far field angle is rounded off to 50°. These and other parameters are listed in Table 3.2.

For the simulation, the product of the grating coupling coefficient and total cavity length, κL_{tot} takes on a value between 1.0 and 3.0. Two other dimensionless parameters are introduced. The first is the ratio of the radiation coefficient to the coupling coefficient, ξ/κ. It ranges from 0.1 to 1.0. The second is the length ratio, defined as L_m / L_{tot}. For all the results presented in this report, L_{tot} is equal to 1000 μm. The length ratio ranges from 0.2 to its maximum value of 1.0. It means that a uniformly pumped DFB has a length ratio of 1.0. A DBR laser can not be described by the length ratio. However, the behavior of a DFBDBR laser with a small length ratio is expected to resemble a DBR because of the relatively long passive Bragg reflectors and short gain section. Therefore, a split nearfield distribution and lasing near the Bragg wavelength are expected.

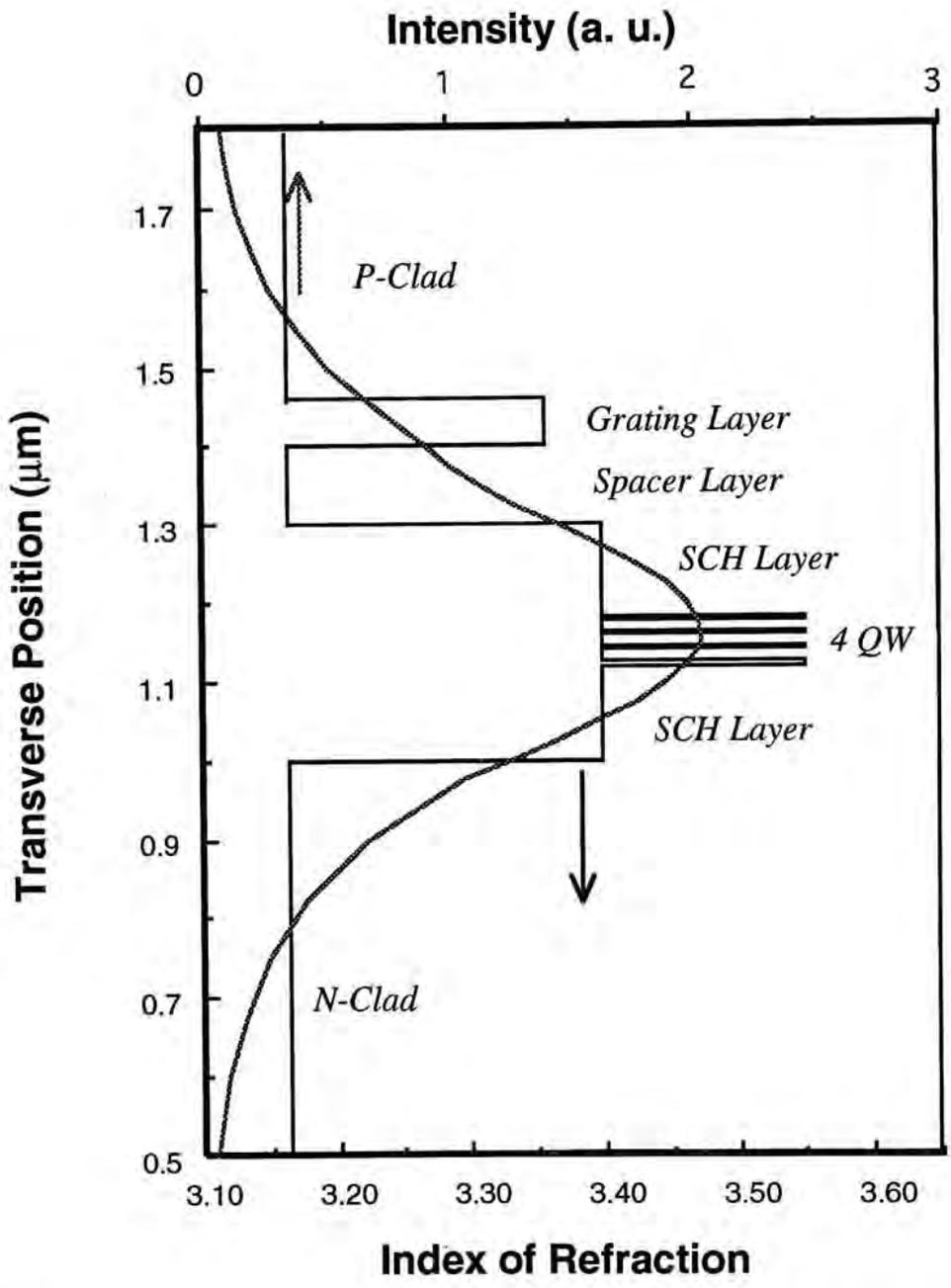

Fig. 3.10 *The refractive index and the transverse optical intensity distribution for a SCH-MQW laser structure used in the above-threshold analysis.*

Parameters	*Values*
Linear carrier lifetime (τ)	∞
Bimolecular carrier recombination coefficient (B_N)	1.0×10^{-10} cm^{3}s^{-1}
Auger carrier recombination coefficient (C_N)	3.0×10^{-29} cm^{6}s^{-1}
Differential gain (a)	4.0×10^{-16} cm^2
Nonlinear gain compression factor (ε)	3.0×10^{-17} cm^3
Transparency carrier density (N_t)	1.5×10^{18} cm^{-3}
Linewidth enhancement factor (α_H)	3.5
Absorption and scattering loss (α)	10.0 cm^{-1}
Grating coupling coefficient (κ_n or κ)	10.0 $\rightarrow$ 30.0 cm^{-1}
Grating radiation coefficient (ξ)	1.0 $\rightarrow$ 10.0 cm^{-1}
Effective phase refractive index (n)	3.26
Effective group refractive index (n_g)	3.68
Total length of the laser cavity (L_{tot})	1000.0 μm
Length of pumped middle section (L_m)	200.0 $\rightarrow$ 1000.0 μm
Active layer thickness (d)	0.016 μm
Effective width parallel to junction ($w_{\|\|}$)	3.5 μm
Effective width perpendicular to junction ($w_\perp$)	0.4 μm
Far-field angular divergence parallel to junction ($\theta_{\|\|}$)	20.0°
Far-field divergence perpendicular to junction ($\theta_\perp$)	50.0°
Active layer confinement factor (Γ)	0.032
Approximate emission wavelength (λ_o)	1.55 μm
Number of divided segments	20

Table 3.2 *Parameters used in the above-threshold analysis of the DFBDBR laser.*

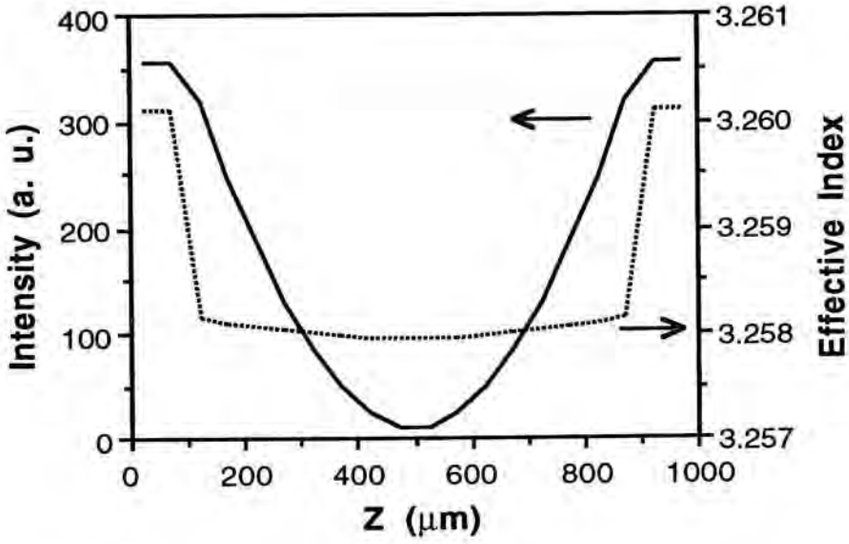

Fig. 3.11a Calculated results with κL_{tot} =1.5, ξ/κ=0.4 and L_m/L_{tot} =0.8: the optical intensity (—) and the effective index (···) distributions along the laser cavity.

3.3.2 Length Ratio

There is a strong correlation between the dominant mode of operation and the length ratio. Results presented in Fig. 3.11a, 3.11b and 3.11c are obtained with κL_{tot} =1.5, ξ/κ=0.4 and L_m/L_{tot} =0.8. Since the length ratio is close to 1.0, the laser operates like a uniformly pumped DFB. Figure 3.11a shows the nearfield intensity and the effective index distribution along the laser cavity at $1.6\times I_{th}$. The nearfield has a null in the cavity center, and the index distribution shows the effect of carrier-induced index depression in the center gain section. Since the unpumped section is absorptive, one might expect the nearfield to be a purely exponential decaying function towards the ends of the laser. But, this is not entirely accurate as the nearfield is governed by the saturation effect and the Bragg reflectivity, namely, the laser round-trip condition, in addition to the material loss; all of these determine how quickly the falloff is. These effects have been included in the model. Moreover, the exact distribution may be obscured by the number of segments used. In this

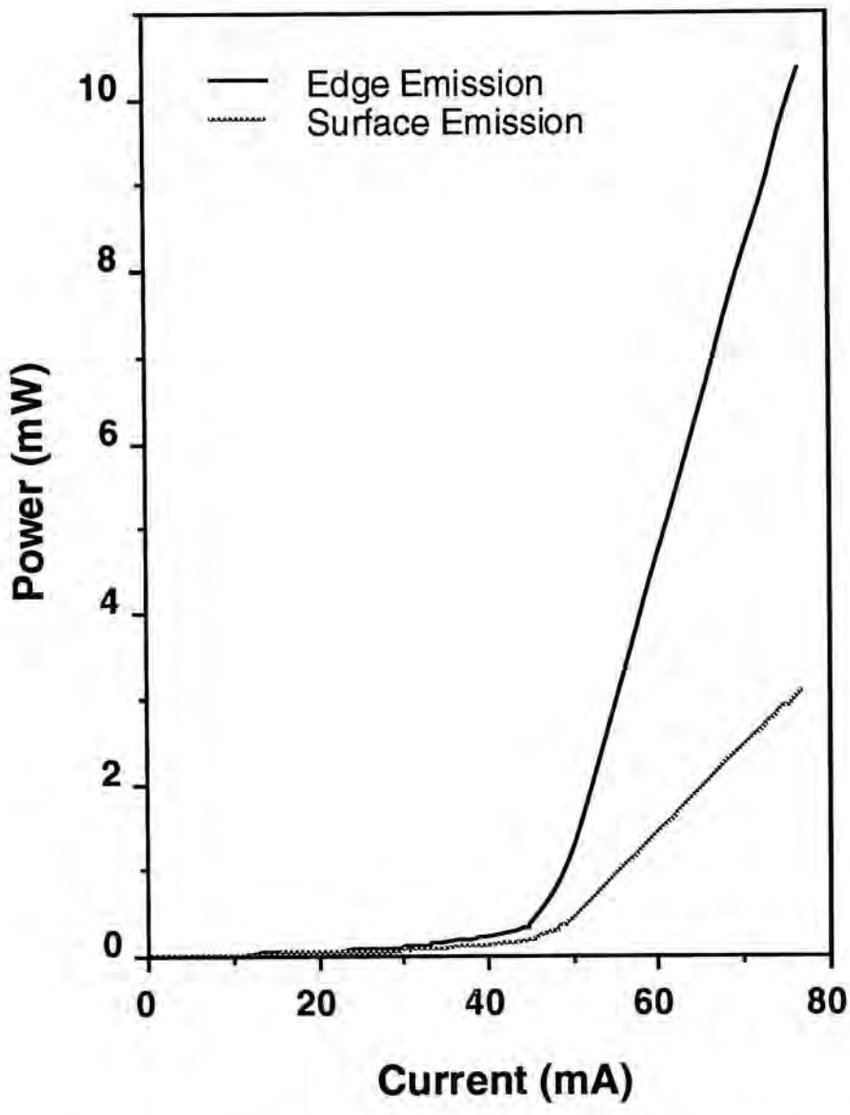

Fig. 3.11b *Calculated results with κL_{tot} =1.5, ξ/κ=0.4 and L_m/L_{tot} =0.8: the power-current characteristics of the edge emission (—) and the surface emission (···).*

particular case, the latter is a more dominant factor because only one segment was assigned in each unpumped section.

The calculated power-current characteristics of the surface emission and that of the total edge emission from both output facets are shown in Fig. 3.11b. Because of the split nearfield distribution, the output power from the surface is about one-third of that from the end-facets. The surface radiation power does not include effects of the

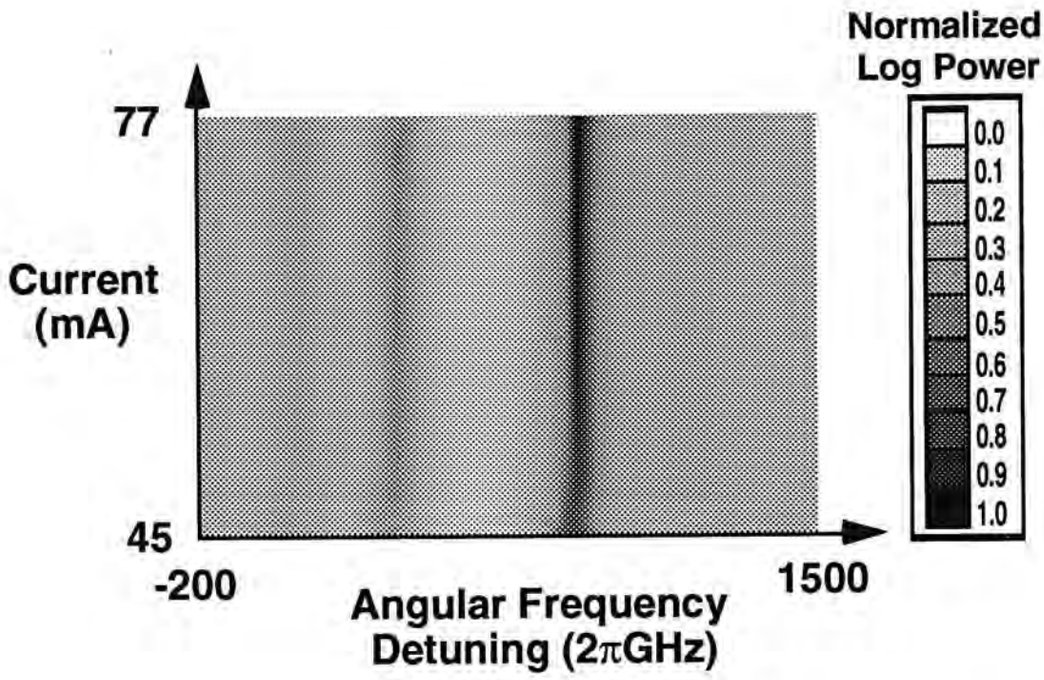

Fig. 3.11c Calculated results with κL_{tot} =1.5, ξ/κ=0.4 and L_m/L_{tot} =0.8: the contour plot of the output power as the injection current and the frequency detuning.

total-internal-reflection at the air interfaces which is expected to lower the net surface output power. The dominant lasing mode is on the shorter wavelength side of the stop-band and shifts monotonically to shorter wavelength (higher frequency) as the drive current increases.

The same calculation is performed for a laser with L_m/L_{tot} =0.6. With a shorter gain section and longer unpumped sections, the mode on the longer wavelength side of the stop-band dominates. The nearfield intensity distribution (Fig. 3.12a) at 1.4× I_{th}, peaks at the center of the laser cavity. This nearfield profile gives rise to nearly equal output power from both the edge emission and the surface emission. As the drive current is increased, the associated spectral output incurs a blue-shift, followed by a more gentle red-shift. The frequency shift is largely determined by the mean index of refraction as perceived by the lasing mode. The blue-shift reflects the overall

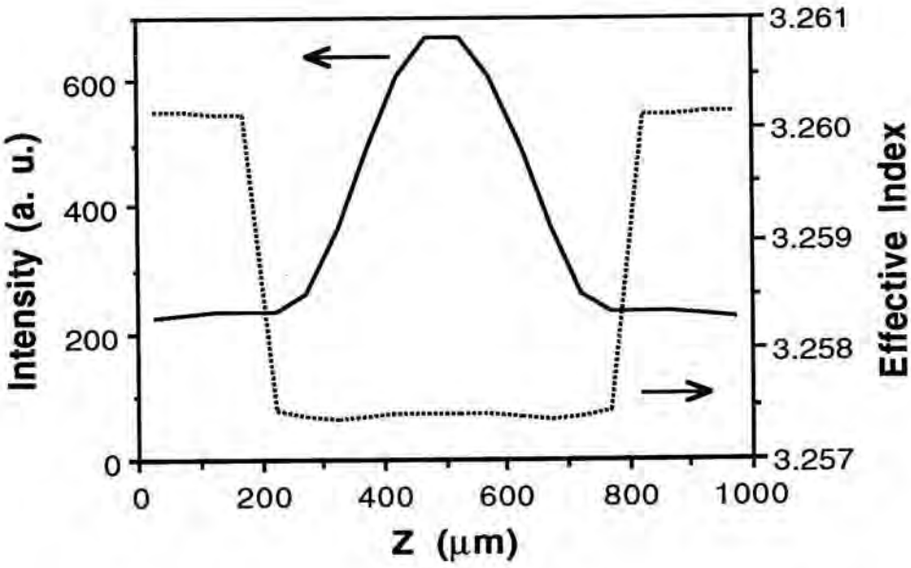

Fig. 3.12a *Calculated results with κL_{tot} =1.5, ξ/κ=0.4 and L_m/L_{tot} =0.6: the optical intensity (—) and the effective index (···) distributions along the laser cavity.*

lower effective index in the presence of larger carrier density. The red-shift is caused by the redistribution of the effective index (becoming more inhomogeneous) along the laser cavity, a consequence of spatial hole burning. As a result, the average index over the pumped section increases slightly rather than decreases with drive current.

The typical relationship between the dominant mode of operation and the length ratio for a given κL_{tot} and ξ/κ. can be seen more clearly in Fig. 3.13. On the left, the log-intensity of the output is plotted as a function of the angular frequency detuning from the Bragg condition. The corresponding nearfield distributions along the laser cavity are shown on the right. The entire laser cavity is divided into 20 segments[1]. The intensity of each segment is represented by a data point on the curve that is placed at the center of the segment. A closed square represents a pumped segment whereas an open circle signifies an unpumped segment. All the curves were obtained at the

1 A segment number larger than 12 was found to give little improvement in accuracy [Zhan92].

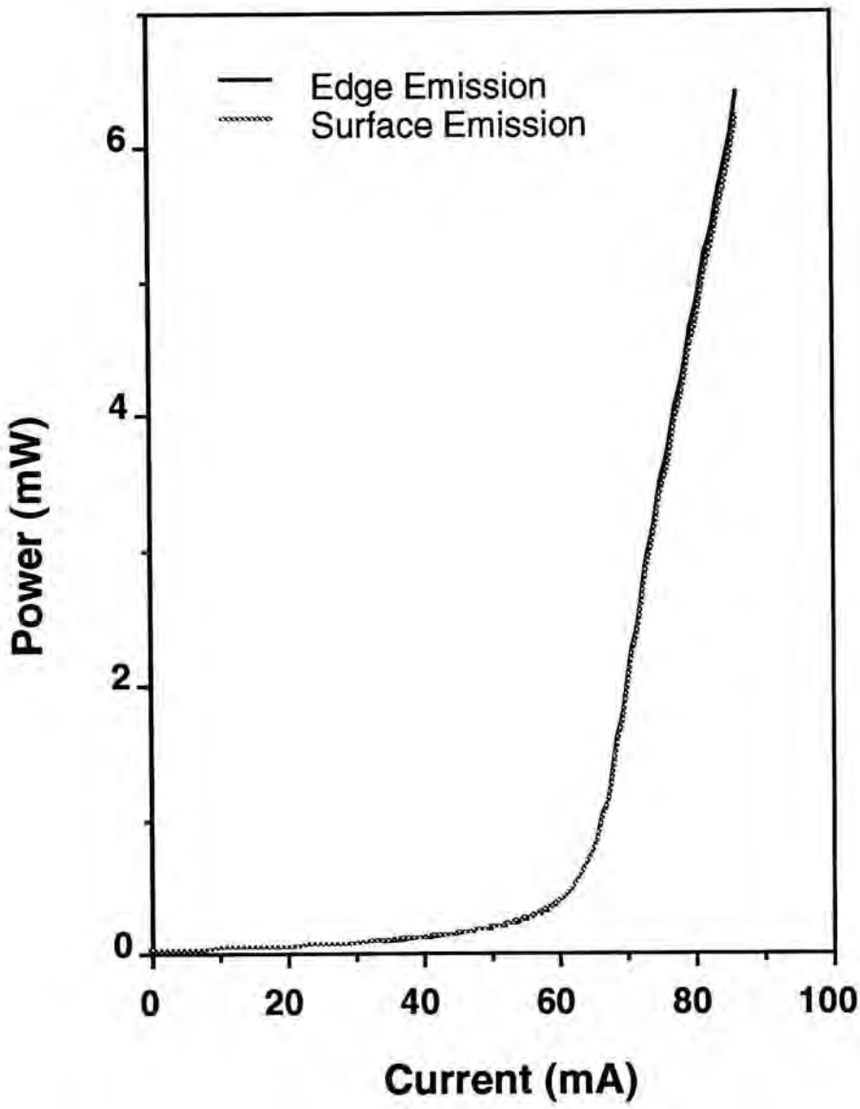

Fig. 3.12b *Calculated results with κL_{tot} =1.5, ξ/κ=0.4 and L_m/L_{tot} =0.6: the power-current characteristics of the edge emission (—) and the surface emission (···).*

total output power (sum of edge and surface radiation) of 6 mW. The laser modes are labeled '-2' (a quasi-DBR mode with split nearfield), '-1' (a DFBDBR mode with peaked nearfield), and '+1' (a DFB mode with split nearfield) in the order of increasing optical frequency (or shorter wavelength). The stop-band is located between Mode '-1' and Mode '+1'.

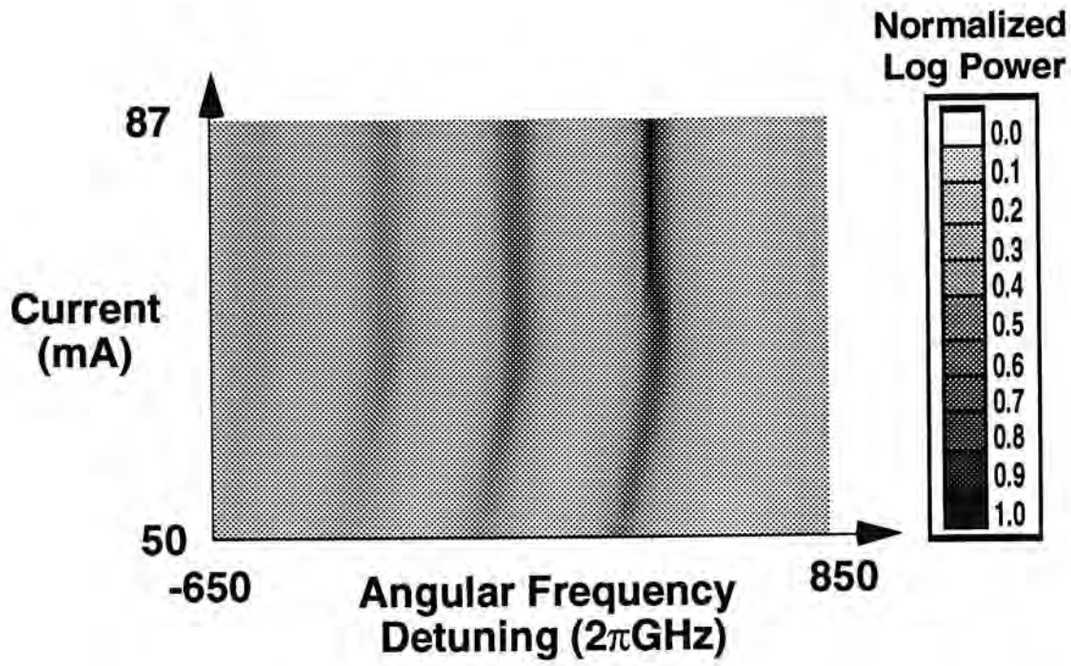

Fig. 3.12c *Calculated results with κL_{tot} =1.5, ξ/κ=0.4 and L_m/L_{tot} =0.6: the contour plot of the output power as the injection current and the frequency detuning.*

The curve at the top is for the case of the uniformly pumped second-order DFB. The DFB laser has a split nearfield distribution and lases at Mode '+1' as discussed earlier. Note that the stop-band is no longer centered at zero detuning but is shifted to shorter wavelengths because of carrier-induced index depression in the gain section. This means that the reflectivity bandwidth of the DFB pumped section also shifts to shorter wavelengths relative to its unbiased state with increasing drive current. The curve at the bottom is computed with L_m/L_{tot} =0.3. Both the split nearfield distribution and the location of the dominant mode near zero detuning (Mode '-2') indicate that the laser behaves like a DBR laser should. For L_m/L_{tot} =0.5 to 0.8, Mode '-1' is the dominant mode with its associated peaked nearfield distribution. Note that this mode is located on the shorter wavelength side of Mode '-2' and is therefore expected to have a smaller effective linewidth enhancement factor compared with the uniformly pumped DFB, as will be explained below.

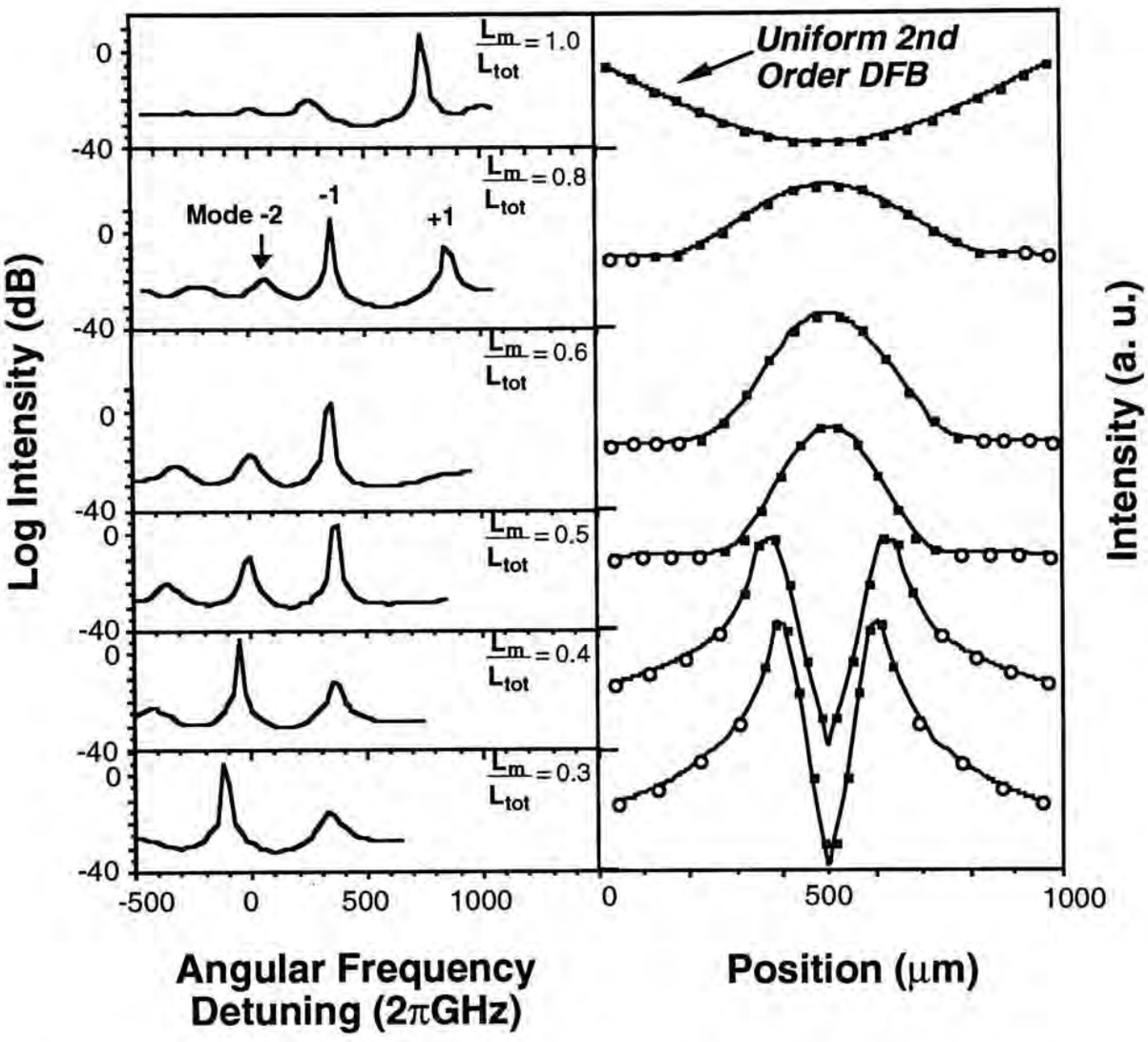

Fig. 3.13 Calculated spectral output and nearfield intensity distribution as functions of the length ratio for κL_{tot} =1.5, ξ/κ=0.2 and total power=6 mW. The lasing modes are labeled '-2' for the DBR with a split nearfield distribution, '-1' for the DFBDBR mode with a peaked nearfield distribution, and '+1' for the uniformly pumped DFB mode with a split nearfield distribution. '■' represents pumped segment and 'o' represents unpumped segment.

As discussed in Ref. [Carl91], the DFBDBR has the dominant mode at Mode '-1' because of the overlap of the bandwidth of the pumped DFB center section and that of the unpumped DBR end-sections. When the laser is unpumped, both bandwidths center at zero detuning with maximum overlap. As the drive current in the center DFB section increases, the DFB bandwidth shifts to shorter wavelengths while that of the

unpumped DBR sections remains relatively unchanged with its maximum close to zero detuning. The overlap of the bandwidths is therefore located between Mode '-2' and Mode '+1'. In other words, Mode '-1' is on the shorter wavelength side of the passive DBR reflectivity maximum.

3.3.3 Design Plot

The exact range of the length ratio that will give rise to Mode '-1' depends on the parameters, κL_{tot} and ξ/κ. Figure 3.14 is a collection of the mode-transition boundary curves computed for κL_{tot} from 1.0 to 3.0. The curves mark the boundary for Mode '-1' in the ξ/κ and L_m/L_{tot} parameter space and they are extrapolated down to ξ/κ=0. For ξ/κ and L_m/L_{tot} that fall under the curves, the dominant mode of operation is Mode '-1'. For parameter values to the right of the curves (higher L_m/L_{tot}), the dominant mode is Mode '+1'. Similarly, for values to the left of the curves (smaller L_m/L_{tot}), Mode '-2' dominates. Above the maximum of each curve, there exists a transition boundary between Mode '-2' and Mode '+1'. The boundary is located at roughly 0.1 to the left of the curve maximum in the L_m/L_{tot} axis. There is no significant shift with further increase of ξ/κ. At smaller κL_{tot}, the range of length ratio for Mode '-1' is narrower but extends to larger ξ/κ values. In contrast, for larger κL_{tot}, the range is wider but covers a smaller range of ξ/κ values. In addition, the peak of the transition curve shifts to smaller L_m/L_{tot} with increasing κL_{tot}. It should be pointed out that these results agree well with the experimental data [Liew91], [Carl91]. Devices with about 18 combinations of active and passive section lengths were fabricated. As shown in Table 3.3, in our notation, they correspond to L_m/L_{tot} = 0.3 to 0.7. κ is estimated to be 20 cm^{-1} and ξ is about 2 cm^{-1}. This means that ξ/κ=0.1 and the equivalent κL_{tot} varies from 1.4 to 3.4. With the exception of only two combinations, all combinations have ξ/κ and L_m/L_{tot} values bounded by the transition curves. It therefore explains why all the working

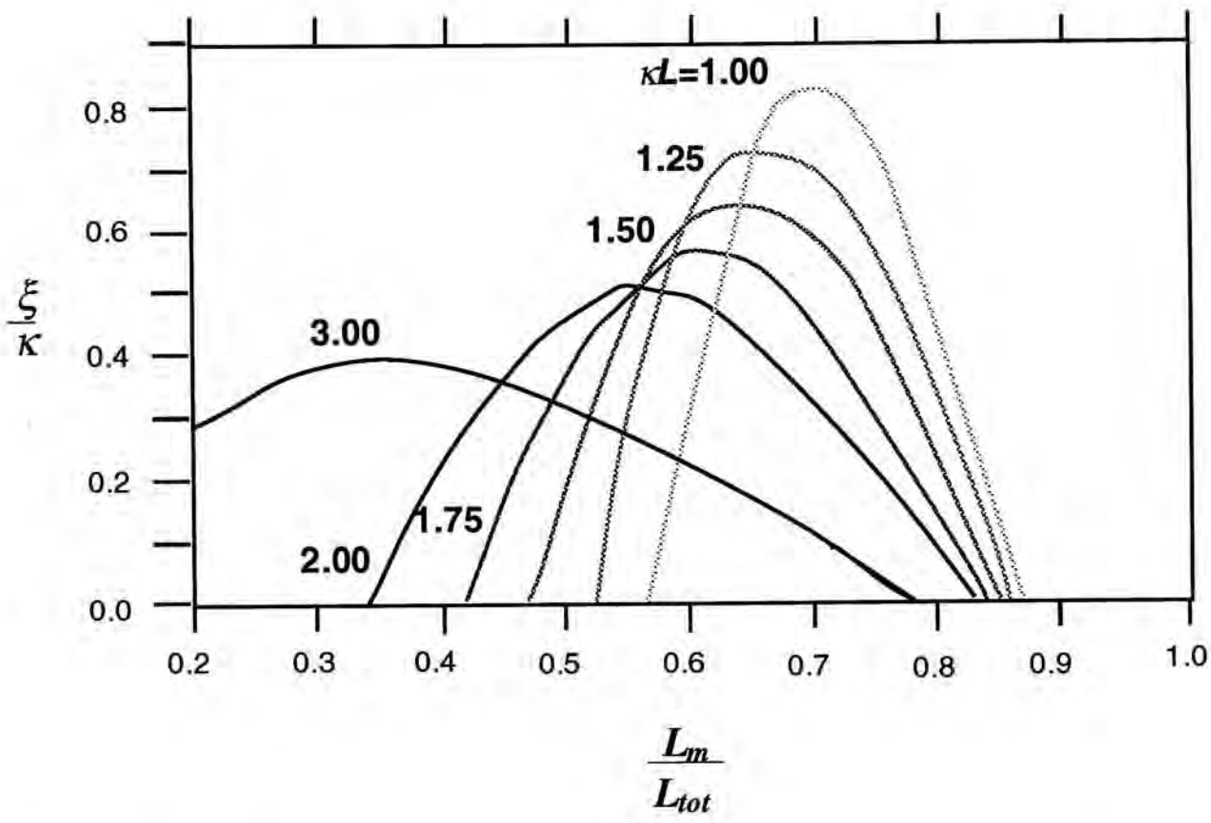

Fig. 3.14 *Design plot of the DFBDBR laser. The curves mark the mode transition boundary between Mode '-2' and Mode '-1' as well as Mode '-1' and Mode '+1'. For DFBDBR lasers with parameter values under the transition curves, the dominant mode is Mode '-1' (the peaked nearfield mode).*

devices lased with a peaked nearfield distribution and single-lobed far field from the surface emission.

Figure 3.14 can be used as a tool in the design of these DFBDBR lasers. To achieve high performance, the regions near the transition curves should be avoided. It is because mode discrimination is poor and there is significant power in the neighboring side modes. As a result, the laser often switches to one of the side modes with drive current. Consequently, for a given κL_{tot} , the optimal length ratio is the one at which ξ/κ reaches its maximum value (peak of the transition curve). For example, for κL_{tot} =1.0, the optimal L_m/L_{tot} is around 0.7. For the same reason, ξ/κ should be at least 0.1 below the curve to avoid potential instabilities. As to the

optimal κL_{tot} values, small κL_{tot} is not desirable because it is more sensitive to the length ratio and as a result, the device is less tolerant to fabrication variations. On the other hand, a large κL_{tot} should not be used because of more severe LSHB effects (to be discussed below).

L_r $(=L_1)$ (μm)	L_m (μm)	L_{tot} (μm)	κL_{tot}	L_m/L_{tot}
*200	300	700	1.4	0.43
200	400	800	1.6	0.50
200	500	900	1.8	0.56
200	600	1000	2.0	0.60
200	700	1100	2.2	0.64
200	900	1300	2.6	0.69
*300	300	900	1.8	0.33
300	400	1000	2.0	0.40
300	500	1100	2.2	0.45
300	600	1200	2.4	0.50
300	700	1300	2.6	0.54
300	900	1500	3.0	0.60
400	300	1100	2.2	0.27
400	400	1200	2.4	0.33
400	500	1300	2.6	0.38
400	600	1400	2.8	0.43
400	700	1500	3.0	0.47
400	900	1700	3.4	0.53

Table 3.3 *Parameters values of fabricated DFBDBR lasers.* κ *is estimated to be 20* cm^{-1} *and* ξ *is about 2* cm^{-1}. *The asterisks mark the sets of parameters that are located outside the boundary curves.*

In terms of output power, the increase in the slope efficiency of the edge emission is almost always accompanied by a decrease in the slope efficiency of the surface emission although not necessarily by the same magnitude. For the edge emission, the efficiency decreases with increasing κL_{tot} and ξ/κ because of stronger end reflections and larger radiation loss. If output power from the facet is of interest, one should choose a smaller ξ/κ ($\leq$0.2, for example) and κL_{tot} <3.0. On the other hand, if output is obtained through surface emission, a larger ξ/κ ($\geq$0.2) is more desirable than a larger κL_{tot} because of LSHB effects.

In summary, some values to consider in designs are κL_{tot} = 1.5 to 2.5, ξ/κ $\leq$0.2 for facet output and $\xi/\kappa \geq 0.2$ for surface output, and L_m/L_{tot} =0.5 to 0.7. In determining the parameters, one should keep in mind that they are interrelated and should ensure that their values are bounded by the respective transition curve. For instance, ξ and κ are not independent [Kaza85], [Hard89]. Their values are influenced by the details of the grating.

3.3.4 Longitudinal Spatial Hole Burning

One advantage of the DFBDBR is the reduced LSHB effect with respect to that of the uniformly pumped second-order DFB. This reduction is much more pronounced when it is compared with devices such as the QWDFB which has highly nonuniform intensity distribution. The LSHB of the DFBDBR laser can be described by the photon variance in the gain section as defined by Eq. (2.4.2-20). A smaller variance implies a flatter distribution along the laser cavity and reduced LSHB. For QWDFB, a relatively flat distribution can be obtained with κL_{tot} = 1.25 [Whit89].

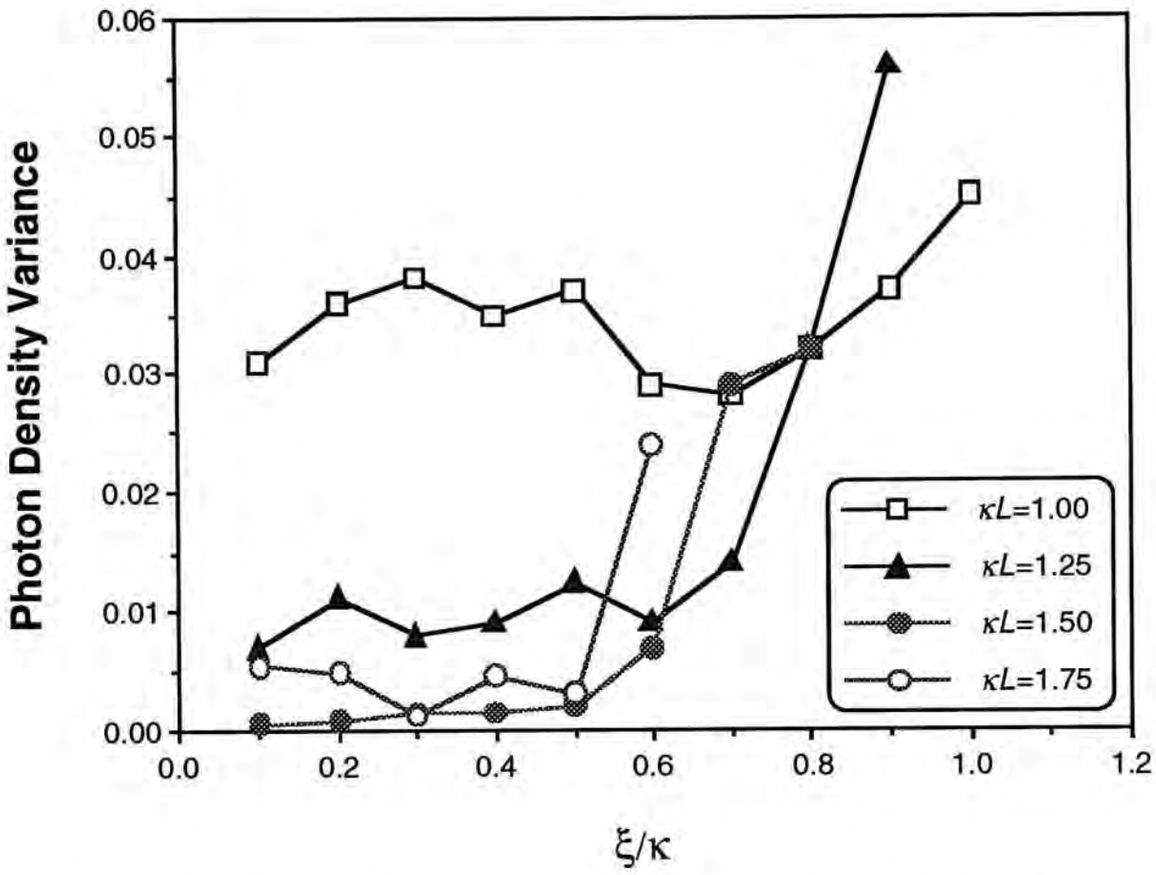

Fig. 3.15 *Plot of the calculated longitudinal mode intensity distribution variance versus ξ/κ. For a given κL_{tot} , L_m/L_{tot} is set at or close to the optimal value. For κL_{tot} = 1.0 and 1.25, L_m/L_{tot} = 0.7. For κL_{tot} = 1.5 and 1.75, L_m/L_{tot} = 0.6.*

The exact magnitude of the variance depends on κL_{tot} and the ξ/κ ratio as shown in Fig. 3.15. In the figure, the variance is computed as a function of ξ/κ for κL_{tot} =1.0 to 1.75. For a given κL_{tot} , the length ratio is set to the optimal value. The graph depicts a minimum in variance at κL_{tot} =1.5 when ξ/κ is under the transition boundary (variance=0.0007 at ξ/κ=0.1). All four curves show an increase in variance for ξ/κ values beyond the transition boundary. For example, the variance for κL_{tot} =1.5 remains relatively unchanged as ξ/κ goes from 0.1 to 0.5. The lasing mode is Mode '-1' in this region. At ξ/κ ~0.6, which marks the transition between Mode '-1' and Mode '+1', the variance increases abruptly. Beyond this point, the

intensity distribution is essentially dominated by Mode '+1'. The sharp increase in variance is sometimes preceded by a small decrease. Recall that in the transition region, the two modes have comparable power. Since their corresponding distributions often rise and fall in opposite directions in the pumped section, they actually complement each other and produce a flatter intensity distribution. For κL_{tot} =2.0 and 3.0 (not shown), the variance shows similar behavior and the average variance is 0.013 and 0.030, respectively, with the laser operating in Mode '-1'.

These variance values may be compared with those of the uniformly pumped second-order DFB and the first-order QWDFB [Whit89]. For the uniform DFB, the minimum variance is located near κL_{tot} =1.5 to 1.75, depending on the magnitude ξ/κ. For example, it is 0.0008 at κL_{tot} =1.5 and ξ/κ =0.4. The value at κL_{tot} =3.0 goes from 0.08 (ξ/κ =0.1) to 0.112 (ξ/κ =0.5). In general, the variance of the DFBDBR laser is typically smaller by a moderate factor of 2 to 3. The improvement is more significant when compared with the QWDFB laser whose value ranges from a minimum of 0.01 (κL_{tot} =1.25) to 0.5 (κL_{tot} =3.0). This is more than 14 times larger than that of the DFBDBR laser.

3.3.5 Effective Linewidth Enhancement Factor

Another advantage of the DFBDBR over the uniformly pumped DFB is the smaller effective linewidth enhancement factor. A smaller linewidth enhancement factor means reduced chirping and narrower spectral linewidth, both of which are important in the modulation of semiconductor lasers. As discussed in Ref. [Shim91] and [Arim90b], there are two contributions for their reduction. One is the coupling to an extended passive resonator [Kaza87]. This is clearly applicable to the DFBDBR laser in which the resonators are the unpumped grating sections. The other is the detuning of the lasing mode to the shorter wavelength side of the gain peak [Ogit86], [Ogit87]. This is satisfied because Mode '-1' is on the shorter wavelength side of the

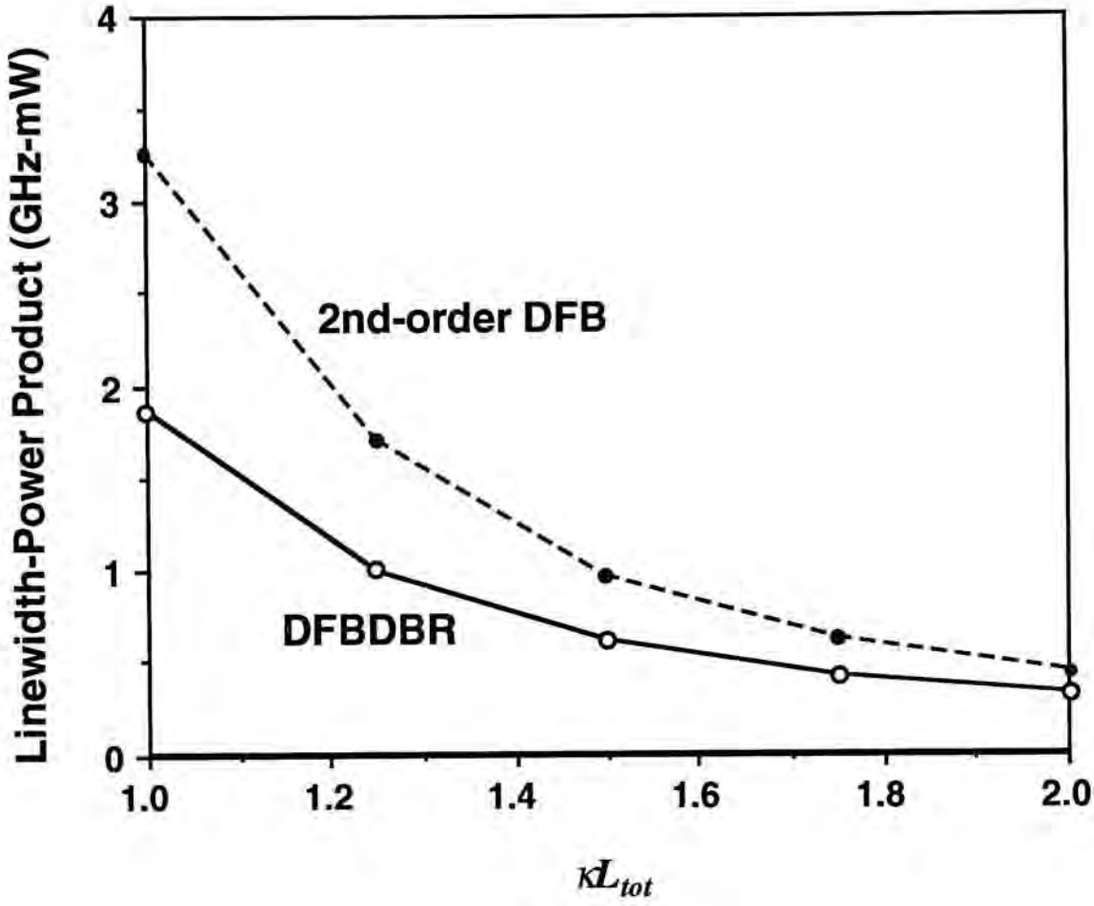

Fig. 3.16 Plot of the calculated spectral linewidth-power product versus κL_{tot} at ξ/κ=0.1. The dotted line is for the uniformly pumped second-order DFB. The solid line is for the DFBDBR laser at the optimal length ratio.

effective gain peak, which is located at the reflectivity maximum of the unpumped DBR sections. In the analysis, the gain profile is assumed to be constant for all frequencies since the bandwidth of the grating is much smaller than that of the material gain. As a result, the effective gain profile, after incorporating effects of the Bragg reflectors, has its maximum located at zero detuning from the Bragg condition.

Figure 3.16 shows the calculated linewidth-power product as a function of κL_{tot} at ξ/κ=0.1. The power is taken as the sum of both the edge emission and the surface emission. The upper curve is for the uniformly pumped DFB and the bottom curve is for the DFBDBR. The results are computed at the optimal length ratio. Both

linewidth-power products decrease with κL_{tot} . The product of the uniformly pumped DFB is larger than that of the DFBDBR in this κL_{tot} range and the difference between the two decreases with increasing κL_{tot} . The ratio of the two products ranges from 0.57 at κL_{tot} =1.0, to 0.75 at κL_{tot} =2.0. This translates to a reduction of the effective linewidth enhancement factor by a factor of 0.73 to 0.85.

Direct comparison with the DR-type laser is difficult because the aforementioned differences. However, some of the design principles of the DR-type lasers may be applied to the DFBDBR because in some respects, the DFBDBR laser may be considered as a special case of the DR laser. These principles actually suggest that the DFBDBR is an optimized version of the DR laser in terms of the phase shift between the active and passive sections. The important differences between the two lasers lie in the fact that the DFBDBR uses a second-order grating with no phase shift between the active and passive sections. In Fig. 2 of Ref. [Arim90b] and Fig. 14 of Ref. [Shim91], it was shown that the effective linewidth enhancement factor is smallest at zero phase shift when the fabricated wavelength detuning is the same in both sections. This suggests that the DFBDBR laser is optimized in terms of reduced effective linewidth enhancement factor as a function of phase shift. In general, a nonzero phase shift is required for the DR laser because the threshold gain difference between the two lowest loss modes is near zero when a first-order grating is employed. In contrast, the second-order grating in the DFBDBR laser provides substantial mode discrimination between the two lowest loss modes.

According to the above-threshold analysis, the linewidth-power product of the DFBDBR could be larger than that of the uniformly pumped DFB when κL_{tot} is increased further or when ξ/κ is large. It is therefore important to design the DFBDBR laser in accordance with the aforementioned criteria in order to achieve stable single-mode operation and reduced chirp and spectral linewidth.

3.3.6 Asymmetric DFBDBR

We have also investigated the effect of asymmetry on the SMSR of the DFBDBR laser. We found that the introduction of asymmetry results in poorer side-mode suppression. An example is shown in Fig. 3.17. The three dimensionless parameters are: κL_{tot} =2.0, ξ/κ=0.2 and L_m/L_{tot} =0.6. The total cavity length is, again, 1000 μm and the sum of the unpumped section lengths is 400 μm. All the spectra are computed at the same relative current level above threshold. They are arranged in a way such that the curve at the top is the most asymmetric with only one unpumped section and the curve at the bottom is the least asymmetric with the unpumped sections of equal length. As the device becomes more asymmetrical, the side-mode intensities of Mode '-2' and Mode '+1' are enhanced while the power of the dominant Mode '-1' decreases. In the extreme case when there is only one unpumped section, the dominant mode is Mode '+1' instead of Mode '-1'. It is because the DBR bandwidth is no longer well-defined, essentially leaving the mode selection to the DFB gain section.

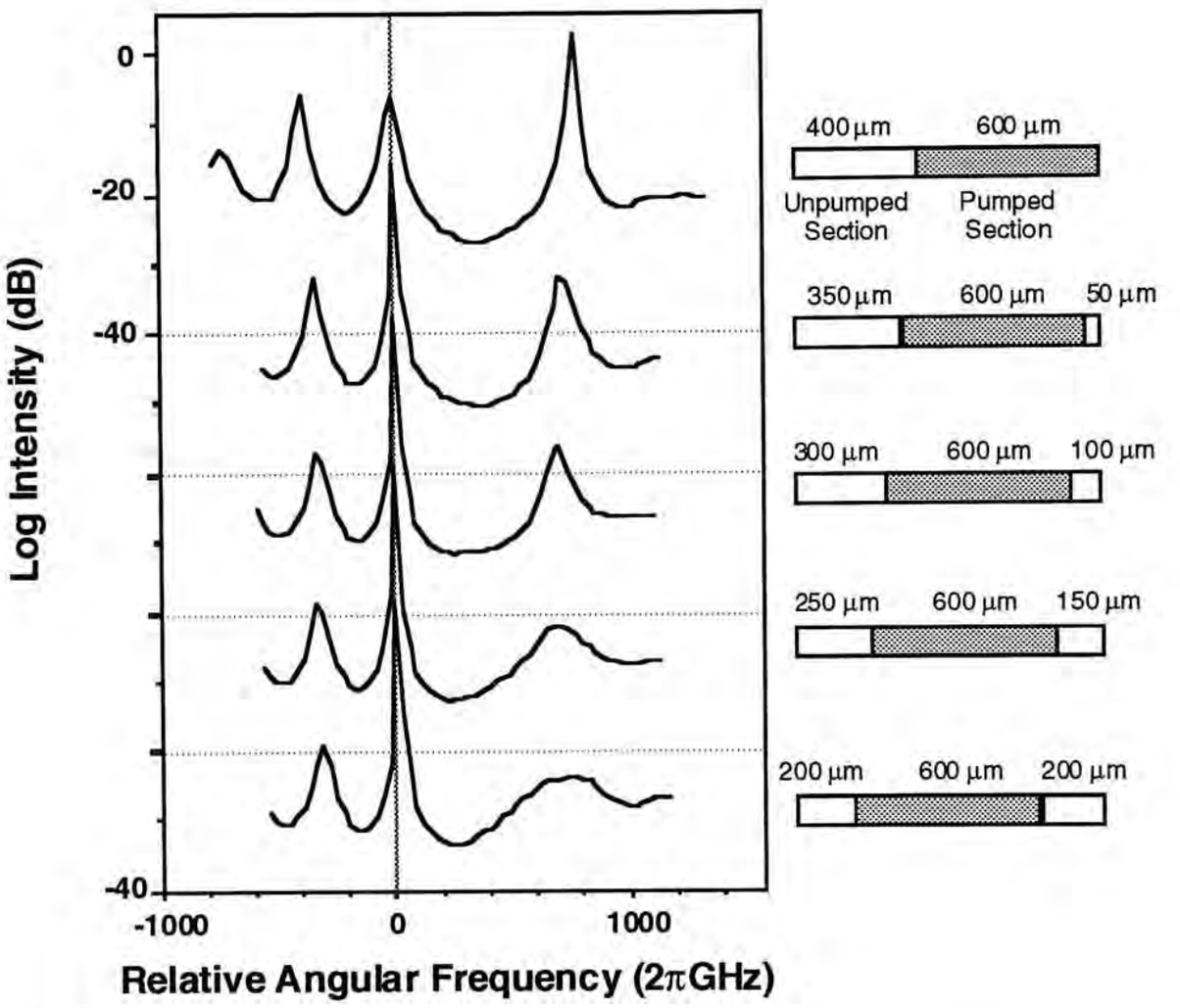

Fig. 3.17 The calculated spectral output of the DFBDBR laser for various degrees of asymmetry . The horizontal axis is the relative angular frequency with respect to Mode '-1'. It shows a decrease in the SMSR with increasing asymmetry in the DFBDBR laser.

3.4 Conclusion

In conclusion, we have performed a detailed analysis of the symmetric three-section DFBDBR laser. It includes operation at below threshold and above-threshold conditions. The results agree well with earlier experimental observations. The dominant mode is associated with its optical intensity peaked in the center of the laser cavity. The subthreshold analysis supports the hypothesis that carrier-induced index change is the mechanism responsible for this particular mode of operation. The above-threshold analysis then identifies the optimal design which is expressed in terms of three dimensionless parameters: κL_{tot} , ξ/κ and L_m/L_{tot}. The values of these parameters should be chosen according to the design plot in Fig. 3.14. The optimal length ratio is located at the transition curve maximum. It typically ranges from 0.5 to 0.7. The ξ/κ ratio should be at least 0.1 below the curve to avoid instabilities. In particular, in terms of slope efficiency, $\xi/\kappa \leq 0.2$ is more advantageous for facet output and $\xi/\kappa \geq 0.2$ is better for surface emission. Since small κL_{tot} is more sensitive to L_m/L_{tot} and large κL_{tot} has aggravated longitudinal spatial hole burning effect, typical value to consider is between 1.5 and 2.5. In comparison with the uniformly pumped second-order DFB laser, the DFBDBR has reduced longitudinal spatial hole burning and smaller effective linewidth enhancement factor. The former reflects the more uniform intensity distribution. The latter is a result of the coupling to the extended passive resonator, and lasing on the shorter wavelength side of the DBR reflectivity maximum. The asymmetric DFBDBR laser is found to have poorer side-mode suppression with respect to its symmetric counterpart. In the extreme case when there is only one unpumped section, the dominant mode is switched to the split nearfield mode associated with the uniformly pumped second-order DFB laser.

4 Analysis of Complex-Coupled DFB

4.1 Introduction

Distributed-feedback lasers with gain- or loss-coupling have high side-mode-suppression ratio and high yield [Davi90], [Luo90], [Borc91], [Borc93], [Li92]. In addition, compared with index-coupled DFB lasers, they are less sensitive to external feedback [Naka89], [Favr91], [Naka91], [Hui94]. They also possess the properties of low chirp, fast modulation response and improved modulation bandwidths [Lu93], [Lowe93], [Sudo94], [Okai94]. More recently, high power and high efficiency have also been demonstrated [Borc94], [Lu94].

Reports on loss-coupled DFB (LCDFB) are relatively scarce. In LCDFB lasers, the coupling between the counter-propagating waves are provided by an absorptive grating with periodic loss. Although the extra loss incurred at the absorptive grating layer increases the threshold current and reduces power efficiency, these negative effects can be minimized by choosing a small grating duty cycle [Cao92]. Experimentally, threshold current below 20 mA has been realized [Tsan94b]. Another method is to use antireflection and high-reflection coatings on the end facets as suggested by [Naka92]. It was shown that, for purely gain-coupled DFB lasers, the ratio of the front-facet (i. e. the facet with lower reflectivity) power to the total power can be increased without significantly degrading the good single-mode property. In contrast, this improvement is not possible on conventional index-coupled DFB without significant degradation in SMSR.

The LCDFB lasers have several potential advantages over GCDFB. First, since the grating coupling coefficient is gain-independent, it is easier to specify in a design. Second, the LCDFB may have narrower spectral linewidth and a higher SMSR [Joha92]. This is because the spontaneous emission noise distribution in a GCDFB is modulated with the grating period.

In this work, LCDFB refers to *purely* loss-coupled DFB laser. The corresponding loss-coupling coefficient is therefore a constant with respect to carrier density. Lasers with both loss-grating and residual periodic index modulation are called complex-coupled DFB (CCDFB) lasers. Gain-coupled DFB (GCDFB) laser refers to DFB laser with *purely* gain-coupled grating, which is formed by periodic gain modulation. The associated gain-coupling coefficient is therefore carrier-dependent.

This chapter reports on the subthreshold and above-threshold analyses [Liew95b] of both LCDFB and the CCDFB lasers. The goal is to optimize the design of these lasers in terms of low threshold, high efficiency and high single-mode yield. Besides the determination of the desirable values of the coupling coefficients, strategies such as the changing of grating duty cycle and the use of facet coatings are investigated. In the above-threshold analysis, the emphasis is on the comparison of the threshold currents and the front-facet power efficiencies, because excessive loss is a common concern in these lasers. These lasers are examined under the influence of three types of facet-coatings: (1) AR-AR (zero facet reflectivity for above-threshold analysis and 1% reflectivity for subthreshold yield analysis); (2) AR-HR (1% and 90% facet reflectivities); and (3) CL-CL (32% reflectivity on both facets).

This work differs from others in the method and the scope of the analysis. For example, loss saturation in the absorptive grating is taken into consideration. When compared with [Naka92], the lasers are analyzed at above-threshold conditions instead of subthreshold conditions. In this way, the power efficiency can be computed

directly. This is important because the supporting evidence of the proposed method in [Naka92] is based on a factor that does not really reflect the actual output power. This proposed method uses asymmetric facet coatings to enhance the output power from a single facet. As explained in the paragraph that follows, this method has a limitation. Moreover, in this work, the effect of residual index-coupling (i. e. CCDFB) is investigated. Other new results are related to the yield analysis. Compared with [Davi91b], this work assumes one extra yield criterion. In addition, we perform calculation on lasers with symmetric as well as asymmetric facet coatings, whereas [Davi91b] contains results only related to symmetric facet coatings.

An overview of our results is as follows. It is discovered that significant improvement of the front-facet power slope efficiency (η) with AR-HR coatings occurs only at small coupling coefficients. For example, for LCDFB, η is higher for AR-HR than for AR-AR coatings when $\kappa_l L < 1.1$. With the addition of index-coupling, η decreases. At $\kappa_n L$ =3.0, efficiency of devices with AR-HR is less than that with AR-AR coatings for all values of $\kappa_l L$. Therefore, although the efficiency ratio between the two facets is much larger than 50% with the application of asymmetric coatings, the actual improvement on the front-facet efficiency does not always take place.

The results also indicate that asymmetric coatings (AR-HR) as compared with symmetric antireflection coatings (AR-AR) reduces threshold current by more than a factor of two for all values of index-coupling coefficients (κ_n) and loss-coupling coefficients (κ_l). They point out that low threshold and high efficiency CCDFB lasers with absorptive gratings are possible with the careful choice of the grating duty cycle and the use of AR-HR coatings together with appropriate coupling coefficient.

Although the application of asymmetric facet coatings enhances the power efficiency of the front facet, it also degrades the single-mode property of the loss-coupled DFB lasers. Since the degradation can be inferred from the theoretical single-

mode yield, a yield analysis of the purely loss-coupled DFB laser is performed [Liew95c]. The yield is subjected to three criteria: threshold gain margin, photon variance and threshold current. The results indicate that small reduction in yield can be achieved by choosing appropriate coupling coefficients.

The rest of this chapter is organized as follows. *Section 4.2* gives an example of a versatile CCDFB laser structure with absorptive gratings that includes the basic epilayer composition and thicknesses. *Section 4.3* presents the above-threshold analysis of CCDFB lasers. The major results are threshold current and front-facet power efficiencies. *Section 4.4* compares results from the subthreshold yield analyses of LCDFB and QWDFB lasers. A summary is given in *Section 4.5*.

4.2 Laser Structure

The above-threshold analysis is performed with a model detailed in *Chapter 2* and [Liew95a]. For the calculation of the front-facet power efficiency, the above-threshold model is necessary. For the yield analysis, however, the linear model is sufficient.

A schematic of the loss-coupled DFB is shown in Fig. 4.1. This example is a SCH-MQW structure based on [Wrig93], [Sudo93], and [Sudo94]. The MQW structure consists of six 75 Å InGaAsP quantum wells and five 150 Å thick InGaAsP barriers that are strain-compensated to circumvent the critical thickness limit. The SCH layers are 0.1 μm thick and its bandgap wavelength (λ_g) is at 1.3 μm. The grating layers are separated from the SCH region by a thin InP spacer layer. The grating is formed by two layers: (1) low index layer (λ_g=1.2 μm) and (2) absorptive layer with a loss coefficient of 10^4 cm^{-1} [Borc91]. These two grating layers are first grown and then etched for grating definition. Then, an antiphase index grating layer (λ_g=1.3 μm) is overgrown on top. As a result, this higher index material fills in the troughs of the grating (thus, the passive regions of pure index-coupling) and is also

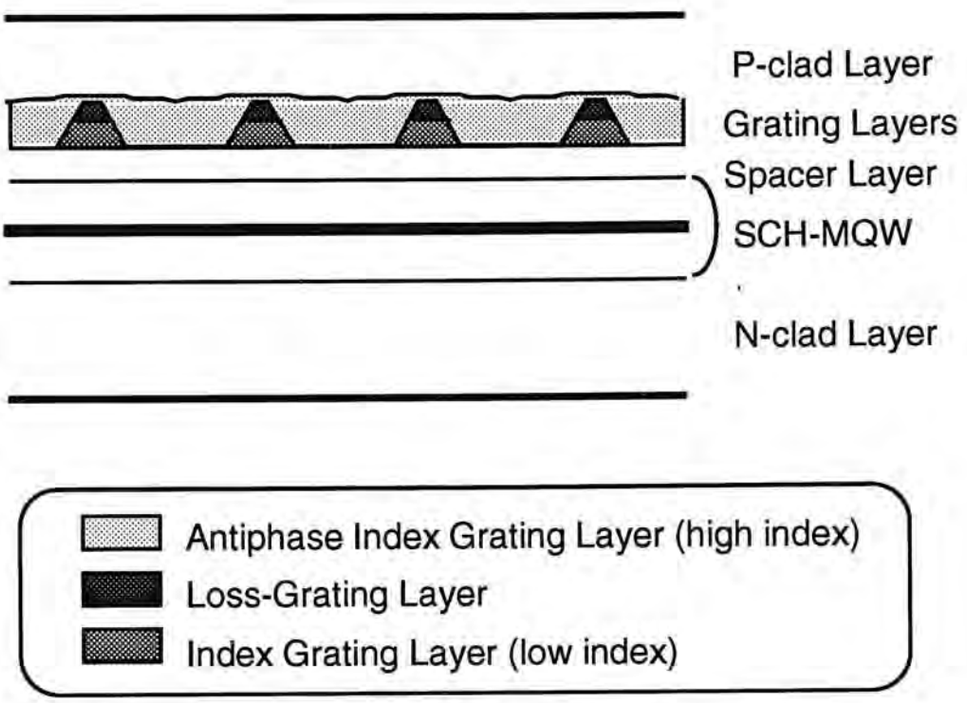

***Fig. 4.1** Laser structure of the CCDFB with absorptive grating.*

deposited as a thinner layer on top of the grating teeth (lossy regions). With this laser structure, both the index- and loss-coupling are provided by the same grating. It implies that the grating phase is either 0 or π radians and that the transfer matrix is symmetrical (see *Section 2.3.1*). For this special case (assumed in this analysis), the complex coupling coefficient are expressed as, $\kappa = \kappa_{fr} = \kappa_{rf} = \kappa_n \pm i\,\kappa_l$. For rectangular grating with the grating duty cycle $\rho < 0.5$, $\kappa_n<0$ [Kaza85]. Therefore, the negative sign refers to $\theta = 0$ (in-phase) and the positive sign corresponds to $\theta = \pi$ (antiphase). The transverse structure of the lossy (passive) grating region is shown in Fig. 4.2a (Fig. 4.2b).

4.2.1 Grating Layer

The antiphase grating layer offers a high degree of flexibility in the design of CCDFB. It is particularly useful when a grating phase of π is needed. The real index

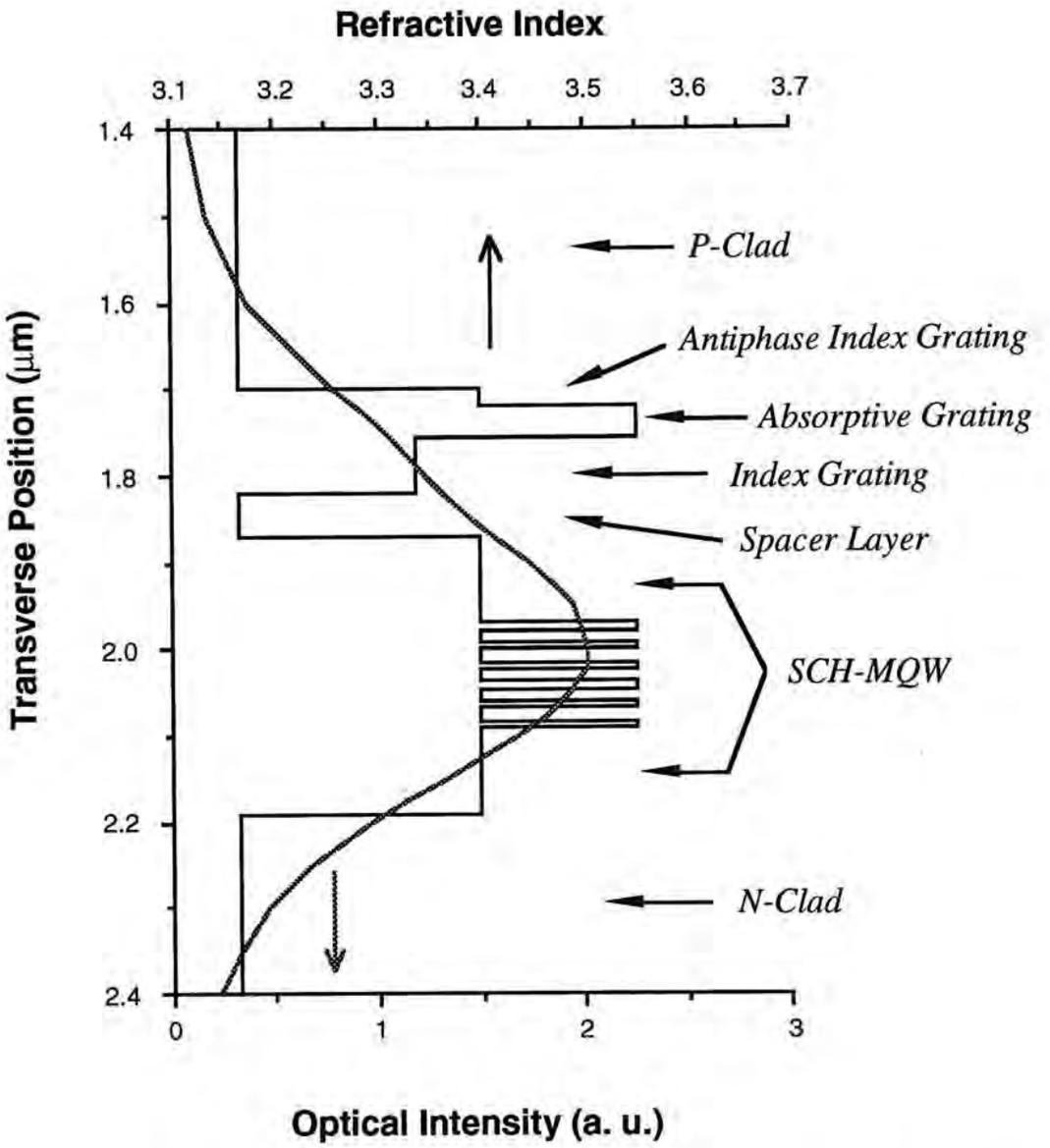

Fig. 4.2a *The refractive index and optical intensity distributions of the transverse laser structure in the lossy grating region. The absorptive grating layer is 35 nm thick and the index grating layer is 65 nm thick. The resulting effective index is 3.2893. The confinement factor of the six quantum wells is 8.70% . The effective power loss is 374 cm^{-1}.*

step between the passive and lossy regions of the grating determines κ_n, whereas the change in the effective loss coefficient yields κ_l. A grating phase of π means that the real index is smaller in the lossy grating region. The antiphase CCDFB lasers have been shown to have reduced effective linewidth enhancement factor [Kudo92],

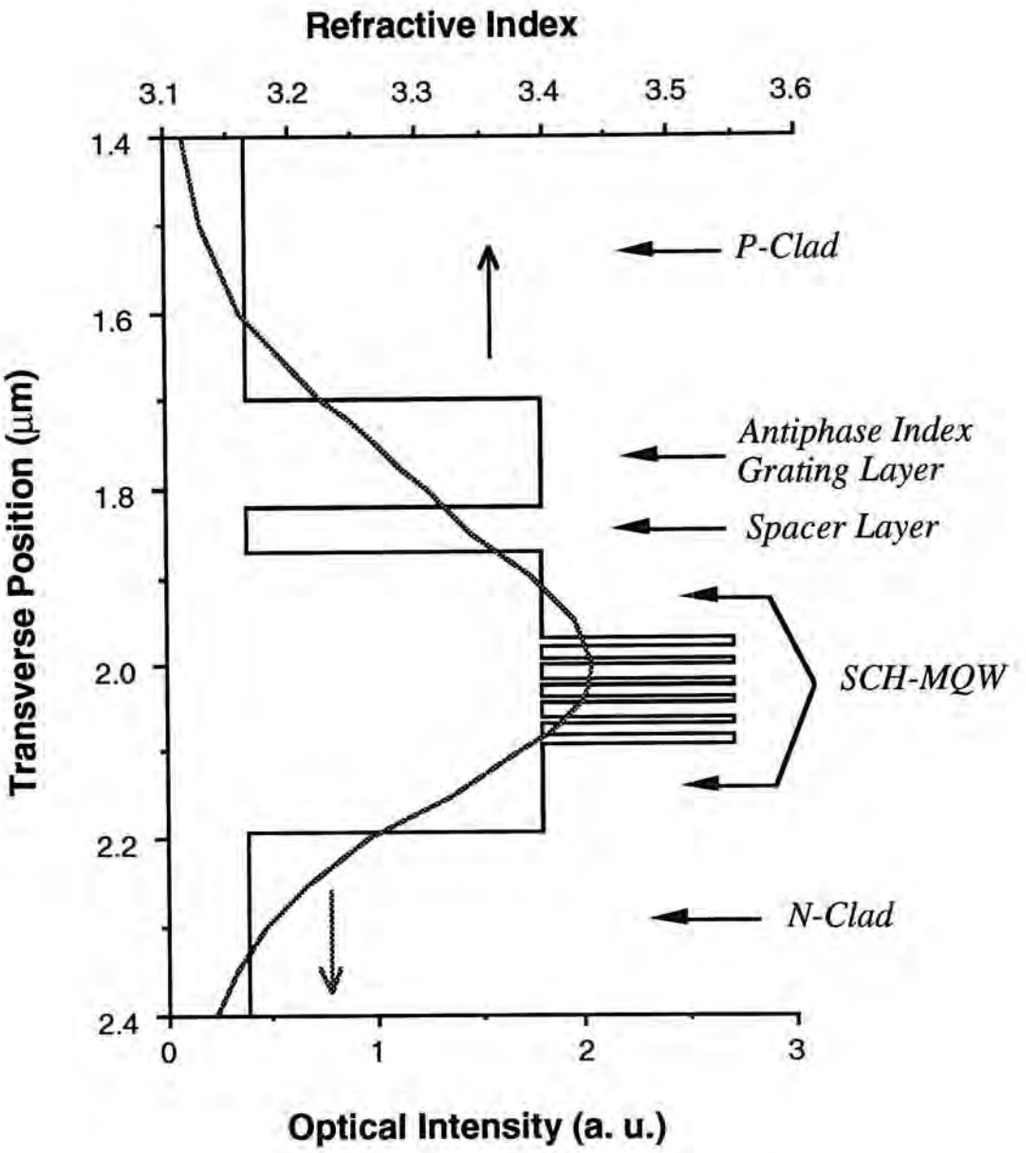

Fig. 4.2b *The refractive index and optical intensity distributions of the transverse laser structure in the passive grating region. The antiphase grating layer is 0.12 μm thick. The resulting effective index is 3.2892. The confinement factor of the six quantum wells is 8.79% . The effective power loss is 5 cm^{-1}.*

[Joha93] and self-suppressed LSHB [Sudo93]. On the other hand, a theoretical and experimental study of in-phase CCDFB lasers revealed possible instability near threshold [Zoz94a].

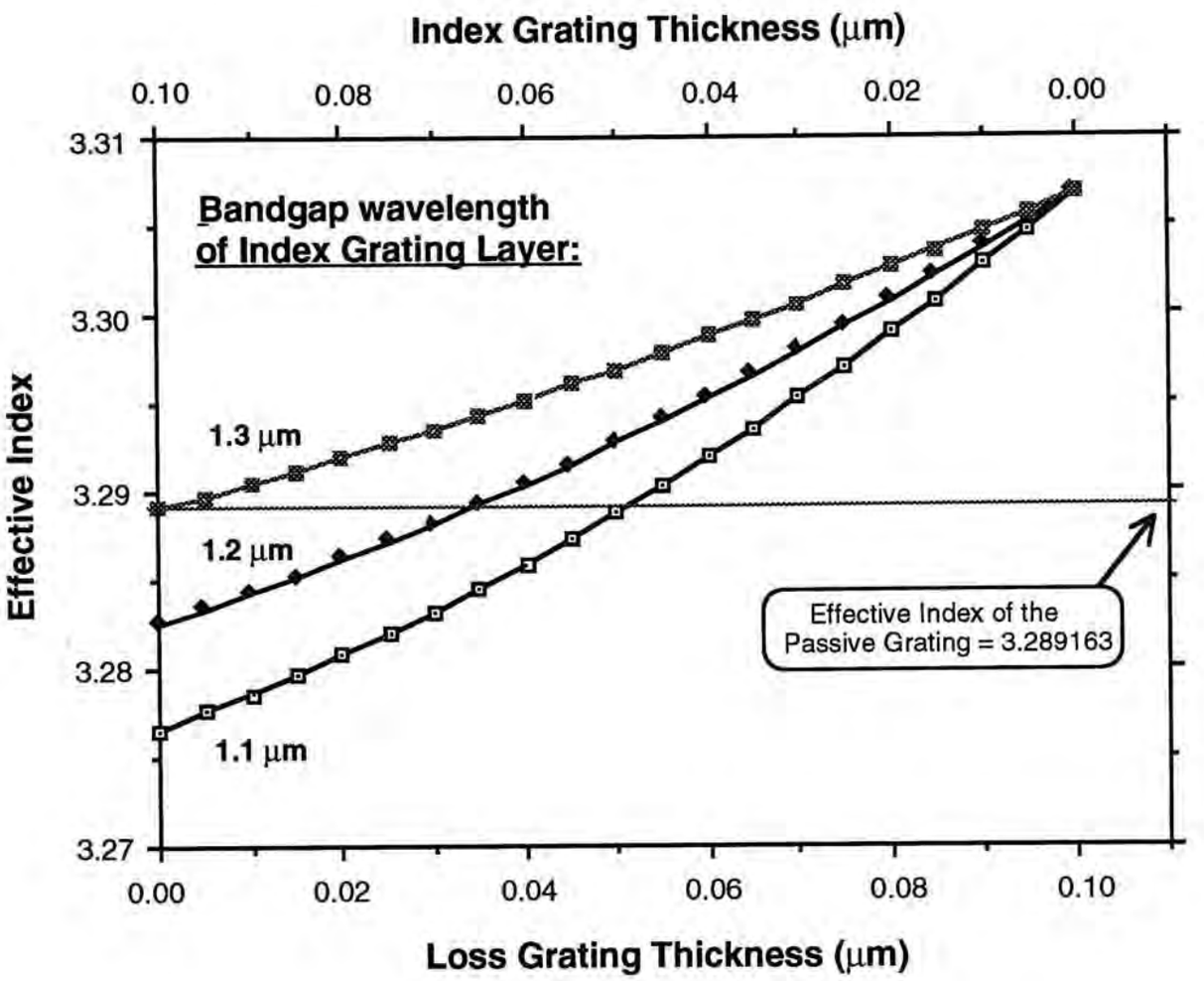

Fig. 4.3 *Effective index of the lossy region as a function of the loss- (or index-) coupled grating thickness and material composition. The horizontal line marks the effective index of the passive grating region. The points of interception locate the parameter values for purely loss-coupling operation.*

The material composition and the thicknesses of the two grating layers control whether the DFB laser has purely absorptive grating, in-phase or antiphase complex grating. An example of the design procedure is as follows. The total layer thickness of the two grating layers is assumed to be constant. This means that as the thickness of one layer increases, the other is reduced by the same amount. As shown in Fig. 4.2b, the real effective index of the passive grating region is 3.2392. Hence, assuming that κ_n is negative, if the real effective index of the lossy grating region is higher, the index-grating is in-phase with the loss-grating. If the opposite is true, they are antiphase. In the case when the two indices are the same, the laser is a purely

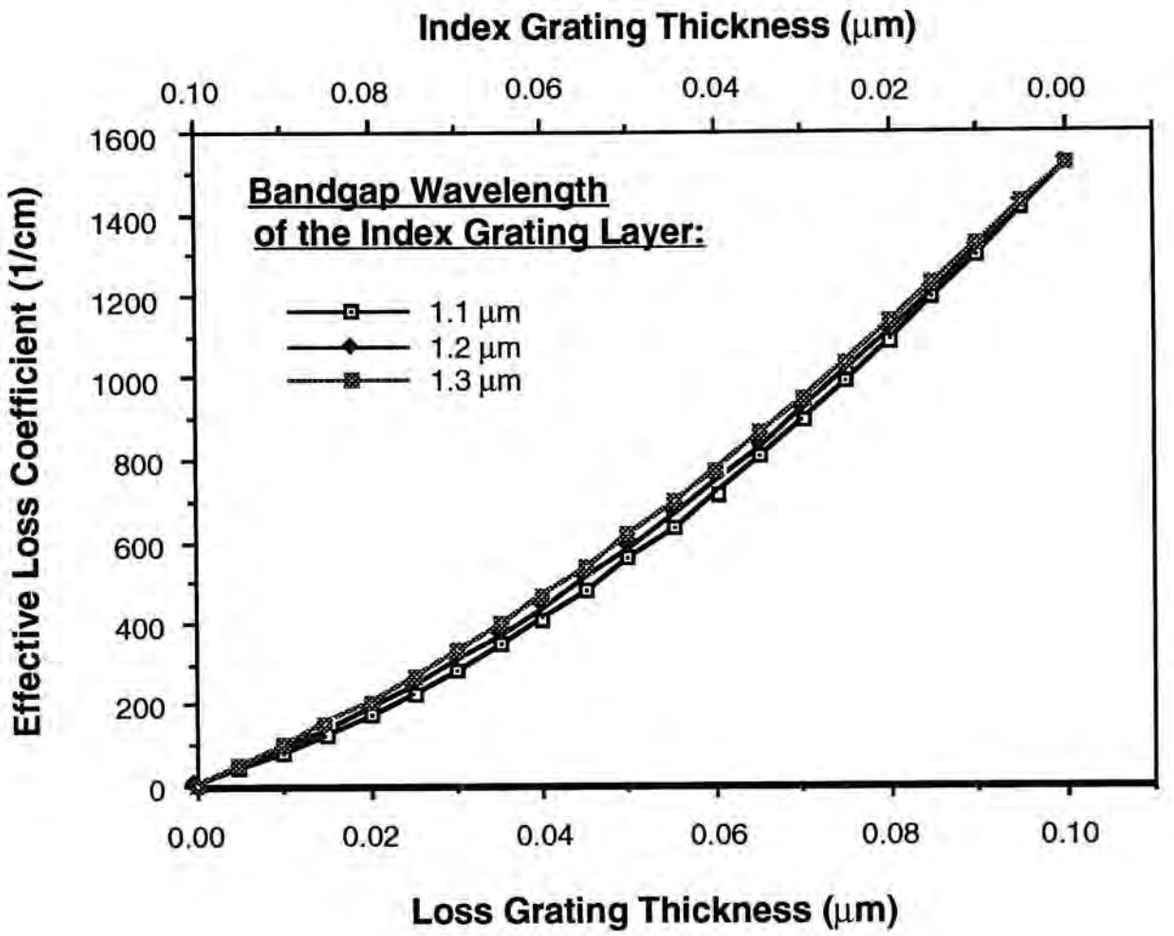

Fig. 4.4 *The loss coefficient of the lossy region as a function of the loss- (or index-) coupled grating thickness and material composition. At a loss grating thickness of 35 nm, the loss coefficient is 374 cm^{-1}.*

LCDFB with no index-coupled grating. The design curves are graphed in Fig. 4.3 with the real effective index versus the layer thicknesses of the index- and loss-gratings for three material compositions. The horizontal line marks the effective index of the passive grating region. For example, for a pure LCDFB, one can choose a ~0.065 μm-thick index grating layer with a bandgap wavelength of 1.2 μm and a ~0.035 μm thick absorptive-grating layer. For in-phase (antiphase) CCDFB, parameter values above (below) the horizontal line are needed.

Just as the grating layers determine the real effective index of the lossy grating regions, the same design parameters control the effective loss coefficient in the same regions. A similar graph is shown in Fig. 4.4 depicting the relationship between the effective loss coefficient and the index- and loss-grating thicknesses and composition. It is obvious that the composition of the index grating layer has little effect on the loss coefficient. The deciding factor is the thickness of the absorptive-grating layer. For the design of the laser structure, the effective index and the effective loss coefficient are interdependent.

The step change of the loss coefficient ($\Delta\alpha$) in the grating yields the loss coupling coefficient. With m being the grating order, the loss coupling coefficient can be written as [Kudo92]

$$\kappa_l = \frac{\sin(m\pi\rho)}{2m\pi}\Delta\alpha \qquad (4.1\text{-}1)$$

4.2.2 Parameter Values

The parameters used are listed in Table 4.1. The index grating and the absorptive grating are assumed to be either in-phase or antiphase. This is automatically satisfied when the loss-coupling and the index-coupling are caused by the same grating. In terms of the spectral properties, a purely gain- or loss-coupled DFB produces a single dominant mode centrally located within the stop-band. When index-coupling is present, the dominant mode is shifted to the blue (red) end of the stop-band for antiphase (in-phase) coupling. We found that other properties are not affected except for the nearfield pattern (caused by the change in the relative phase between F and R). That is, the photon density distribution and P-I characteristic are identical for both in-phase and antiphase coupling. A discussion on the effects of the grating phase can be found in [Card95]. For the following analyses, ρ is set at 0.15 and 0.36. Duty cycle of 0.15 is among the optimal values [Cao92] for low threshold gain independent of the order of the grating. In practice, grating duty cycle below

~0.1 is very difficult to obtain. The loss-grating coupling coefficient has included the high photon density saturation effect and is expressed phenomenologically as [Sudo93]

$$\kappa_l(\psi) = \frac{\kappa_{lo}}{(1+\varepsilon_a \psi)}, \tag{4.2.1-1}$$

where κ_{lo} is the loss coupling coefficient at transparency which can be calculated from Eq. (4.1-1). ψ is the photon density and ε_a is the absorption compression factor which is assumed to be 1.0×10^{-18} cm^3. The extra power loss in the presence of loss grating is given by [Davi91a]

$$\alpha_{extra} = \frac{2\pi\rho}{\sin(\pi\rho)} \kappa_l . \tag{4.2.1-2}$$

Although gain-coupled grating is not considered in this analysis, its dependence on carrier density has been incorporated in the model. A discussion is included in *Appendix A.3*.

Parameters	*Values*
Linear carrier lifetime (τ)	1.0 ns
Bimolecular carrier recombination coefficient (B_N)	1.0×10^{-10} cm^3s^{-1}
Auger carrier recombination coefficient (C_N)	3.0×10^{-29} cm^6s^{-1}
Differential gain (a)	6.0×10^{-16} cm^2
Nonlinear gain compression factor (ε)	3.0×10^{-17} cm^3
Transparency carrier density (N_t)	1.5×10^{18} cm^{-3}
Linewidth enhancement factor (α_H)	2.0
Absorption and scattering loss (α)	10.0 cm^{-1}
Grating coupling coefficient (κ_n)	$0.0 \rightarrow 75.0$ cm^{-1}
Loss grating coupling coefficient (κ_l)	$0.0 \rightarrow 100.0$ cm^{-1}
Effective phase refractive index (n)	3.289
Effective group refractive index (n_g)	3.75
Total length of the laser cavity (L)	400.0 μm
Active layer thickness (d)	0.045 μm
Effective width parallel to junction ($w_{\|\|}$)	2.0 μm
Effective width perpendicular to junction ($w_{\perp}$)	0.44 μm
Far-field angular divergence parallel to junction ($\theta_{\|\|}$)	30.0°
Far-field divergence perpendicular to junction ($\theta_{\perp}$)	55.8°
Active layer confinement factor (Γ)	0.087
Approximate emission wavelength (λ_o)	1.55 μm
Number of divided segments	15

Table 4.1 *The parameters values used in the analysis of LCDFB and CCDFB lasers.*

4.3 Above-Threshold Analysis of CCDFB

For the complex-coupled DFB lasers, the threshold currents (I_{th}) and the front-facet power efficiency ($\eta = \frac{dP}{dI}$) are calculated as functions of the dimensionless $\kappa_n L$ and $\kappa_l L$ [Liew95b]. The value of $\kappa_n L$ varies from 0.0 to 3.0 whereas $\kappa_l L$ takes on a value of 0.0 to 4.0. The calculations are repeated for three sets of facet coatings: AR-AR, AR-HR, and CL-CL. The focus here is on the distribution of I_{th} and η. Results are detailed in the next section. In order to reduce computational time, the yield calculation is only performed for the purely loss-coupled DFB (i.e. $\kappa_n L$ =0.0) as the introduction of gain-coupling has already been shown to improve the single-mode yield in complex-coupled DFB lasers [Davi90], [Davi91b]. Our emphasis is on the differences in yield of the purely loss-coupled DFB with various facet coatings when spatial-hole burning and I_{th} are taken into consideration. The spatial hole burning has the effect of reducing yield at large $\kappa_l L$ whereas the I_{th} criterion has the same effect at small $\kappa_l L$.

4.3.1 Threshold Current

Grating Duty Cycle = 0.36

With ρ = 0.36, the I_{th} results for CCDFB are shown in Fig. 4.5 (perfectly AR-AR), Fig. 4.6 (AR-HR) and Fig. 4.7 (CL-CL). The threshold current is graphed as a function of $\kappa_l L$ for a number of $\kappa_n L$ values.

The results for the perfectly AR-coated CCDFB are shown in Fig. 4.5. The curves give a good demonstration of the tradeoffs between higher grating reflection coefficient (larger κ_l) and higher loss (higher I_{th}). The curve on top is for the case of purely LCDFB. I_{th} reaches its peak (58.0 mA) at $\kappa_l L$ =0.2 as the loss resulted from the absorptive grating increases. Meanwhile, the grating strength remains too weak to

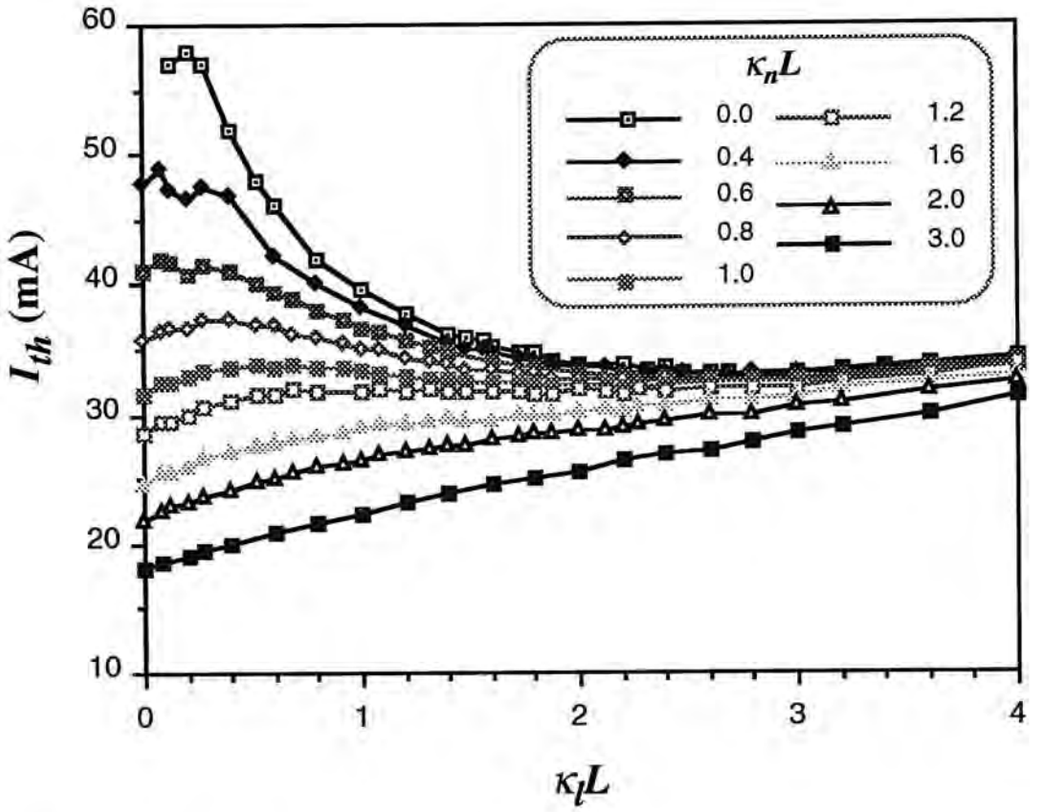

Fig. 4.5 *Threshold current as a function of $\kappa_l L$ for $\kappa_n L$ =0.0 to 3.0. The device is a CCDFB with ρ =0.36 and perfectly AR-coated facets.*

provide any substantial optical feedback until $\kappa_l L$ >0.2. The subsequent decline in I_{th} exhibits a minimum at $\kappa_l L \cong 2.5$ as the increase in grating strength with larger $\kappa_l L$ can no longer offset the extra loss in the absorptive grating. For $\kappa_l L$ >2.5, I_{th} increases very gradually and finally at $\kappa_l L$ =4.0, I_{th} = 33.2 mA.

Moving from top to bottom in Fig. 4.5, for CCDFB with $\kappa_n L \leq 1.2$, I_{th} starts off at a progressively lower value, then increases and falls with $\kappa_l L$. In contrast, for CCDFB with $\kappa_n L$ >1.2, I_{th} increases monotonically with $\kappa_l L$. The reason is the already significant feedback that is provided by the original index grating. The introduction of loss-grating only increases the total loss but does not significantly affect the reflection coefficient. It should be pointed out that the abrupt changes at small $\kappa_l L$ (most notably at $\kappa_n L$ =0.4) are caused by mode degeneracy. Overall, the

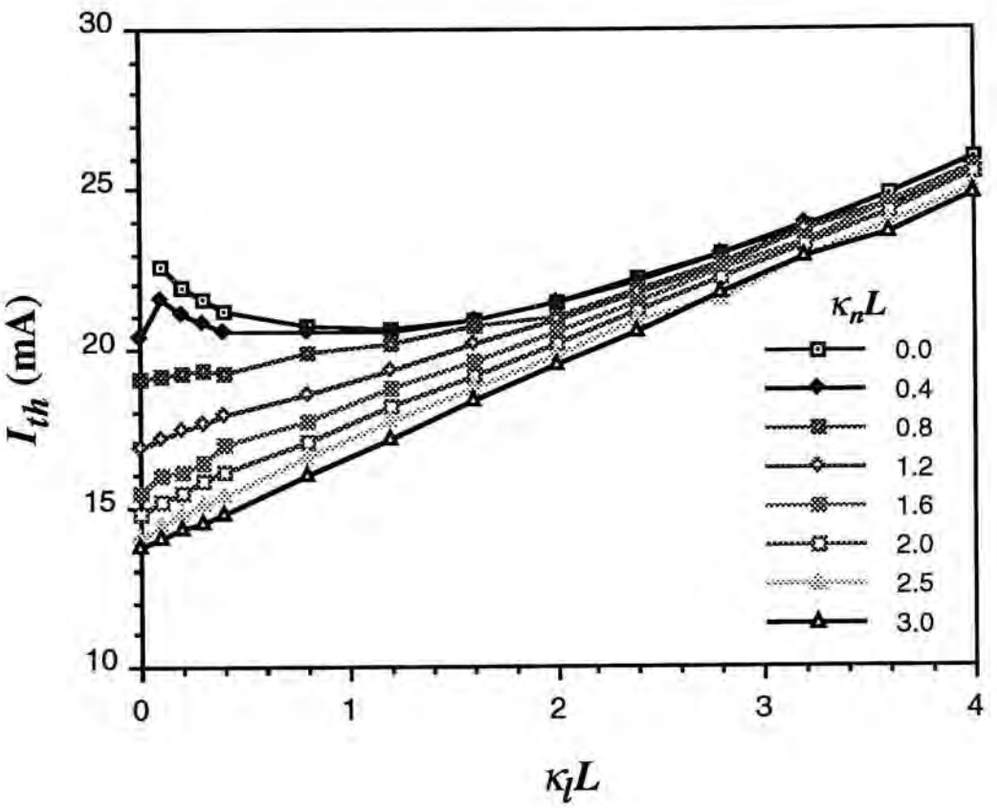

Fig. 4.6 *Threshold current as a function of $\kappa_l L$ for $\kappa_n L$ =0.0 to 3.0. The device is a CCDFB with ρ =0.36 and AR-HR-coated facets.*

variation in I_{th} is large (from below 20 mA to 58 mA) at small $\kappa_l L$, and it is relatively insensitive to $\kappa_n L$ at large $\kappa_l L$: at $\kappa_l L$ =4.0, I_{th} =30.0 ± 3.0 mA.

The same exercise has been carried out for the CCDFB with AR-HR coatings (Fig. 4.6). The use of asymmetric coatings is expected to boost the front-facet (the one with lower reflectivity) output power efficiency. Compared with the AR-AR case, there is also a net increase in reflectivity which leads to lower I_{th} . For the case of purely LCDFB, I_{th} =22.7 mA at $\kappa_l L$ =0.1. It then decreases and reaches a minimum value of 20.6 mA at $\kappa_l L$ =1.2. After that, it increases and I_{th} =25.9 mA at $\kappa_l L$ =4.0. As in the case of AR-AR CCDFB, the threshold current increases monotonically with $\kappa_l L$ for larger values of $\kappa_n L$ (>0.8). The value of I_{th} ranges from 13.7 mA to 25.9 mA for all $\kappa_l L$ and $\kappa_n L$ used in this analysis. The range of variation is reduced

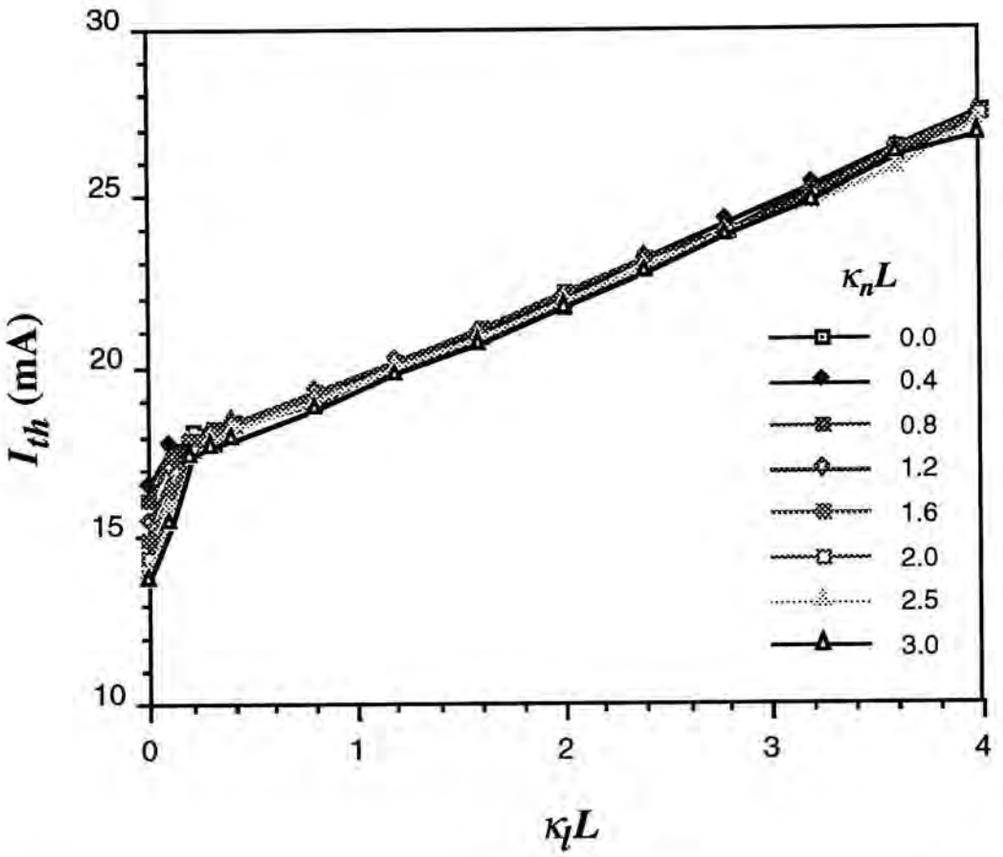

Fig. 4.7 *Threshold current as a function of $\kappa_l L$ for $\kappa_n L$ =0.0 to 3.0. The device is a CCDFB with ρ =0.36 and as-cleaved facets.*

substantially compared with the AR-AR case because of the pre-existed facet reflectivities.

For the case of CCDFB with as-cleaved facets, the variation in I_{th} is reduced further, as shown in Fig. 4.7. The value of I_{th} is almost independent of $\kappa_n L$ except for small $\kappa_l L$ (<0.2). Its value ranges from I_{th} =17.7 ± 0.3 mA at $\kappa_l L$ =0.2 to I_{th} =27.2 ± 0.3 mA at $\kappa_l L$ =4.0. It should be pointed out again that the abrupt changes at small $\kappa_l L$ are direct results of the sudden switching of the dominant mode between the two degenerate modes closest to the stop-band.

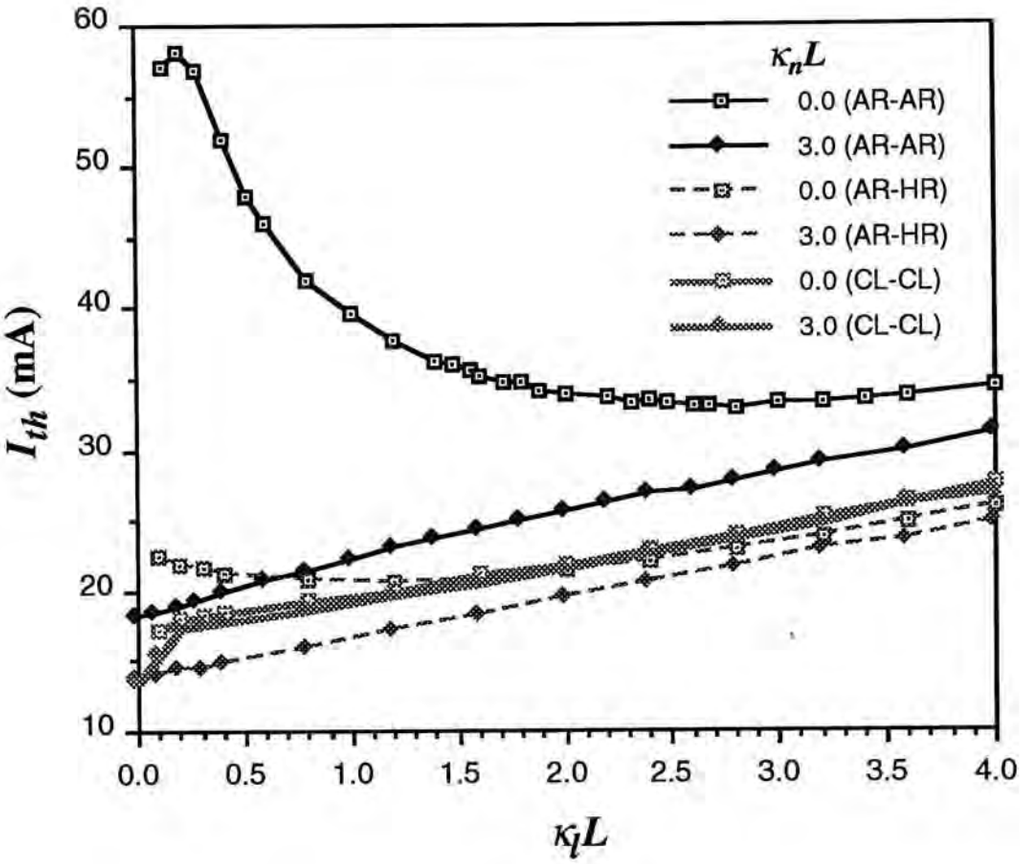

Fig. 4.8 *Threshold current as a function of $\kappa_l L$ for $\kappa_n L$ =0.0 and 3.0. The device is a CCDFB with ρ =0.36 and AR-AR (solid curve), AR-HR (broken curve) and CL-CL (lightly-shaded curve) facets.*

The ranges of I_{th} for the three sets of facet reflectivities are best compared by combining the three preceding figures (see Fig. 4.8). Figure 4.8 only displays the curves at $\kappa_n L$ =0.0 and 3.0 for clarity as the other curves are bounded by them. The value of I_{th} is reduced by a large amount going from AR-AR to AR-HR coatings for all $\kappa_n L$. As we will see later that, AR-HR also improves the power efficiency for some values of $\kappa_l L$. For the case of CL-CL coatings, I_{th} is smaller than those of the AR-AR case but the reduction is not as universal when compared to the AR-HR case. In some cases (e.g. $\kappa_l L$ >2.0), it is actually larger. This behavior has to do with the

effective reflectivity which includes the reflectivities due to the facets in addition to the gratings. Nonetheless, the range of I_{th} is clearly reduced.

Perhaps, the more important information than one can draw out of these threshold current data is how adversely I_{th} is going to be affected by the absorptive grating for a given effective grating coupling coefficient, $|\kappa| = \sqrt{\kappa_n^2 + \kappa_l^2}$. In other words, if one replaces a fraction of the index-coupling with loss-coupling while keeping the absolute magnitude of κ unchanged, what is the resulting increase in I_{th}? The answer can be found by using a contour plot as shown in Fig. 4.9. In this figure, the vertical axis is the imaginary part of κL ($\kappa_l L$) and the horizontal axis is the real part of κL ($\kappa_n L$). Note that I_{th} at $|\kappa L|=0.0$ is infinite and the surrounding area is obtained by extrapolation. The concentric arcs in the diagram mark the constant $|\kappa L|$ in steps of 0.5. If the loss effect is minimal, the contour of I_{th} will be circular when one increases the phase angle of κ from zero (that is, increase the proportion of loss-coupling). As it turns out, the contours are more elliptical with the elongated direction along $\kappa_l L$. It means that I_{th} is higher with loss-coupling as expected. For example, moving along the arc $|\kappa L| = 1.5$, $I_{th} \cong 26$ mA at the horizontal intercept and gradually increases to ~30 mA at the angle of 30°, then 34 mA at 60° and finally 36 mA at 90°. The change in I_{th} is larger for larger $|\kappa L|$ and the contour lines are more circular at smaller $|\kappa L|$. For example, I_{th} is increased by only ~6 mA at $|\kappa L|=0.5$. Another feature is that the center of the ellipses is not at $|\kappa L|=0$ but rather shifted up in the vertical axis; recall that I_{th} peaks at $\kappa_l L > 0$.

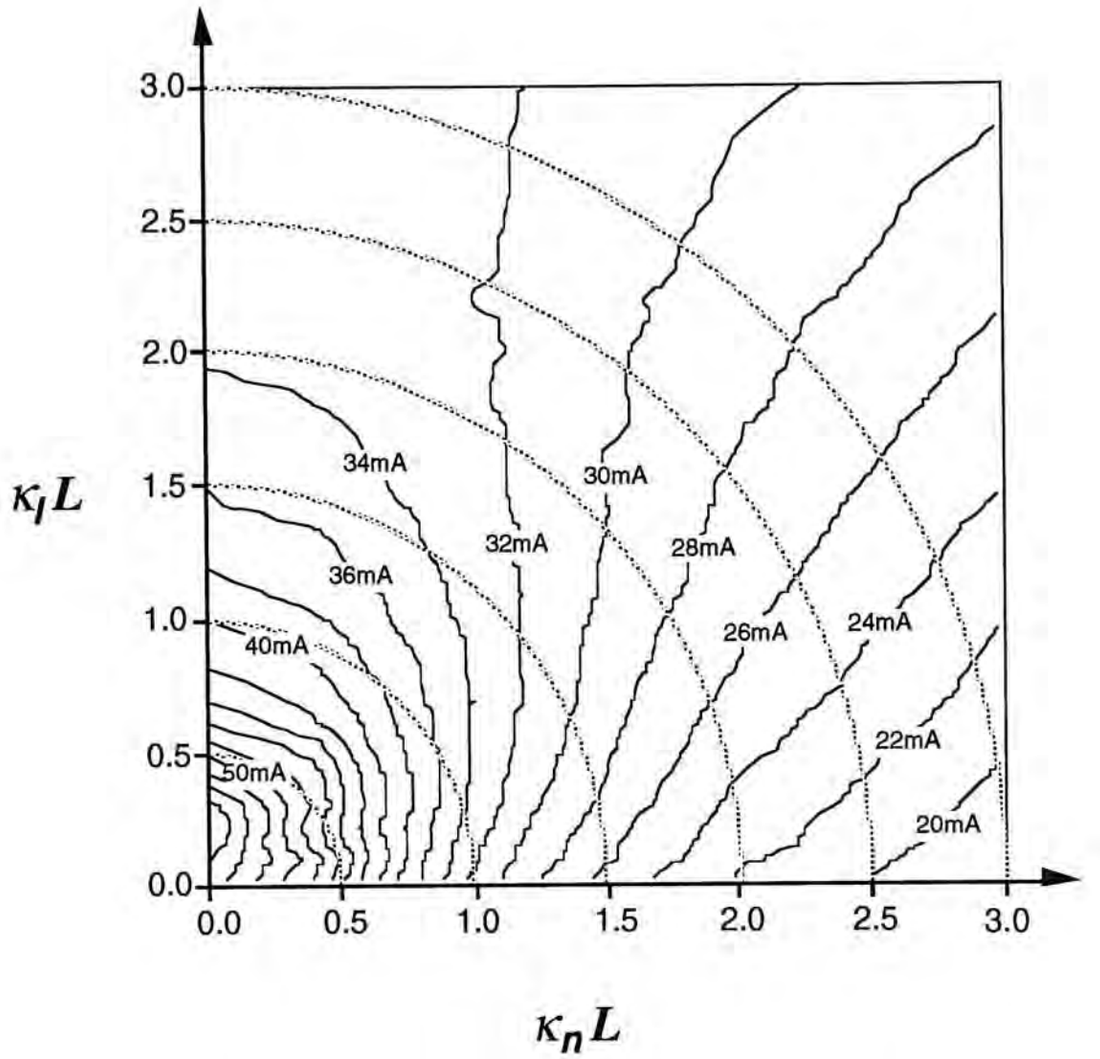

Fig. 4.9 *Contour plot of I_{th} versus $\kappa_n L$ and $\kappa_l L$ for CCDFB lasers with ρ =0.36. The arcs denote constant $|\kappa L|$.*

Grating Duty Cycle = 0.15

When the grating duty cycle is reduced to a more optimal value, $\rho = 0.15$, The general behavior of I_{th} does not change. However, the improvement in I_{th} becomes more prominent for $\kappa_l L > 0.8$ as depicted in Fig. 4.10 (to reduce the clutter, only the results at $\kappa_n L$ =0.0 and 3.0 are plotted). This improvement amounts to roughly a 10 mA reduction at large $\kappa_l L$. For purely LCDFB ($\kappa_n L$ =0.0) with AR-AR and AR-HR coatings, no minimum is observed for $\kappa_l L$ =0.0→4.0. The slopes of the other curves are also more gentle. Consequently, this grating duty cycle is a better choice for low threshold operation.

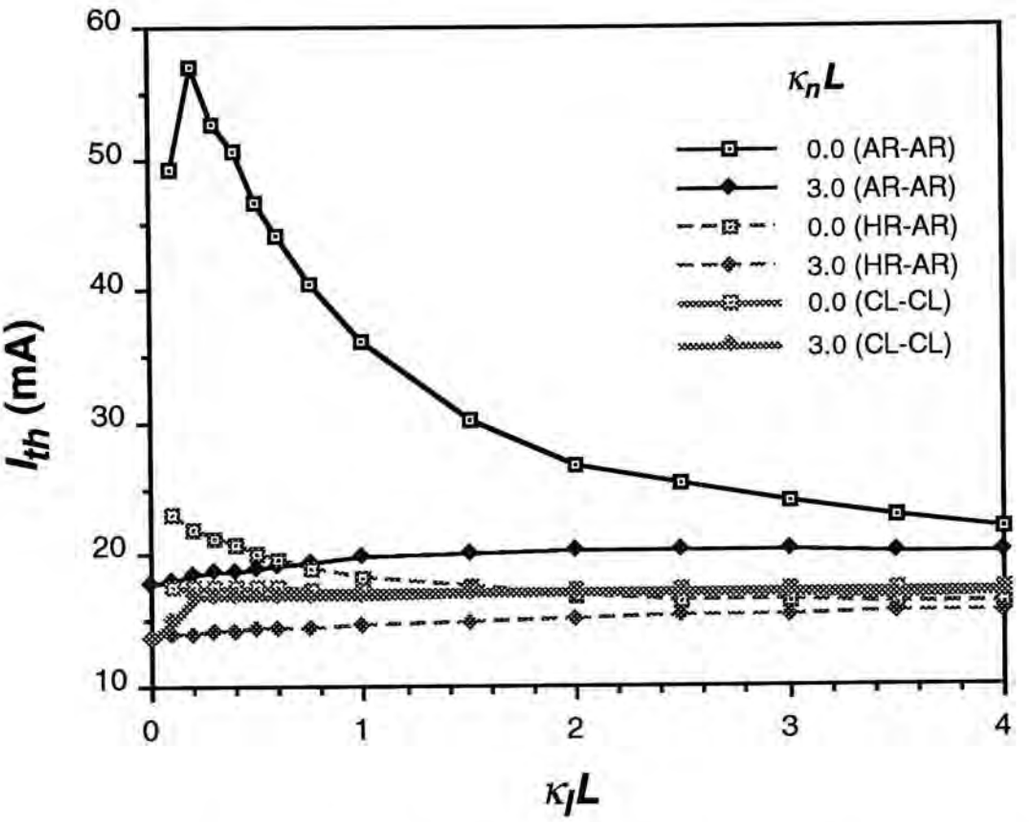

Fig. 4.10 *Threshold current as a function of $\kappa_l L$ for $\kappa_n L$ =0.0 and 3.0. The device is a CCDFB with ρ =0.15 and AR-AR (solid curve), AR-HR (broken curve) and CL-CL (lightly-shaded curve) facets.*

To emphasize this point, the contour plot of the threshold current versus $\kappa_n L$ and $\kappa_l L$ is shown in Fig. 4.11. Again, I_{th} at $|\kappa L|$=0.0 is infinite and the surrounding area is obtained by extrapolation. Compared with Fig. 4.9, the contour lines are significantly different at large $|\kappa L|$. They are much more circular, meaning that low threshold currents can be obtained even at large $\kappa_l L$. For example, at $|\kappa L|$=3.0, I_{th} only goes up by about 6 mA when the coupling mechanism is purely absorptive as compared with a change of ~13 mA when ρ =0.36. The most circular contour lines are located at $0.5 \leq |\kappa L| \leq 1.0$ where the additional loss due to the absorptive grating is relatively small. For example, I_{th} is only increased by ~3 mA at $|\kappa L|$=0.5 and by ~4 mA at $|\kappa L|$=1.0. For $|\kappa L| \leq 0.5$, the operation becomes unstable with poor mode discrimination among the lasing modes because of the weak grating.

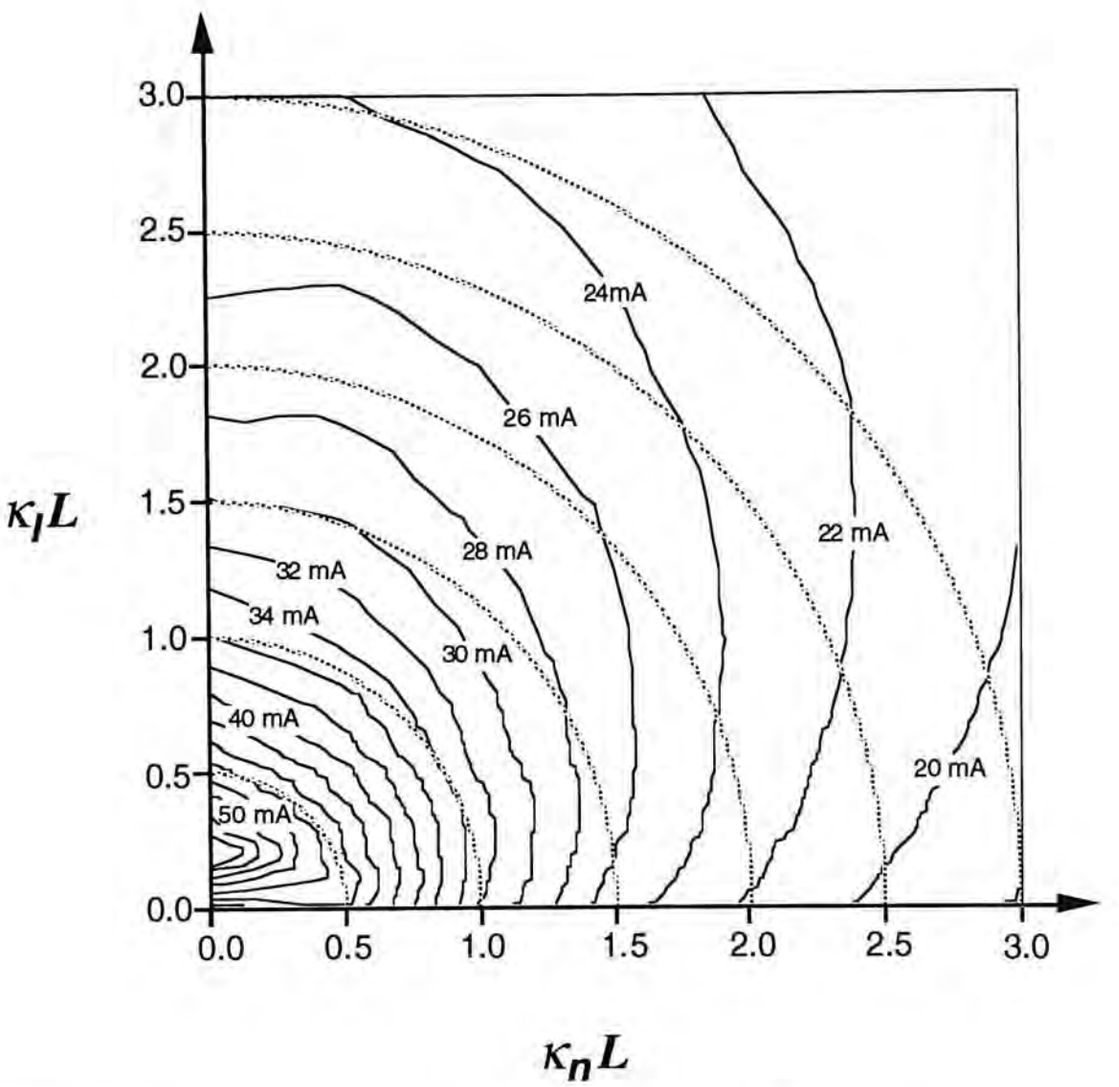

Fig. 4.11 *Contour plot of I_{th} versus $\kappa_n L$ and $\kappa_l L$ for CCDFB lasers with ρ =0.15. The arcs denote constant $|\kappa L|$.*

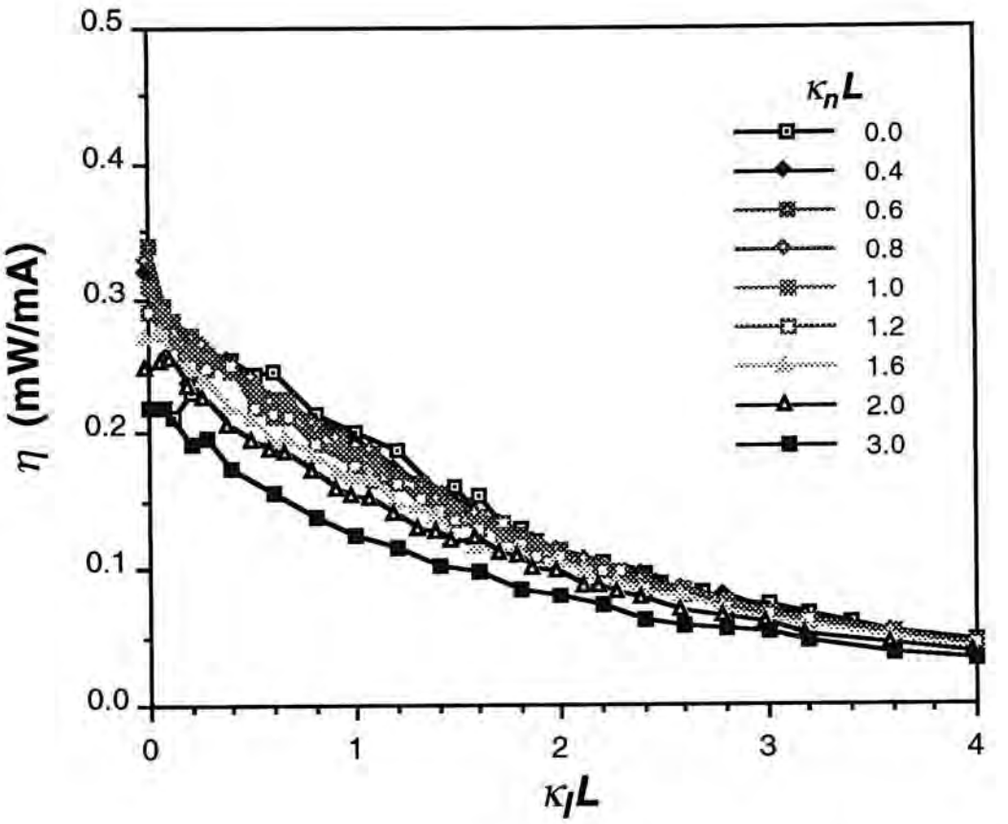

Fig. 4.12 *Front facet power efficiency as a function of $\kappa_l L$ for $\kappa_n L$ =0.0 to 3.0. The device is a CCDFB with ρ =0.36 and perfectly AR-coated facets.*

4.3.2 Power Efficiency

Power slope efficiency is another measurement of the effect of the extra loss caused by the absorptive grating in CCDFB lasers. More specifically, the front-facet power efficiency for the three sets of facet coatings are investigated.

Grating Duty Cycle = 0.36

In accordance with the previous line of reasoning, the case with $\rho = 0.36$ is presented first. The resulting η for CCDFB is shown in Fig. 4.12 (perfectly AR-AR), Fig. 4.13 (AR-HR) and Fig. 4.14 (CL-CL). It is graphed as a function of $\kappa_l L$ for various $\kappa_n L$ values. The variation in η with $\kappa_l L$ is greatest for the AR-HR case,

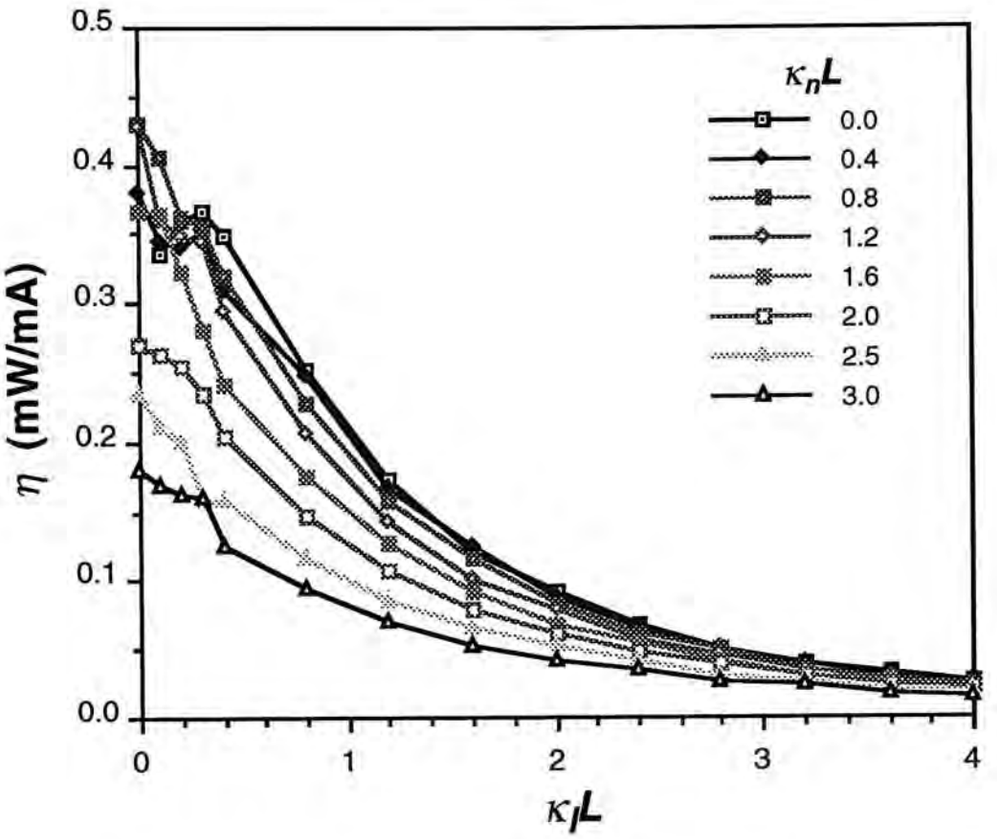

Fig. 4.13 *Front facet power efficiency as a function of $\kappa_l L$ for $\kappa_n L$ =0.0 to 3.0. The device is a CCDFB with ρ =0.36 and AR-HR coated facets.*

spanning a maximum of 25.1% for a given $\kappa_n L$. The range of η for the other two symmetric facet coatings is 12.1% (AR-AR) and 13.5% (CL-CL). These maximum variations are obtained at small $\kappa_l L$. For the case of CL-CL, the variation is less than 1% for $\kappa_l L$ >0.3, that accounts for most $\kappa_l L$. The same reason applies as given in the last section concerning the magnitude of the preexisted reflectivities.

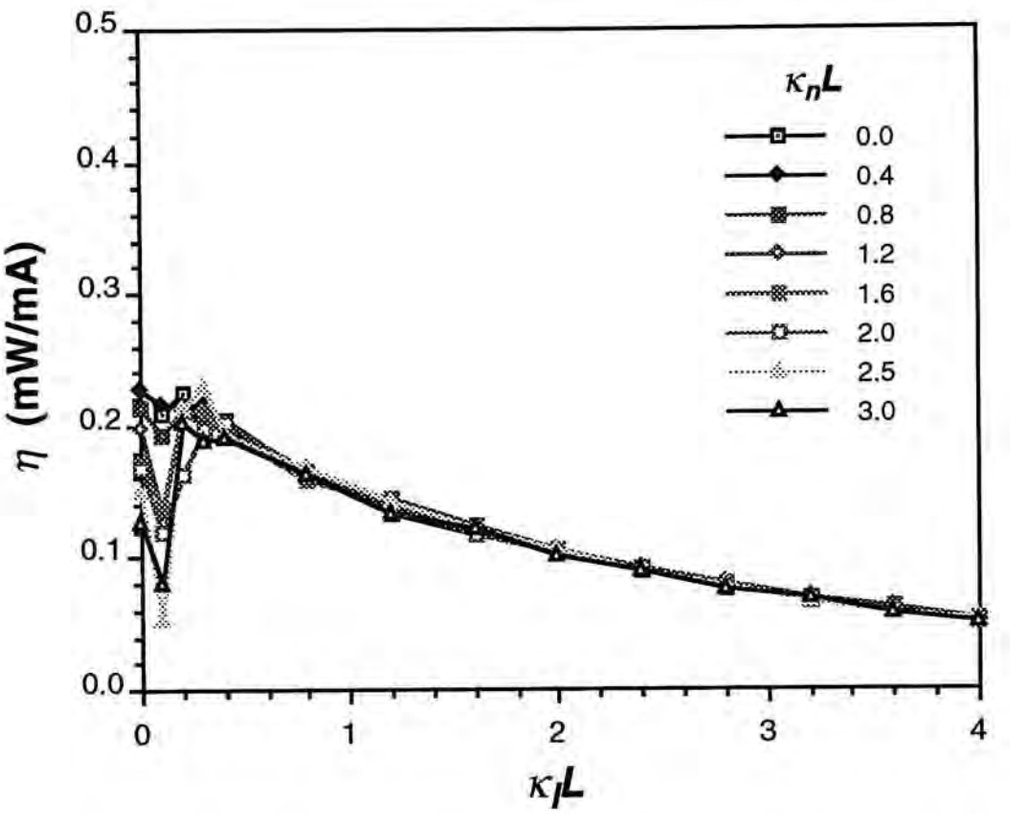

Fig. 4.14 Front facet power efficiency as a function of $\kappa_l L$ for $\kappa_n L$ =0.0 to 3.0. The device is a CCDFB with ρ =0.36 and as-cleaved facets.

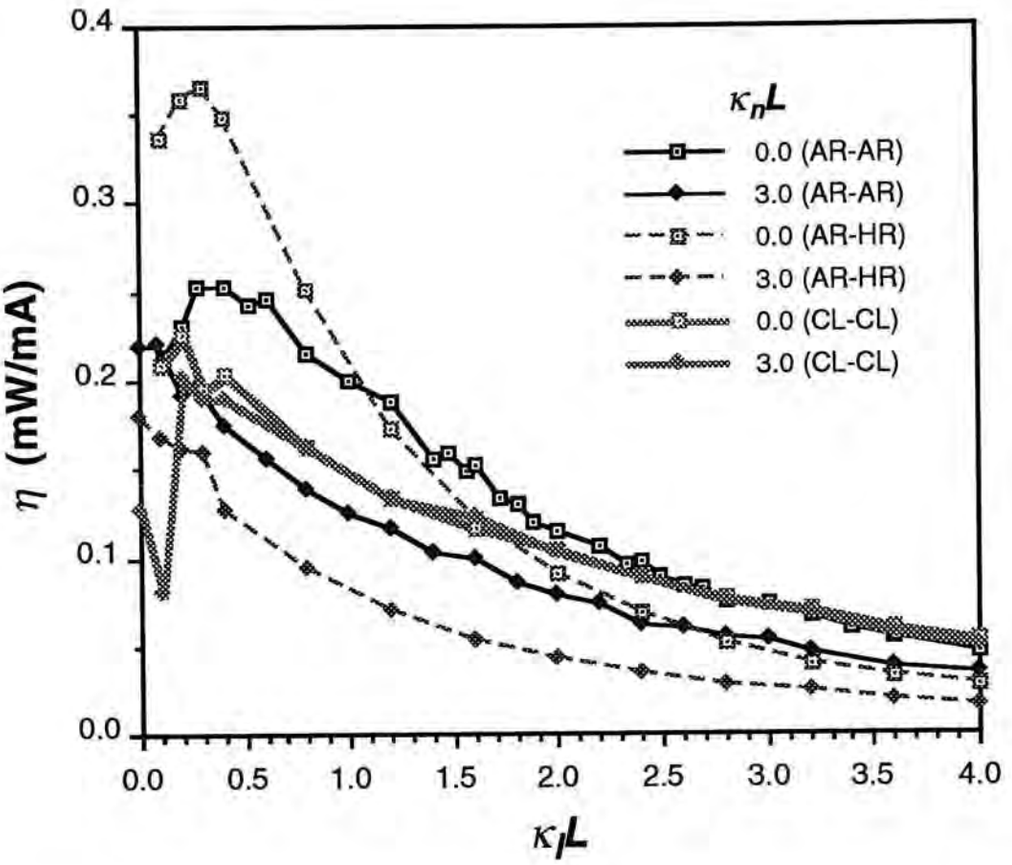

Fig. 4.15 *Front facet power efficiency as a function of $\kappa_l L$ for $\kappa_n L$ =0.0 and 3.0. The device is a CCDFB with ρ =0.36 and AR-AR (solid curve), AR-HR (broken curve) and CL-CL (lightly-shaded curve) facet coatings.*

Compared with AR-AR coatings, the use of AR-HR coatings not only lowers the threshold current (as discussed in the preceding section), it also enhances the front-facet output power efficiency. However, it is interesting that the enhancement is not for all $\kappa_n L$ and $\kappa_l L$. Figure 4.16 comprises of the last three plots showing only the results at $\kappa_n L$ =0.0 and 3.0. For purely LCDFB ($\kappa_n L$ =0.0), η for AR-HR is only larger than those for the other two cases at small $\kappa_l L$; $\kappa_l L$ =0.0→1.1 (AR-AR) and $\kappa_l L$ =0.0→1.6 (CL-CL). For AR-AR, the largest improvement (13%) occurs at $\kappa_l L$ =0.2. For CL-CL, the largest improvement (17.0%) occurs at $\kappa_l L$ =0.3 . This limited advantage slowly diminishes with increasing $\kappa_n L$.

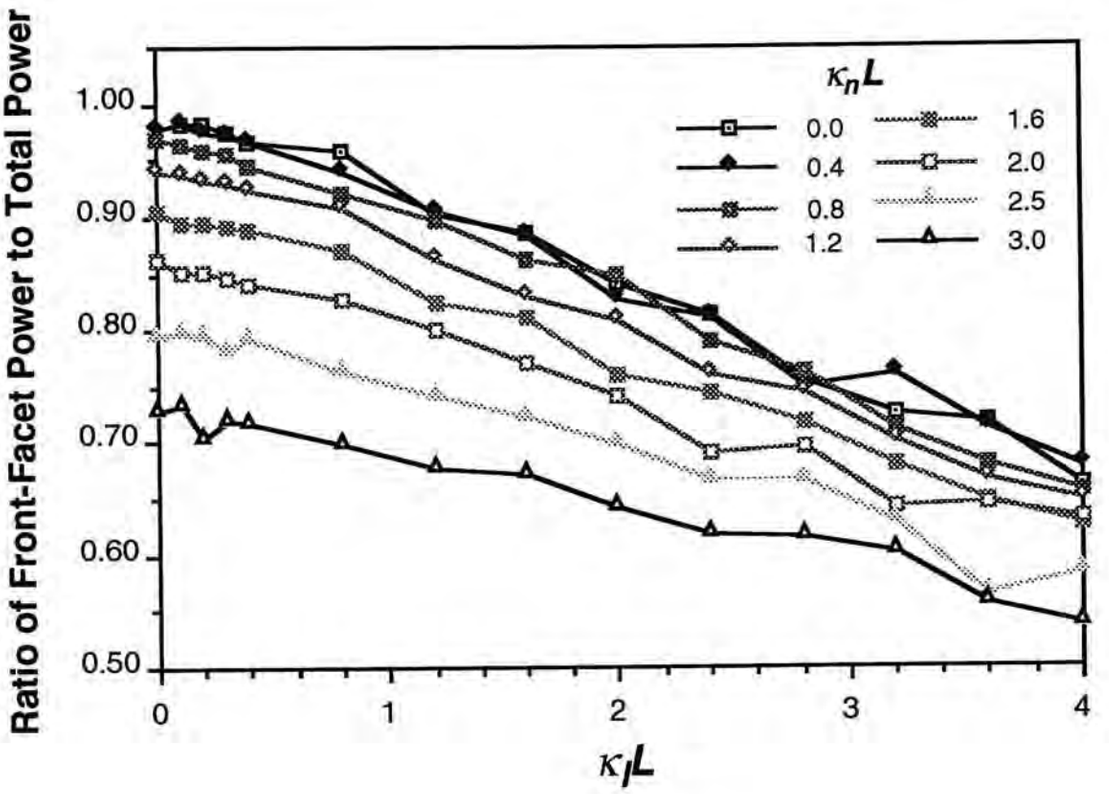

Fig. 4.16 *The ratio of the front-facet power to total power as a function of $\kappa_l L$ at various $\kappa_n L$. The device is a CCDFB laser with ρ =0.36 and AR-HR coatings.*

The dependence on the coupling coefficients can be explained by the effective reflectivity, which is dependent on both the facet and the grating reflectivities. Although AR-HR coating means 1% and 90% reflectivities at the end-facets, the actual front-facet-to-total-output-power ratio (from the 1% facet) can range anywhere from 99% down to ~50% (Fig. 4.16). The larger $\kappa_n L$ or $\kappa_l L$ is, the closer the ratio is to 50%. The reduction is caused by the increased effective reflectivities that reduces the output power. The effect is more apparent in the 1% facet output because the effective reflectivity is increased more significantly by comparison.

Despite the limited range of enhanced power efficiency, the application of AR-HR-coating is a viable method in boosting the device performance (as opposed to AR-AR or CL-CL coatings) in view of the much lower I_{th} for all κ.

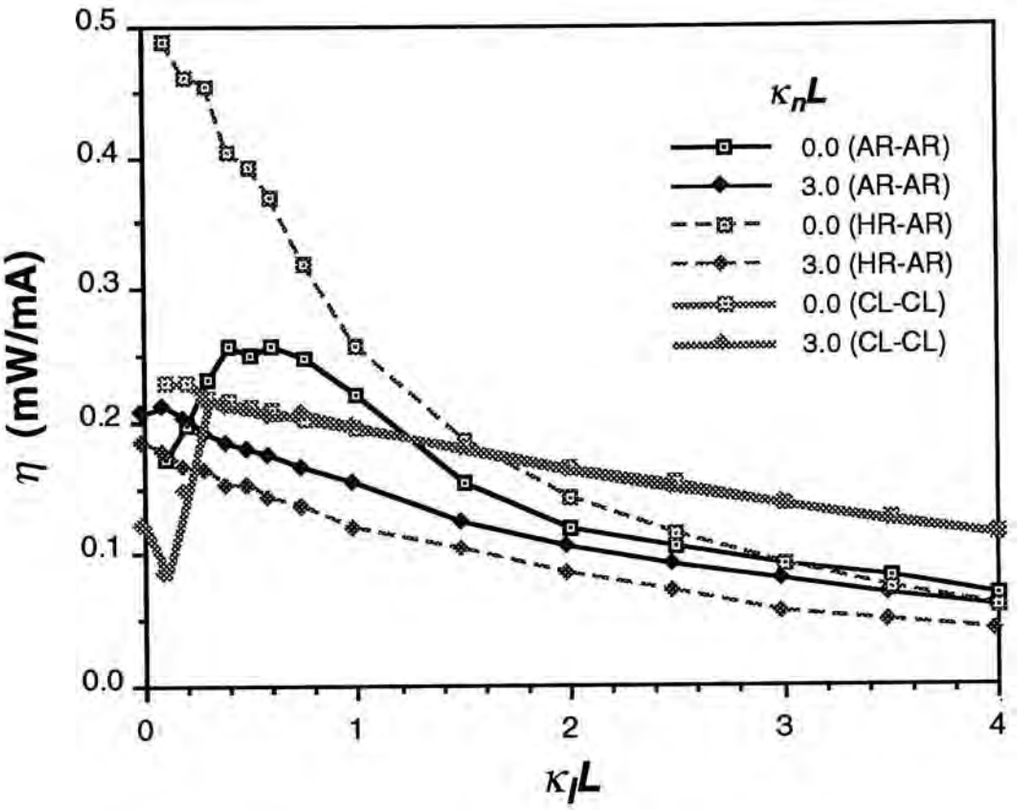

Fig. 4.17 *Front facet power efficiency as a function of $\kappa_l L$ for $\kappa_n L$ =0.0 and 3.0. The device is a CCDFB with ρ =0.15 and AR-AR (solid curve), AR-HR (broken curve) and CL-CL (lightly-shaded curve) facet coatings.*

Grating Duty Cycle = 0.15

With the reduction of extra loss through a smaller grating duty cycle (ρ =0.15), the power efficiency is improved. Much of the improvement occurs at large $\kappa_l L$ as shown in Fig. 4.17. This figure is a plot of η versus $\kappa_l L$ for three facet coatings at $\kappa_n L$ =0.0 and 3.0. The value ofη at small $\kappa_l L$ (<1.0) is very close to that at ρ =0.36. At larger $\kappa_l L$, η is about 1.5 times larger. For instance, at $\kappa_l L$ =4.0 with CL-CL coatings, η =5.4% for ρ =0.36 and η =8.4% for ρ =0.15. In any case, the trend with $\kappa_n L$ and $\kappa_l L$ hardly shows any deviation.

4.3.3 Summary

In summary, the use of an optimized ρ for CCDFB lasers has a bigger impact on I_{th} than η although both quantities show improvements. The use of AR-HR facet coatings on CCDFB gives rise to a substantial reduction in I_{th} and limited enhancement on η. The difference depends on both $\kappa_n L$ and $\kappa_l L$ with the improvement diminishes with increasing κL. In addition, we have observed instabilities at small $\kappa_l L$ due to mode degeneracy and a convergence of I_{th} and η at large $\kappa_l L$. Behaviors such as the reduced ratio of front-facet power to total power at large κL and others can be explained by the effective reflectivity. Although there is often a tradeoff between low I_{th} and high η in a given laser design, the two methods investigated here (facet coatings and grating duty cycle) have much to offer in the improvement of both of these quantities. Of course, the exact $\kappa_n L$ and $\kappa_l L$ must still be determined based on the tolerances on I_{th} and η. It should also be pointed out that the improvement in η with asymmetric coatings is not possible on conventional index-coupled DFB without significant degradation in SMSR. It is through the introduction of gain/loss-coupling that better performance is achieved [Naka92]. Furthermore, the gain/loss-coupling enhances the single-mode yield as detailed in the next section.

4.4 Yield Analysis of LCDFB and QWDFB

4.4.1 Introduction

Although the application of AR-HR coatings improves the threshold current and efficiency as shown in the preceding section, it also degrades the single-mode property of the loss-coupled DFB laser. The extent of this deleterious effect, however, is expected to be moderate [Naka92]. Since the degradation can be inferred from the expected single-mode yield, a yield analysis of the purely loss-coupled DFB (LCDFB) laser is carried out. Both the purely LCDFB and the index-coupled QWDFB lasers are examined. The CCDFB laser is not investigated since the addition of index-coupling is already known to degrade the yield [Davi91b]. As discussed in *Section 2.4.2*, for DFB lasers, the uncertainty arises from the fact that the grating phase at the cleaved facet is random and uncontrollable. This phase angle can have a positive or negative effect on the laser performance and its sensitivity varies with different laser designs. The yield is therefore a good indicator of the robustness of the design and its manufacturability.

The devices with the same three sets of facet coatings (AR-AR with 1% reflectivities, AR-HR with 1% and 90% reflectivities and CL-CL with 32% reflectivities) are studied.

In the analysis that follows, the yield is computed based on three criteria:

(1) single-mode quality: the product of the threshold gain margin and cavity length is greater than or equal to 0.3 ($\Delta g_{th} L \geq 0.3$);

(2) LSHB: the variance of the photon density distribution is less than or equal to 0.1 ($\sigma_{\psi} \leq 0.1$); and

(3) the threshold current is less than or equal to 35 mA ($I_{th} \leq 35$ mA).

The requirement that $\Delta g_{th} L \geq 0.3$ is stringent. It is because $\Delta g_{th} L > 0.05$ is regarded as adequate in realizing single-longitudinal-mode operation in 1.6 Gbits/s

optical communication systems. Conventional index-coupled DFB lasers with cleaved facets generally have $\Delta g_{th} L < 0.1$. The second criterion ($\sigma_\psi \leq 0.1$) is important and was first suggested by David, *et. al.* [Davi91b]. It provides a better fit between theoretical prediction and experimental results. It is also a stringent requirement since a laser with $\sigma_\psi \geq 0.3$ may be regarded as having strong LSHB. In [Davi91b], the LSHB criterion is expressed in terms of a factor f which is the ratio of the minimum to maximum power density along z (*see also Section 2.5*). Although the two definitions are principally different, by comparison of the calculated results, $\sigma_\psi \leq 0.1$ appears to be closely related to $0.2 < f < 0.4$. Finally, our yield results indicate that 12.8 mA$\leq I_{th} \leq$42.7 mA for QWDFB and 16.8 mA$\leq I_{th} \leq$53.8 mA for LCDFB lasers. The threshold current criterion ($I_{th} \leq$35 mA) is chosen because 35 mA is roughly the median value for the LCDFB lasers. More stringent criteria are chosen so as to better reflect the disparity in performances.

A closely-related analysis was reported by David *et. al.* [Davi91b], [Davi90]. His focus is on the yield of the GCDFB with AR-AR and CL-CL coatings. The yield is adjusted for LSHB and the threshold criterion is not applied. Another report on the yield of a multiple phase-shifted DFB laser (including QWDFB and LSHB) can be found in [Kino89]. As discussed in the previous section, the use of AR-HR coatings is capable of improving the power efficiency and the threshold current of CCDFB. In this work, the emphasis is on LCDFB in an effort to investigate if the single-mode yield suffers or improves as a result of the facet coatings. As a comparison, it is known that asymmetric facet coating severely lowers the single-mode yield of index-coupled DFB lasers; in particular, the QWDFB lasers. Furthermore, a more sophisticated description of κ_l that includes the large photon density suppression is employed. The analysis on QWDFB is performed for comparison purposes. In general, the yield of QWDFB is strongly dependent on its facet coatings. For example, perfectly AR-coated QWDFB shows a high yield which rapidly deteriorates

with reflectivities of only a few percent [Kino89]. In contrast, the yield of LCDFB is less affected.

4.4.2 Method

We have calculated $\Delta g_{th} L$, σ_ψ and I_{th} for LCDFB and QWDFB devices with each of the three facet coatings for various $\kappa_l L$ (for LCDFB) and $\kappa_n L$ (for QWDFB). The parameter values are the same as those in Table 4.1 with the exception that the number of segments is 15. Since ρ =0.15 is a value that is likely to be selected for real LCDFB lasers, this value is assumed in this yield analysis. For QWDFB, the quarterwave phase-shifter is centrally placed in the cavity. Values of $\kappa_l L$ and $\kappa_n L$ (or κL for the rest of the section) are varied from 0.5 to 4.0 in steps of 0.5 or smaller. The random phases of the facet reflectivities are simulated with 20×20 combinations (20 increments from 0 to 2π radians for each facet). In practice, only a smaller number of calculations is needed because of symmetry. For each phase combination, the linear model is invoked to compute the optical spectrum until the thresholds of the two lowest-loss modes (the lasing mode and the most dominant side mode) are reached. The $\Delta g_{th} L$ of these two modes as well as the σ_ψ and I_{th} for the lowest-loss mode are noted. Once all the combinations are accounted for, the yield (probability) is calculated by imposing the aforementioned criteria.

In general, the yield is higher for devices with lower facet reflectivities. The reason is the reduced mode competition from the Fabry-Perot modes caused by the end-mirrors. The $\Delta g_{th} L$ criterion usually favors devices with relatively large κL . By applying the LSHB or the I_{th} criterion simultaneously, the yield is altered in opposing ways along κL (with the LSHB criterion lowers the yield at large κL). It may be interesting to see (in the following section) how the yield of the devices with highly asymmetric facet coatings (e.g. AR-HR) is modified when subjected to the LSHB

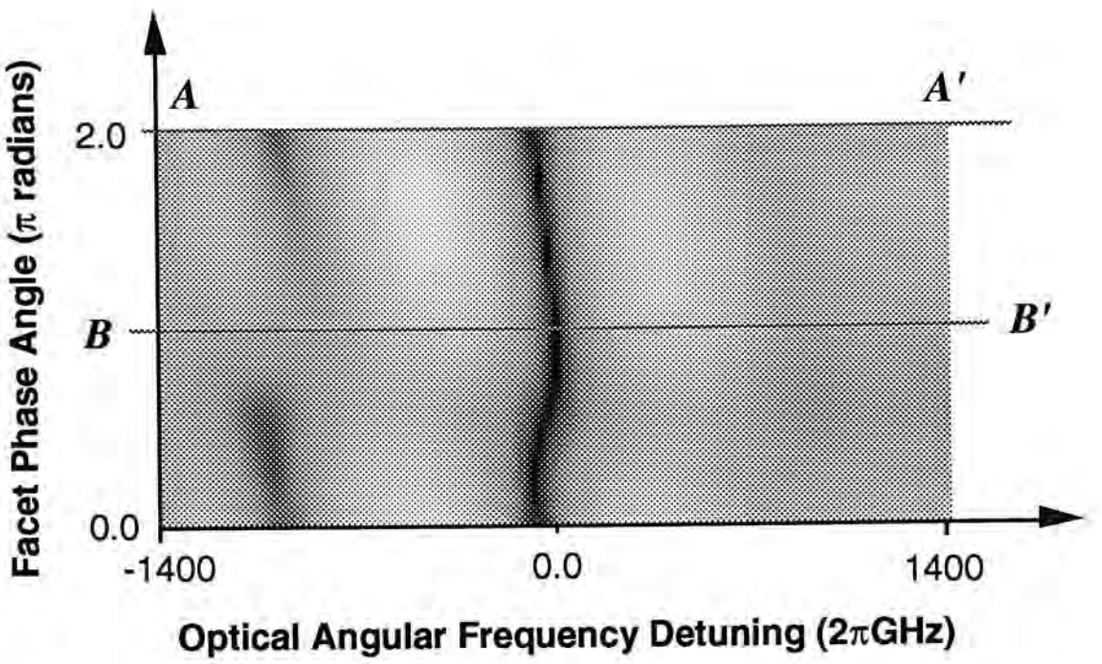

Fig. 4.18a *Optical spectrum as a function of one of the facet phase angles for a QWDFB laser with κL =1.25 and AR-AR coatings. The phase angle of the other facet is fixed at 0.0. The dominant mode shifts only slightly from zero detuning with respect to the phase angle.* ***A—A'*** *and* ***B—B'*** *mark the cross-section locations where the spectrum is plotted in the Fig. 4.18b and Fig. 4.18c, respectively.*

criterion because the photon density distribution is rather inhomogeneous even at small κL .

4.4.3 Results

Facet Phase Angle

Before the yield data is shown, a brief look at how the laser performance changes with the facet phase angle (i. e. grating phase angle at facet) is in order. A report on the facet phase influence on the wavelength shift can be found in [Hill94a].

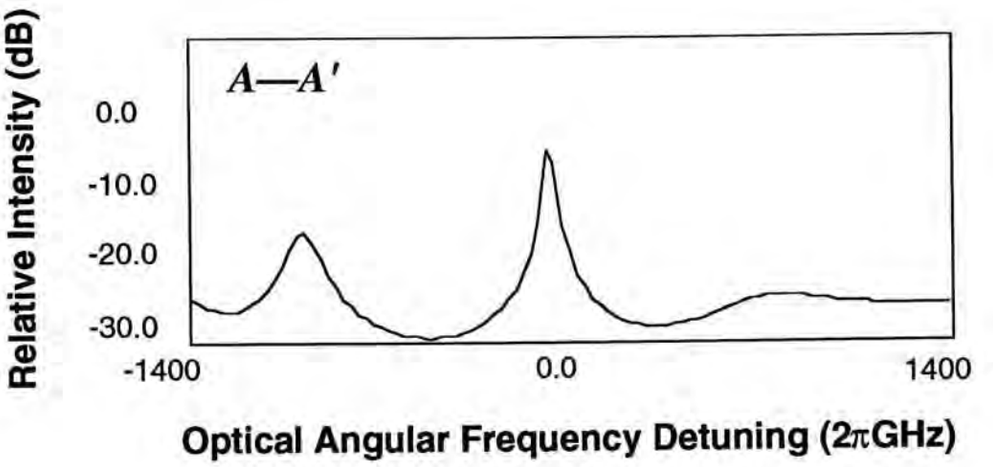

Fig. 4.18b Optical spectrum along A—A' (facet phase angle=0.0 or 2π) as indicated in Fig. 4.18a.

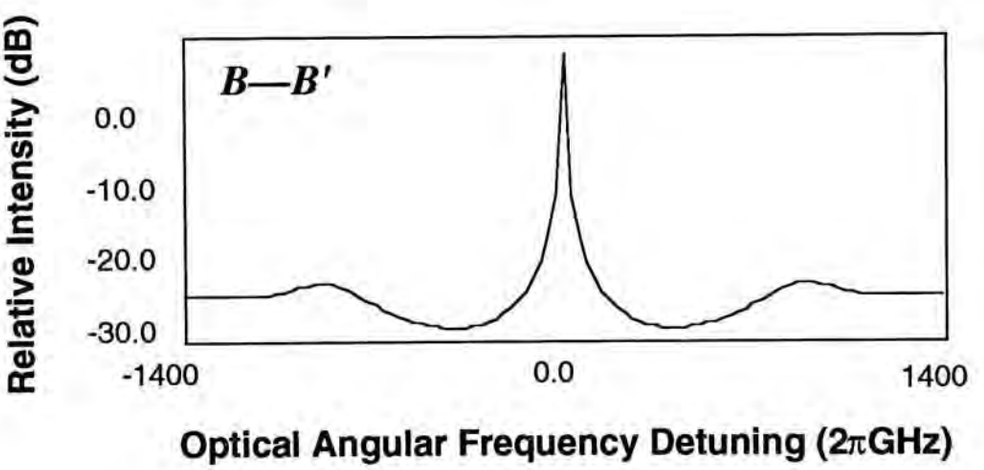

Fig. 4.18c Optical spectrum along B—B' (facet phase angle=0.0 or 2π) as indicated in Fig. 4.18a.

The first example is one that exhibits minor changes when the phase angle of one facet varies from 0.0 to 2π (shown in Fig. 4.18a). The phase of the other facet is fixed at 0.0. This laser is a QWDFB with κL =1.25 and AR-AR facet coatings; the photon density distribution is known to be relatively flat. The dominant mode (indicated by the darkest shade) is located close to zero detuning despite the change in

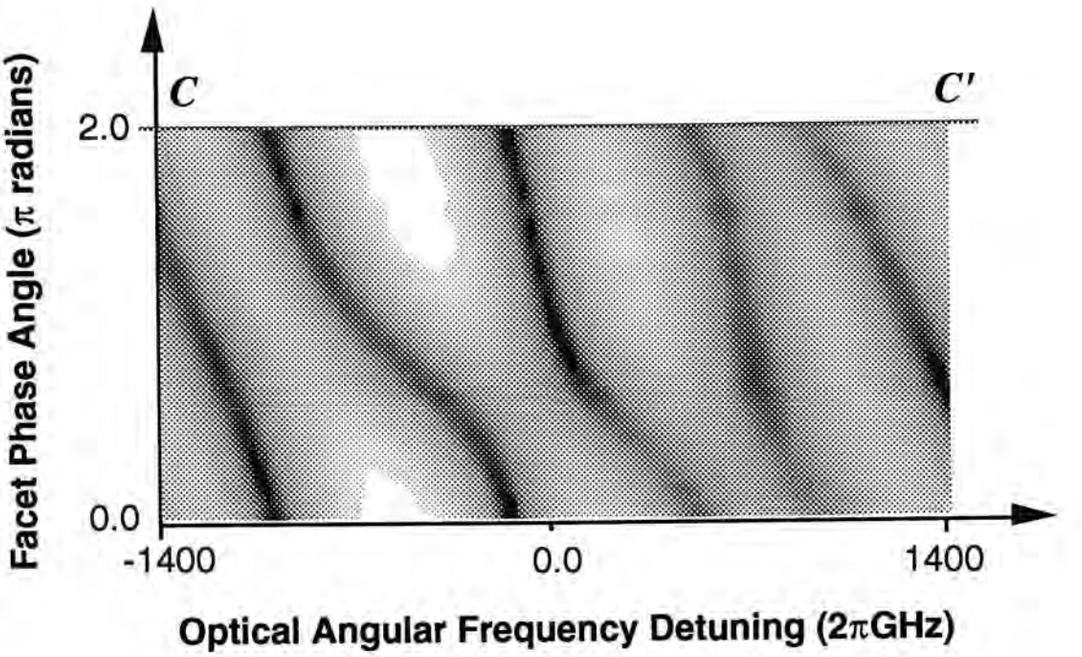

Fig. 4.19a *Optical spectrum as a function of one of the facet phase angles for a QWDFB laser with κL =1.25 and as-cleaved facets. The phase angle of the other facet is fixed at 0.0. The spectrum at* ***C—C'*** *is plotted in Fig. 4.19b.*

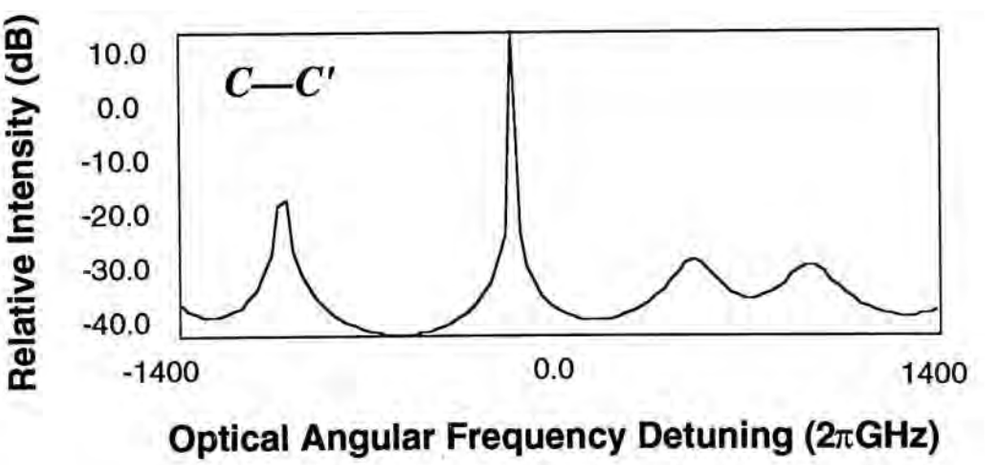

Fig. 4.19b *Optical spectrum along* ***C—C'*** *(facet phase angle=0.0 or 2π) as indicated in Fig. 4.19a.*

the facet phase angle. The intensity versus the optical frequency at 2π (marked by ***A—A'***) and π (marked by ***B—B'***) are graphed in Fig. 4.18b and Fig. 4.18c, respectively. The SMSR is larger at π.

Another example of the effect of facet phase angle is one that exhibits a much larger frequency shift with changes in the phase angle of one facet (Fig. 4.19a). This device is the same QWDFB laser except that the facets are now as-cleaved (CL-CL). The corresponding spectrum at 2π (marked by ***C—C'*** in Fig. 4.19a) is plotted in Fig. 4.19b. It reveals higher asymmetry and more side-modes because of the residual facet reflectivities. The dominant mode is shifted by more than 10.7 Å (133.7 GHz) compared with the ~1 Å displacement experienced by the QWDFB with AR-AR coatings (in the previous example). This phenomenon is important because this spectral behavior is found to be correlated with the single-mode yield in which larger frequency displacement is usually accompanied by poorer single-mode yield.

Quarterwave Phase-Shifted DFB Laser

The yield results for a QWDFB laser are shown in Fig. 4.20, Fig. 4.21 and Fig. 4.22 for AR-AR, CL-CL and AR-HR coatings, respectively. As expected, the single-mode yield for the AR-AR case is close to or equal to 100% (κL >1.5) when the only criterion is $\Delta g_{th} L$ (Fig. 4.20). However, a dramatic reduction takes place when the LSHB requirement is imposed. For κL >2.5, the yield is almost zero, indicating that the hole burning effect is very severe in this region. Although κL =1.25 gives the most uniform photon density distribution, it does not result in the highest single-mode yield partly because the grating is relatively weak and that the yield is also dependent on the exact LSHB criterion. A further enforcement of the threshold current criterion for this and the other two sets of facet coatings does not change the results in any ways. Therefore, it can be concluded that the first two requirements have successfully discriminated against those devices with high thresholds. The yield is 100% at κL =1.75 at its maximum and then deteriorates very rapidly with deviations in κL. Therefore, it can be inferred that high yield is difficult to achieve in index-coupled QWDFB lasers in practice.

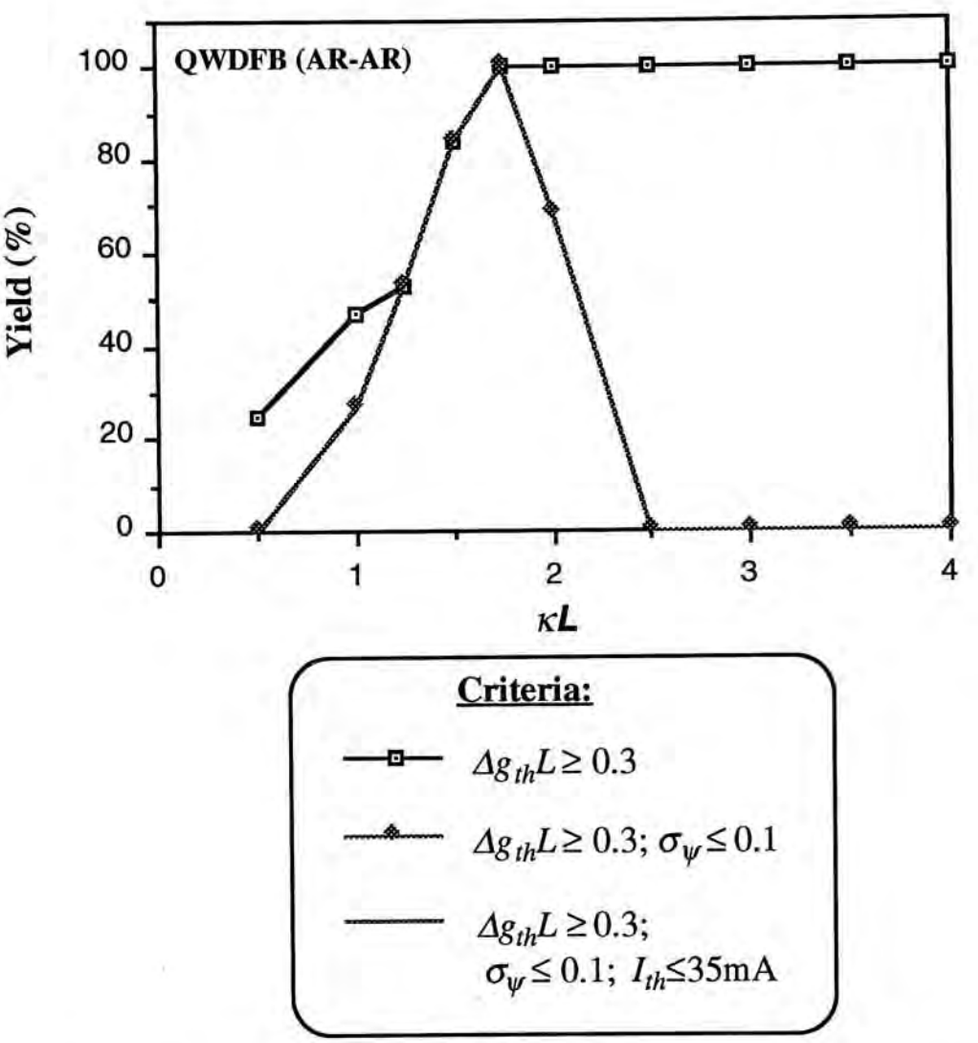

Fig. 4.20 *The yield for the QWDFB laser with AR-AR coatings as a function of* κL *when subjected to the three criteria.*

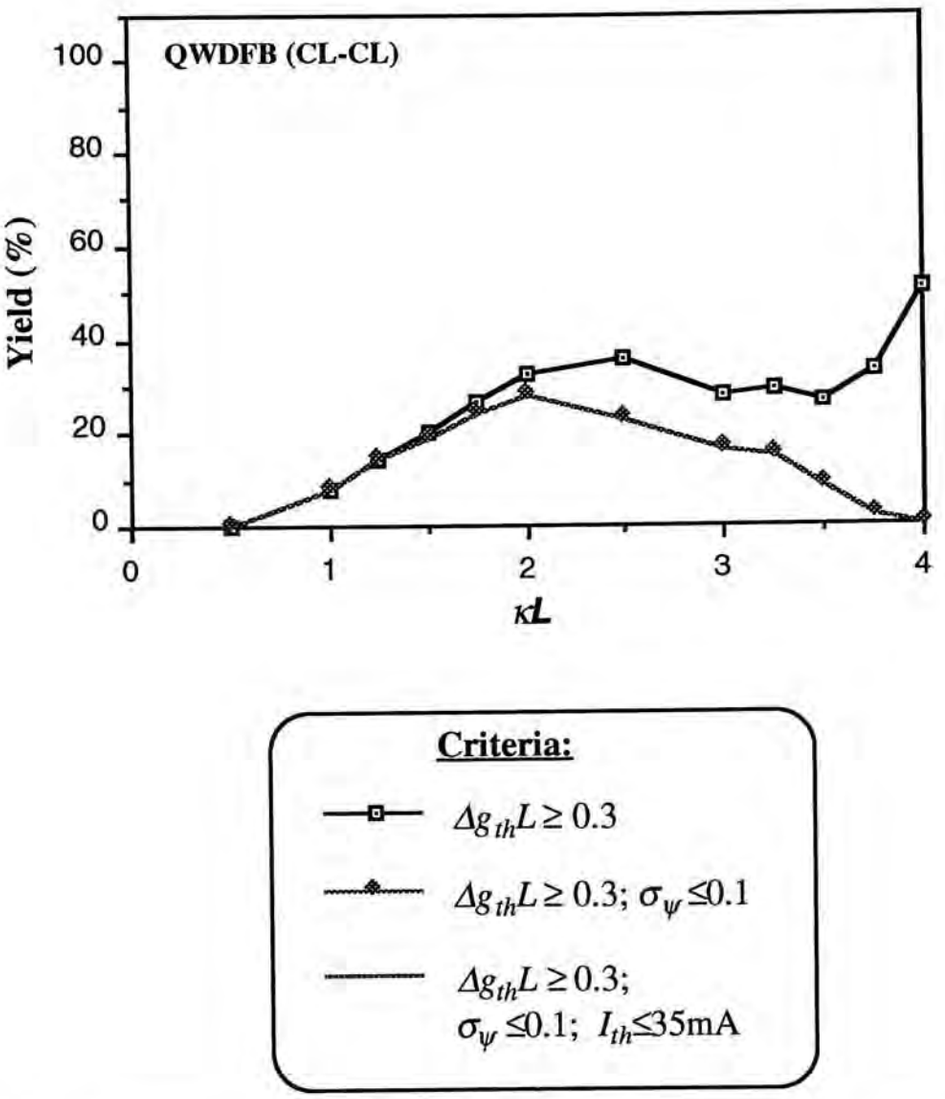

Fig. 4.21 *The yield for the QWDFB laser with as-cleaved facets as a function of κL when subjected to the three criteria.*

For the as-cleaved QWDFB lasers, with the $\Delta g_{th} L$ criterion, the yield is less than 40% except at κL =4.0, at which the yield is 50.5%. The rise in single-mode yield for κL >3.5 may be a result of the stronger optical feedback by the diffractive grating as opposed to that by the facets. With the addition of the $\sigma_\psi \leq 0.1$ requirement, the maximum yield is reduced to below 30% (28% at κL =2.0).

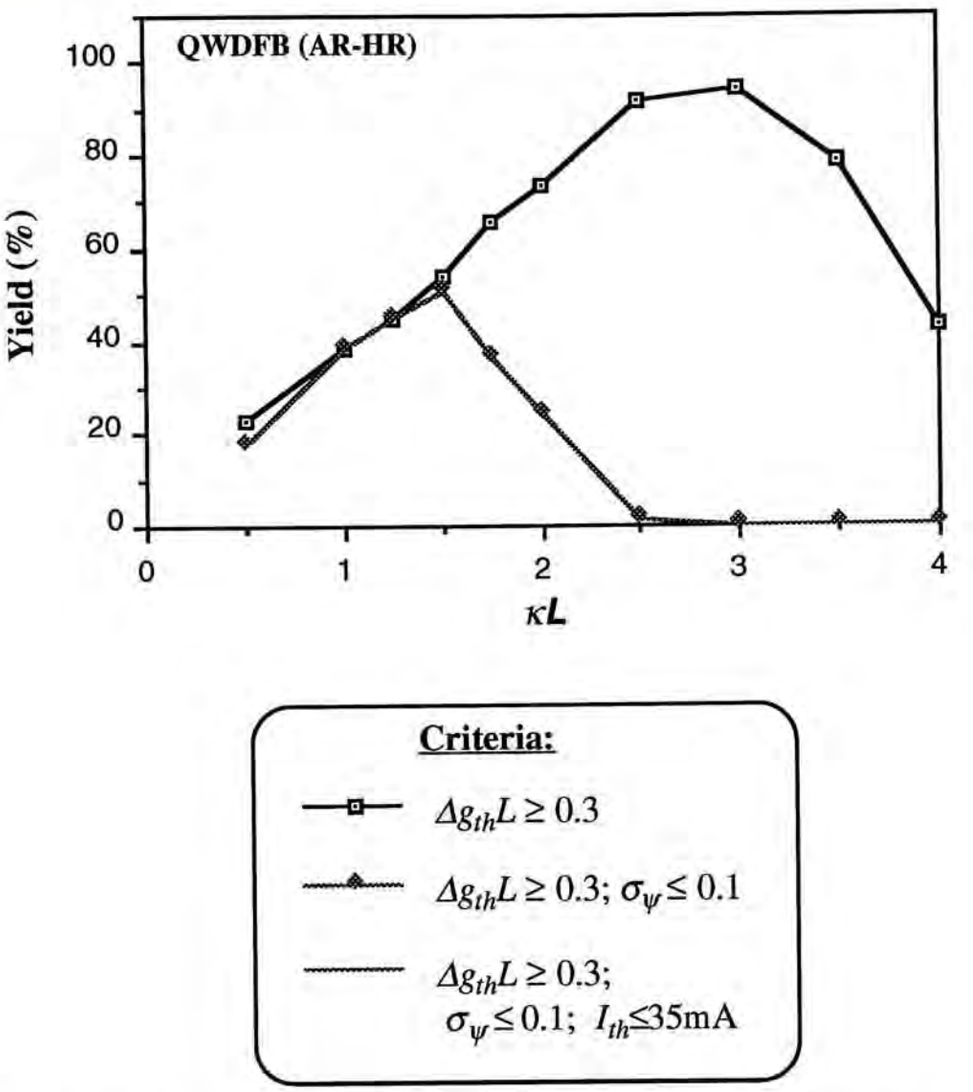

Fig. 4.22 *The yield for the QWDFB laser with AR-HR coatings as a function of κL when subjected to the three criteria.*

For AR-HR coated QWDFB, the single-mode yield peaks at κL =3.0 with a value of 94.5% when the $\Delta g_{th} L$ criterion is imposed. This result is much better than the yield of the as-cleaved QWDFB. However, with the addition of the $\sigma_\psi \leq 0.1$ requirement, its maximum value is reduced to 51.0% at κL =1.5.

It is clear from the data that facet reflectivities plays an important role in the yield of QWDFB lasers. It also indicates that the yield is very sensitive to κL which makes good yield difficult to achieve in practice. In addition, it shows that LSHB is very strong in QWDFB lasers and has to be taken into account. This analysis is in good agreement with the reports found in the literature. A direct comparison can be made

for the QWDFB with AR-AR coated facets with [Davi91b] in which the criterion $\Delta g_{th} L \geq 0.3$ is also used. The functional dependence of the yield on κL is in good agreement (see Fig. 5d of [Davi91b]). This comparison further validates our DFB model (see *Section 2.5*).

Loss-Coupled DFB Laser

The single-mode yield of the LCDFB laser is computed with the same set of criteria. The results for AR-AR, CL-CL and AR-HR coatings are shown in Fig. 4.23, Fig. 4.24 and Fig. 4.25, respectively. All three graphs indicate good yield over a broad range of κL which is in sharp contrast with that of the index-coupled QWDFB lasers.

The best yield is achieved with two AR-coated facets as expected (Fig. 4.23). The percentage yield is 100% for $\kappa L \geq 1.0$ when the probability is calculated based on $\Delta g_{th} L \geq 0.3$. With the additional criteria, $\sigma_\psi \leq 0.1$ and $I_{th} \leq 35$ mA, the yield is reduced at both small and large κL values. The reason is the inhomogeneous photon density distribution at large and small κL and the high threshold current at small κL. The photon density distribution at small κL tends to have a minimum in the center of the laser cavity because of relatively weak grating reflectivities. As a result, the yield with the LSHB criterion is reduced in this region. Nevertheless, perfect yield can still be obtained in the region: $2.0 \leq \kappa L \leq 3.0$.

For LCDFB lasers with as-cleaved facets, perfect yield is possible at $\kappa L \geq 2.75$ under the condition: $\Delta g_{th} L \geq 0.3$ (see Fig. 4.24). The maximum yield is reduced to 97.3% at $\kappa L = 2.25$ when the additional LSHB criterion is imposed. While the yield at $\kappa L \leq 2.25$ remains unchanged, it is drastically reduced at large κL. For example, the yield drops from 100% to 22.3% at $\kappa L = 4.0$. The maximum yield is reduced further to 87.3% at $\kappa L = 2.25$ when $I_{th} \leq 35$ mA is required simultaneously. The threshold criterion only lowers the yield at mid-range values of κL from 1.5 to 3.0 and the

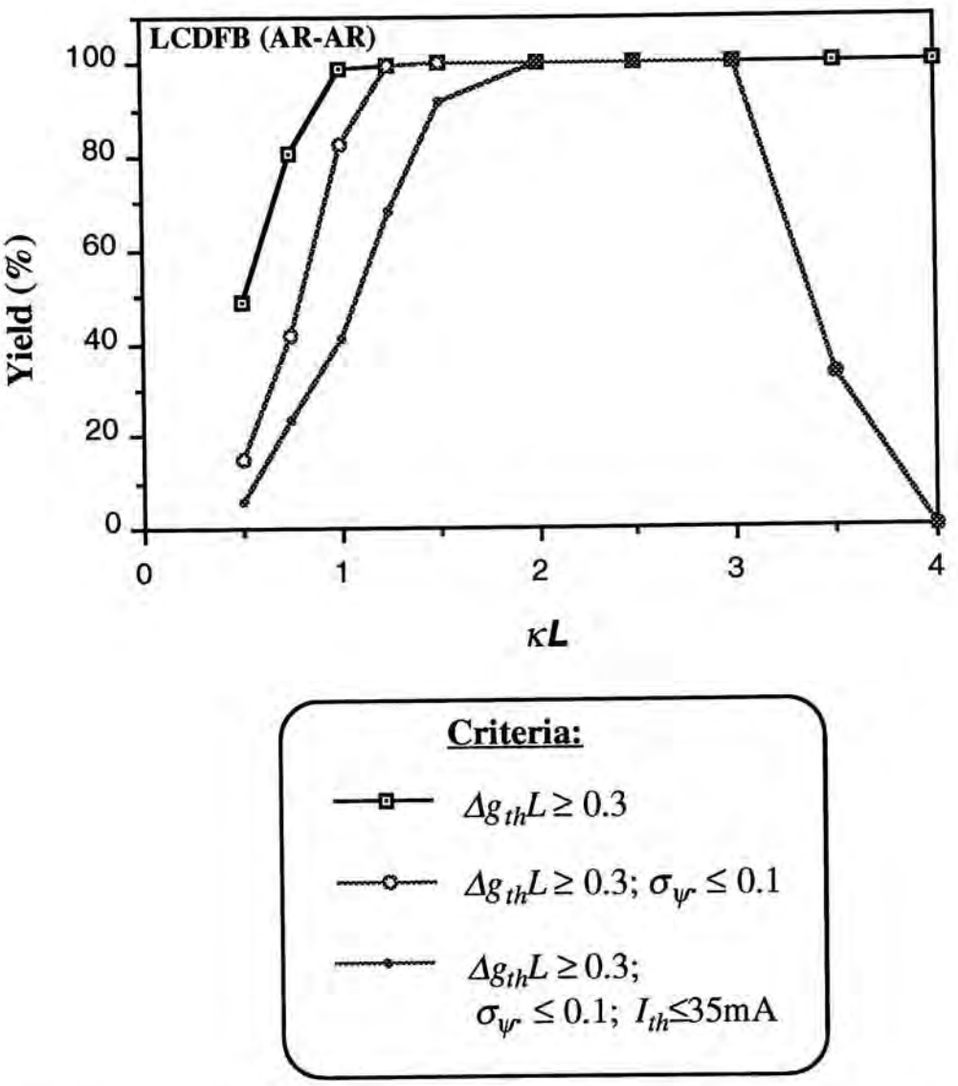

Fig. 4.23 *The yield for the LCDFB laser with AR-AR coatings as a function of κL when subjected to the three criteria.*

reduction is less than or equal to 10.5%. Good yield is obtainable over a broad range (e. g. yield ≥ 60% for $1.0 \leq \kappa L \leq 3.2$). It should be noted that Fig. 4.24 agrees quite well with Fig. 14 in [Davi91b] in which a purely gain-coupled DFB laser is also analyzed.

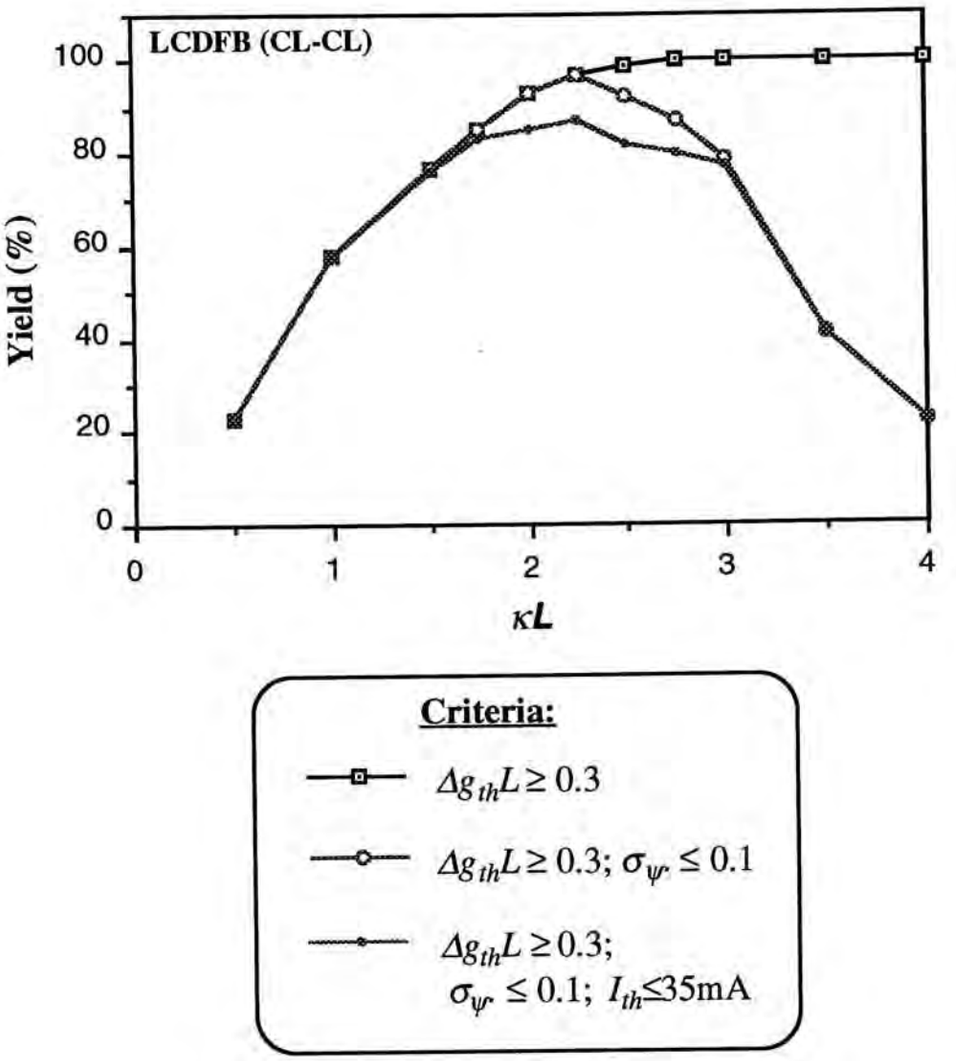

Fig. 4.24 *The yield for the LCDFB laser with as-cleaved facets as a function of* κL *when subjected to the three criteria.*

The most interesting case is the purely LCDFB lasers with AR-HR coatings. Its single-mode yield is shown in Fig. 4.25. With only the first criterion, $\Delta g_{th} L \geq 0.3$, the yield is not very different from those of the other two cases with symmetric facet coatings. Perfect yield is possible at large κL (≥ 2.5). When both the first and the LSHB criteria are imposed, three regions suffer reduction. Minor decrease (~7%) is seen at $\kappa L = 0.5$. Moderate changes (up to 25%) occur in the mid-κL region ($1.7 < \kappa L \leq 3.0$) and sharp reduction is observed for $\kappa L \geq 3.0$. The yield is down from 100% to 18% at $\kappa L = 4.0$. The first two regions are more strongly influenced by the highly asymmetric facet coatings and the last region is affected more by the grating.

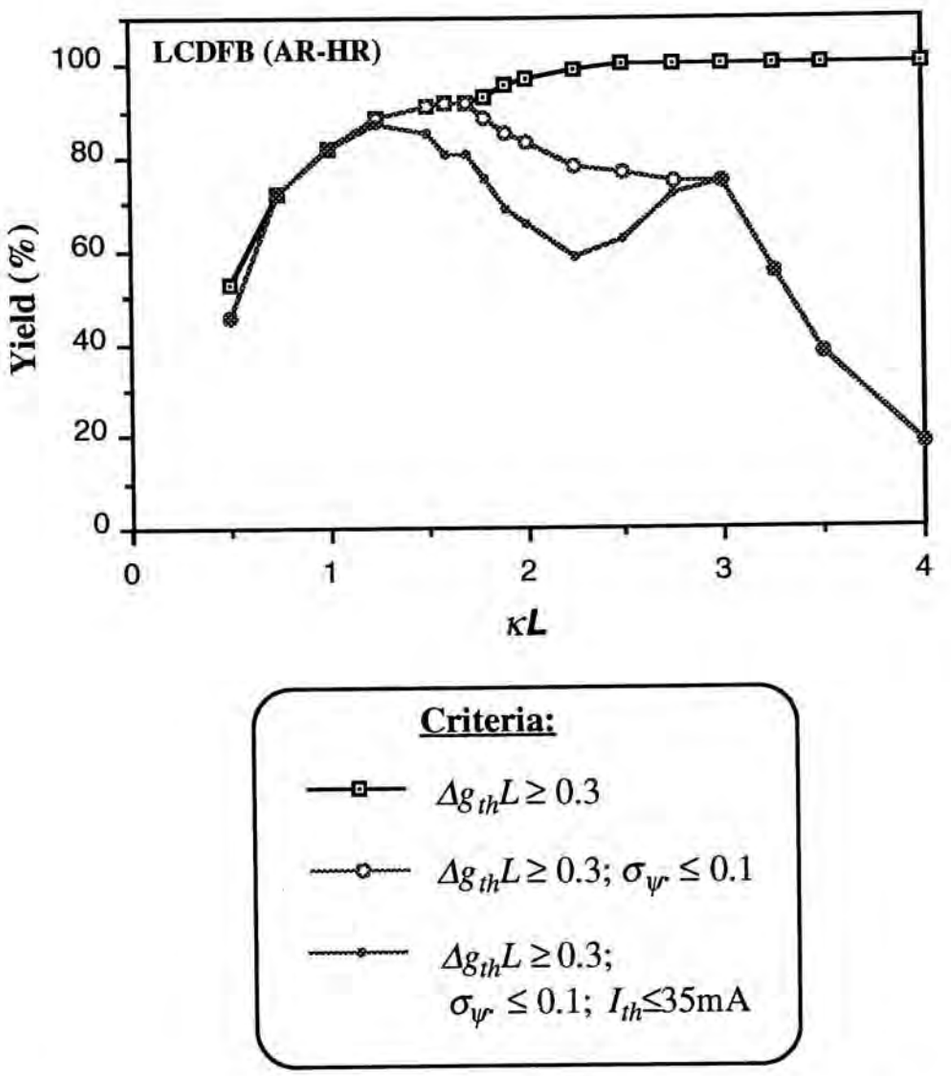

Fig. 4.25 *The yield for the LCDFB laser with AR-HR coatings as a function of κL when subjected to the three criteria.*

The same reasoning for the QWDFB laser also applies here. Interestingly, when additional requirement, $I_{th} \leq 35$ mA, is imposed, the curve becomes double-lobed indicating two regions with higher yield. The peaks, 87.5% and 75%, are located at $\kappa L = 1.25$ and $\kappa L = 3.0$, respectively. Again, the threshold criterion only lowers the yield at mid-κL region ($1.0 \leq \kappa L \leq 3.0$) while leaving the rest unchanged. It can be inferred that devices in this region have a significant portion of its loss derived from the absorptive grating, which is not completely compensated by the increase in the effective reflectivities.

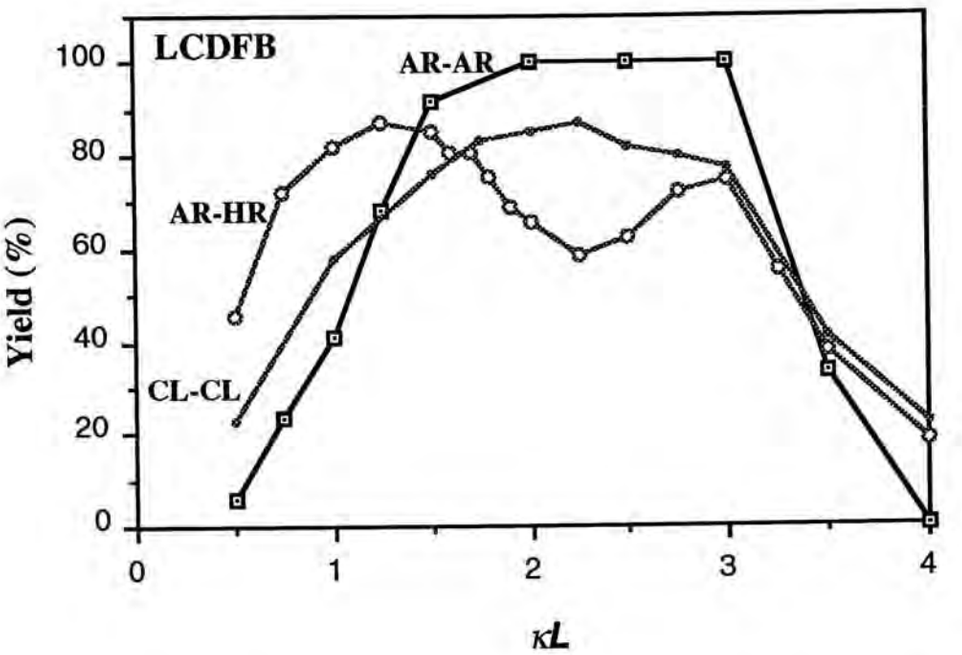

Fig. 4.26 *Yield results for purely LCDFB lasers with AR-AR, AR-HR and CL-CL facets that have been subjected to three simultaneous criteria:* $\Delta g_{th} L \geq 0.3$; $\sigma_\psi \leq 0.1$ *and* $I_{th} \leq 35$ *mA.*

To see more clearly the differences in yield for the three sets of facet coatings, the results that have been subjected to the three criteria are plotted again in Fig. 4.26. They are taken from Fig. 4.23, Fig. 4.24 and Fig. 4.25. Although lasers with AR-AR coatings have perfect yield at $2.0 \leq \kappa L \leq 3.0$, those with AR-HR and CL-CL facets have better yield at small κL ($\kappa L \leq 1.0$) as well as at large κL ($\kappa L \geq 3.5$). This result, together with those from the above-threshold analysis, points to the important advantages of using asymmetric facet coatings (such as AR-HR) in CCDFB lasers. Recall that the AR-HR-coated CCDFB lasers have significantly larger front-facet power efficiency than those of AR-AR-coated or as-cleaved CCDFB lasers, especially in the region of small $\kappa_l L$ (≤ 1.5, approximately). In addition, I_{th} is also much smaller than that of AR-AR-coated CCDFB and is comparable with that of CL-CL CCDFB lasers. From Fig. 4.26, this region coincides with one of the two high yield areas of the AR-HR-coated LCDFB, namely the one near $\kappa_l L = 1.0$. The yield is over 70% at $0.75 \leq \kappa_l L \leq 1.8$. Consequently, the optimal region of operation for the

purely LCDFB laser is around $0.75 \leq \kappa_l L \leq 1.5$, where good yield (>70%) along with low I_{th} (≤20 mA) and high front-facet power efficiency (from 20% to over 30%) are achieved. With the addition of index-coupling (i. e. CCDFB), the yield is expected to deteriorate and the optimized region of operation to shift.

4.5 Conclusion

In this chapter, three analyses have been presented: an above-threshold analysis for the CCDFB laser, and subthreshold yield analyses for both the LCDFB laser and the index-coupled QWDFB laser. They are performed for three sets of end-facets: AR-AR, CL-CL and AR-HR coatings. The above-threshold analysis focuses on the differences in threshold current (I_{th}) and front-facet power efficiency (η). The single-mode yield is calculated based on three criteria: $\Delta g_{th} L \geq 0.3$, $\sigma_{\psi} \leq 0.1$ and $I_{th} \leq 35$ mA. In this study, good laser performance is characterized by low threshold, high efficiency and high single-mode yield. Two methods have been applied to enhance device performance: namely, the use of small grating duty cycle and asymmetric facet coatings. Although the usefulness of asymmetric facet coatings is limited to devices with small coupling coefficients, the parameter values for optimized performance have been obtained.

For CCDFB with perfect AR-coated facets, the above-threshold analysis reveals small to moderate increase in I_{th} with the introduction of absorptive grating. The increase in I_{th} depends on the grating duty cycle (ρ). The dependence of I_{th} at various degrees of loss-coupling can be seen from the contour plots of I_{th} versus the complex κL (Fig. 4.9 and Fig. 4.11). That the contour lines for ρ =0.15 are more circular than those for ρ =0.36 indicates that the increase in I_{th} is in general smaller for ρ =0.15. The differences in I_{th} between these two cases become more significant at large $\kappa_l L$ ($|\kappa L| \geq 2.0$). For ρ =0.15 , the increase in I_{th} is about 10 mA smaller. The use of a smaller ρ also improves η. Again, the enhancement is more apparent at large $\kappa_l L$. Therefore, it can be concluded that low threshold loss-coupled devices are possible with careful choice of ρ.

Further improvements on I_{th} and η are achieved with AR-HR facet coatings. As compared with the perfectly AR-coated CCDFB lasers, substantial reduction in I_{th} of up to 36 mA (at $\kappa_l L$ =0.2) is obtained. This advantage gradually diminishes with increasing $\kappa_l L$. The enhancement on η is limited to $\kappa_l L \leq 1.1$ for ρ =0.36 and $\kappa_l L \leq 3.0$ for ρ =0.15. Nevertheless, this method is attractive because it does not degrade the SMSR significantly. However, results from the yield analysis place further restriction on the choice of $\kappa_l L$ for high yield, low I_{th} and high η performance.

I_{th} and η for CCDFB lasers with as-cleaved facets show only weak dependence on $\kappa_l L$ and $\kappa_n L$. The lower efficiency makes CL-CL facets less desirable than AR-HR coatings at small $\kappa_l L$. However, I_{th} is low for most $\kappa_l L$ and $\kappa_n L$. At large $\kappa_l L$, η may actually be larger (see Fig. 4.17), which makes it a feasible alternative for low threshold and high efficiency. In addition, unlike purely index-coupled devices, high single-mode yield may be obtained.

The linear yield analysis on index-coupled QWDFB reconfirms the validity of our DFB model as the results obtained are in good agreement with those reported in the literature. The yield is highest for lasers with AR-AR coatings but it is very sensitive to $\kappa_n L$. The increase in facet reflectivities (by CL-CL or AR-HR coatings) deteriorates the yield to less than 30% in the case of CL-CL facets and to less than 52% in case of AR-HR coatings. A dramatic reduction in yield takes place at large κL when the criterion $\sigma_\psi \leq 0.1$ is imposed in addition to the $\Delta g_{th} L \geq 0.3$ requirement. This indicates the presence of strong LSHB effect. A further restriction on I_{th} does not alter the yield.

In contrast, the increase in facet reflectivities in purely LCDFB lasers (ρ =0.15) does not have a detrimental effect on the calculated yield. As in QWDFB, the yield is highest for devices with AR-AR coatings and perfect yield is obtainable spanning the region from $\kappa_l L$ =2.0 to 3.0. Slightly lower yield (with a maximum of 87.3% at

$\kappa_l L$ =2.25) is computed for lasers with as-cleaved facets over the same region. The yield as a function of $\kappa_l L$ for LCDFB with AR-HR coatings has an interesting double-peaked profile. The two maxima, 87.5% and 75%, are located at $\kappa_l L$ =1.25 and $\kappa_l L$ =3.0, respectively.

The threshold criterion is the major cause for the reduction in the yield at the mid-$\kappa_l L$ region ($1.0 \leq \kappa_l L \leq 3.0$). When the loss-coupling coefficient ($\kappa_l L$) increases, two effects take place. The first is the increase in the effective reflectivities, which has the effect of lowering I_{th}. The second is the increase in the cavity loss because of the extra loss in the absorptive grating. This extra loss has the opposite effect of increasing I_{th}. In the region with $\kappa_l L$ <3.0, the increase in I_{th} due to the additional loss is not fully compensated by the decrease resulted from the enhanced reflectivities. The first peak coincides remarkably with the region for low I_{th} and high η. As a result, it is possible to obtain an optimal $\kappa_l L$, which has values between 0.75 and 1.5 where good yield (>70%) together with relatively low I_{th} (≤20 mA) and high η (20% to over 30%). In comparison with QWDFB lasers, LCDFB is less sensitive to the facet reflectivities and good yield is possible for both as-cleaved and AR-HR coated devices.

5 SUMMARY AND CONCLUSION

Section 5.1 of this chapter summarizes the major results of this thesis. *Section 5.2* provides a list of possible future endeavors that extends this work.

5.1 Summary

5.1.1 Summary of Major Contributions

A nonlinear multisection DFB laser model has been successfully developed in this work. As seen from the last two chapters, the model is a very powerful tool in the design and study of DFB-type lasers. The linear yield analysis provides a quick preview of the sensitivity of the single-mode operation to critical parameters such as $\Delta g_{th} L$, σ_ψ and I_{th}. The above-threshold model gives further information on the output power, power efficiency, SMSR, and spectral characteristics.

In this thesis, the major contributions in the area of modeling are as follows:

(1) a generalization on the PMM approach;

(2) a static nonlinear model that can perform a full multimode above-threshold analysis on DFB-type lasers with up to three sections;

(3) improved accuracy in the computation of spectral lineshape by eliminating approximation;

(4) improved accuracy in the calculation of output power (both edge- and surface-emission), and photon density by direct summation; and

(5) inclusion of more sophisticated gratings:

— first- and second-order grating;

— gain-coupled grating together with induced index-grating;

— absorptive grating with loss saturation at large photon densities.

For device analysis, important and interesting information on two novel DFB lasers have been obtained for the first time. For the three-section second-order DFBDBR laser, the achievements are:

(1) first above-threshold analysis of this laser;

(2) good agreement between calculated results and experimental observation;

(3) conclusion on the dominant mode of operation is consistent with earlier linear analysis;

(4) the determination of critical design parameters and their desirable values;

(5) the assessment of longitudinal spatial hole burning effect showing improvement with this DFB design compared with conventional single-section DFB lasers; and

(6) the comparison of the linewidth enhancement factor illustrating another advantage of this DFB design.

For the loss-coupled DFB laser, the major conclusion and results are as follows.

(1) Improvement on the threshold current and front-facet power efficiency can be achieved by the application of asymmetric facet coatings and small grating duty cycle (~0.15). However, it was found that the use of asymmetric facet coatings only improves the efficiency at small coupling coefficients.

(2) For asymmetric facet coatings, the range of coupling coefficients for low threshold and high efficiency coincides remarkably with that for high single-mode yield.

(3) The values of the design parameters have been determined based on the above-threshold analysis and the subthreshold yield analysis.

(4) The effect on the threshold current and front-facet power efficiency at the introduction of absorptive grating has been investigated.

5.1.2 Summary of Modeling and Validation

The model is a generalization of the power matrix method, which is based on the commonly used transfer matrix approach and coupled-wave equations. It is nonlinear and self-consistent, and enables calculations of the static laser properties at above-threshold conditions. It also takes into account nonlinear effects such as spontaneous emission, gain saturation, carrier-induced index change. In this thesis, the model was built specifically for a DFB-type laser with up to three sections[1]. Each section was subdivided into a number of equal-length segments to model the inhomogeneous longitudinal distribution of parameters. This segmentation offers greater flexibility in the study of novel laser designs. The generalization of the modeling approach was also extended to the description of the grating. We can now consider first- and second-order gratings, gain-grating with induced index-grating, and absorptive-grating with loss saturation. Other modifications were aimed at improving the accuracy of the calculation. They are the expansion of the method to enable a fully multimode calculation. In addition, direct and more accurate computation of the spectral lineshape, output power and photon density is possible.

The results that can be calculated include:

---

1 The model can also be modified in a straightforward manner to accommodate a larger number of sections.

- the output power from the end-facets and surface emission that is perpendicular to the junction plane;
- the longitudinal distributions and variances of the carrier density, photon density, effective index and nearfield intensity;
- the optical spectrum together with the SMSR and the spectral linewidth,
- the subthreshold spectrum; and
- the single-mode yield based on the threshold gain margin, the photon density distribution variance, and the threshold current criteria.

In *Chapter 2*, the implementation of the computer model has been described in detail. An overview of the computer program supported by a flowchart and subroutine calling sequences is presented. The numerical algorithms and their corresponding implementation are also described. During the course of developing the model, a number of challenges and difficulties were encountered. These together with their solutions are discussed.

The model was validated through comparisons with other independently developed models in the literature. On the yield analysis of index-coupled QWDFB and the LCDFB lasers, the results showed good agreement with those by the CLADISS model [Vank90]. On the above-threshold analysis of QWDFB laser, the results obtained are almost identical with those of [Zhan92]. On the subthreshold analysis of the DFBDBR laser, the calculated results agree with those obtained by a network model [Aman90]. In addition, the design plot obtained with the above-threshold analysis is consistent with the reported experimental data, further validating of the model.

5.1.3 Summary of Model Applications

The model has been applied on three DFB devices: the novel three-section second-order DFBDBR laser, the CCDFB with index- and loss-coupling (including

purely LCDFB), and the index-coupled QWDFB laser. The analysis on the QWDFB laser was mainly for comparison purposes. The emphasis was on the other two lasers. For both the DFBDBR and the LCDFB lasers, the regions for optimal performance have been determined. The criteria for good performance were chosen to be small LSHB (uniform optical density distribution), large SMSR, high single-mode yield, low threshold and high power efficiency.

DFBDBR Laser

The DFBDBR laser with a continuous second-order grating has been analyzed for below- and above-threshold behaviors. The laser has a center pumped section that is terminated by two unpumped grating sections. The calculated results confirm earlier experimental observation that the laser operates with a peaked nearfield intensity distribution along the laser cavity. The values of the grating parameters and the active-section-to-total-cavity-length ratio associated with this mode of operation were obtained. They are κL_{tot} = 1.5 to 2.5, $\xi/\kappa \leq 0.2$ for facet output and $\xi/\kappa \geq 0.2$ for surface output, and L_m/L_{tot} =0.5 to 0.7. The values indicate good tolerance in these design parameters. A comparison with a distributed-reflector laser was also presented. The DFBDBR laser shares most of advantages of this laser, yet has reduced complexity in fabrication.

The DFBDBR laser was also found to have reduced longitudinal spatial hole burning and a smaller effective linewidth enhancement factor compared with those of a uniformly pumped single-section second-order DFB laser. The former reflects the more uniform intensity distribution. The latter is a result of the coupling to the extended passive resonator, and lasing on the shorter wavelength side of the DBR reflectivity maximum. In general, the photon variance of the DFBDBR laser is typically smaller by a moderate factor of 2 to 3. The improvement is 14 times when compared with the QWDFB laser. The effective linewidth enhancement factor is smaller by a factor of 0.73 (at κL_{tot} =1.0) to 0.85 (at κL_{tot} =2.0). The introduction

of asymmetric passive grating sections in the DFBDBR laser results in deteriorating SMSR. In the extreme case when there is only one unpumped section, the dominant mode is switched to the split nearfield mode associated with the uniformly pumped second-order DFB laser.

Loss-Coupled DFB Laser

The CCDFB lasers with three sets of end-facets were analyzed at above-threshold conditions. Since a common concern is the extra loss introduced by the absorptive grating, the analysis focused on the threshold current and front-facet power efficiency. It was found that the extra loss introduced by the absorptive grating could be reduced to an acceptable level by using a small grating duty cycle (e. g. $\rho = 0.15$). This is evident by comparing the contour plots of the threshold current as a function of the complex coupling coefficient at two grating duty cycles. The threshold current for CCDFB laser with perfectly AR-AR facets experiences a slight to moderate increase at the introduction of loss-coupling when $\rho = 0.15$. In addition, when the end-facets are asymmetrically coated (i. e. AR-HR), the threshold current is reduced substantially. Furthermore, the output power from the front facet was also enhanced, although the improvement occurs only at small coupling coefficients. This means that low threshold and high efficiency CCDFB lasers with absorptive gratings are possible.

Unfortunately, these improvements are also accompanied by the degradation of the single-mode property of the loss-coupled DFB laser. Since the degradation can be inferred from the theoretical single-mode yield, a yield analysis of the purely loss-coupled DFB laser was carried out. It was found that the single-mode yield of the LCDFB laser with AR-HR coatings exhibited an interesting double-peaked profile as a function of the coupling coefficient when a maximum threshold current criterion was imposed. The first of the two peaks coincides remarkably with the region of low threshold and high efficiency. The results suggest that high efficiency and small reduction in yield along with low threshold can be achieved by choosing appropriate

coupling coefficients. Thus, the use of asymmetric facet coating is a viable method in improving the performance of loss-coupled DFB lasers.

5.2 Topics for Future Studies

The topics for future work on the DFB modeling has been listed in *Section 2.5.3* and will not be repeated here. The following is a list of possible topics for future endeavors in the area of device analyses.

The following suggestions do not require any changes in the computer program.

- *Yield of DFBDBR*

  Single-mode yield of the three-section DFBDBR laser may be compared with second-order DFB and DBR lasers.

- *DFBDBR with non-zero facet reflectivity*

  This can reveal whether the DFBDBR laser is sensitive to external optical feedback.

- *CCDFB with various grating phases*

  It has been suggested that CCDFB laser can be further optimized by tuning the phase difference between the index grating and the gain/loss gratings [Card95]. It is interesting to see if the benefits outweigh the added complexity in the fabrication of the two individual gratings.

- *Yield of LCDFB with power efficiency criterion*

  This analysis will require calculation of the output power at above-threshold conditions similar to Ref. [Borc90]. It may be quite time-consuming because iterations are necessary. However, the consideration of the power efficiency in addition to the threshold criterion may provide a

more complete picture of the yield since the two are tradeoffs of each other.

- *CCDFB with unpumped grating end-sections*

  Although the presence of loss coupling has been shown to improve the SMSR of a DFB laser, the influence of additional unpumped grating is not clear. However, some enhancement of performance is expected much like in the case of the DFBDBR laser.

- *GCDFB*

  The behavior of the GCDFB laser and the LCDFB laser should be very similar. Nevertheless, the threshold current should be different. However, the threshold current of the LCDFB may not necessary be higher. It is because while the LCDFB introduces additional loss, the gain in the GCDFB has to be sufficiently high in order to reach lasing threshold.

The following topics require modifications in the computer program.

- *DFB with chirped gratings*

  The use of chirped gratings has the advantages of reduced LSHB and enhanced frequency tunability. It is therefore worthy of an investigation. Only minor changes in the computer program is needed. They concern the assignment of the grating coupling coefficients in the divided cavity segments.

- *Multisection DFB lasers for tuning purposes*

  Wavelength tunable DFB lasers which are used in dense WDM applications are typically composed of three active sections. Investigation into the optimization of the laser design with respect to broad continuous

tuning range is valuable. This analysis will require further modifications of the program to include all active sections.

- *Large-signal and small-signal dynamic analyses*

  Major expansion of the model are needed to perform these dynamic analyses. The new model will enable the study of large-signal and small-signal modulation responses of DFB lasers. Q-switching, wavelength switching, beam steering during pulsing and integrated device such as a DFB laser with modulator are some possible research topics.

REFERENCES

[Agra87] G. P. Agrawal, "Gain Nonlinearities in Semiconductor Lasers: Theory and Application to Distributed Feedback Lasers," *IEEE Journal of Quantum Electronics*, Vol. QE-23, No. 6, pp. 860-868, June 1987.

[Agra88a] G. P. Agrawal, J. E. Geusic, and P. J. Anthony, "Distributed Feedback Lasers with Multiple Phase-shift Regions," *Applied Physics Letters, Vol.* 53, pp. 178-179, July 1988.

[Agra88b] G. P. Agrawal and A. H. Bobeck, "Modeling of DFB Semiconductor Lasers with Axially-Varying Parameters," *IEEE Journal of Quantum Electronics*, Vol. QE-24, No. 12, pp. 2407-2414, December 1988.

[Agra90] G. P. Agrawal, "Effect of Gain and Index Nonlinearities on Single-Mode Dynamics in Semiconductor Lasers," *IEEE Journal of Quantum Electronics*, Vol. QE-26, No. 11, pp. 1901-1909, November 1990.

[Agra93] G. P. Agrawal and N. K. Dutta, "Semiconductor Lasers," second edition, New York: Van Nostrand Reinhold Co., 1993.

[Aman90] R. Amantea, N. W. Carlson, S. L. Palfrey, G. A. Evans, J. M. Hammer, and M. Lurie, "Network Analysis of the Modes of Two-Dimensional Grating-Surface-Emitting Diode Laser Arrays," *IEEE Journal of Quantum Electronics*, Vol. 26, No. 6, June 1990, pp. 1023-1038.

[Aman94] R. Amantea, J. Abeles, P. L. Demers, and D. J. Channin, "Modular Approach to Optoelectronic CAD Simplifies Modeling," *Laser Focus World*, pp. 93-100, December 1994.

[Arim90a] I. Arima, J. Shim, S. Arai, I. Morita, R. Somchai, Y. Suematsu, and K. Komori, "1.5 μm GaInAsP/InP Distributed Reflector (DR) Lasers with SCH Structure," *IEEE Photonics Technology Letters*, Vol. 2, No. 6, pp. 385-387, June 1990.

[Arim90b] I. Arima, K. Komori, S. Arai, and Y. Suematsu, "Linewidth Enhancement Factor of Distributed Reflector (DR) DSM Laser," *The Transactions of IEICE,* Vol. E73, No. 12, pp. 2014-2016, December 1990.

[Baet93] R. G. Baets, K. David, and G. Morthier, "On the Distinctive Features of Gain Coupled DFB Lasers and DFB Lasers with Second-Order Grating," *IEEE Journal of Quantum Electronics*, Vol. 29, No. 6, pp. 1792-1798, June 1993.

[Bjor87] G. Bjork and O. Nilsson, "A New Exact and Efficient Numerical Matrix Theory of Complicated Laser Structures: Properties of Asymmetric Phase-Shifted DFB Lasers," *IEEE Journal of Lightwave Technology*, Vol. LT-5, No. 1, pp. 140-146, January 1987.

[Borc90] B. Borchert and B. Stegmuller, "Yield Analysis of Distributed-Feedback Metal-Clad Ridge-Waveguide Laser diodes for Coherent System Applications," *IEE Proceedings--Optoelectron.*, Vol. 137, No. 4, pp. 265-272, August 1990.

[Borc91] B. Borchert, K. David, B. Stegmuller, R. Gessner, M. Beschorner, D. Sacher, and G. Franz, "1.55 μm Gain-Coupled Quantum-Well Distributed Feedback Lasers with High Single-Mode Yield and Narrow Linewidth," *IEEE Photonics Technology Letters*, Vol. 3, No. 11, pp. 955-957, November 1991.

[Borc93] B. Borchert, B. Stegmuller, and R. Gessner, "Fabrication and Characteristics of Improved Strained Quantum-Well GaInAlAs Gain-Coupled DFB Lasers," *Electronics Letters*, Vol. 29, No. 2, pp. 210-211, 21st January 1993.

[Borc94] B. Borchert, J. Rieger, and B. Stegmuller, "High Power Quantum-Well Gain-Coupled (GC) DFB Lasers at 1.3 μm and 1.55 μm," *Proceedings: 14th IEEE International Semiconductor Laser Conference*, pp. 47-48, September 1994.

[Bour91] D. P. Bour, N. W. Carlson, G. A. Evans, S. K. Liew, J. B. Kirk, and W. F. Reichert, "Surface-emitting, distributed feedback InGaAs/AlGaAs lasers by organometallic vapor phase epitaxy", *J. Appl. Phys.* 70 (9) 1 Nov. 1991, pp. 4687-4693.

[Butl89] J. K. Butler, G. A. Evans, and N. W. Carlson, "Nonlinear Characterization of Modal Gain and Effective Index Saturation in Channeled-Substrate-Planar Double-Heterojunction Lasers," *IEEE Journal of Quantum Electronics*, Vol. 25, No. 7, pp. 1646-1651, July 1989.

[Card95] D. A. Cardimona, M. P. Sharma, V. Kovanis, and A. Gavrielides, "Dephased Index and Gain Coupling in Distributed Feedback Lasers," *IEEE Journal of Quantum Electronics*, Vol. 31, No. 1, pp. 60-66, January 1995.

[Carl91] N. W. Carlson, S. K. Liew, R. Amantea, D. P. Bour, G. A. Evans and E. A. Vangieson, "Mode Discrimination in Distributed Feedback Grating Surface Emitting Lasers Containing a Buried Second-Order Grating," *IEEE Journal of Quantum Electronics*, Vol. QE-27, No. 6, pp. 1746-1752, June 1991.

[Carl92] N. W. Carlson, P. Gardner, R. Menna, J. Andrews, R. Stolzenberger, A. Triano, E. Vangieson, D. Bour, G. A. Evans, S. K. Liew, J. Kirk, and W. Reichert, "Demonstration of an InGaAsP/InGaAs Multiquantum Well Active-Grating Surface-Emitting Amplifier," *IEEE Photonics Technology Letters*, Vol. 4, No. 9, pp. 988-990, September 1992.

[Carl93] N. W. Carlson, R. Menna, P. Gardner, S. K. Liew, J. Andrews, A. Triano, J. Kirk, and W. Reichert, "High-power, Single-Frequency Operation of an InGaAsP/InGaAs Active-Grating Surface Emitting Amplifier at l=1.7 μm," *Appl. Phys. Lett.* Vol. 62, No. 17, pp. 2006-2008, 26 April 1993.

[Carl94] N. W. Carlson, "Monolithic Diode-Laser Arrays," Berlin: Springer-Verlag, 1994.

[Cao92] H. L. Cao, Y. Luo, Y. Nakano, K. Tada, M. Dobashi, and H. Hosomatsu, "Optimization of Grating Duty Factor in Gain-Coupled DFB Lasers with Absorptive Grating--Analysis and Fabrication," *IEEE Photonics Technology Letters*, Vol. 4, No. 10, pp. 1099-1102, October 1992.

[Carr93] J. E. Carroll, L. M. Zhang, and M. E. Bray, "A Bragg about Lasers," *Electronics & Communication Engineering Journal*, pp. 325-337, December 1993.

[Cold87] L. A. Coldren and S. W. Corzine, "Continuously-Tunable Single-Frequency Semiconductor Lasers," *IEEE Journal of Quantum Electronics*, Vol. QE-23, No. 6, pp.903-908, June 1987.

[Dabb72] F. W. Dabby, A. Kestenbaum, and U. C. Paek, *Opt. Commun.* **6**, 125 (1972).

[Davi90] K. David, G. Morthier, P. Vankwikelberge, and R. Baets, "Yield Analysis of Non-AR-Coated DFB Lasers with Combined Index and Gain Coupling," *Electronics Letters*, Vol. 26, No. 4, pp. 238-239, 15th February 1990.

[Davi91a] K. David, J. Buus, G. Morthier, and R. Baets, "Coupling Coefficients in Gain-Coupled DFB Lasers: Inherent Compromise Between Coupling Strength and Loss," *IEEE Photonics Technology Letters*, Vol. 3, No. 5, pp. 439-441, May 1991.

[Davi91b] K. David, G. Morthier, P. Vankwikelberge, R. G. Baets, T. Wolf, and B. Borchert, "Gain-Coupled DFB Lasers Versus Index-Coupled and Phase-Shifted DFB Lasers: A Comparison Based on Spatial Hole Burning Corrected Yield," *IEEE Journal of Quantum Electronics*, Vol. QE-27, No. 6, pp. 1714-1723, June 1991.

[Davi92] K. David, J. Buus, and R. G. Baets, "Basic Analysis of AR-Coated, Partly Gain-Coupled DFB Lasers: The Standing Wave Effect," *IEEE Journal of Quantum Electronics*, Vol. 28, No. 2, pp. 427-433, February 1992.

[Duan92] G. -H. Duan, P. Gallion, and G. P. Agrawal, "Effective Nonlinear Gain in Semiconductor Lasers," *IEEE Photonics Technology Letters*, Vol. 4, No. 3, pp. 218-220, March 1992.

[Dutt84] N. K. Dutta, N. A. Olsson, and W. T. Tsang, "Carrier Induced Refractive Index Change in AlGaAs Quantum Well Lasers," *Applied Physics Letters*, Vol. 45, No. 8, pp. 836-837, 15 October 1984.

[Evan93] G. A. Evans and J. M. Hammer, "Surface Emitting Semiconductor Lasers and Arrays," Boston: Academic Press, 1993.

[Favr91] F. Favre, "Sensitivity to External Feedback for Gain-Coupled DFB Semiconductor Lasers," *Electronics Letters*, Vol. 27, No. 5, pp. 433-435, 28th February 1991.

[Glin87] J. Glinski and T. Makino, "Yield Analysis of Second-Order DSM DFB Lasers and Implications for Design," *IEEE Journal of Quantum Electronics*, Vol. QE-23, No. 6, pp. 849--859, June 1987.

[Goma90] B. N. Gomatam and A. P. DeFonzo, "Theory of Hot Carrier Effects on Nonlinear Gain in GaAs-GaAlAs Lasers and Amplifiers," *IEEE Journal of Quantum Electronics*, Vol. QE-26, No. 10, pp. 1689-1704, October 1990.

[Hadj90] G. Hadjicostas, J. K. Butler, G. A. Evans, N. W. Carlson, and R. Amantea, "A Numerical Investigation of Wave Interactions in Dielectric Waveguides with Periodic Surface Corrugations," *IEEE Journal of Quantum Electronics*, Vol. 26, No. 5, May 1990, and references [10] to [16] within.

[Hans92] S. Hansmann, "Transfer Matrix Analysis of the Spectral Properties of Complex Distributed Feedback Laser Structures," *IEEE Journal of Quantum Electronics*, Vol. 28, No. 11, pp. 2589-2595, November 1992.

[Hans94] S. Hansmann, H. Burkhard, H. Walter, and H. Hillmer, "A Tractable Large-Signal Dynamic Model--Application to Strongly Coupled Distributed Feedback Lasers," *IEEE Journal of Lightwave Technology* Vol. 12, No. 6, pp. 952-956, June 1994.

[Hard89] A. Hardy, D. F. Welch, and W. Streifer, "Analysis of Second-Order Gratings," *IEEE Journal of Quantum Electronics*, Vol. 25, No. 10, pp. 2096-2105, October 1989.

[Hash92] J. -I. Hashimoto, Y. Nakano, and K. Tada, "Influence of Facet Reflection on the Performance of a DFB Laser Integrated with an Optical Amplifier/Modulator," *IEEE Journal of Quantum Electronics*, Vol. 28, No. 3, pp. 594-603, March 1992.

[Haus76] H. A. Haus and C. V. Shank, "Antisymmetric Taper of Distributed Feedback Lasers," *IEEE Journal of Quantum Electronics*, Vol. QE-12, No. 9, pp. 532-539, September 1976.

[Haus84] Chapter 3 in H. A. Haus, Waves and Fields in Optoelectronics Prentice-Hall, Inc., New Jersey, 1984.

[Henr82] C. H. Henry, "Theory of the Linewidth of Semiconductor Lasers," *IEEE Journal of Quantum Electronics*, Vol. QE-18, No. 2, pp. 259-264, February 1982.

[Henr85] C. H. Henry, R. F. Kazarinov, R. A. Logan and R. Yen, "Observation of Destructive Interference in the Radiation Loss of Second-Order Distributed Feedback Lasers," *IEEE Journal of Quantum Electronics*, Vol. QE-21, No. 2, pp. 151-153, February 1985.

[Henr86] C. Henry, "Theory of Spontaneous Emission Noise in Open Resonators and Its Application to Lasers and Optical Amplifiers," *IEEE Journal of Lightwave Technology*, Vol. LT-4, No. 3 , pp. 288-297, March 1986.

[Hill93] H. Hillmer, K. Magari, and Y. Suzuki, "Chirped Gratings for DFB Laser Diodes Using Bent Waveguides," *IEEE Photonics Technology Letters*, Vol. 5, No. 5, pp. 10-12, January 1993.

[Hill94a] H. Hillmer, S. Hansmann, H. Walter, and H. Burkhard, "Experimental and Theoretical Study of the Facet Phase Influence on the Wavelength Shift in InGaAs/InAlGaAs Quantum Well Distributed Feedback Lasers," *Applied Physics Letters*, Vol. 64, No. 6, pp. 698-700, 7 February 1994.

[Hill94b] H. Hillmer, H. -L. Zhu, S. Hansmann, A. Grabmaier, K. Magari, and H. Burkhard, "Tailored DFB Laser Properties by Individually Chirped Gratings Using Bent Waveguides," *Conference Proceedings of 14th International Semiconductor Laser Conference*, Hawaii, U. S. A., pp. 55-56, 1994.

[Hui94] R. Hui, M. Kavehrad, and T. Makino, "External Feedback Sensitivity of Partly Gain-Coupled DFB Semiconductor Lasers," *IEEE Photonics Technology Letters*, Vol. 6, No. 8, pp. 897-899, August 1994.

[Inou91] T. Inoue, S. Nakajima, Y. Luo, T. Oki, H. Iwaoka, Y. Nakano, and K. Tada, "CW Operation of an InGaAsP/InP Gain-Coupled Distributed Feedback Laser with a Corrugated Active Layer," *IEEE Photonics Technology Letters*, Vol. 3, No. 11, pp. 958-960, November 1991.

[Joha92] T. W. Johannes and W. Harth, "Spontaneous Emission Rate of Gain-Coupled DFB Lasers: Loss Grating Against Gain Grating," *Electronics Letters*, Vol. 28, No. 14, pp. 1347-1349, 2nd July 1992.

[Joha93] T. W. Johannes, M. -C. Amann and B. Borchert, "Reduced Effective Linewidth Enhancement Factor α_{eff} of Complex-Coupled DFB Lasers with Absorptive Gratings," *Electronics Letters*, Vol. 29, No. 15, pp. 1367-1369, 22nd July 1993.

[John82] Chapter 2 in R. L. Johnston, "Numerical Methods A Software Approach," New York: John Wiley & Sons, Inc., 1982.

[Kapo82] E. Kapon, A. Hardy, and A. Katzir, "The Effect of Complex Coupling Coefficients on Distributed Feedback Lasers," *IEEE Journal of Quantum Electronics*, Vol. QE-18, No. 1, pp. 66-71, January 1982.

[Kaza85] R. F. Kazarinov and C. H. Henry, "Second-Order Distributed Feedback Lasers with Mode Selection Provided by First-Order Radiation Losses," *IEEE Journal of Quantum Electronics*, Vol. QE-21, No. 2, pp. 144-150, February 1985.

[Kaza87] R. F. Kazarinov and C. H. Henry, "The Relation of Line Narrowing and Chirp Reduction Resulting from the Coupling of a Semiconductor Laser to a Passive Resonator," *IEEE J. of Quantum Electron.* Vol. 23, No. 9, pp. 1401-1409, September 1987.

[Kazm94] C. Kazmierski, D. Robein, D. Mathoorasing, A. Ougazzaden, and M. Filoche, "1.5 μm DFB Lasers with New Current Induced Gain Gratings," *Proceedings: 14th IEEE International Semiconductor Laser Conference*, Postdeadline Paper: PD11, September 1994.

[Kete91] L. T. P. Ketelsen, I. Hoshino, and D. A. Ackerman, "The Role of Axially Nonuniform Carrier Density in Altering the TE-TE Gain Margin in InGaAsP-InP DFB Lasers," *IEEE Journal of Quantum Electronics*, Vol. QE-27, No. 4, pp. 957-964, April 1991.

[Kino89] J. Kinoshita and K. Matsumoto, "Yield Analysis of SLM DFB Lasers with an Axially-Flattened Internal Field," *IEEE Journal of Quantum Electronics*, Vol. 25, No. 6, pp. 1324-1332, June 1989.

[Kino90] J. -I. Kinoshita, "Axial Profile of Grating Coupled Radiation from Second-Order DFB Lasers with Phase Shifts," *IEEE Journal of Quantum Electronics*, Vol. 26, No. 3, pp. 407-412, March 1990.

[Kino94] J. Kinoshita, "Modeling of High-Speed DFB Lasers Considering the Spatial Holeburning Effect Using Three Rate Equations," *IEEE Journal of Quantum Electronics*, Vol. 30, No. 4, pp. 929-938, April 1994.

[Kita93] M. Kitamura, H. Yamazaki, H. Yamada, S. Takano, K. Kosuge, Y. Sugiyama, M. Yamaguchi, and I. Mito, "High Performance and Highly Reliable λ/4 Shifted MQW-DFB-DC-PBH-LD's for Gb/s Coherent Optical Communication Systems," *IEEE J. of Quantum Electron.* Vol. 29, No. 6, pp. 1728-1735, June 1993.

[Koch90] T. L. Koch and U. Koren, "Semiconductor Lasers for Coherent Optical Fiber Communications," *IEEE Journal of Lightwave Technology*, Vol. LT-8, No. 3, pp. 274-293, March 1990.

[Koge72] H. Kogelnik and C. V. Shank, "Coupled-Wave Theory of Distributed Feedback Lasers," *Journal of Applied Physics*, Vol. 43, No. 5, pp. 2327-2335, May 1972.

[Koji88] K. Kojima and K. Kyuma, "Analysis of the Linewidth of Distributed Feedback Laser Diodes Using the Green's Function Method," *Japan Journal of Applied Physics*, Vol. 27, No. 9, pp. L1721-L11723, September 1988.

[Komo89] K. Komori, S. Arai, Y. Suematsu, I. Arima, and M. Aoki, "Single-Mode Properties of Distributed-Reflector Lasers," *IEEE Journal of Quantum Electronics*, Vol. 25, No. 6, pp. 1235-1244, June 1989.

[Kuo90] C. Y. Kuo, M. S. Lin, S. J. Wang, A. Ackerman, and L. J. T. Ketelsen, "Static and Dynamic Characteristics of DFB Lasers with Longitudinal Nonuniformity," *IEEE Photonics Technology Letters*, Vol. 2, No. 7, pp. 461-463, July 1990.

[Kudo92] K. Kudo, J. I. Shim, K. Komori, and S. Arai, "Reduction of Effective Linewidth Enhancement Factor α_{eff} of DFB Lasers with Complex Coupling Coefficients," *IEEE Photonics Technology Letters*, Vol. 4, No. 6, pp. 531-534, June 1992.

[Li92] G. P. Li, T. Makino, R. Moore, and N. Puetz, "1.55 μm Index/Gain Coupled DFB Lasers with Strained Layer Multiquantum-Well Active Grating," *Electronics Letters*, Vol. 28, No. 18, pp.1726-1727, 27th August 1992.

[Li93a] G. P. Li, T. Makino, and H. Lu, "Simulation and Interpretation of Longitudinal-Mode Behavior in Partly Gain-Coupled InGaAsP/InP Multiquantum-Well DFB Lasers," *IEEE Photonics Technology Letters*, Vol. 5, No. 4, pp. 386-389, April 1993.

[Li93b] G. P. Li, T. Makino, R. Moore, N. Puetz, K. Leong, and H. Lu, "Partly Gain-Coupled 1.55 μm Strained-Layer Multiquantum-Well DFB Lasers," *IEEE Journal of Quantum Electronics*, Vol. 29, No. 6, pp. 1736-1742, June 1993.

[Li93c] G. P. Li and T. Makino, "Single-Mode Yield Analysis of Partly Gain-Coupled Multiquantum-Well DFB Lasers," *IEEE Photonics Technology Letters*, Vol. 5, No. 11, pp. 1282-1284, November 1993.

[Liew90] S. K. Liew, N. W. Carlson, R. Amantea, D. P. Bour, G. A. Evans, E. Van Gieson, "Operation of Distributed-Feedback Grating-Surface-Emitting Laser with a Buried Grating Structure", *IEEE Lasers and Electro-Optics Society 1990 Annual Meeting (LEOS'90)*, Talk SDL2.7/TuL7.

[Liew91] S. K. Liew, N. W. Carlson, D. P. Bour, G. A. Evans, and E. Van Gieson, "Demonstration of InGaAs/AlGaAs Strained-Layer Distributed-Feedback Grating-Surface-Emitting Lasers with a Buried Second-Order Grating Structure," *Applied Physics Letters*, Vol. 58, No. 3, pp. 228-230, 21 January 1991.

[Liew92] So Kuen Liew and Nils W. Carlson, "Method for Obtaining a Collimated Near-Unity Aspect Ratio Output Beam from a DFB-GSE Laser with Good Beam Quality", *Applied Optics*, Vol. 31, No. 15, 20 May 1992, pp. 2743-2746.

[Liew93] S. K. Liew, N. W. Carlson, R. Amantea, G. A. Evans, J. K. Butler, J. Andrews, J. H. Abeles, N. A. Hughes, P. K. York, and J. C. Connolly, "Very Low Threshold InGaAs/GaAs Grating-Coupled Surface-Emitting Distributed-Feedback Laser," *Technical Digest of Conference on Lasers and Electro-optics* , pp. 320-321, 1993.

[Liew94] S. K. Liew, "Above Threshold Analysis of Three-Section DFB/DBR Lasers with Second-Order Gratings", *Proceedings: IEEE Lasers and Electro-Optics Society 1994 Annual Meeting (LEOS'94)* , Paper SL1.3, Boston, MA, October 31-November 3, 1994, pp. 99-100.

[Liew95a] So Kuen C. Liew, "Above Threshold Analysis of Three-Section DFB/DBR Lasers with Second-Order Gratings", *IEEE J. of Selected Topics in Quantum Electron.*, Vol. 1, No. 2, June 1995, pp. 363-370.

[Liew95b] S. K. Liew, "Above-Threshold Analysis of Loss-Coupled DFB Lasers: Threshold Current and Power Efficiency," to appear in *IEEE Photonics Technology Letters.*, December, 1995.

[Liew95c] S. K. Liew, "Yield Analysis of Loss-Coupled DFB Lasers with Asymmetric Facet Coatings," submitted to *Electronics Letters.*

[Lowe90] A. J. Lowery, "New Dynamic Model for Multimode Chirp in DFB Semiconductor Lasers," *IEE Proceedings*, Vol. 137, Pt. J, No. 5, pp. 293-300, October, 1990.

[Lowe92] A. J. Lowery, "Comparison Between Two Recent Large-Signal Dynamic DFB Laser Models," *IEE Proceedings-J*, Vol. 139, No. 6, pp. 402-406, December 1992.

[Lowe93] A. J. Lowery and D. Novak, "Enhanced Maximum Intrinsic Modulation Bandwidth of Complex-Coupled DFB Semiconductor lasers," *Electronics Letters*, Vol. 29, No. 5, pp. 461-463, 4th March 1993.

[Lowe94] A. J. Lowery, and Dalma Novak, "Performance Comparison of Gain-Coupled and Index-Coupled DFB Semiconductor Lasers," *IEEE Journal of Quantum Electronics*, Vol. 30, No. 9, pp. 2051-2063, September 1994.

[Lu93] H. Lu, S. McGarry, G. P. Li and T. Makino, "Beyond 20 GHz Bandwidth of Partly Gain-Coupled 1.55 μm Strained Multiquantum Well DFB Lasers," *Electronics Letters*, Vol. 29, No. 15, pp. 1369-1370, 22nd July 1993.

[Lu94] H. Lu, C. Blaauw, B. Benyon, and T. Makino, "High-Power and High-Speed Performance of Gain-Coupled 1.3 μm Strained-Layer MQW DFB Lasers," *Proceedings: 14th IEEE International Semiconductor Laser Conference*, pp. 51-52, September 1994.

[Luo90] Y. Luo, Y. Nakano, K. Tada, T. Inoue, H. Hosomatsu, and H. Iwaoka, "Purely Gain-Coupled Distributed Feedback Semiconductor Lasers," *Applied Physics Letters*, Vol. 56, No. 17, pp. 1620-1622, 23 April 1990.

[Luo91] Y. Luo, Y. Nakano, K. Tada, T. Inoue, H. Hosomatsu, and H. Iwaoka, "Fabrication and Characteristics of Gain-Coupled Distributed Feedback Semiconductor Lasers with a Corrugated Active Layer," *IEEE Journal of Quantum Electronics*, Vol. 27, No. 6, pp. 1724-1731, June 1991.

[Luo94] H. J. Luo and P. S. Zory, "Ray Optics Determination of the DFB Coupling Coefficient in Separate Confinement and Multiquantum-Well Laser Structure," *IEEE Journal of Quantum Electronics*, Vol. 30, No. 1 , pp. 10-14, January 1994.

[Ma95] T. -A. Ma, Z. -M. Li, T. Makino, and M. S. Wartak, "Approximate Optical Gain Formulas for 1.55-μm Strained Quaternary Quantum-Well Lasers," *IEEE Journal of Quantum Electronics*, Vol. 31, No. 1 , pp. 29-34, January 1995.

[Maki88a] T. Makino and J. Glinski, "Effects of Radiation Loss on the Performance of Second-Order DFB Semiconductor Lasers," *IEEE Journal of Quantum Electronics*, Vol. QE-24, No. 1, pp. 73-82, January 1988.

[Maki88b] T. Makino and J. Glinski, "Transfer Matrix Analysis of the Amplified Spontaneous Emission of DFB Semiconductor Laser Amplifier," *IEEE Journal of Quantum Electronics*, Vol. 24, No. 8 , pp. 1507-1518, August 1988.

[Maki91] T. Makino and D. M. Adams, "TE- and TM-Coupling Coefficients in Multiquantum Well Distributed Feedback Lasers," *IEEE Photonics Technology Letters*, Vol. 3, No. 11, pp. 963-965, November, 1991.

[Mart94] Private communication with Dr. R. U. Martinelli, November 1994.

[Mats92] M. Matsumoto, "Analysis of Blazing Effect in Second-Order Gratings," *IEEE Journal of Quantum Electronics*, Vol. 28, No. 10, pp. 2016-2023, October 1992.

[Math87] Pages 70-74 in J. H. Mathews, "Numerical Methods for Computer Science, Engineering, and Mathematics," New Jersey: Prentice Hall, Inc., 1987.

[Mort90a] G. Morthier, P. Vankwilelberge, K. David, and R. Baets, "Improved Performance of AR-Coated DFB Lasers by the Introduction of Gain Coupling," *IEEE Photonics Technology Letters*, Vol. 2, No. 3, pp. 170-172, March 1990.

[Mort90b] G. Morthier, K. David, P. Vankwikelberge, and R. Baets, "A New DFB-Laser Diode with Reduced Spatial Hole Burning," *IEEE Photonics Technology Letters*, Vol. 2, No. 6, pp. 388-390, June 1990.

[Moze85] A. P. Mozer, S. Hausser, and M. H. Pilkuhn, "Quantitative Evaluation of Gain and Losses in Quaternary Lasers," *IEEE Journal of Quantum Electronics*, Vol. QE-21, No. 6, pp. 719-725, June 1985.

[Mura93] S. Murata, A. Tomita, and A. Suzuki, "Influence of Free Carrier Plasma Effect on Carrier-Induced Refractive Index Change for Quantum-Well Lasers," *IEEE Photonics Technology Letters*, Vol. 5, No. 1, pp. 16-19, January 1993.

[Naka88] Y. Nakano and K. Tada, "Analysis, Design, and Fabrication of GaAlAs/GaAs DFB Lasers with Modulated Stripe Width Structure for Complete Single Longitudinal Mode Oscillation," *IEEE Journal of Quantum Electronics*, Vol. 24, No. 10, pp. 2017-2033, October 1988.

[Naka89] Y. Nakano, Y. Luo, and K. Tada, "Facet Reflection Independent, Single Longitudinal Mode Oscillation in a GaAlAs/GaAs Distributed Feedback Laser Equipped with a Gain-Coupling Mechanism," *Applied Physics Letters*, Vol. 55, No. 16, pp. 1606-1608, 16 October 1989.

[Naka91] Y. Nakano, Y. Deguchi, K. Ikeda, Y. Luo, and K. Tada, "Reduction of Excess Intensity Noise Induced by External Reflection in a Gain-Coupled Distributed Feedback Semiconductor Laser," *IEEE Journal of Quantum Electronics*, Vol. 27, No. 6, pp. 1732-1735, June 1991.

[Naka92] Y. Nakano, Y. Uchida, and K. Tada, "Highly Efficient Single Longitudinal-Mode Oscillation Capability of Gain-Coupled Distributed Feedback Semiconductor Lasers--Advantage of Asymmetric Facet Coating," *IEEE Photonics Technology Letters*, Vol. 4, No. 4, pp. 308-311, April 1992.

[Obri94] S. O'Brien, R. Lang, D. F. Welch, R. Parke, and D. Scifres, "2.2 W cw Diffraction-Limited Monolithically Integrated Master Oscillator Power Amplifier at 854 nm," *Proceedings: 14th International Semiconductor Laser Conference*, Hawaii, U. S. A., pp. 249-250, 1994.

[Ogit86] S. Ogita, M. Yano, and H. Imai, "Theoretical Calculation of the Linewidth Enhancement Factor of DFB Lasers," *Electron. Letters*, Vol. 22, No. 11, pp. 580-581, 22 May 1986.

[Ogit87] S. Ogita, M. Yano, H. Ishikawa, and H. Imai, "Linewidth Reduction in DFB Laser by Detuning Effect," *Electron. Letters*, Vol. 23, No. 8, pp. 393-394, 9 April 1987.

[Okai91] M. Okai, T. Tsuchiya, K. Uomi, A. Takai, N. Chinone, and T. Harada, "Corrugation-Pitch Modulated MQW-DFB Lasers with Narrow Spectral Linewidth," *IEEE Journal of Quantum Electron.* Vol. 27, No. 6, pp. 1767-1772, June 1991.

[Okai94] M. Okai, M. Suzuki, T. Taniwatari, and N. Chinone, "Complex-Coupled $\lambda/4$-Shifted DFB Lasers with a Flat FM Response from 10 kHz to 17 GHz," *Proceedings: 14th IEEE International Semiconductor Laser Conference*, pp. 49-50, September 1994.

[Olof92] L. Olofsson and T. G. Brown, "The Influence of Resonator Structure on the Linewidth Enhancement Factor of Semiconductor Lasers," *IEEE Journal of Quantum Electronics*, Vol. 28, No. 6, pp. 1450-1458, June 1992.

[Osin87] M. Osinski and J. Buus, "Linewidth Broadening Factor in Semiconductor Lasers--An Overview," *IEEE Journal of Quantum Electronics*, Vol. QE-23, No. 1 , pp. 9-27, January 1987.

[Pan92] X. Pan, H. Olesen, B. Tromborg, and H. E. Lassen, "Analytic Description of the Standing Wave Effect in DFB Lasers," *IEE Proceedings--Optoelectron.*, Vol. 139, No. 3, pp.189-193, June 1992.

[Pan94] J. J. Pan and F. Liang, "Optoelectronic Components Make WDM Networks Practical," *Laser Focus World*, January 1994, pp. 111-115.

[Park93] R. Parke, D. F. Welch, A. Hardy, R. Lang, D. Mehuys, S. O'Brien, K. Dzurko, and D. Scifres, "2.0 W CW, Diffraction-Limited Operation of a Monolithically Integrated Master Oscillator Power Amplifier," *IEEE Photonics Technology Letters*, Vol. 5, No. 3, pp. 297-300, March 1993.

[Phil92] M. R. Phillips, T. E. Darcie, and E. J. Flynn, "Experimental Measure of Dynamic Spatial-Hole Burning in DFB Lasers," *IEEE Photonics Technology Letters*, Vol. 4, No. 11, pp. 1201-1203, November 1992.

[Rabi89] W. S. Rabinovich and B. J. Feldman, "Spatial Hole Burning Effects in Distributed Feedback Lasers," *IEEE Journal of Quantum Electronics*, Vol. QE-25, No. 1, pp. 20-30, January 1989.

[Salz94] J. Salzman, H. Olesen, A. Moller-Larsen and O. Albrektsen, "The S-bent Waveguide Distributed Feedback Laser, "Conference *Proceedings of 14th International Semiconductor Laser Conference*, Hawaii, U. S. A., pp. 57-58, 1994.

[Shim91] J. I. Shim, K. Komori, S. Arai, I. Arima, Y. Suematsu and R. Somchai, "Lasing Characteristics of 1.5 μm GaInAsP-InP SCH-BIG-DR Lasers," *IEEE J. of Quantum Electron.* Vol. QE-27, No. 6, pp. 1736-1745, June 1991.

[Soda87] H. Soda, Y. Kotaki, H. Sudo, H. Ishikawa, S. Yamakoshi, and H. Imai, "Stability in Single Longitudinal Mode Operation in GaInAsP/InP Phase-Adjusted DFB Lasers," *IEEE Journal of Quantum Electronics*, Vol. QE-23, No. 6, pp. 804-814, June 1987.

[Stre75a] W. Streifer, R. D. Burnham, and D. R. Scifres, "Effect of External Reflectors on Longitudinal Modes of Distributed Feedback Lasers," *IEEE Journal of Quantum Electronics*, Vol. QE-11, No. 4, pp. 154-161, April 1975.

[Stre75b] W. Streifer, D. R. Scifres, and R. D. Burnham, "Coupling Coefficients for Distributed Feedback Single- and Double-Heterostructure Diode Lasers," *IEEE Journal of Quantum Electronics*, Vol. QE-11, No. 11, pp. 867-873, November 1975.

[Stre76a] W. Streifer, D. R. Scifres, and R. D. Burnham, "Analysis of Grating-Coupled Radiation in GaAs:GaAlAs Lasers and Waveguides," *IEEE Journal of Quantum Electronics*, Vol. QE-12, No. 7, pp. 422-428, July 1976.

[Stre76b] W. Streifer, R. D. Burnham, and D. R. Scifres, "Analysis of Grating-Coupled Radiation in GaAs:GaAlAs Lasers and Waveguides--II: Blazing Effects," *IEEE Journal of Quantum Electronics*, Vol. QE-12, No. 8, pp. 494-499, August 1976.

[Stre76c] W. Streifer, R. D. Burnham, and D. R. Scifres, "Radiation Losses in Distributed Feedback Lasers and Longitudinal Mode Selection," *IEEE Journal of Quantum Electronics*, Vol. QE-12, No. 11, pp. 737-739, November 1976.

[Stre77] W. Streifer, D. R. Scifres, and R. D. Burnham, "Coupled Wave Analysis of DFB and DBR Lasers," *IEEE Journal of Quantum Electronics*, Vol. QE-13, No. 4 , pp. 134-141, April 1977.

[Sudo93] T. K. Sudoh, Y. Nakano, K. Tada, K. Kikuchi, T. Hirata, and H. Hosomatsu, "Self-Suppression Effect of Longitudinal Spatial Hole Burning in Absorptive-Grating Gain-Coupled DFB Lasers," *IEEE Photonics Technology Letters*, Vol. 5, No. 11, pp.1276-1278, November, 1993.

[Sudo94] T. K. Sudoh, Y. Nakano, K. Tada, and T. Hirata, "Anomalous Dynamic Wavelength Chirp in Gain-Switched Short Optical Pulses from Absorptive-Grating Gain-Coupled DFB Lasers," *Proceedings: 14th IEEE International Semiconductor Laser Conference*, pp. 53-54, September 1994.

[Tami77] T. Tamir and S. T. Peng, "Analysis and Design of Grating Couplers," *Applied Physics*, Vol. 14, pp. 235-254, 1977.

[Tkac86] R. W. Tkach, and A. R. Chraplyvy, "Regimes of Feedback Effects in 1.5-μm Distributed Feedback Lasers," *IEEE Journal of Lightwave Technology*, Vol. LT-4, No. 11, pp. 1655-1661, November 1986.

[Tsan94a] C. F. Tsang, D. D. Marcenac, J. E. Carroll, and L. M. Zhang, "Comparison Between 'Power Matrix Model' and 'Time Domain Model' in Modelling Large Signal Responses of DFB Lasers," *IEE Proc.-Optoelectron.*, Vol. 141, No. 2, pp. 89-96, April 1994.

[Tsan94b] W. T. Tsang, M. C. Wu, Y. K. Chen, F. S. Choa, R. A. Logan, S. N. G. Chu, A. M. Sergent, P. Magill, K. C. Reichmann, and C. A. Burrus, "Long-Wavelength InGaAsP/InP Multiquantum Well Distributed Feedback and Distributed Bragg Reflector Lasers Grown by Chemical Beam Epitaxy," *IEEE Journal of Quantum Electronics*, Vol. 30, No. 6, pp. 1370-1380, June 1994.

[Uomi91] K. Uomi, T. Tsuchiya, M. Aoki, and N. Chinone, "Oscillation Wavelength and Laser Structure Dependence of Nonlinear Damping Effect in Semiconductor Lasers," *Applied Physics Letters*, Vol. 58, No. 7, pp. 675-677, 18 February 1991.

[Vank89] P. Vankwikelberge, F. Buytaert, A. Franchois, R. Baets, P. I. Kuindersma, and C. W. Fredriksz, "Analysis of the Carrier-Induced FM Response of DFB Lasers: Theoretical and Experimental Case Studies," *IEEE Journal of Quantum Electronics*, Vol. 25, No. 11, pp. 2239-2254, November 1989.

[Vank90] P. Vankwilelberge, G. Morthier, and R. Baets, "CLADISS--A Longitudinal Multimode Model for the Analysis of the Static Dynamic and Stochastic Behavior of Diode Laser with Distributed Feedback," *IEEE Journal of Quantum Electronics*, Vol. 26, No. 10 , pp.1728-1741, October 1990.

[West86] L. D. Westbrook, "Measurements of dg/dN and dn/dN and Their Dependence on Photon Energy in λ=1.5 μm InGaAsP Laser Diodes," *IEE Proceedings--Optoelectron*, Vol. 133, No. 2, pp. 135-142, April 1986.

[Whit89] J. E. A. Whiteaway, G. H. B. Thompson, A. J. Collar, and C. J. Armistead, "The Design and Assessment of λ/4 Phase-Shifted DFB Laser Structures," *IEEE Journal of Quantum Electronics*, Vol. 25, No. 6, pp. 1261-1279, June 1989.

[Whit92] J. E. A. Whiteaway, B. Garrett, G. H. B. Thompson, A. J. Collar, C. J. Armistead, and M. J. Fice, "The Static and Dynamic Characteristics of Single and Multiple Phase-Shifted DFB Laser Structures," *IEEE Journal of Quantum Electronics*, Vol. 28, No. 5, pp. 1277-1293, May 1992.

[Wrig93] A. P. Wright, A. T. R. Briggs, A. D. Smith, R. S. Baulcomb and K. J. Warbrick, "22 GHz-Bandwidth 1.5 μm Compressively Strained InGaAsP MQW Ridge-Waveguide DFB Lasers," *Electronics Letters*, Vol. 29, No. 21, pp. 1848-1849, 14 October 1993.

[Yama78a] Y. Yamamoto, T. Kamiya, and H. Yanai, "Improved Coupled Mode Analysis of Corrugated Waveguides and Lasers," *IEEE Journal of Quantum Electronics*, Vol. QE-14, No. 4, pp. 245-258, April 1978.

[Yama78b] M. Yamada and Y. Suematsu, "Theory of Single Mode Injection Lasers Taking Account of Electronic Intra-band Relaxation," *Japanese Journal of Applied Physics*, pp. 347-354, 1978.

[Yari75] A. Yariv and A. Gover, "Equivalence of the coupled-mode and Floquet-Bloch formalisms in periodic optical waveguides," *Applied Physics Letters*, Vol.26, No. 9, 1 May 1975, pp. 537--539.

[Yu93] S. F. Yu, L. M. Zhang, R. G. S. Plumb, and J. E. Carroll, "Effect of External Reflectors on Radiation Profile of Grating Coupled Surface Emitting Lasers," *IEE Proceedings-J*, Vol. 140, No. 1, pp. 30-38, February 1993.

[Yu94] S. F. Yu, R. G. S. Plumb, L. M. Zhang, M. C. Nowell, and J. E. Carroll, "Large-Signal Dynamic Behavior of Distributed-Feedback Lasers Including Lateral Effects," *IEEE Journal of Quantum Electronics*, Vol. QE-30, No. 8, pp. 1740-1750, August 1994.

[Zhan92] L. M. Zhang and J. E. Carroll, "Large-Signal Dynamic Model of the DFB Laser," *IEEE Journal of Quantum Electronics*, Vol. QE-28, No. 3, pp. 604-611, March 1992.

[Zhan94] L. M. Zhang, S. F. Yu, M. C. Nowell, D. D. Marcenac, J. E. Carroll, and R. G. S. Plumb, "Dynamic Analysis of Radiation and Side-Mode Suppression in a Second-Order DFB Laser Using Time-Domain Large-Signal Traveling Wave Model," *IEEE Journal of Quantum Electronics*, Vol. 30, No. 6, pp. 1389-1395, June 1994.

[Zory93] P. S. Zory, Jr., "Quantum Well Lasers," San Diego: Academic Press, Inc., 1993.

[Zoz94a] J. Zoz and B. Borchert, "Dynamic Behaviour of Complex-Coupled DFB Lasers with In-Phase Absorptive Grating," *Electronics Letters*, Vol. 30, No. 1, pp. 39-40, 6th January 1994.

APPENDICES

Appendix A. Derivations

A.1 Noise Power

As pointed out in *Section 2.4.2*, the spontaneous emission noise vector ($\vec{\mathbf{P}}$) at frequency ω is unknown because of the random phase (being equally likely over 2π radians). Nevertheless, its magnitude can be calculated because it is a function of the carrier density, N. Moreover, the average power that is coupled into the forward and reverse waves can be assumed to be equal. It is given by

$$\varphi = i_F^* i_F = i_R^* i_R = \zeta_1 l\, \omega N^2 \tag{A.1-1}$$

where ζ_1 is a coefficient based on the device structure and the material parameters. ζ_1 is chosen such that the unit of φ is power per unit angular frequency. It is given by

$$\zeta_1 = \frac{1}{2}\left(\frac{\theta_{\|}\,\theta_{\perp}}{4\,n}\right)\left(\frac{h\,B_N\,d\,w}{2\pi\,\Delta\omega_{sp}}\right) \tag{A.1-2}$$

where $\theta_{\|}$ (or $\theta_{\perp}$) is the FWHM of the far field divergence angle parallel (perpendicular) to the junction plane, h is the Planck's constant, and B_N is the bimolecular carrier recombination coefficient, d and w are the active layer thickness and the lateral width of the waveguide, respectively, and $\Delta\omega_{sp}$ is the FWHM of the spontaneous emission spectrum in optical frequency. Equation (A.1-2) includes a spontaneous emission coupling factor given by

$$f_s = \frac{\theta_{\|}\,\theta_{\perp}}{4\,n}\,\frac{1}{\Delta\omega_{sp}}\,. \tag{A.1-3}$$

In this expression, there is an assumption that the spontaneous emission power is evenly distributed over $\Delta\omega_{sp}$. This assumption should not incur any significant error because the bandwidth of the Bragg grating is much smaller than the bandwidth of the noise spectrum. The noise power that is effectively coupled into the laser cavity is further reduced by a factor of the solid angle subtended by the waveguide divided by 4π. Alternatively, this factor can be replaced by a constant which is more commonly encountered.

Since the noise power originates from between adjacent segments, the carrier densities and the segment lengths of both segments have to be taken into account. For better accuracy, the following conversion is needed:

$$l\,N^2 \rightarrow \frac{l_{k-1}}{2} N_{k-1}^2 + \frac{l_k}{2} N_k^2 \quad \text{for } (k\text{-}1)\text{- and } k\text{-th segments,} \tag{A.1-4}$$

except for the first and the last segment in which full segment lengths are used.

A.2 Product of Field Vector and Its Adjoint

The calculation of the product of the field vector and its adjoint involves the products of the spontaneous currents. Because the spontaneous field is incoherent and the left and right flows are equal, the following relationships are valid:

$$|i_{Fk}| = |i_{Rk}| ;$$

$$i_{Fm}{}^{*} i_{Fn} = |i_{Fm}|^2 \delta_{mn} ;$$

$$i_{Rm}{}^{*} i_{Rn} = |i_{Rm}|^2 \delta_{mn} ;$$

$$i_{Fm}{}^{*} i_{Rn} = 0 \text{ ; and}$$

$$i_{Rm}{}^{*} i_{Fn} = 0 . \tag{A.2-1}$$

Here, '$*$' denotes complex conjugate. In the following expressions, '$\dagger$' and 'T' represent conjugate transpose and transpose, respectively. Let $\varphi_k = |i_{Fk}|^2 = |i_{Rk}|^2$, and $\mathbf{Y} = \begin{bmatrix} y_{11} & y_{12} \\ y_{21} & y_{22} \end{bmatrix}$. Then,

$$\vec{\mathbf{P}}_k^{\dagger}\mathbf{Y}\vec{\mathbf{P}}_k = (y_{11} + y_{22})\,\varphi_k \text{, and} \tag{A.2-2}$$

$$\vec{\mathbf{P}}_k^{\dagger}\mathbf{Y}^{\dagger}\mathbf{Y}\vec{\mathbf{P}}_k = \left(|y_{11}|^2 + |y_{12}|^2 + |y_{21}|^2 + |y_{22}|^2\right)\varphi_k \,. \tag{A.2-3}$$

With these relationships, the field vector product can be calculated as follows. First, we expand each field vector in matrix form in terms of the matrices defined by:

$$\mathbf{X}_{Ik} = \mathbf{D}_I\mathbf{K}^{-1}\mathbf{S}^{(k+1)},$$

$$\mathbf{X}_{rk} = \mathbf{D}_r\mathbf{K}^{-1}\mathbf{S}^{(k+1)}, \tag{A.2-4}$$

$$\mathbf{Y}_k^{(m)} = \left(\prod_{j=1}^{m}\mathbf{T}_j\right)\mathbf{X}_{Ik} + \mathbf{I}\delta_{mk} \tag{A.2-5}$$

and the identity matrix, $\mathbf{I} = \begin{bmatrix} 1 & 0 \\ 0 & 1 \end{bmatrix}$. $\mathbf{Y}_k^{(m)}$ is related to $\vec{\mathbf{V}}_k$ by

$$\vec{\mathbf{V}}_k = \begin{bmatrix} \mathbf{Y}_k^{(1)} & \mathbf{Y}_k^{(2)} & \cdots & \mathbf{Y}_k^{(M-1)} \end{bmatrix}\begin{bmatrix} \vec{\mathbf{P}}_1 & \cdots & \vec{\mathbf{P}}_{M-1} \end{bmatrix}^{T}. \tag{A.2-6}$$

From Eq. (2.4.2-4), we get

$$\vec{\mathbf{V}}_0 = \begin{bmatrix} \mathbf{X}_{I1} & \mathbf{X}_{I2} & \cdots & \mathbf{X}_{IM-1} \end{bmatrix}\begin{bmatrix} \vec{\mathbf{P}}_1 & \cdots & \vec{\mathbf{P}}_{M-1} \end{bmatrix}^{T};$$

$$\vec{\mathbf{V}}_1 = \begin{bmatrix} (\mathbf{T}_1\mathbf{X}_{I1} + \mathbf{I}) & \mathbf{T}_1\mathbf{X}_{I2} & \cdots & \mathbf{T}_1\mathbf{X}_{IM-1} \end{bmatrix} \cdot \begin{bmatrix} \vec{\mathbf{P}}_1 & \cdots & \vec{\mathbf{P}}_{M-1} \end{bmatrix}^{T}$$

or

$$\vec{\mathbf{V}}_1 = \begin{bmatrix} \left(\mathbf{T}_1\mathbf{Y}_1^{(0)} + \mathbf{I}\right) & \mathbf{T}_1\mathbf{Y}_2^{(0)} & \cdots & \mathbf{T}_1\mathbf{Y}_{M-1}^{(0)} \end{bmatrix}\begin{bmatrix} \vec{\mathbf{P}}_1 & \cdots & \vec{\mathbf{P}}_{M-1} \end{bmatrix}^{T};$$

$$\vec{\mathbf{V}}_2 = \begin{bmatrix} \mathbf{T}_2\mathbf{Y}_1^{(1)} & \left(\mathbf{T}_2\mathbf{Y}_2^{(1)} + \mathbf{I}\right) & \cdots & \mathbf{T}_2\mathbf{Y}_{M-1}^{(1)} \end{bmatrix}\begin{bmatrix} \vec{\mathbf{P}}_1 & \cdots & \vec{\mathbf{P}}_{M-1} \end{bmatrix}^{T};$$

$\vdots$

$$\overrightarrow{\mathbf{V}_{M-1}}=\left[\ \mathbf{T}_{M-1}\mathbf{Y}_1^{(M-2)} \quad \cdots \quad \mathbf{T}_{M-1}\mathbf{Y}_{M-2}^{(M-2)} \quad \left(\mathbf{T}_{M-1}\mathbf{Y}_{M-1}^{(M-2)}+\mathbf{I}\right)\right] \cdot\left[\ \overrightarrow{\mathbf{P}_1} \quad \cdots \quad \overrightarrow{\mathbf{P}_{M-1}}\right]^{T};$$

and

$$\overrightarrow{\mathbf{V}_M}=\left[\ \mathbf{T}_M\mathbf{Y}_1^{(M-1)} \quad \cdots \quad \mathbf{T}_M\mathbf{Y}_{M-1}^{(M-1)} \ \ \mathbf{T}_M\mathbf{Y}_{M-1}^{(M-1)}\ \right]\left[\ \overrightarrow{\mathbf{P}_1} \quad \cdots \quad \overrightarrow{\mathbf{P}_{M-1}}\right]^{T}$$

or

$$\overrightarrow{\mathbf{V}_M}=\left[\ \mathbf{X}_{r1} \ \ \mathbf{X}_{r2} \quad \cdots \quad \mathbf{X}_{rM-1}\ \right]\left[\ \overrightarrow{\mathbf{P}_1} \quad \cdots \quad \overrightarrow{\mathbf{P}_{M-1}}\right]^{T}. \tag{A.2-7}$$

At the k-th segment,

$$\overrightarrow{\mathbf{V}_k}^{\dagger}\overrightarrow{\mathbf{V}_k} = \left(\sum_{j=1}^{M-1}\mathbf{Y}_j^{(k)}\overrightarrow{\mathbf{P}_j}\right)^{\dagger}\left(\sum_{i=1}^{M-1}\mathbf{Y}_i^{(k)}\overrightarrow{\mathbf{P}_i}\right)$$

$$=\sum_{i=1}^{M-1}\sum_{j=1}^{M-1}\left(\overrightarrow{\mathbf{P}_j}^{\dagger}\mathbf{Y}_j^{(k)\dagger}\mathbf{Y}_i^{(k)}\overrightarrow{\mathbf{P}_i}\right)$$

By applying the relationships in Eq. (A.2-1), it becomes

$$\overrightarrow{\mathbf{V}_k}^{\dagger}\overrightarrow{\mathbf{V}_k}=\sum_{j=1}^{M-1}\left(\overrightarrow{\mathbf{P}_j}^{\dagger}\mathbf{Y}_j^{(k)\dagger}\mathbf{Y}_j^{(k)}\overrightarrow{\mathbf{P}_j}\right) \tag{A.2-8}$$

With Eq. (A.2-3), we obtain

$$\overrightarrow{\mathbf{V}_k}^{\dagger}\overrightarrow{\mathbf{V}_k}=\sum_{j=1}^{M-1}\left(\left|\left(\mathbf{Y}_j^{(k)}\right)_{11}\right|^2+\left|\left(\mathbf{Y}_j^{(k)}\right)_{12}\right|^2+\left|\left(\mathbf{Y}_j^{(k)}\right)_{21}\right|^2+\left|\left(\mathbf{Y}_j^{(k)}\right)_{22}\right|^2\right)\varphi_j, \tag{A.2-9}$$

or

$$\overrightarrow{\mathbf{V}_k}^{\dagger}\overrightarrow{\mathbf{V}_k}=\sum_{j=1}^{M-1}\mathrm{tr}\left(\left(\mathbf{Y}_j^{(k)}\right)^{\dagger}\left(\mathbf{Y}_j^{(k)}\right)\right)\varphi_j, \tag{A.2-10}$$

where $\left(\mathbf{Y}_j^{(k)}\right)_{mn}$ is the matrix element of $\mathbf{Y}_j^{(k)}$ with (m, n = 1,2) and '$\mathrm{tr}\left(\mathbf{Y}^{\dagger}\mathbf{Y}\right)$' is the trace of $\mathbf{Y}^{\dagger}\mathbf{Y}$, which is the sum of the magnitude-square of each of the elements of $\mathbf{Y}$. Note that no phase information of the spontaneous emission is needed in the expression.

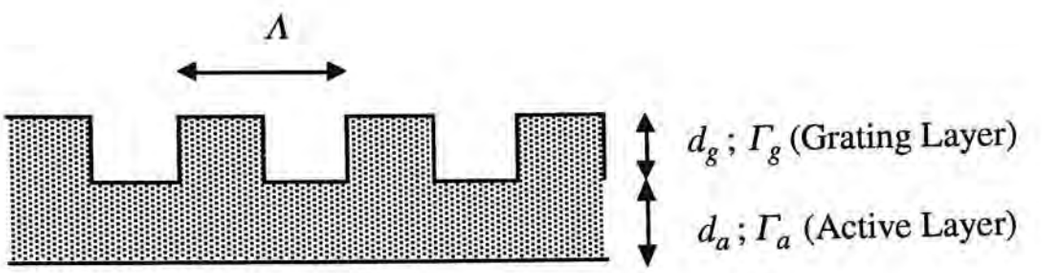

Fig. A.1 A schematic drawing of the gain grating and the active region in a GCDFB.

A.3 Gain-Coupling Coefficient

Perhaps, the most important difference between gain-grating and loss-grating is that the gain-coupling coefficient, κ_g, is a function of the gain step in the grating layer (that is, carrier-dependent). In general, the gain-coupling is caused by the modulation of the optical confinement factor rather than that on the carrier density because the carrier diffusion length is larger than the grating period. An exception to this has been reported in which the gain grating is formed on a current blocking layer [Kazm94] which in effect modulates the carrier density directly.

For simplicity, we assume that there is no absorptive grating. Moreover, the gain grating is formed on top of the active layer and that it has a square profile with 50% duty cycle (see Fig. A.1). GCDFB devices have been fabricated in this manner [Li93b]. Others have the gain grating formed on a patterned-providing layer [Luo91], [Inou91]. The effective confinement factor for the calculation of the gain can therefore be approximated by

$$\Gamma = \Gamma_a + \frac{\Gamma_g}{2} \tag{A.3-1}$$

where Γ_a is the confinement factor of the active layer and Γ_g, the confinement factor of the grating layer. In this expression, the transverse optical intensity distribution is

assumed to be constant over the active and the grating layers. Similarly, the effective active layer thickness is given by

$$d = d_a \left(1 + \frac{\Gamma_g}{2\,\Gamma_a}\right) \tag{A.3-2}$$

where d_a is the thickness of the unpatterned active layer. These expressions are valid as long as the layer thicknesses are small. The resulting step change in gain is written as

$$\Delta g \cong \frac{\Gamma_g a\,(N - N_t)}{2\,(1 + \varepsilon\,\psi)} = \frac{\Gamma_g}{\Gamma} g \tag{A.3-3}$$

where g is the average gain. As a result, we obtain [Davi91a]

$$\kappa_g = \frac{\Delta g}{2\pi} \cong \frac{1}{2\pi}\left(\frac{\Gamma_g}{\Gamma} g\right). \tag{A.3-4}$$

There are a number of theoretical studies on the effect of standing waves on the DFB lasers. The standing wave phenomenon aggravates the gain nonlinearity. Because the maximum gain compression occurs at the peaks of the standing wave, where the maximum stimulated emission also occurs, the gain suppression factor is enhanced [Pan92]. The modified gain suppression factor has been included in the transmission-line laser model [Lowe94]. On the other hand, for GCDFB or LCDFB lasers, the gain is enhanced because the standing wave has maxima at the points of high gain and minima at the points of low gain. This effect explains the negative threshold gain that is possible in GCDFB lasers. To include this effect, the stimulated emission rate in the rate equation has to be modified with a standing wave factor [Davi92], [Baet93]. However, the calculation of this factor is rather tedious. An approximation has been included in our model but we found that the effect on the static laser performance is hardly noticeable.

In addition to the gain-coupling effects, the modulation in gain also gives rise to an index step change (that is index grating) due to carrier-induced index change. The index step is related by

$$\Delta n = -\frac{\alpha_H \lambda_o}{4\pi} a \Gamma_g (N-N_t) \tag{A.3-5}$$

and the induced index-coupling coefficient is simply given by [Kudo92], [Olof92],

$$\kappa_i = \frac{\Delta n}{\lambda_o}. \tag{A.3-6}$$

Therefore, as the drive current increases, the gain-coupling becomes stronger, and this in turns gives rise to an induced index-coupling that is antiphase. If there is a built-in index grating in the laser structure, this induced index-grating may either enhance or reduce the net coupling strength depending on the polarity of the original index step. In general, purely gain-coupled DFB can only be obtained by very careful design because of this induced index-grating [Luo90]. Another difficulty in the design is the control of the grating coupling coefficients (both gain and index) because of the carrier dependency.

Appendix B. Subroutines in Computer Program

This appendix lists all the subroutines in the computer program. They are grouped into four files by their functionality as described in *Section 2.4.3*. Also consult Fig. 2.11 and Fig. 2.12a through Fig. 2.12d for the program flowchart and the subroutine calling sequences.

B.1 Subroutines in 'drive.f'

- *Program 'lsdfb'*

  This is the main program that controls the program flows. It reads device parameters and program controls and transfers the control to the designated subroutines according to the input directive.

- *Subroutine 'dfltpr'*

  It sets default parameter values.

- *Subroutine 'rsdflt'*

  It resets the default parameters back to their original values.

- *Subroutine 'getdata'*

  It gets the 3 character key directive for reading inputs from an input file.

- *Subroutine 'rdmat'*

  It reads the material parameters from the input file.

- *Subroutine 'rdgra'*

  It reads the grating parameters from the input file.

- *Subroutine 'rddim'*

  It reads the device dimensions from the input file.

- *Subroutine 'rdcnt'*

  It reads the control directive from the input file; e. g. convergence criteria.

- *Subroutine 'rddrv'*

  It reads the estimated threshold current and the final drive current from the input file.

- *Subroutine 'rdprc'*

  It reads the procedure directive such as 'yield' (to perform single-mode yield), 'adaptive' (to use adaptive stepsize), etc..

- *Subroutine 'errstp'*

  It interrupts the program execution especially when an error is encountered during the reading of the input file.

- *Function 'sval'*

  This function gets parameter values from the ASCII characters in the input file.

- *Subroutine 'fopen'*

  It opens the file specified by the calling command; e. g. input and output files.

- *Subroutine 'apnm'*

  It appends two names without blanks in between.

- *Subroutine 'chkdata'*

  It outputs the parameter values obtained to an output file and computer monitor for verification purposes.

B.2 Subroutines in 'Core.f'

- *Subroutine 'abovethr'*

  This subroutine is an implementation of the nonlinear DFB model (above-threshold model). It calculates the laser behavior at each current step by

finding a self-consistent solution. The user has a choice of using constant or adaptive current stepsize. If adaptive current stepsize is selected, the stepsize is reduced whenever a converged solution is not obtained or when the power is rising too rapidly. The relative output power versus frequency is stored in a file with the suffix '.abv' in its filename. The longitudinal distribution of the carrier density, photon density, nearfield intensity, and the real and imaginary grating coupling coefficients are saved in a file with the suffix '.nf'. Finally, a summary chart is written to the output file (with suffix '.out') which contains information such as the lasing frequency, spectral linewidth, SMSR, and the mean values of the photon distribution variance, the effective index and the grating coupling coefficients. All of them are listed as a function of injection current.

- *Subroutine 'subthr'*

  This subroutine performs linear analyses of DFB lasers (subthreshold model). It basically does the same calculations as the nonlinear model except without any iterations or carrier-induced index changes. It calculates the spectrum as a function of g_{th} assuming that none of the modes has reached threshold. The results are stored in a file with the filename suffix '.sub'. It also calculates the yield due to uncertain facet phases. It first computes the threshold of the first lowest-loss mode and then the second lowest-loss mode assuming that the first mode has not reached threshold. The threshold gain difference, Δg_{th}, between the two modes can then be obtained. The optical spectrum of the first mode at threshold is saved. This exercise is repeated for difference combinations of the facet phases from 0 to 2π. The resulting Δg_{th} can then be used to compute the single-mode yield. The saved spectra are stored in a file with a filename suffix of '.yld'.

- *Subroutine 'gainstep'*

  It seeks a self-consistent solution with or without antiguiding effects.

- *Subroutine 'nffile'*

  This subroutine outputs the 'zoom-in' spectrum (in frequency) to file with suffix '.nf'.

- *Subroutine 'Ndoutput'*

  It prepares the carrier density data for output to a file with suffix '.nf'.

- *Subroutine 'antiguide'*

  This subroutine locates the self-consistent solution with the effective index as a convergence criterion. The effective index is only modified after the solution has passed other convergence tests. The trial solution is estimated by the secant method.

- *Subroutine 'solution'*

  This checks the converged solution to make sure that it does not incur large sudden drop in the photon density or output power. If it does, another trial solution is attempted until an acceptable solution is found or the maximum number of attempts is exceeded.

- *Subroutine 'convergence'*

  This subroutine performs a search for a converged solution. It computes the power and photon density over a broad frequency range (*'freqloop'*), performs a frequency expansion to improve the accuracy (*'zoomin'*), reconstructs the optical spectrum with the results, and checks for self-consistency. Finally, this process is repeated until a converged solution is found or until the number of iterations becomes too large (*'errtreat'*).

- *Subroutine 'freqloop'*

  This subroutine computes the transfer matrices and then the output power and photon density over a frequency range.

- *Subroutine 'zoomin'*

  This subroutine calculates the output power and photon density over an expanded frequency range at each lasing mode. This process is done by locating the lasing modes and by adding more data points in the frequency axis. Further *zoom-in* is performed until the FWHM of the lasing mode converges. Finally, the spectrum is reconstructed in the original frequency scale.

- *Subroutine 'freqlpzm'*

  It is essentially the same as the subroutine '*freqloop*' except that the array sizes of all the frequency dependent variables are increased to reflect the changes in the number of data points.

- *Subroutine 'Pandp'*

  This subroutine calculates the facet output power, the photon density, and the nearfield intensity of the device.

- *Subroutine 'smatrix'*

  This subroutine computes the partial product, $\mathbf{S}^{(m)}$, of the 2×2 transfer matrices, $\mathbf{T}_k$, such that $\mathbf{S}^{(m)} = \prod_{k=m}^{M} \mathbf{T}_k$.

- *Subroutine 'TMdfb'*

  This subroutine constructs the transfer matrix for a DFB segment as expressed in Eq. (2.3.1-4).

- *Subroutine 'TMqwave'*

  This subroutine constructs the transfer matrix to include a quarterwave phase-shifter in the center of the segment. The transfer matrix for the quarterwave phase-shifter is given by:

$$\mathbf{T}_{\lambda/4} = \begin{pmatrix} -i & 0 \\ 0 & i \end{pmatrix}. \qquad \text{(B-1)}$$

B.3 Subroutines in 'initial.f'

- *Subroutine 'setthr'*

  This subroutine sets the initial values for the variables and parameters used in the subthreshold analysis.

- *Subroutine 'setvalue'*

  This subroutine sets the initial values for the variables and parameters used in the above-threshold analysis.

- *Subroutine 'setsoln'*

  This subroutine stores the calculated output power for later use.

- *Subroutine 'Ginitial'*

  This subroutine sets the initial values of the carrier density and the gain coefficient for each current loop with the input current density.

- *Subroutine 'Wupdate'*

  This subroutine updates the values of carrier density and the gain coefficient for each solution-check loop (subroutine '*solution*').

- *Subroutine 'zoominit'*

  This subroutine initializes the variables and parameters for the subroutine '*zoomin*'.

B.4 Subroutines in 'misc.f'

- *Subroutine 'carrier'*

  This subroutine solves for the carrier density N from the cubic rate equation (Eq. (2.4.2-25)) relating N to the current density J and the total photon density ψ in the segment. Standard formulas are used and double precision is needed to compute the coefficients.

- *Subroutine 'gain'*

  This subroutine calculates the field gain coefficient from the carrier density and the photon density according to Eq. (2.2.2-1).

- *Subroutine 'setnoise'*

  This subroutine calculates the spontaneous emission noise power from the carrier densities of two adjacent segments according to *Appendix A.1*.

- *Subroutine 'setneff'*

  This subroutine calculates the new effective index as a function of the carrier densities according to Eq. (2.2.3-1).

- *Subroutine 'setdweff'*

  This subroutine calculates the new frequency deviation from Bragg condition caused by the carrier-induced index change based on Eq. (2.2.3-2).

- *Subroutine 'Linpeaks'*

  This subroutine locates the maxima in a curve and their respective spreads. It ignores peaks that have poor *peak-to-valley* ratio, low power, and those with relatively large FWHM.

- *Subroutine 'sumPpzm'*

  This subroutine sums the power and photon density over frequency.

- *Subroutine 'sumpow'*

  This subroutine sums the power over frequency.

- *Subroutine 'errtreat'*

  This subroutine prescribes a treatment when error occurs. It makes use of the secant method to obtain faster convergence.

- *Subroutine 'secant'*

  This subroutine uses the secant method to set the trial solution for the next iteration.

- *Subroutine 'loopreset'*

  This subroutine stores the initial photon density distribution for later use.

- *Subroutine 'staircase3'*

  This subroutine arranges the data points in an array for better visualization when plotted.

- *Subroutine 'vmagsq'*

  This subroutine calculates the magnitude-square of a complex vector.

- *Subroutine 'average'*

  This subroutine calculates the mean value of a variable with spatial dependence over the middle section only.

- *Subroutine 'variance'*

  This subroutine calculates the normalized variance of a parameter with spatial dependence over the middle section according to Eq. (2.4.2-20).

- *Subroutine 'sortd'*

  This subroutine sorts an array of data in descending order.

- *Subroutine 'm2trace'*

  This subroutine calculates the trace of a 2×2 matrix, **Y**, as follows:

$$\mathrm{tr}\left(\mathbf{Y}^{\dagger}\mathbf{Y}\right)=|y_{11}|^2+|y_{12}|^2+|y_{21}|^2+|y_{22}|^2, \tag{B-2}$$

  where y_{ij} denotes the matrix element in the *i*th row and *j*th column.

- *Subroutine 'm2invrs'*

  This subroutine calculates the inverse of a 2×2 matrix.

- *Subroutine 'm2trns'*

  This subroutine calculates the transpose of a 2×2 matrix.

- *Subroutine 'm2conj'*

  This subroutine calculates the complex conjugate of a 2×2 matrix.

- *Subroutine 'm2set'*

  This subroutine stores the input 2×2 matrix into another 2×2 matrix.

- *Subroutine 'm2add'*

  This subroutine performs the addition of two 2×2 matrices.

- *Subroutine 'm2mlt'*

  This subroutine calculates the product of two 2×2 matrices.

- *Subroutine 'm21mlt'*

  This subroutine calculates the product (a 2×1 vector) of a 2×2 matrix with a 2×1 vector.

- *Subroutine 'm1add'*

  This subroutine adds an identity matrix to a 2×2 matrix.

- *Subroutine 'm2det'*

  This subroutine computes the determinant of a 2×2 matrix.

Appendix C. List of Figures

Appendix D. List of Tables

Appendix E. List of Abbreviations and Acronyms

Abbreviation	*Name*
AR	Antireflection Coating
CAD	Computer Aided Design
CCDFB	Complex-Coupled DFB Laser
CL	As-Cleaved Facet
cw	Continuous Wave
DBR	Distributed Bragg Reflector
DFB	Distributed Feedback Laser
DFBDBR	Distributed Feedback Distributed Bragg Reflector Laser
FP	Fabry Perot Laser
GCDFB	Gain-Coupled DFB Laser
GRINSCH	Graded Index Separate Confinement Heterostructure
HR	High Reflection Coating
ICDFB	Index-Coupled DFB Laser
LCDFB	Loss-Coupled DFB Laser
LSHB	Longitudinal Spatial Hole Burning
MOPA	Master-Oscillator-Power-Amplifier
MQW	Multiple Quantum Wells
OEIC	Optoelectronic Integrated Circuit
PMM	Power Matrix Method
QWDFB	Quarterwave Phase-Shifted DFB Laser
SMSR	Side-Mode-Suppression Ratio (in dB)
SQW	Single Quantum Well
WDM	Wavelength Division Multiplexing

Appendix F. List of Symbols

Symbols	*Name*	*Value and Unit*
a	Differential gain	cm^2
A_o	Cross-sectional area of the optical intensity	μm^2
B_N	Bimolecular carrier recombination coefficient	$cm^3 \cdot s^{-1}$
C_N	Auger carrier recombination coefficient	$cm^6 \cdot s^{-1}$
d	Thickness of active layer	μm
e	Electron charge	1.602×10^{-19} coul
$E(x,z)$	TE-polarized electric field	V/m
f_s	Spontaneous coupling factor	$(2\pi GHz)^{-1}$
F	Complex amplitude of the forward-propagating wave	
g	Field gain coefficient	cm^{-1}
g_{th}	Threshold gain coefficient	cm^{-1}
h	Planck's constant	6.626×10^{-13} $mW \cdot ns^2$
i_F	Complex spontaneous driving current for the forward wave	$\sqrt{mW \cdot (2\pi GHz)^{-1}}$
i_R	Complex spontaneous driving current for the reverse wave	$\sqrt{mW \cdot (2\pi GHz)^{-1}}$
I_{th}	Threshold current	mA
J	Current density	$mA \cdot \mu m^{-2}$
l	Length of laser segment	μm
L	Length of laser cavity	μm
L_m	Length of the middle pumped section in a three-section laser	μm
L_{tot}	Total length of laser cavity in multisection device	μm
M	Maximum number of divided segments	
n	Effective index of refraction	
n_g	Effective group index of refraction	
N	Carrier density	cm^{-3}
N_t	Carrier density at transparency	cm^{-3}
$\vec{\mathbf{P}}$	Spontaneous emission noise vector	
P_l	Output power from the left end-facet	mW

P_r	Output power from the right end-facet	mW
P_{se}	Power of surface emission	mW
R	Complex amplitude of the reverse-propagating wave	
r_1	Reflection coefficient of the left facet	
r_2	Reflection coefficient of the right facet	
T	Temperature	°C
$\mathbf{T}$	2×2 transfer matrix	
$\vec{\mathbf{V}}$	Field amplitude vector	
v_g	Group velocity of light in active region	$m \cdot s^{-1}$
w	Waveguide width	μm
$w_{\parallel}$	Lateral beam width (parallel to junction plane)	μm
$w_{\perp}$	Transverse beam width (perpendicular to junction plane)	μm
x	Distance in the transverse direction	μm
z	Distance in the longitudinal direction	μm
α	Power loss coefficient	cm^{-1}
α_H	Linewidth enhancement factor	
β	Propagation constant in wavenumber	cm^{-1}
β_B	Bragg wavenumber	cm^{-1}
Γ	Optical confinement factor of the active layer	
$\Delta\alpha$	Step change of loss coefficient in absorptive grating	cm^{-1}
$\Delta\beta$	Deviation from Bragg condition in wavenumber	cm^{-1}
Δf_{sp}	Bandwidth of spontaneous emission spectrum	nm
Δg_{th}	Difference in threshold gain coefficients or threshold gain margin	cm^{-1}
Δn	Change in effective index of refraction	
$\Delta\omega$	Deviation from Bragg condition in angular frequency	2πGHz
$\Delta\omega_{sp}$	Bandwidth of spontaneous emission spectrum	2πGHz
ε	Nonlinear gain suppression factor	cm^3
ε_a	Nonlinear absorption compression factor	cm^3
η	Front facet power efficiency	$mW \cdot mA^{-1}$

θ	Phase angle between the index-grating and the gain/loss-grating	radian
$\theta_{\parallel}$	Far field divergence angle parallel to the junction plane	radian
$\theta_{\perp}$	Far field divergence angle perpendicular to the junction plane	radian
κ	Complex grating coupling coefficient	cm^{-1}
κ_{fr}	Forward to reverse grating coupling coefficient	cm^{-1}
κ_g	Gain-grating coupling coefficient	cm^{-1}
κ_i	Induced index-grating coupling coefficient	cm^{-1}
κ_l	Loss-grating coupling coefficient	cm^{-1}
κ_{lo}	Loss-grating coupling coefficient at transparency	cm^{-1}
κ_n	Index-grating coupling coefficient	cm^{-1}
κ_{rf}	Reverse to forward grating coupling coefficient	cm^{-1}
Λ	Bragg grating period	μm
λ_B	Bragg wavelength in free space	μm
λ_g	Bandgap wavelength	μm
λ_o	Lasing wavelength in free space	μm
ξ	Grating outcoupling (radiation) coefficient	cm^{-1}
ρ	Grating teeth duty cycle	
σ_{ψ}	Normalized variance of the longitudinal distribution of the photon density	
τ	Linear carrier lifetime	ns
φ	Noise power per angular frequency	$mW\cdot(2\pi GHz)^{-1}$
ψ	Photon density	$\#/cm^{-3}$
ω	Angular frequency	$2\pi GHz$

Appendix G. List of Publications

Complex-Coupled DFB Laser

1. S. K. Liew, "Above-Threshold Analysis of Loss-Coupled DFB Lasers: Threshold Current and Power Efficiency," to be published in *IEEE Photonics Technology Letters*, December, 1995.

2. S. K. Liew, "Yield Analysis of Loss-Coupled DFB Lasers with Asymmetric Facet Coatings," submitted to *Electronic. Letters.*

DFBDBR Laser

3. So Kuen C. Liew, "Above Threshold Analysis of Three-Section DFB/DBR Lasers with Second-Order Gratings", *IEEE J. of Selected Topics in Quantum Electron.*, Vol. 1, No. 2, June 1995, pp. 363-370.

4. S. K. Liew, "Above Threshold Analysis of Three-Section DFB/DBR Lasers with Second-Order Gratings", *Proceedings: IEEE Lasers and Electro-Optics Society 1994 Annual Meeting (LEOS'94)* , Paper SL1.3, Boston, MA, pp. 99-100, Oct. 31-Nov. 3, 1994.

5. S. K. Liew, N. W. Carlson, R. Amantea, G. A. Evans, J. K. Butler, J. Andrews, N. A. Hughes, P. K. York and J. C. Connolly, "Very low Threshold InGaAs/GaAs Grating-Coupled Surface-Emitting Distributed Feedback Laser", *Technical Digest: Conference on Lasers and Electro-Optics 1993 (CLEO'93)* , Baltimore, MD, pp. 320-321, May 2-7, 1993.

6. So Kuen Liew and Nils W. Carlson, "Method for Obtaining a Collimated Near-Unity Aspect Ratio Output Beam from a DFB-GSE Laser with Good Beam Quality", *Applied Optics*, Vol. 31, No. 15, pp. 2743-2746, 20 May 1992.

7. S. K. Liew, N. W. Carlson, D. P. Bour, G. A. Evans, E. Van Gieson, "Demonstration of InGaAs/AlGaAs Strained-Layer Distributed-feedback Grating-Surface-Emitting Lasers with a Buried Second Order Grating Structure", *Appl. Phys. Lett.* 58 (3), pp. 228-230, 21 Jan. 1991.

8. S. K. Liew, N. W. Carlson, R. Amantea, D. P. Bour, G. A. Evans, E. Van Gieson, "Operation of Distributed-Feedback Grating-Surface-Emitting Laser with a Buried Grating Structure", *IEEE Lasers and Electro-Optics Society 1990 Annual Meeting (LEOS'90)*, Talk SDL2.7/TuL7.

9. N. W. Carlson, S. K. Liew, R. Amantea, D. P. Bour, G. A. Evans, E. Van Gieson, " Mode Discrimination in distributed feedback grating surface emitting lasers containing a buried second order grating", *IEEE J. of Quantum Electron.* QE-27 No. 6, pp. 1746-1752, June 1991.

10. D. P. Bour, N. W. Carlson, G. A. Evans, S. K. Liew, J. B. Kirk, and W. F. Reichert, "Surface-emitting, distributed feedback InGaAs/AlGaAs lasers by organometallic vapor phase epitaxy", *J. Appl. Phys.* 70 (9), pp. 4687-4693, 1 Nov. 1991.

Monolithic Master-Oscillator-Power-Amplifiers

11. S. K. Liew, N. W. Carlson, and R. Amantea, "Narrow Spectral Linewidth in the Far Field Zone of Active-grating Surface Emitting Semiconductor Laser-Amplifier", *IEEE Photonics Technology Letters*, 5 (2), pp. 209-211, Feb. 1993.

12. S. K. Liew, N. W. Carlson, R. Amantea and J. H. Abeles, "Spectral Linewidth and Coherence of Distributed Output Coupled Master Oscillator Power Amplifier Semiconductor Laser", *IEEE Lasers and Electro-Optics Society 1992 Annual Meeting (LEOS'92)*, Talk DLTA10.4, Boston, MA, November 15-20 1992.

13. N. W. Carlson, R. Menna, P. Gardner, S. K. Liew, J. Andrews, A. Triano, J. Kirk, and W. Reichert, "High-power, single-frequency operation of an InGaAsP/InGaAs active-grating surface emitting amplifier at λ=1.7μm", *Appl. Phys. Lett.* 62 (17), pp. 2006-2008, 26 April 1993.

14. N. W. Carlson, S. K. Liew, R. Menna, P. Gardner, J. Andrews, J. Kirk, J. K. Butler, A. Triano, and W. Reichert, "Coherent, High-power Operation of InGaAsP/InGaAs Multiple-Quantum Well Active Grating-Surface-Emitting Amplifier Lasers", *Proc. SPIE* 1850, pp. 60-68, 26, 1993.

15. J. H. Abeles, P. K. York, N. W. Carlson, J. T. Andrews, W. F. Reichert, J. B. Kirk, N. A. Dinkel, C. G. Dupuy, J. T. McGinn, J. H. Thomas, T. J. Zamerowski, S. K. Liew, J. C. Connolly, G. A. Evans, and J. K. Butler, "High-power Index-Guided Distributed Out-Coupled Grating Surface Emitting Laser-Amplifiers with Narrow Spectra and High-Quality Beams", *Appl. Phys. Lett.* 62, pp. 955-957, 1993.

16. N. W. Carlson, P. Gardner, R. Menna, J. Andrews, R. Stolzenberger, A. Triano, E. Vangieson, D. Bour, G. A. Evans, S. K. Liew, J. B. Kirk, and W. F. Reichert, "Demonstration of an InGaAsP/InGaAs Multiquantum Well Active-Grating Surface-Emitting Amplifier", *IEEE Photonics Technology Letters* 4 (9), pp. 988-990, Sept. 1992.

17. N. W. Carlson, S. K. Liew, R. Amantea, J. H. Abeles, "Spectral Linewidth and Coherence Properties of Distributed Output Coupled Master Oscillator Power Amplifier Semiconductor Laser",*13th Int'l IEEE Semiconductor Laser Conference Digest*, Takamatsu, Japan, Sept. 21-25, 1992.

18. J. H. Abeles, R. Amantea, N. W. Carlson, J. T. Andrews, P. K. York, J. C. Connolly, R. Rios, W. F. Reichert, J. B. Kirk, T. J. Zamerowski, D. B. Gilbert, S. K. Liew, N. A. Hughes, J. K. Butler, G. A. Evans, S. Y. Narayan, and D. J. Channin, "Monolithic Fanned-Out Amplifier-Laser Master Oscillator Power Amplifiers",*13th Int'l IEEE Semiconductor Laser Conference Digest*, Takamatsu, Japan, Sept. 21-25, 1992.

19. J. H. Abeles, P. K. York, N. W. Carlson, J. T. Andrews, W. F. Reichert, J. B. Kirk, N. A. Dinkel, C. G. Dupuy, J. T. McGinn, J. H. Thomas, T. J. Zamerowski, S. K. Liew, J. C. Connolly, G. A. Evans, and J. K. Butler, "High-Power CW Distributed Out-Coupled Surface Emitting Laser-Amplifiers," *13th IEEE Int'l Semiconductor Laser Conference*, paper PD-12, Takamatsu, Japan, Sept. 21-25, 1992.

20. N. W. Carlson, J. H. Abeles, R. Amantea, J. K. Butler, G. A. Evans, S. K. Liew, "Characteristics of Active Grating-Surface-Emitting Amplified Lasers", *Proc. SPIE Vol. 1634 Laser Diode Technology and Applications IV*, pp.39-47, 1992.

21. N. W. Carlson, S. K. Liew, G. A. Evans, D. P. Bour, J. H. Abeles, R. Amantea, "CW operating characteristics of grating-surface-emitting master oscillator power amplifier laser arrays", *Technical Digest: Conference on Lasers and Electro-Optics (CLEOS 1991)* Vol. 11, pp. 250-251, 1991.

22. N. W. Carlson, J. H. Abeles, D. P. Bour, S. K. Liew, W. F. Reichert, P. S. D. Lin, and A. S. Gozdz, "Demonstration of a Monolithic, Grating-Surface-Emitting Laser Master Oscillator-Cascaded Power Amplifier Array", *IEEE Photonics Technology Letters* Vol. 2, No. 10, pp. 708-710, Oct. 1990.

2-Dimensional Grating-Surface-Emitting Laser Arrays

23. S. K. Liew, N. W. Carlson, G. A. Evans, R. Amantea, D. P. Bour, J. M. Hammer, J. B. Kirk, W. F. Reichert, R. Stolzenberger, J. K. Butler, R. K. DeFreez, M. Felisky, C. A. Wang, H. K. Choi, J. N. Walpole, "Coherent Continuous Wave Operation of 10x10x2 Grating-Surface-Emitting Laser Arrays in a Ring Configuration", *Journal of Applied Physics* 70 (12), pp. 7645-7647, 15 Dec. 1991.

24. S. K. Liew, G. A. Evans, N. W. Carlson, R. Amantea, D. P. Bour, J. K. Butler, J. M. Hammer, J. B. Kirk, W. F. Reichert, R. Stolzenberger, R. K. DeFreez, M. Felisky, C. A. Wang, H. K. Choi, J. N. Walpole, "Coherent cw operation of one- and two-dimensional grating-surface-emitting semiconductor lasers", *Technical Digest: Conference on Lasers and Electro-Optics (CLEO 1991)*, Talk CWE4, May, 1991.

25. M. Felisky, R. K. DeFreez, G. A. Wilson, G. A. Evans, N. W. Carlson, S. K. Liew, R. Amantea, J. H. Abeles, C. A. Wang, H. K. Choi, J. N. Walpole, H. G. Winful, "Dynamics of cw grating-surface-emitting laser arrays", *Technical Digest: Conference on Lasers and Electro-Optics (CLEO 1991)*, Talk CWE6, May, 1991.

26. G. A. Evans, D. P. Bour, N. W. Carlson, R. Amantea, J. M. Hammer, H. Lee, M. Lurie, R. Lai, P. Pelka, R. Farkas, J. B. Kirk, S. K. Liew, W. F. Reichert, C. A. Wang, H. K. Choi, J. N. Walpole, J. K. Butler, and W. E. Ferguson, R. K. DeFreez, and M. Felisky, "Characteristics of Coherent Two Dimensional Grating Surface Emitting Diode Laser Arrays During CW Operation", *IEEE Journal of Quantum Electronics* QE-27, No. 6, pp. 1594-1608, June 1991.

27. N. W. Carlson, D. R. Patterson, P. J. Stabile, S. K. Liew, D. P. Bour, G. A. Evans, "Demonstration of Digital Pulse Modulation of a Grating-Surface-Emitting Diode Laser", *Electronics Letters* Vol. 26, No. 20, pp. 1695-1696, 27th Sept. 1990.

28. N. W. Carlson, D. P. Bour, G. A. Evans, R. Amantea, and S. K. Liew, "Stable single mode operation of grating-surface-emitting laser arrays under frequency-modulated operation", *Appl. Phys. Lett.* 57 (8), pp. 756-758, 20 Aug. 1990.

29. G. A. Evans, N. W. Carlson, D. P. Bour, J. M. Hammer, M. Lurie, J. K. Butler, R. Amantea, S. K. Liew, J. B. Kirk, W. F. Reichert, R. K. DeFreez, and D. J. Bossert, "Two dimensional grating surface emitting laser arrays with wide lateral extent", *Electronics Letters* Vol. 26 No. 13, pp. 907-908, 21st June 1990.

30. N. W. Carlson, D. P. Bour, G. A. Evans, and S. K. Liew, "Spectral Linewidth Narrowing in Monolithic Grating-Surface-Emitting Laser Arrays", *IEEE Photonics Technology Letters*, Vol. 2, No. 4, pp.242-243, April 1990.

31. J. M. Hammer, G. A. Evans, N. W. Carlson, D. P. Bour, M. Lurie, S. L. Palfrey, R. Amantea, S. K. Liew, L. A. Carr, E. A. James, J. B. Kirk, and W. F. Reichert, "Lateral beam steering in mutual injection coupled Y-branch grating-surface-emitting diode laser arrays", *Appl. Phys. Lett.* 56 (3), pp.224-226, 15 Jan. 1990.

32. N. W. Carlson, G. A. Evans, M. Lurie, J. M. Hammer, C. J. Kaiser, and S. K. Liew, "Coherent coupling of independent grating-surface-emitting diode laser arrays using an external prism", *Appl. Phys. Lett.* 56 (2), pp. 114-116, 8 Jan. 1990.

33. N. W. Carlson, G. A. Evans, D. P. Bour, and S. K. Liew, "Demonstration of a grating-surface-emitting diode laser with low-threshold current density", *Appl. Phys. Lett.* 56 (1), pp. 16-18, 1 Jan. 1990.

34. N. W. Carlson, R. Amantea, G. A. Evans, D. P. Bour, and S. K. Liew, "Applications of Surface Emitting Lasers to Coherent Communications Systems", *IEEE Lasers and Electro-Optics Society 1994 Annual Meeting (LEOS'90) Conference Proceedings*, pp. 406-409, 1990.

35. M. Lurie, G. A. Evans, N. W. Carlson, D. P. Bour, R. Amantea, J. M. Hammer, T. F. A. Bibby, D. B. Gilbert, and S. K. Liew, "Coherent CW Operation of 2-D Grating Surface Emitting diode Laser Arrays", *Proc. SPIE Vol. 1219 Laser-Diode Technology and Applications II* , pp. 233-241, 1990.

36. G. A. Evans, D. P. Bour, N. W. Carlson, J. M. Hammer, M. Lurie, J. K. Butler, S. L. Palfrey, R. Amantea, L. A. Carr, F. Z. Hawrylo, E. A. James, J. B. Kirk, S. K. Liew, and W. F. Reichert, "Coherent, monolithic two-dimensional strained InGaAs/AlGaAs quantum well laser arrays using grating surface emission", *Appl. Phys. Lett.* 55 (26), pp. 2721-2723, 25 Dec. 1989.

37. D. P. Bour, N. W. Carlson, G. A. Evans, and S. K. Liew, "Low threshold current density grating-surface-emitting lasers by OMVPE", *Int'l Electron Devices Meeting (IEDM) 1989 Technical Digest*, pp. 857-860, 1989.

38. N. W. Carlson, G. A. Evans, S. K. Liew, and C. J. Kaiser, "High-Speed Switching of Monolithic Arrays of Grating-Surface-Emitting Diode Lasers", *IEEE Journal of Lightwave Technology* Vol. 7, No. 10, pp. 1520-1524, Oct. 1989.

39. N. W. Carlson, G. A. Evans, S. K. Liew, and C. J. Kaiser, "Sub-nanosecond Electrooptic Switching of Coherent Grating Surface Emitting Diode Laser Arrays", *7th Int'l Conf. on Integrated Optics and Optical Fiber Communication, Technical Digest,* p. 27, July 1989.

Laser Array in External Cavity

40. R. H. Rediker, C. Corcoran, L. Y. Pang, and S. K. Liew, "Validation of Model of External-Cavity Semiconductor Laser and Extrapolation from Five-Element to Multielement Fiber-Coupled High-Power Laser", *IEEE Journal of Quantum Electronics,* Vol. QE-25, No. 6, pp. 1547-1552, June 1989.

Phase-locked Laser Array

41. N. W. Carlson, S. K. Liew, G. A. Evans, and J. K. Butler, "Observation of Self-Sustained Pulsations from a Highly Coherent Channeled Substrate Planar Diode Laser Array", *Conference on Lasers and Electro-Optics 1989 (CLEO'89) Technical Digest* , Vol. 11, pp. 302-303, April 1989.

INDEX

CUHK Libraries
000294051